THE UNIVERSITY OF QUEENSLAND

AUSTRALIA

Direct Numerical Simulations of Instabilities in the Entropy Layer over a Hypersonic Blunted Slender Cone

Lachlan Whyborn

0000-0002-3084-4496

A thesis submitted for the degree of Doctor of Philosophy at The University of Queensland in 2023

School of Mechanical and Mining Engineering

Abstract

The prediction of boundary layer transition remains a significant hurdle in the design of hypersonic vehicles. This thesis is focussed on the early stages of transition on blunted slender vehicles in hypersonic flow, characteristic of forebodies on high-speed vehicles. Direct numerical simulations are employed to investigate the response of the flow to external disturbances, in particular the response of the flow in the entropy layer outside the boundary layer. The geometry and conditions of Stetson et al., Mach 8 flow over a 17.78mm nose radius cone with a 7 degree half-angle, are used to attempt to explain their observations of mass flux fluctuations at the generalised inflection point in the entropy layer.

The compressible fluid dynamics software Eilmer, developed in-house at the University of Queensland, is used to perform these simulations. A high-order Summation-by-Parts finite difference method is implemented within a finite volume framework for the convective fluxes. The accuracy and performance of the Summation-by-Parts method is tested using Isentropic Vortex Advection, Inviscid Taylor-Green Vortex and Kelvin-Helmholtz instability canonical test cases. The method achieves high order accuracy, maintains kinetic energy and entropy in systems without viscosity and accurately captures the evolution of flow instabilities. Comparison is made to the approximate Riemann methods which are popular in finite volume frameworks. Splitting the numerical error into dissipation and dispersion components shows that the approximate Riemann methods cannot achieve high-order accuracy, even with highly accurate Riemann state construction, due to the dispersion error. A particular test problem, the Steepening Wave problem, is extended to act as a pseudo Modified Wavenumber analysis to quantify the resolution required to accurately capture a given wavelength. The Modified Wavenumber analysis can be non-trivial for complicated numerical schemes, so this simple test problem provides a useful alternative that can be applied universally.

The practical considerations required for preparing a basic flow state for direct numerical simulations within the Eilmer software are described in detail. The Newton-Krylov steady-state accelerator was found to be numerical unstable when the linear preconditioner was constructed using the high-order Summation-by-Parts convective fluxes, which was addressed by reverting to an approximate Riemann scheme for preconditioner construction. This is advantageous over traditional implicit approaches which construct the Jacobian using dissipative schemes, as the final solution is unaffected by additional numerical dissipation.

Axisymmetric simulations forced by white noise in the freestream show that disturbances in the density field in the entropy layer are the dominant fluctuations in the flow. The pressure and velocity fluctuations barely rise above the background noise level, so the fluctuations are entropic in nature. There are multiple distinct disturbance types that appear in the entropy layer: one associated with the generalised inflection point, one which amplifies downstream of the location where the inflection point merges with the boundary layer, and one along the edge of the entropy layer. The frequency band associated with these disturbances remains in

the 20-100kHz range for all of these distinct disturbances. The behaviour of these disturbances is not strongly affected by the flow in the nose region.

Further high fidelity axisymmetric and three dimensional simulations on a domain that begins downstream of the nose region show that the magnitude of the axisymmetric density disturbances are a minimum at the generalised inflection point, while three dimensional disturbances are a maximum at this location. The phase of the density fluctuations is discontinuous at the inflection point, indicating that the disturbances consist of neutral supersonic waves. These fluctuations grow transiently in space as evidenced by the linear spatial amplification. This is in agreement with the conclusion that the disturbances consist of neutral supersonic waves, which permit a continuous spectrum of solutions generally associated with transient growth phenomena. The relationship between these computational results and experimental observations is discussed.

Declaration by author

This thesis is composed of my original work, and contains no material previously published or written by another person except where due reference has been made in the text. I have clearly stated the contribution by others to jointly-authored works that I have included in my thesis.

I have clearly stated the contribution of others to my thesis as a whole, including statistical assistance, survey design, data analysis, significant technical procedures, professional editorial advice, financial support and any other original research work used or reported in my thesis. The content of my thesis is the result of work I have carried out since the commencement of my higher degree by research candidature and does not include a substantial part of work that has been submitted to qualify for the award of any other degree or diploma in any university or other tertiary institution. I have clearly stated which parts of my thesis, if any, have been submitted to qualify for another award.

I acknowledge that an electronic copy of my thesis must be lodged with the University Library and, subject to the policy and procedures of The University of Queensland, the thesis be made available for research and study in accordance with the Copyright Act 1968 unless a period of embargo has been approved by the Dean of the Graduate School.

I acknowledge that copyright of all material contained in my thesis resides with the copyright holder(s) of that material. Where appropriate I have obtained copyright permission from the copyright holder to reproduce material in this thesis and have sought permission from co-authors for any jointly authored works included in the thesis.

Publications included in this thesis

1. [1] **Lachlan Whyborn**, Rowan Gollan and Peter Jacobs, Quantitative Comparison of Numerical Errors for High-Speed Flux Schemes, *Proceedings of the 22nd Australasian Fluid Mechanics Conference*.

2. [2] **Lachlan Whyborn**, Rowan Gollan and Peter Jacobs, Multiple Instabilities in the Entropy Layer of a Hypersonic Blunt Cone, *Proceedings of the 2nd International Conference on Flight Vehicles, Aerothermodynamics and Re-entry Missions*.

3. [3] **Lachlan Whyborn**, Rowan Gollan and Peter Jacobs, Hypersonic Entropy Layer Instabilities Forced by Coherent Freestream Disturbances, *Proceedings of the 23rd Australasian Fluid Mechanics Conference*.

4. [4] **Lachlan Whyborn**, Rowan Gollan and Peter Jacobs, Simulation of Multiple Instabilities in the Entropy Layer of a Hypersonic Blunt Cone, *AIAA SciTech Forum 2023*.

Submitted manuscripts included in this thesis

No manuscripts submitted for publication.

Other publications during candidature

No other publications.

Contributions by others to the thesis

No contributions by others.

Statement of parts of the thesis submitted to qualify for the award of another degree

No works submitted towards another degree have been included in this thesis.

Research involving human or animal subjects

No animal or human subjects were involved in this research.

Acknowledgments

First thanks go to my supervisors, Dr. Rowan Gollan and Dr. Peter Jacobs. For Rowan's advice and guidance on the overall trajectory of this project and countless instances of feedback. Peter for the corridor conversations on computational and physical ideas, and on what people actually want to know. Second to my colleagues at the Technical University of Munich, Professor Christian Stemmer, Frederick Ulrich and Giuseppe Chiapparino. To Professor Stemmer, the many zoom and (Covid delayed) in person discussion on the finer details of the theory and physics of boundary layer transition, and to Giuseppe and Fritz for the insightful questions and feedback during our meetings.

To others within the Centre for Hypersonics, special thanks go to Nick and Kyle for discussions about the Eilmer code and some of the numerical considerations that went into this work. To many others, namely Christine, Kyri, Reece and Rob, for being a sounding board for my lunchtime thoughts and providing valuable feedback on these ideas. The Centre for Hypersonics has made the last 4 years and enjoyable and truly valuable experience.

To my Dad and Deb, who have of course been providing support throughout my thesis. These things are really not possible without a support group outside work.

Finally, to my Mum. Passed at the lowest point in my life, I wish you could have been here to see me at my highest.

Financial support

This research was supported by an Australian Government Research Training Program Scholarship.

Keywords

hypersonics, boundary layers, transition, computational fluid dynamics

Australian and New Zealand Standard Research Classifications (ANZSRC)

ANZSRC code: 090107, Hypersonic Propulsion and Hypersonic Aerodynamics, 100%

Fields of Research (FoR) Classification

FoR code: 0901, Aerospace Engineering, 100%

Contents

Abstract ii

Contents **viii**

List of Figures **x**

1 Introduction **1**
1.1 Motivations 1
1.1.1 Hypersonic Boundary Layer Transition over Blunted Slender Bodies . 1
1.1.2 Numerical Methods for High-Fidelity Simulations 4
1.1.3 Thesis Aims 5

2 The State of the Art **7**
2.1 Boundary Layer Transition 7
2.1.1 A Brief Overview 7
2.1.2 Linear Stability Theory of Compressible Flow 10
2.1.3 Transition Reversal on Blunted Bodies 16
2.1.4 Medium Bluntness 22
2.2 Numerical Schemes for Direct Numerical Simulations 32
2.2.1 Methods for Computational Fluid Dynamics 34

3 Numerical Schemes within Eilmer **39**
3.0.1 Approximate Riemann Schemes in Eilmer 39
3.1 The Summation-by-Parts Alpha-Split-Flux Convective Flux Scheme 40
3.1.1 Approximate Riemann Solvers in Eilmer 42
3.2 Verification 42
3.2.1 Advection of an Isentropic Vortex 42
3.2.2 Steepening Wave 53
3.3 Validation 54
3.3.1 Inviscid Taylor-Green Vortex 54
3.3.2 Continuous Kelvin-Helmholtz Instability 59
3.4 Concluding Remarks 63

4 Preliminary Simulations of Stetson's Blunt Cone 65
4.1 Generation of the Base Flow . . . 65
4.1.1 Numerical Considerations . . . 66
4.1.2 First Stage: Shock Fitting . . . 67
4.1.3 Mesh Generation . . . 69
4.1.4 The Newton-Krylov Steady-State Accelerator . . . 72
4.2 Time-Accurate Simulations . . . 81
4.2.1 Frequency Domain . . . 82
4.2.2 Concluding Remarks . . . 92

5 High-Fidelity Simulations of Stetson's Blunt Cone 95
5.1 Axisymmetric Simulations . . . 97
5.1.1 Relationship to the theory of Lees and Lin [5] . . . 99
5.1.2 Transfer of Energy from the Base Flow to Disturbances . . . 102
5.2 Three-Dimensional Domain . . . 109
5.3 Relationship with other Numerical and Experimental Results . . . 117
5.3.1 Concluding Remarks . . . 120

6 Conclusions 123
6.1 Method Development and Verification . . . 123
6.2 Findings from Direct Numerical Simulations . . . 124
6.2.1 Workflow for Base Flow Generation in Eilmer . . . 124
6.2.2 Findings from Time-Accurate Simulations . . . 125
6.3 Contributions of this Work . . . 127
6.4 Further Work . . . 128

Bibliography 129

List of Figures

1.1 Visual representations of the transition process 3
1.2 Morkovin and Reshotko's paths to transition 4

2.1 Oscillogram of velocity oscillations from Schubauer and Skramstad 8
2.2 Viscous and inviscid stability diagrams 13
2.3 Transition N-factors for Mach 5.8 sharp cone flow in BAM6QT in conventional and quiet mode 14
2.4 Comparison of Navier-Stokes, Parabolised Stability Equations and One-Way Navier Stokes wave treatment 15
2.5 Reshotko's paths to transition 17
2.6 Schematic of the entropy layer 17
2.7 Visualisation of entropy layer extent over increasing nose bluntness cones 18
2.8 Softley's collation of transition results with nose bluntness 19
2.9 Transition trend demonstrating nose bluntness regimes 20
2.10 Comparison of sharp and blunt nose boundary layer spectra 21
2.11 Surface pressure power spectral density measurements for small bluntnesses 21
2.12 Shifting of unstable region with nose bluntness computed by Linear Stability Theory 21
2.13 Effect of surface roughness on transition for small and large nose bluntness at Mach 5.9 22
2.14 Inflected angular momentum profile for the conditions studied in this work 23
2.15 Experimental mass flux fluctuations profiles for the conditions studied in this work 24
2.16 Schlieren visualisation of structures in the entropy layer 25
2.17 Surface pressure spectra over a cone-ogive cylinder at Mach 6 26
2.18 Disturbance shape yielding optimal growth in an incompressible boundary layer 29
2.19 N-factors for computed optimal disturbances for Mach 5.9 flow over a 5.08mm nose radius cone 30
2.20 Turbulent breakdown via entropy layer disturbances 31
2.21 Full domain direct numerical simulations of a 5.2mm nose radius cone in Mach 8 flow 32
2.22 Effect of increasing order of accuracy on resolution of a step function 35

2.23 Effect of grid alignment on flow convergence 37

3.1 Illustration of the construction of the left and right Riemann states in Eilmer. This particular example uses quadratic polynomials for state construction; fourth order polynomials which use 6 cell stencils are also available. The cell states Q are the state variable vectors, and L is the width of the cell in the interface normal direction. 40
3.2 Initial density field for the Isentropic Vortex 44
3.3 Evolution of the Isentropic Vortex with different flux schemes 45
3.4 Comparison of density profiles of the Isentropic Vortex with different convective flux schemes on a uniform grid 46
3.5 L2 error norms on a uniform grid 46
3.6 Dissipation and dispersion errors on a uniform grid 47
3.7 Density profile of the Isentropic Vortex after 10 advections periods using the Summation-by-Parts scheme 48
3.8 Gaussian clustered mesh for the Isentropic Vortex 49
3.9 L2 error norms on a non-uniform grid 50
3.10 Dissipation and dispersion errors on a non-uniform grid 51
3.11 Density profiles of the Isentropic Vortex on a non-uniform grid 52
3.12 Steepening wave problem 53
3.13 Comparison of spatial resolution for different convective flux schemes using the Steepening wave 55
3.14 Initial conditions for the Inviscid Taylor-Green Vortex 56
3.15 Evolution of kinetic energy and entropy for the Inviscid Taylor-Green Vortex . . 57
3.16 Visulations of the Inviscid Taylor-Green Vortex using different convective flux schemes 58
3.17 Initial velocity conditions for the Kelvin-Helmholtz instability 60
3.18 Density field of the Kelvin-Helmholtz instability at $\tau = 25$ with different convective flux schemes 60
3.19 Growth rate of the Kelvin-Helmholtz instability 61
3.20 Streamlines showing singularity in the Kelvin-Helmholtz solution 62

4.1 Geometry and conditions used in this work 66
4.2 Shock detector smoothing process in Eilmer 68
4.3 Starting and final meshes after shock fitting 68
4.4 GridPro topology used to generate refined mesh 70
4.5 Wall-normal profiles of density, temperature and streamwise velocity 72
4.6 Wall-normal profiles of streamwise velocity, enthalpy and entropy increment . . 73
4.7 Mesh used for base flow generation 74
4.8 Numerical instability encountered using the Newton-Krylov scheme 74
4.9 Visualisation of converged streamwise velocity and density fields 75

4.10 Total, mass, and energy residuals (relative to initial residuals) with the Jacobian-Free Newton-Krylov scheme. 77
4.11 Boundary and entropy layer thickness over the model 77
4.12 Unit Reynolds and Mach number at the boundary layer edge 78
4.13 Wall-normal profiles of density, velocity shear and compressible shear 79
4.14 Location of the entropy layer inflection point over the model 80
4.15 Instantaneous snapshots of fluctuation density, streamwise velocity, pressure and mass flux with white noise freestream forcing in the nose region 83
4.16 Instantaneous snapshots of fluctuation density, streamwise velocity, pressure and mass flux with white noise freestream forcing in the frustum region 84
4.17 Demonstration of disturbance amplitude calculation 85
4.18 Magnitude of density, pressure, streamwise velocity and mass flux disturbance amplitudes along the model 87
4.19 Magnitude and real part of 80kHz Fourier field of the pressure 88
4.20 Magnitude and real part of the 55kHz Fourier field of the density 89
4.21 Magnitude and real part of the 90kHz Fourier field of the density in the nose region 90
4.22 Magnitude and real part of the 90kHz Fourier field of the density in the frustum region 91
4.23 Truncated domain used in Chapter 5 92

5.1 Shape of forcing function on the truncated domain 96
5.2 Truncated mesh 97
5.3 Relative amplitude of density and vorticity fluctuations over the model 98
5.4 Growth trends of the density fluctuations 99
5.5 Magnitude and real part of the 60kHz Fourier field of density in the frustum region 100
5.6 Schlieren visualisation of structures in the entropy layer 102
5.7 Wall-normal profiles of the entropy gradient and RMS of the density fluctuations 104
5.8 Wall-normal profiles of $\frac{1}{T}\frac{du_\xi}{d\eta}$ and density fluctuations at select frequencies 106
5.9 Growth trends of vorticity fluctuations 107
5.10 Fourier field of the vorticity at 20kHz with the path of a characteristic from the epicentre of the forcing function 108
5.11 Real and imaginary parts of the 20kHz vorticity mode 109
5.12 Comparison of instantaneous density fluctuations in the axisymmetric and three dimensional domains 110
5.13 Peak amplitude of the density fluctuations 111
5.14 Growth trends of the 10kHz and 40kHz density fluctuations 112
5.15 Magnitude of the density Fourier field at 10kHz for the axisymmetric and first 2 spanwise modes 113

5.16 Real part of the density Fourier field at 10kHz for the axisymmetric and first 2 spanwise modes . . . 114
5.17 Comparison of root-mean-square fluctuations to Stetson's measurements . . . 116
5.18 Survey of noise levels in hypersonic wind tunnels . . . 118
5.19 Schlieren visualisation of second mode structures . . . 119
5.20 Schlieren visualisation of entropy layer structures . . . 119

6.1 Instantaneous fluctuations of density and pressure with white noise freestream forcing . . . 126
6.2 Magnitude and real part of the Fourier field of density at 40kHz in the frustum region . . . 127

Chapter 1

Introduction

The space industry has undergone massive growth in the preceding decade, with increasing partnerships between government and private industry driven in large part by the success of commercial entities such as SpaceX. Commerical interests bring an increased desire for long-term reusability and reliability. There are a range of viable approaches for access-to-space applications, each coming with design challenges. These vehicles reach hypersonic speeds in both ascent and descent, so regardless of the choice of vehicle type, it must be able to withstand immense heat loads. This introduces conflicting design objectives— techniques to address the heat loads add weight to the vehicle, but the vehicle should be as light as possible to minimize fuel required for a given mission. The accurate prediction of heat loads during flight is a huge benefit as it allows finely tailored thermal protection or mitigation systems with minimised added weight. For accurate heating predictions, the state of the fluid layer at the vehicle surface, known as the boundary layer, must be known.

The study of flow phenomena in the hypersonic regime is hindered by the extreme conditions generated by such a flow. Flight experiments are expensive and are difficult to measure, while artificially generated hypersonic flows in wind tunnels have limitations reproducing the conditions that will be experienced in flight. Computational methods are a powerful complement to physical experiments. With the exponential growth in computing power, high fidelity simulations allow the in-depth study of these hypersonic flow phenomena. Developing and validating computational methods for simulating hypersonic flow is essential for the progress of high-speed atmospheric and space flight.

1.1 Motivations

1.1.1 Hypersonic Boundary Layer Transition over Blunted Slender Bodies

The state of the boundary layer has first-order effects on aerodynamic heating and drag, with flow-on effects on the action of control surfaces and fuel mixing in air-breathing engines.

Current numerical methods provide accurate predictions of both laminar and turbulent flow effects, but predictions of the point of transition between these states are, at best, rough estimates. With such poor prediction methods, components such as thermal protection and control surfaces must be designed conservatively to address the span of possible transition points. This technical deficiency was a key factor leading to the cancellation of the US' National Aerospace Plane [6].

The precise location of transition is incredibly difficult to predict. Anderson [7] writes that the expression for the transition Reynolds number can be written as

$$\mathrm{Re}_T = f\left(M_e, \theta_c, T_w, \dot{m}, \alpha, k_R, E, \frac{\partial p}{\partial x}, R_N, \mathrm{Re}_\infty/\mathrm{ft}, \frac{x}{R_N}, V, C, \frac{\partial w}{\partial z}, T_0, d*, \tau, Z\right) \tag{1.1}$$

which is a mathematical way of saying "The transition location is generally dependent on everything". While simple transition correlations do exist, most are at best empirical relations loosely based on the underlying physics, at worst purely empirical with no link to the physics involved, and all have such significant uncertainties involved that they provide limited benefit to the design process. There are empirical relations based on various forms of the Reynolds number, built through parameter sweeps in wind tunnels. There are N-factor correlations, which combine calculations from linear theory with tunnel measurements. But these methods do not take into account environmental factors, and do not translate well to other configuration or outside the original parameter space.

It seems unlikely that there will ever be accurate transition correlations that can be done with pen and paper, so one could fairly ask "Why study transition at all?". The answer is a solid understanding of the underlying phenomena will allow the development of simplified computational models based on the physics which could be run on a local workstation. It is analogous to the development of turbulence models: a deeper understanding of turbulence does not allow the design engineer to directly simulate turbulence, but it does lead to the development of turbulence models which emulate the effect of turbulence.

The process of boundary layer transition is understood in broad strokes. An initially laminar boundary layer is seeded with minute disturbances or fluctuations through environmental factors such a freestream variations and surface roughness, which grow in space due to locally favourable flow gradients and, once the fluctuations are large enough, nonlinear mechanisms cause the laminar flow to break down to turbulence. This process is demonstrated schematically and experimentally in Figure 1.1. The transition process contains multiple complex stages and is dependent on the flow conditions, vehicle orientation and geometry, making the development of empirical correlations a pipe dream, at least with the current state of the art.

The laminar boundary layer can take one of many routes to transition, with the route primarily dependent on the magnitude of the environmental disturbances, most often roughness on the surface of the vehicle and natural variations in the incoming fluid. The

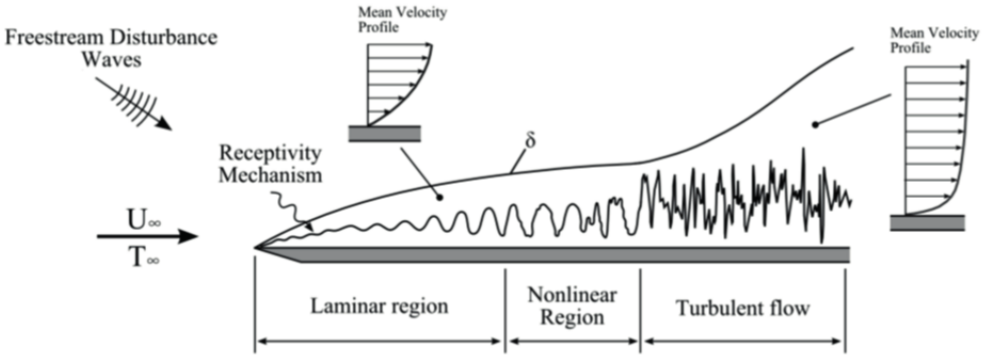

(a) Schematic of the boundary layer transition process [8].

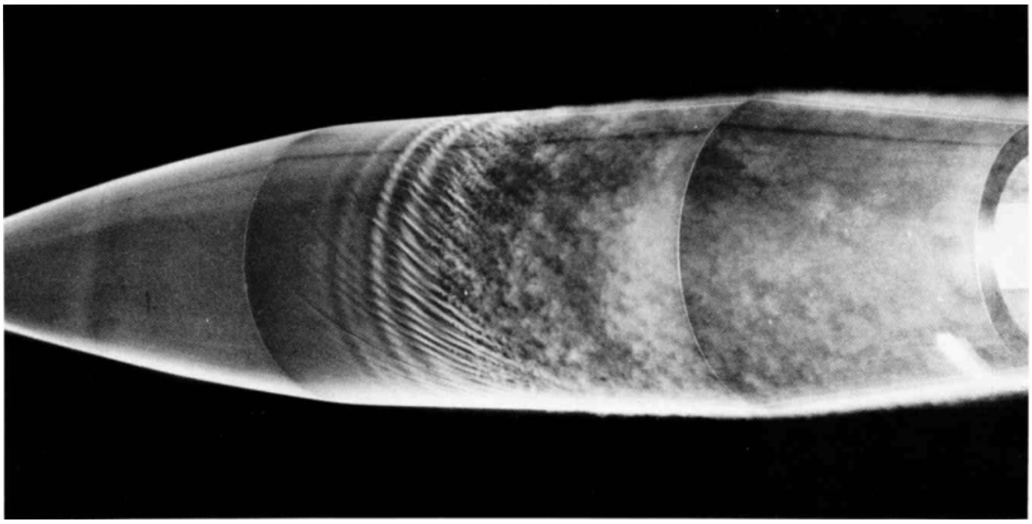

(b) The transition process visualised using smoke injection in a low speed flow over a rotating body. Flow is travelling from left to right. Periodic structures appear approximately 1/3 of the way along the body, amplify downstream then break down to turbulence. From An Album of Fluid Motion [9].

Figure 1.1: Schematic and experimental visualisations of the boundary layer transition process.

possible routes are described in Figure 1.2 from Reshotko [10] (originally due to Morkovin et al. [11]), with the paths A to E corresponding to increasingly large environmental disturbances. Transition in free flight scenarios takes the paths A through C in most tunnel experiments, and given the environmental disturbances are generally much greater in tunnels than in free flight it is expected that flight transition should take the same paths.

In broad terms, this thesis concerns the early stages of transition (i.e. receptivity, transient growth and eigenmode growth) in the low hypersonic regime i.e. Mach 5-10. These stages are relatively well understood in this flight regime for flat plate like geometries i.e. sharp wedges and cones. Unfortunately realistic flight vehicles do not have sharp leading edges; the significant heat loads concentrated on such a small volume make such a configuration impossible without significant advances in materials science and thermal protection systems. Blunting of the leading edge mitigates the heat load, with the additional benefit of delaying boundary layer transition up to a point. The trend of transition delay with increasing leading

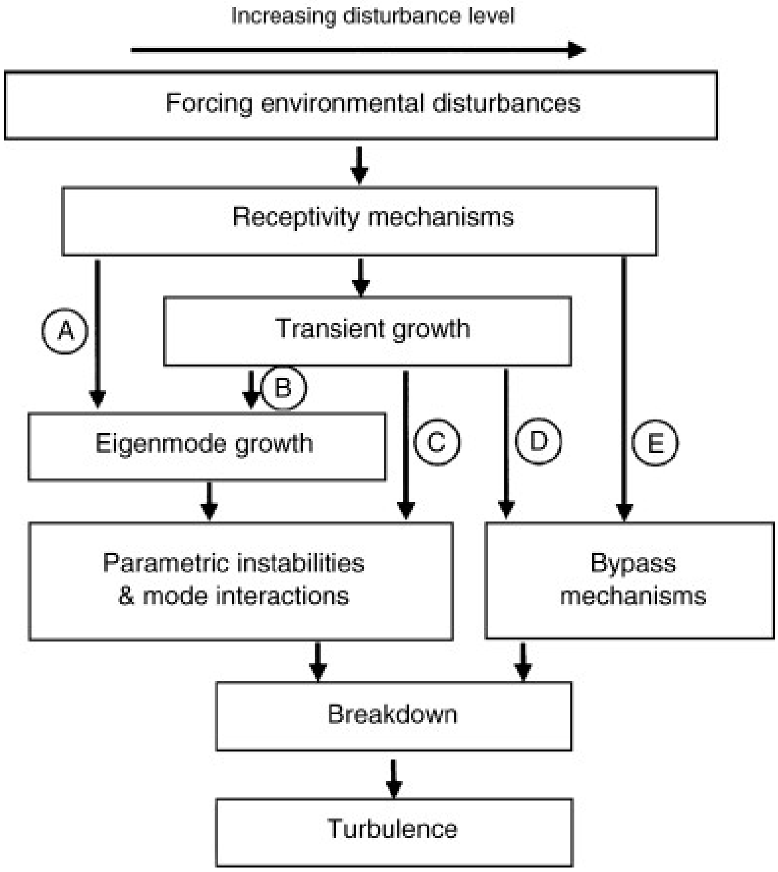

Figure 1.2: Morkovin and Reshotko's paths to transition. Paths A-E denote paths with increasing environmental disturbances. Paths A-C are most relevant to flight vehicles.

edge bluntness holds up until a point, at which the trend reverses and the transition front shifts back upstream, a phenomenon known as transition reversal [12, 13]. Both the cause of this reversal in trend and the mechanism driving transition close to it are not well known and as such are the primary focus of this work. If the mechanism is understood, it may be possible to design for and exploit for performance improvements.

1.1.2 Numerical Methods for High-Fidelity Simulations

Numerical techniques are an essential complement to tunnel and flight testing, particularly in the hypersonic regime. Flight testing is very expensive due to the difficulty of achieving the desired conditions, and tunnel testing is hindered by the difficulty of generating such high speed gas flows and the noisiness of such generated flows. There is the additional requirement that any instrumentation must be non-intrusive, meaning off-surface measurements are very difficult, although significant progress has been made in this area with the development of laser-based measurement techniques [14–16]. Computational techniques are not hindered by such limitations, so make ideal tools for investigating the finer details that are difficult to measure in experiments. They are instead limited by the fact they are only simulating a model of reality, not the reality itself.

Before drawing any conclusions from computational techniques, one must be confident that the models used provide a sufficiently accurate replica of the real world phenomena they are trying to imitate. Given the lack of understanding regarding the transition phenomena, the physics must be captured directly which introduces immense computational cost. The computational cost can be mitigated by improving the accuracy of the numerical techniques used to simulate the fluid dynamics. The choice and implementation of a highly-accurate numerical scheme for the purpose of Direct Numerical Simulations (DNS) within the in-house computational fluid dynamics (CFD) program Eilmer [17] is the secondary objective of this thesis.

1.1.3 Thesis Aims

The primary aims of the thesis follow a logical progression from the development of numerical tools to the usage of said numerical tools for investigation of the fundamental physics underlying blunt cone transition. The first aim is to choose and implement a numerical scheme appropriate for the DNS of laminar and early transitional flows. The implementation is verified through a series of canonical test problems, as well as a simple new test problem that tests the scheme's spatial resolution with respect to wave behaviour in Chapter 3.

Once the scheme has been verified, it is utilised to investigate the nature of instabilities in the entropy layer of a blunt cone in Chapter 4. Axisymmetric simulations are performed first as the reduced computational cost allows for exploratory simulations. The best practices for preparing a transitional DNS in the Eilmer code are determined.

The results of the axisymmetric simulations are used to inform targeted high fidelity axisymmetric and three dimensional simulations in a sub-domain of the cone flow. These results are analysed in the Fourier space then compared to experimental results on the same geometry and numerical predictions on similar geometries. Some insight into the nature of the disturbances in the entropy layer is gained through the theory of Lees and Lin [5] in Chapter 5.

In a broader context, this project is a step in a new direction for the computational group within the Centre of Hypersonics at the University of Queensland. There is minimal expertise within the group on boundary layer transition or DNS, and with the exponential increase in computing resources available, it seems beneficial to develop this expertise. In many areas, there are subtleties to particular techniques that are passed through word of mouth, corridor conversations and such, which one otherwise learns through doing. It was certainly found to be the case for some of the work in this thesis.

Chapter 2

The State of the Art

This literature review covers the state of the art of boundary layer transition knowledge, particularly on blunted slender bodies. A brief introduction to the underlying theories of boundary layer transition, applicable to transition in all scenarios, begins the review. The different transition mechanisms that manifest in blunted body boundary layers at hypersonic speeds are addressed, highlighting recent experimental work and the areas still lacking in understanding.

The state of the art regarding the numerical tools relevant to this work will be addressed after the transition theory has been covered.

2.1 Boundary Layer Transition

2.1.1 A Brief Overview

The method of small disturbances, which forms the basis of transitional study today, originated with Tollmien and Schlichting in the 1920's and 30's. In a series of papers inspired by the works of Taylor and Prandtl, who independently demonstrated that viscosity can destabilize a flow, Tollmien [18,19] and Schlichting [20–23] developed a theory of 2D viscous instability in a flat plate incompressible boundary layer (Blasius layer) with some limited numerical results. The theory described the growth rate of initially small disturbances within the boundary layer using linear approximations. The amplification rates of these disturbances would be defined via their frequency, such that the stability of a boundary layer would depend on the frequency of the initial disturbances and the local Reynolds number, rather than the disturbance amplitudes. Any reference to the 'stability' of a boundary layer refers to the rates of amplification of disturbances within layer; a boundary layer is considered unstable if any frequency and wavenumber pair is locally amplified. The experiment of Schubauer and Skramstad [24] later verified at least the fundamentals of their theory, that transition is dominated by the growth of initially small disturbances, which has since become the basis of almost all transition studies. Figure 2.1 from said experiment illustrates the amplification process of initially small mass-flow disturbances excellently.

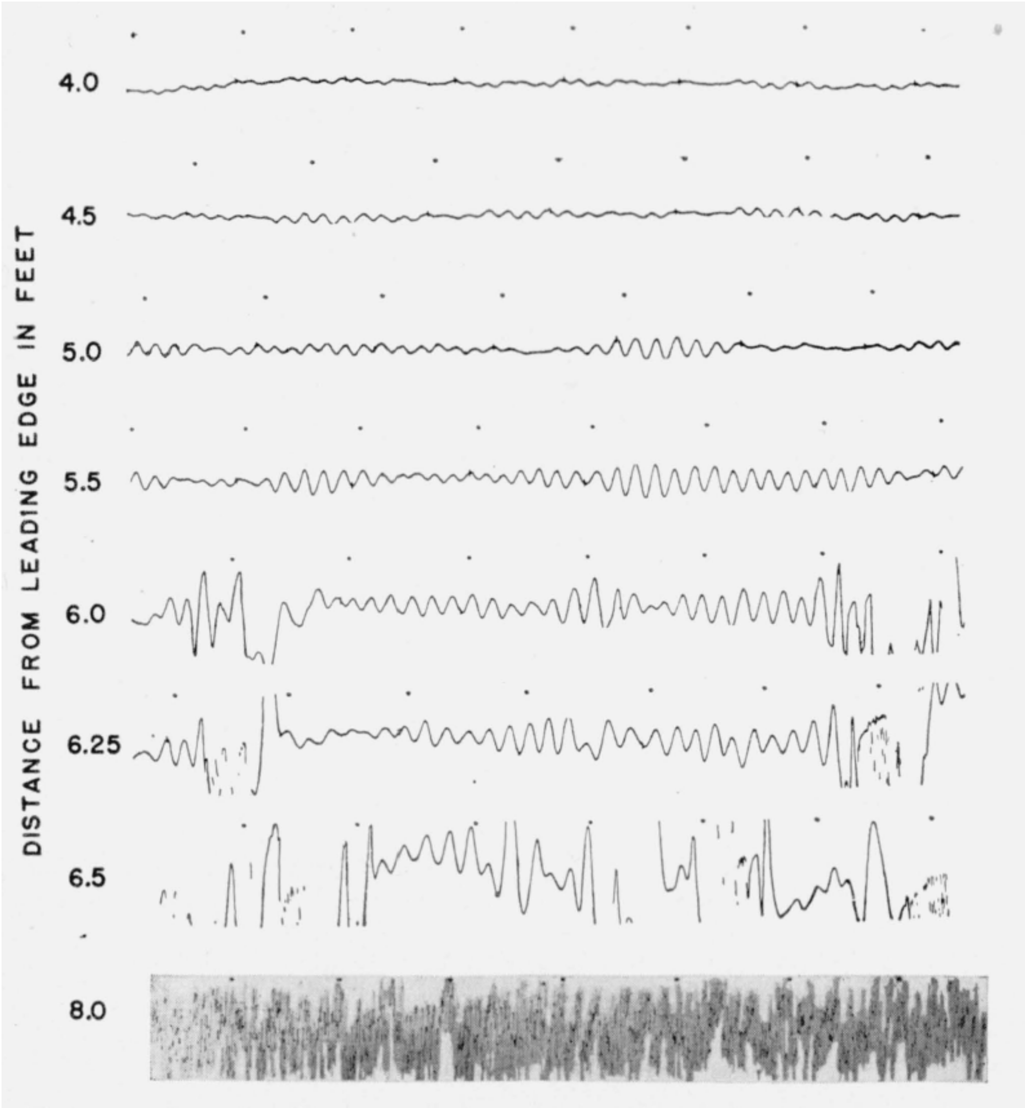

Figure 2.1: Oscillograms of u-fluctuations showing in boundary layer of flat plate. Distance from surface=0.023 in. U_0=80 ft/sec. Time interval between dots=1/30 sec. Schubauer and Skramstad [24].

Complexities in the transition process, investigated over the subsequent 30 years, most of which are still far from resolved, are listed:

- Effect of pressure gradients on stability [25–27].
- Effect of wall heating and cooling on stability [5,26,28].
- Three dimensional effects (even in 2D boundary layers) [29–31].
- Existence of additional instability modes at high speeds [32,33].
- So called 'blunt-body paradox' of premature transition on blunt bodies [34,35].
- The effect of nose bluntness and transition reversal [12,13].

- Surface roughness effects on stability [36–38].
- Crossflow instabilities [39, 40].

Note that the references here are obviously far from comprehensive; rather being examples of early observations of such phenomena. For holistic reviews of boundary layer transition, refer to the works of Tani [41], Reshotko [42] [43] and Kachanov [44], and for particular focus on hypersonic transition, Morkovin [45] [46] [47], Stetson [48], Fedorov [49] or Schneider [50] [51]. The area particularly relevant to this work is the effects of nose bluntness on transition.

2.1.2 Linear Stability Theory of Compressible Flow

Before reviewing the state of the art regarding transition on blunted bodies, a brief overview of Linear Stability Theory (LST) is warranted as it provides a solid framework for transition study and results from LST are regularly referred to in other works. The linear base equations are built by assuming each flow quantity can be described by a mean flow component $\bar{q}$ and a small fluctuating component q', as in Equation 2.1 which are then substituted into the Navier-Stokes equations, removing terms that are quadratic or higher in the fluctuation variable. Further simplification is achieved through the assumption of parallel flow in the boundary layer, meaning that derivatives of the mean flow in the streamwise and spanwise directions are negligible, which gives rise to the parallelized Linear Navier-Stokes equations in Equation 2.2.

$$q(x,y,z,t) = \bar{q}(x,y,z) + q'(x,y,z,t) \tag{2.1}$$

$$
\begin{aligned}
&\frac{\partial\rho'}{\partial t}+\overline{\rho}\left(\frac{\partial u'}{\partial x}+\frac{\partial v'}{\partial y}+\frac{\partial w'}{\partial z}\right)+v'\frac{d\rho}{dy}+\overline{u}\frac{\partial\rho'}{\partial x}+\overline{w}\frac{\partial\rho'}{\partial z}=0\\
&\overline{\rho}\left(\frac{\partial u'}{\partial t}+\overline{u}\frac{\partial u'}{\partial x}+v'\frac{\partial\overline{u}}{\partial y}+\overline{w}\frac{\partial u'}{\partial z}\right)=-\frac{1}{\gamma M^2}\frac{\partial p}{\partial x}+\frac{1}{\mathrm{Re}}\left[2\mu\frac{\partial^2u'}{\partial x^2}+\mu\left(\frac{\partial^2u'}{\partial y^2}+\frac{\partial^2u'}{\partial z^2}+\frac{\partial^2v'}{\partial x\partial y}+\frac{\partial^2w'}{\partial x\partial z}\right)+\right.\\
&\qquad\frac{2}{3}(\lambda-\mu)\left(\frac{\partial^2u'}{\partial x^2}+\frac{\partial^2v'}{\partial x\partial y}+\frac{\partial^2w'}{\partial x\partial z}\right)+\frac{d\mu}{dT}\frac{d\overline{T}}{dy}\left(\frac{\partial u'}{\partial y}+\frac{\partial v'}{\partial x}\right)+\\
&\qquad\left.\frac{d\mu}{dT}\left(\frac{d^2\overline{u}}{\partial y^2}T'+\frac{d\overline{u}}{dy}\frac{\partial T'}{\partial y}\right)+\frac{d^2\mu}{dT^2}\frac{d\overline{T}}{dy}\frac{d\overline{u}}{dy}T'\right]\\
&\overline{\rho}\left(\frac{\partial v'}{\partial t}+\overline{u}\frac{\partial v'}{\partial x}+\overline{w}\frac{\partial v'}{\partial z}\right)=-\frac{1}{\gamma M^2}\frac{\partial p}{\partial y}+\frac{1}{\mathrm{Re}}\left[2\mu\frac{\partial^2v'}{\partial y^2}+\mu\left(\frac{\partial^2v'}{\partial x^2}+\frac{\partial^2v'}{\partial z^2}+\frac{\partial u'}{\partial x\partial y}+\frac{\partial^2w'}{\partial y\partial z}\right)+\right.\\
&\qquad\frac{2}{3}(\lambda-\mu)\left(\frac{\partial^2u'}{\partial x\partial y}+\frac{\partial^2v'}{\partial y^2}+\frac{\partial^2w'}{\partial y\partial z}\right)+\frac{d\mu}{dT}\left(2\frac{d\overline{T}}{dy}\frac{\partial v'}{\partial y}+\frac{d\overline{u}}{dy}\frac{\partial T'}{\partial x}\right.\\
&\qquad\left.\left.+\frac{d\overline{w}}{dy}\frac{\partial T'}{\partial z}\right)+\frac{2}{3}\frac{d\overline{T}}{dy}\left(\frac{d\lambda}{dT}-\frac{d\mu}{dT}\right)\left(\frac{\partial u'}{\partial x}+\frac{\partial v'}{\partial y}+\frac{\partial w'}{\partial z}\right)\right]\\
&\overline{\rho}\left(\frac{\partial w'}{\partial t}+\overline{u}\frac{\partial w'}{\partial x}+v'\frac{\partial\overline{w}}{\partial y}+\overline{w}\frac{\partial w'}{\partial z}\right)=-\frac{1}{\gamma M^2}\frac{\partial p}{\partial z}+\frac{1}{\mathrm{Re}}\left[2\mu\frac{\partial^2w'}{\partial z^2}+\mu\left(\frac{\partial^2w'}{\partial y^2}+\frac{\partial^2w'}{\partial x^2}+\frac{\partial^2v'}{\partial y\partial z}+\frac{\partial^2u'}{\partial x\partial z}\right)+\right.\\
&\qquad\frac{2}{3}(\lambda-\mu)\left(\frac{\partial^2w'}{\partial x^2}+\frac{\partial^2v'}{\partial y\partial z}+\frac{\partial^2u'}{\partial x\partial z}\right)+\frac{d\mu}{dT}\frac{d\overline{T}}{dy}\left(\frac{\partial w'}{\partial y}+\frac{\partial v'}{\partial z}\right)+\\
&\qquad\left.\frac{d\mu}{dT}\left(\frac{d^2\overline{w}}{\partial y^2}T'+\frac{d\overline{w}}{dy}\frac{\partial T'}{\partial y}\right)+\frac{d^2\mu}{dT^2}\frac{d\overline{T}}{dy}\frac{d\overline{w}}{dy}T'\right]\\
&\overline{\rho}\left(\frac{\partial T'}{\partial t}+\overline{u}\frac{\partial T'}{\partial x}+v'\frac{d\overline{T}}{dy}+\overline{w}\frac{\partial T'}{\partial z}\right)=-(\gamma-1)\left(\frac{\partial u'}{\partial x}+\frac{\partial v'}{\partial y}+\frac{\partial w'}{\partial z}\right)+\frac{\gamma\mu}{\mathrm{PrRe}}\left[\frac{\partial^2T'}{\partial x^2}+\frac{\partial^2T'}{\partial y^2}+\frac{\partial^2T'}{\partial z^2}+\right.\\
&\qquad\left.\frac{1}{\kappa}\frac{d\kappa}{dT}\frac{d^2\overline{T}}{dy^2}T'+\frac{2}{\kappa}\frac{d\kappa}{dT}\frac{d\overline{T}}{dy}\frac{\partial T'}{\partial y}+\frac{1}{\kappa}\frac{d\kappa^2}{dT^2}\left(\frac{d\overline{T}}{dy}\right)^2T'\right]\\
&\qquad+\gamma(\gamma-1)M^2\frac{1}{\mathrm{Re}}\left[2\mu\frac{d\overline{u}}{dy}\left(\frac{\partial u'}{\partial y}+\frac{\partial v'}{\partial x}\right)+\right.\\
&\qquad\left.2\mu\frac{d\overline{w}}{dy}\left(\frac{\partial v'}{\partial z}+\frac{\partial w'}{\partial y}\right)+\frac{d\mu}{dT}\left(\frac{d\overline{u}}{dy}\right)^2T'+\frac{d\mu}{dT}\left(\frac{d\overline{w}}{dy}\right)^2T'\right]
\end{aligned}
\tag{2.2}
$$

Here the flow quantities (T, p, ρ, u, v, w) are the temperature, pressure, density and the velocities in the streamwise, wall-normal and azimuthal directions. These values are non-dimensionalised by a reference length scale and the freestream quantities. The coefficients (μ, λ, κ) denote the first and second viscosity coefficients and the thermal conductivity, ratio of specific heats given by γ. The Mach number at the edge of the boundary layer is denoted by M. The non-dimensional quantities of the Reynolds number and the Prandtl number are denoted by Re and Pr.

The eigenvalues and corresponding eigenmodes of the system can then be calculated with the application of appropriate boundary conditions [52,53]. The eigenvalues contain information regarding the frequency (ω) and wavenumber (α) of a given mode. Common practice is to consider the equations as evolving in space, to fit more logically with experimental observations, so the frequency is purely real and the wavenumber is complex. In this framework, the imaginary component of the wavenumber is the logarithmic growth rate of the mode. A mode is neutral if $\alpha_{im} = 0$, damped for $\alpha_{im} > 0$ and amplified for $\alpha_{im} < 0$. Stability diagrams can be constructed from these results, which visually describe the stability of the flow. Typical viscous and inviscid stability curves are shown in Figure 2.2.

Numerical work from Mack [54,55] and Gill [56] demonstrated that the solution α is not unique by inspection of the inviscid stability equations. When there exist waves which are supersonic with respect to the freestream, the inviscid stability equations become hyperbolic, rather than elliptic (see Section 9.5 in [52]), and as such permit an infinite series of solutions. The modes can be identified by the number of turning points in the pressure eigenfunction: the number of turning points in the profile of the eigenfunction is one less than the mode number. It is this second solution that is the Mack mode that is typically dominant in hypersonic flows.

The critical Reynolds number is then the lowest Reynolds number at which there is an unstable mode. Simply knowing whether an unstable mode exists is not particularly useful in and of itself- one must know how rapidly it is growing, and how much it has grown in the past (in a spatial sense). As stated prior, α_{im} denotes the instantaneous logarithmic growth rate, and it is customary to measure the net growth of these unstable modes with the N-factor, the logarithmic ratio of mode amplitude at any point to its initial amplitude i.e. $\ln(A(x)/A_0) = N$. This growth is computed with Equation 2.3 [52] for two dimensional disturbances, where x_0* is typically the location where the mode first becomes unstable. Initially referring specifically to the amplitudes predicted by LST, the N-factors usage has been generalised to describe the growth of any disturbance over a chosen domain.

$$N = -\int_{x_0*}^{x*} \alpha_{im} * dx* \tag{2.3}$$

It is this N-factor which forms the most widely used physics-based transition prediction method, called the e^N method. Unfortunately, the computed N-factor at experimentally measured transition locations varies significantly between tunnels and conditions. For hypersonic flow in wind tunnels, such computed N-factors range from 3-10 (based on linear methods) depending on the conditions and setup, particularly between different tunnels. For example, Figure 2.3 from Alba et al. [57] compares computations made with linear techniques to experimentally measured pressure fluctuations at similar conditions in the Boeing/AFOSR Mach 6 Quiet Tunnel (BAM6QT) operating in both conventional and 'quiet' mode, where significant efforts are made to minimise the freestream noise. In conventional mode, the boundary layer had transition to turbulence by the second streamwise station at $x = 0.360m$, where the computed N-factor was 8, but the boundary layer remained laminar over the entire model in quiet mode despite the computed N-factor being > 10.

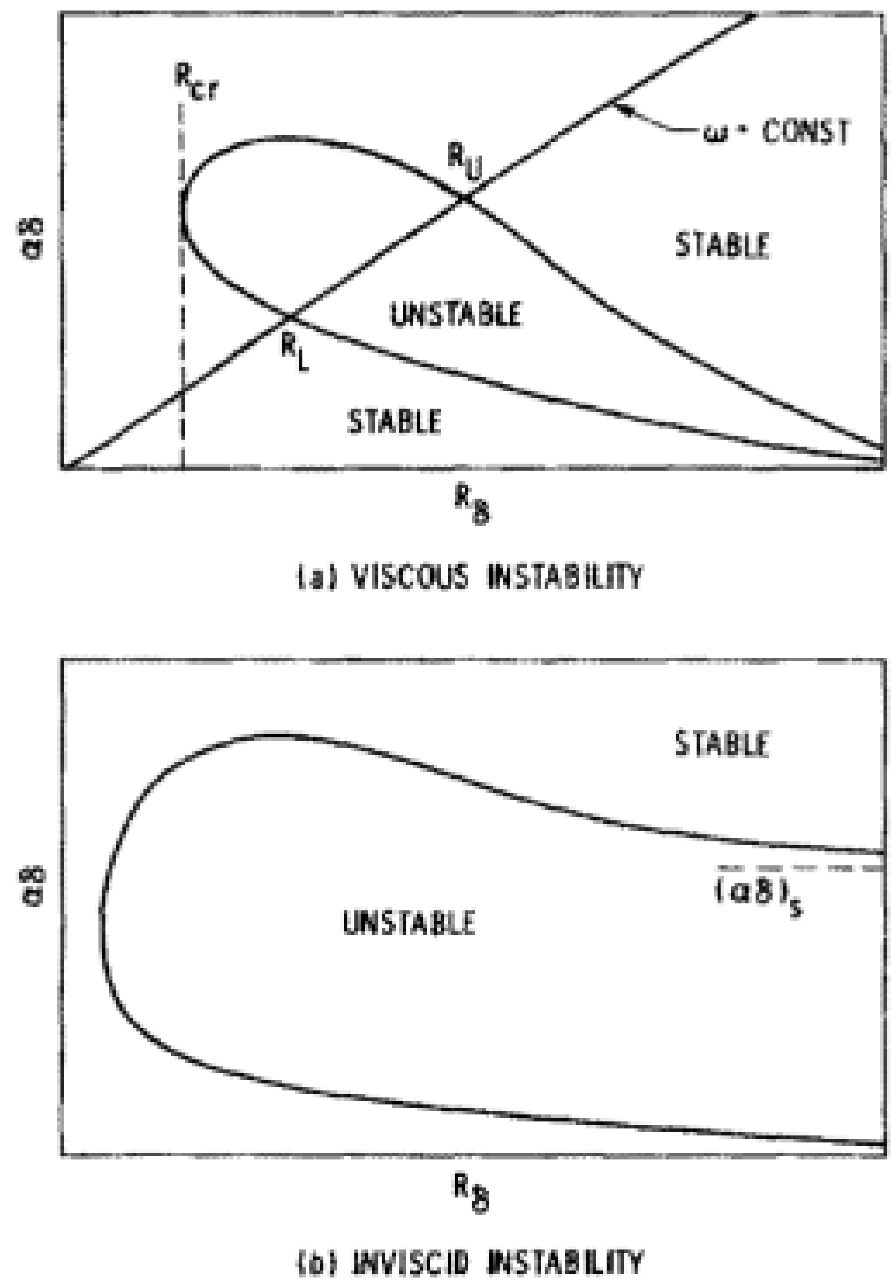

Figure 2.2: Example stability diagrams for flow over a flat plate. The x- and y- axes show the boundary layer thickness Reynolds number and wavenumber non-dimensionalised by layer thickness respectively. The wavenumber characterises an eigenmodal disturbance, and the location of said wavenumber on these diagrams determines whether the eigenmode will amplify or dampen in space. Top shows a viscous instability, characterised by the unstable region vanishing at $Re \to \infty$, bottom shows an inviscid instability where this unstable region remains for $Re \to \infty$. From Mack [52].

A topic which is addressed somewhat briefly by Mack [52], and in exceptional detail by Lees and Lin [5], is that of purely inviscid disturbances. The work of Lees and Lin is the foundation upon which much of compressible stability theory is built, and they address the case of purely inviscid waves in some detail, especially in the case as the wall-normal

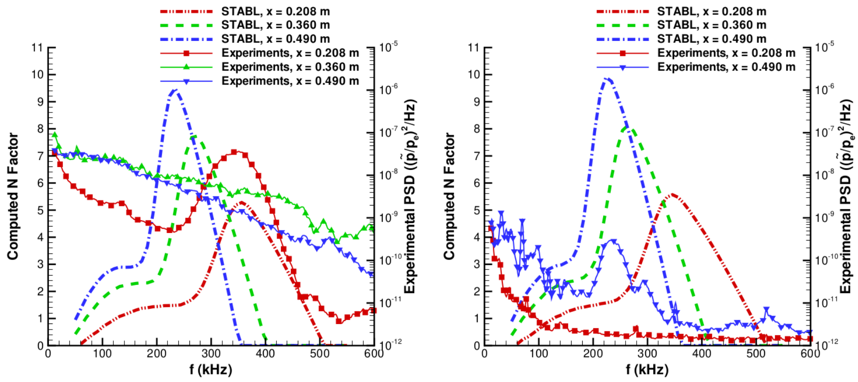

Figure 2.3: N-factors calculated via linear techniques and experimentally measured pressure fluctuations amplitudes for Mach 5.8 flow over a 7° sharp cone at in conventional mode (left) and 'quiet' mode (right) at similar Reynolds numbers ($10.4 \times 10^6 \mathrm{m}^{-1}$ and $10.3 \times 10^6 \mathrm{m}^{-1}$) from Alba et al. [57].

coordinate becomes large i.e. outside the boundary layer. They found that sonic or supersonic waves (relative to some freestream velocity) have continuous solutions to the wave equation, while subsonic waves only have discrete solutions. It was this idea that Mack built on to prove the existence of the second mode that is dominant in hypersonic flows.

Further techniques for studying the evolution of disturbances within flows were developed in the following decades to address the limitations of traditional LST. The most common of these is the Parabolized Stability Equations [58] (PSE). PSE tracks the evolution of a prescribed disturbance, determined by a local stability analysis at the starting location, in the downstream direction. In contrast to LST, PSE can include contributions from multiple eigenmodes of the Linearized Navier-Stokes (LNS) operator which are coupled linearly through the streamwise variation of the flow, and nonlinearly through triadic interactions (interactions between a trio of frequencies). The method is still a linear method in practice, and was the method used in the work of Alba et al. [57] discussed in relation to the e^N method. PSE can be applied to more problems than simply studying the modal dynamics of a flow: other applications have been optimal growth analysis [59, 60], adjoint-based sensitivity and control [61–63] and modeling acoustic emissions [64].

PSE methods are limited in their ability to simulate multiple modes. This is due to the presence of evanescent upstream-travelling modes which remain in the LNS operator that place significant restrictions on the space marching scheme. This effect is illustrated in Figure 2.4. For example, explicit space marching methods are unconditionally unstable, and a minimum spatial step is required for implicit methods for stability in the presence of these upstream-travelling modes. In many cases, this minimum spatial step is large enough to modify the behaviour of the downstream travelling modes, and in some cases even destabilise them. The review of Towne et al. [65] provides a more in-depth assessment of the PSE method and its limitations.

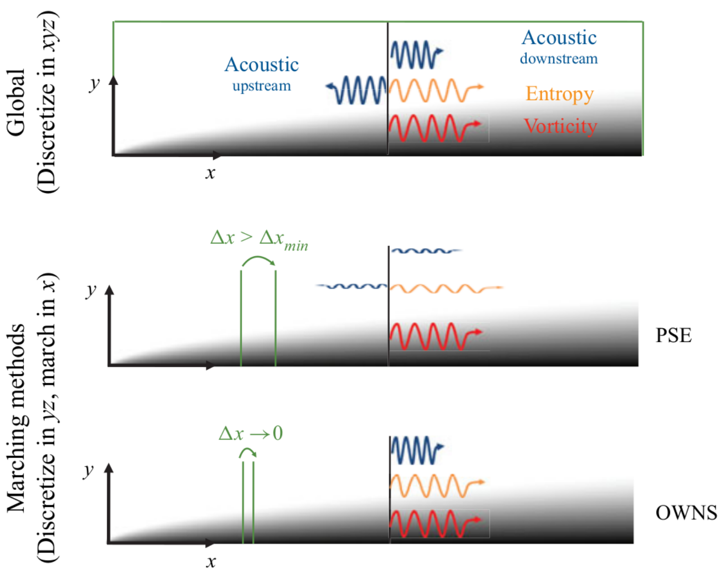

Figure 2.4: Illustration of the behaviour of the waves in the complete Navier-Stokes equations compared to the space marching techniques of PSE and the One-Way Navier Stokes (OWNS) equations. From Towne et al. [65].

The limitations of the PSE method led to the recent development of the One-Way Navier-Stokes equations (OWNS) by Towne and Colonius [66]. This method addresses the issue of the upstream-travelling modes in the space marching by only retaining the downstream travelling modes. The travelling direction of the modes are determined by the eigenvalues of the local LNS operator, with modes associated with positive eigenvalues travelling downstream and modes associated with negative values travel upstream. The system can be spatially integrated with arbitrary accuracy without lower limits on the spatial step, allowing resolution of an arbitrary number of modes. This technique has been applied successfully to canonical problems in transition as well as the HIFiRE 5 geometry by Kamal et al. [67].

2.1.3 Transition Reversal on Blunted Bodies

For hypersonic flow over blunted bodies, it has been experimentally shown that the transition location moves downstream as the bluntness of the nose increases, at least for small bluntnesses [68–70]. When the bluntness reaches some critical radius, the trend reverses, with transition shifting upstream as the nose radius becomes larger [12, 13, 71–73]. This phenomenon is known as transition reversal. The mechanism of the initial downstream movement is loosely understood to be a combination of unit Reynolds number reduction [12, 69, 70] and stabilisation of the boundary layer to second mode instabilities [74–76]. However, while the unit Reynolds number reduction reaches a maximum at a finite bluntness, the stability theory predicts the ever-increasing stability of the boundary layer (to second-mode disturbances) as the bluntness increases.

This theoretical prediction of stability is not necessarily incompatible with experimental observations of reversal: it simply suggests that the mechanism of transition shifts from that of second mode dominated breakdown to some unknown mechanism. Indeed, the existence of the 'blunt body paradox', where transition on very blunt bodies occurs at very low Reynolds numbers (an order of magnitude or more lower than on an equivalent sharp cone [34, 35]), had already indicated that modal mechanisms cannot be dominant in all scenarios. The different paths to transition were visualised by Reshotko [77] in Figure 2.5.

To appreciate the observations and conclusions in the prior art, the concept of the entropy layer should first be explained. The entropy layer is a region of high entropy and vorticity around the nose that differentiates blunt nose flow from flow over an equivalent sharp nose. However, similar to the fashion in which boundary layer flow *asymptotically* approaches the freestream solution, blunted cone flow asymptotically approaches its sharp cone counterpart. The strict definition of the entropy layer is the region which contains the entire mass flow from the curved portion of the shock. The concept is illustrated in detail by Morretti and Pandolfi [78] in Figure 2.6. In practice, this location is difficult to measure, and instead approximate methods are used to calculate the entropy layer swallowing distance, based on entropy gradients, boundary layer profiles or Reynolds numbers [79–81]. This entropy layer swallowing is the point where the edge of the entropy layer meets the boundary layer and thus its effects become negligible compared to the viscous effect of the wall. These approximate methods are not consistent between authors, and can lead to small discrepancies

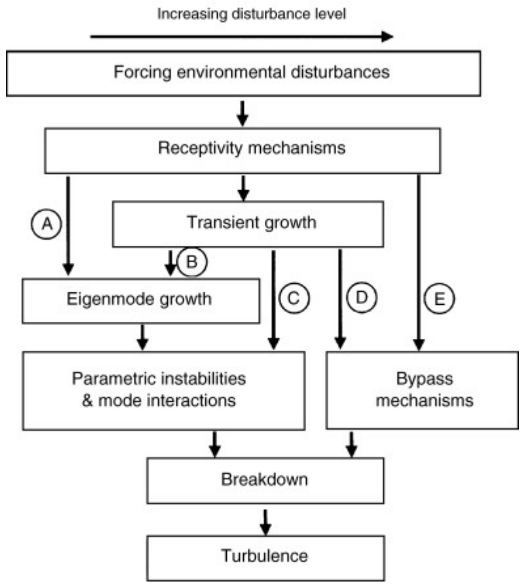

Figure 2.5: Summary of the different possible to paths to transition, with the magnitude of the environmental disturbances increasing from left to right. From Reshotko [77].

in results. The effect of nose bluntness on the extent of the entropy layer edge is shown in Figure 2.7, using the entropy layer edge defintion of Paredes et al. [82].

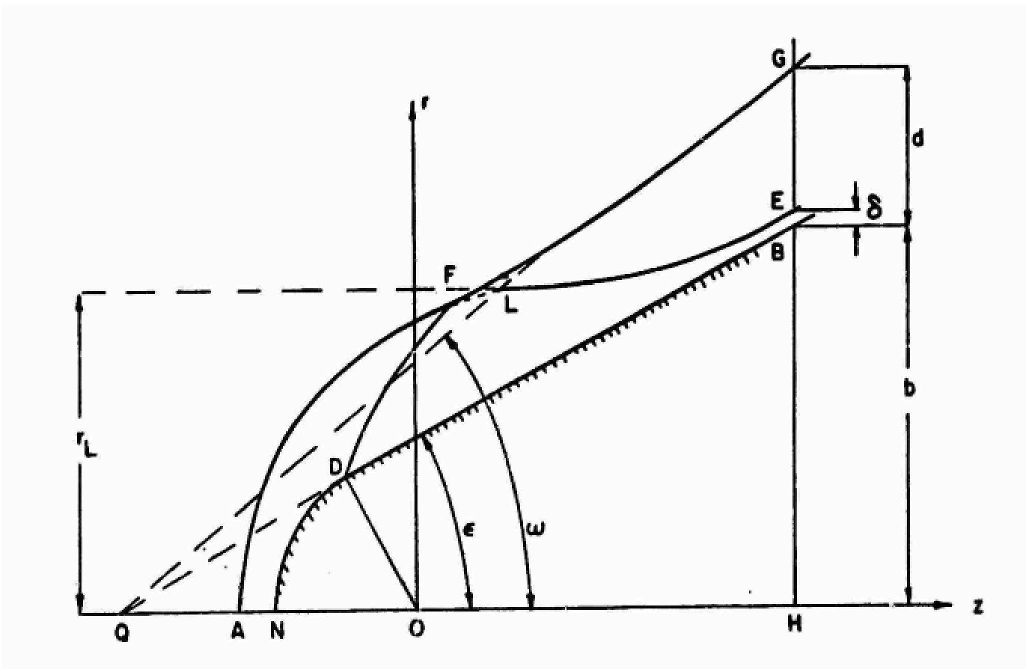

Figure 2.6: Schematic depiction of the shock and entropy layer over a blunted cone. The line AF is the bow shock affected by the spherical nose, F is the intersection between the shock and the characteristic from the sphere-frustum junction D and L is the streamline emanating from F. The edge of the entropy layer is then the line AE. From Moretti and Pandolfi [78].

Initial experiments by Stetson and Rushton [12] and Softley [13] make measurements of the transition location and Reynolds number and first make the connection between entropy layer effects and reversal. Their results are collated by Softley in Figure 2.8. Here the quantities S_B and S_{cr} denote the location of the beginning of transition and S_{cr} is the point

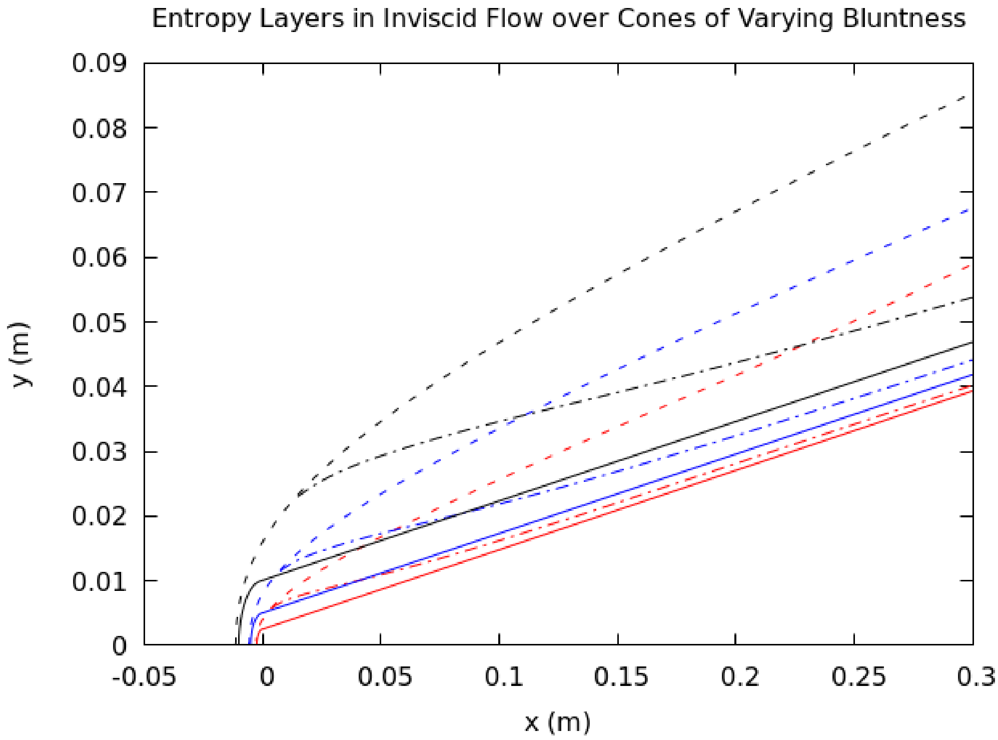

Figure 2.7: Entropy layer edge (dot-dash) over 2.5mm (red), 5mm (blue) and 10mm (black) nose cones using the entropy layer edge definition of Paredes at al. [82]. Cone surface and leading shock denoted by solid and dashed lines.

where the boundary layer edge is sonic with respect to the equivalent sharp cone boundary layer edge. In neither of these experiments were microscopic measurements of the boundary layer made, so no attempt was made to uncover the physics of transition reversal. Note that the y-axis shows Reynolds number at transition, integrated along the boundary layer edge, rather than an absolute location, so transition may still be moving downstream after the change due to unit Reynolds number reduction effects induced by bluntness.

Further experiments of transition over blunted bodies suggest that the problem can be split into three bluntness regimes [79, 83]: small, medium and large bluntness. Small bluntness, where the growth of the second mode leads to transition. The second mode is stabilised by the entropy layer, and this stabilisation becomes stronger with increasing Mach number. For these flows, the critical Reynolds number is greater than the sharp cone equivalent, and transition will occur closely downstream from said Reynolds number. The medium bluntness regime is where transition occurs upstream of the entropy layer swallowing. The cause of transition in this region is not well known, but experimental evidence suggests that disturbances originating outside the boundary layer are significant here. This medium bluntness regime is the regime of interest in this work. At large bluntness, disturbances originating from surface roughness around the nosetip become dominant. The point of reversal occurs in the vicinity of this interface between medium and large bluntnesses, perhaps where roughness-type disturbances become large enough to strongly interact with the external disturbances to trigger transition at reduced fluctuation amplitudes. It is important to remember that these

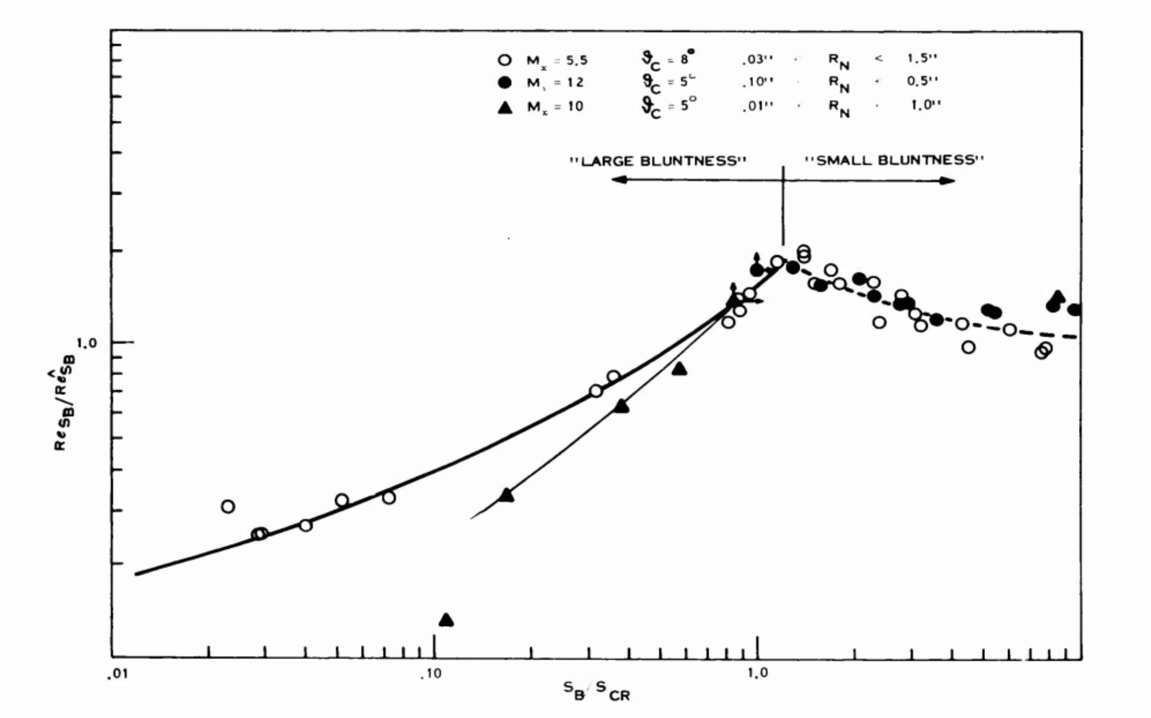

Figure 2.8: Collation of Stetson and Rushton's [12] and Softley's [13] transition results. From Softley [13].

'regimes' are characterised by a particular type of transition, rather than a specific bluntness range. Stetson's interpretation of these regions is demonstrated in Figure 2.9.

Small Bluntness

The small bluntness regime is characterised by the presence of second mode instabilities prior to transition. The entropy layer effects strongly stabilise the boundary layer to second mode disturbances, due to both unit Reynolds number reductions and increase of the critical Reynolds number. Experimental evidence suggests the second mode unstable region shifts to higher Reynolds number and lower frequencies as the nose bluntness increases [83, 85]. This is supported by stability studies [76] and DNSs [75, 86]. However, once unstable, the second mode growth rate is greater than the sharp cone and more broadband in nature [83, 85]. Figure 2.10 from Stetson [85] shows mass flow fluctuations within the boundary layer over equivalent sharp and small bluntness cones. Transition in this regime is relatively well described by stability theory.

Note that for this flow condition over the blunt cone, the entropy layer swallowing distance was at approximately $S/R_N = 128$ or $Re_x = 5.3 \times 10^6$. This places this case to the far right of Figure 2.9, where $X_T/X_{sw} > 1$. Marineau et al. [83] show that the second mode can be unstable prior to entropy layer swallowing for cases where the ratio X_T/X_{sw} is still close to one. Figure 2.11 shows the power spectral density in the boundary layer for both the sharp cone and a blunt cone case with $X_T/X_{sw} \approx 0.4$. Note the downstream and frequency shift of the unstable region, consistent with numerical predictions of Lei and Zhong [76] using LST

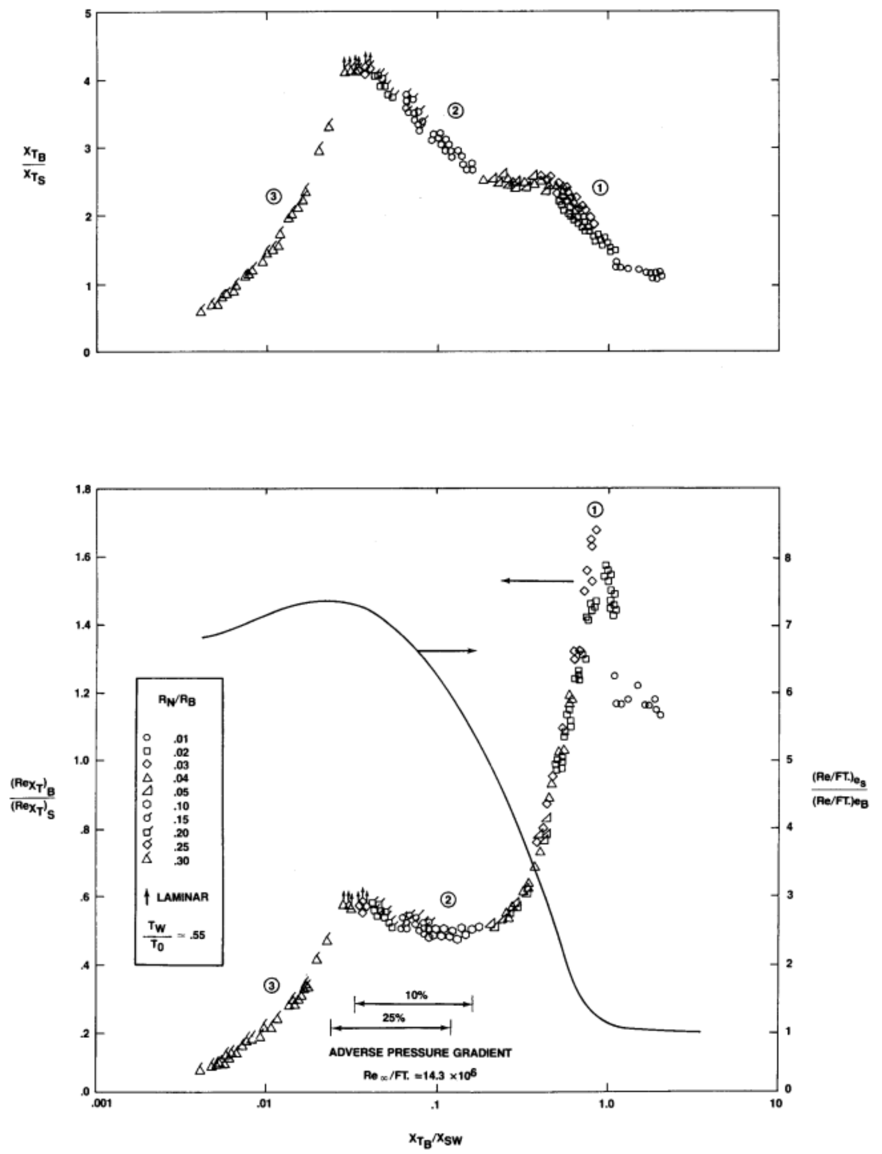

Figure 2.9: Results from Stetson's 1983 experiments, with small, medium and large bluntness regions denoted by 1, 2 and 3 respectively. X axis shows transition location relative to the entropy layer swallowing distance, calculated with the method of Rotta [84], with the y-axes showing distance and Reynold's number of transition relative to the sharp cone. Model base radius R_B was 2in (51.2mm). From Stetson [79].

(Figure 2.12).

Nose bluntness also affects the receptivity of the boundary to incoming disturbances from the freestream. Numerical work showed that the receptivity of the boundary layer to acoustic waves is reduced by three orders of magnitude for blunt cones, based on the magnitude of pressure fluctuations at the wall relative to the freestream [86,88].

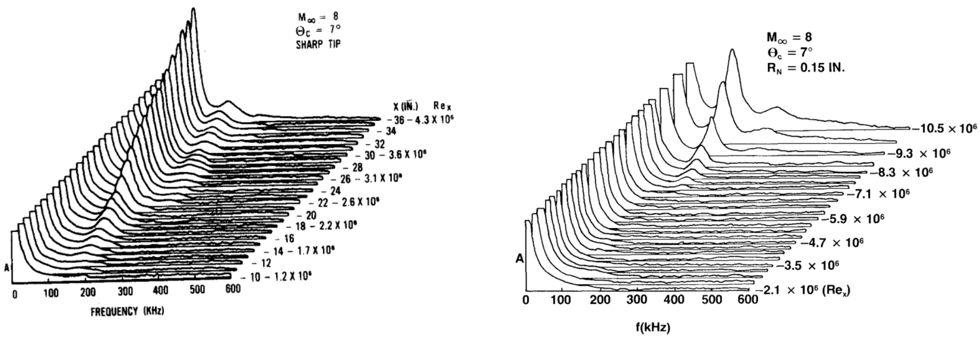

Figure 2.10: Comparison of fluctuation spectra in the sharp (left) and blunt (right) cone boundary layers. First peak corresponds to predicted second mode frequency. From Stetson et al. [87] [85].

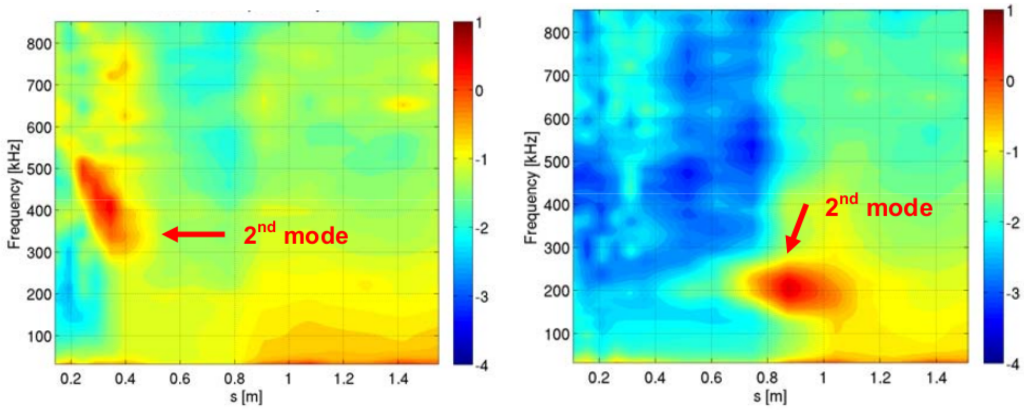

Figure 2.11: Power Spectral Density plots for sharp and 5mm bluntness cones in Mach 11, $Re = 17 \times 10^6$/m flow. From Marineau et al. [83].

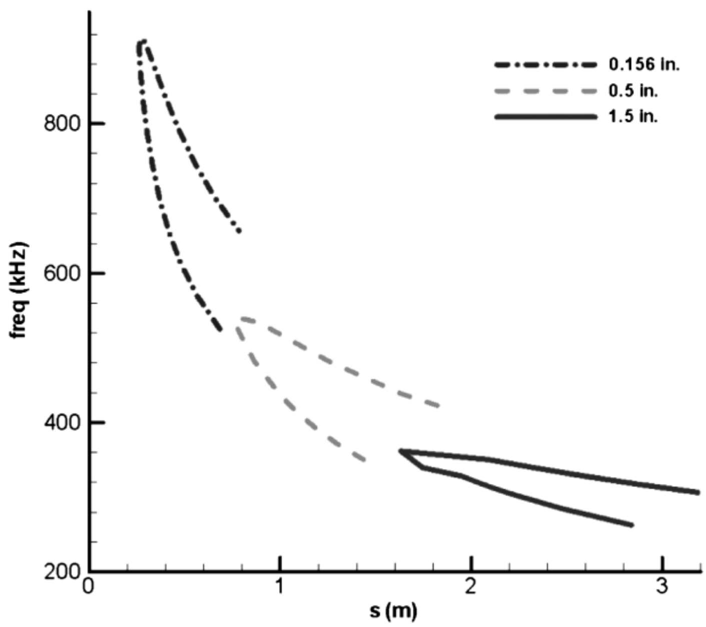

Figure 2.12: Neutral stability curves for cones of increasing bluntess computed by Lei and Zhong [76] using LST. The shift of the unstable second mode region is consistent with the experiments of Marineau et al. [83].

Large Bluntness

The large bluntness regime is characterised by strong sensitivity to surface roughness around the nosetip region. Heat flux measurements by Paredes et al. [89] show that transition on large bluntness cones is highly sensitive to roughness elements on the nosetip, while small bluntnesses were insensitive (Figure 2.13). Stetson et al. [79] found that, for transition, measurements were not repeatable at high bluntness; runs at the same conditions saw wildly varying transition locations. Polishing of the nosetip did see strong stabilisation of the boundary layer, often causing the layer to be stable over the entire model, while having no effect at low bluntness.

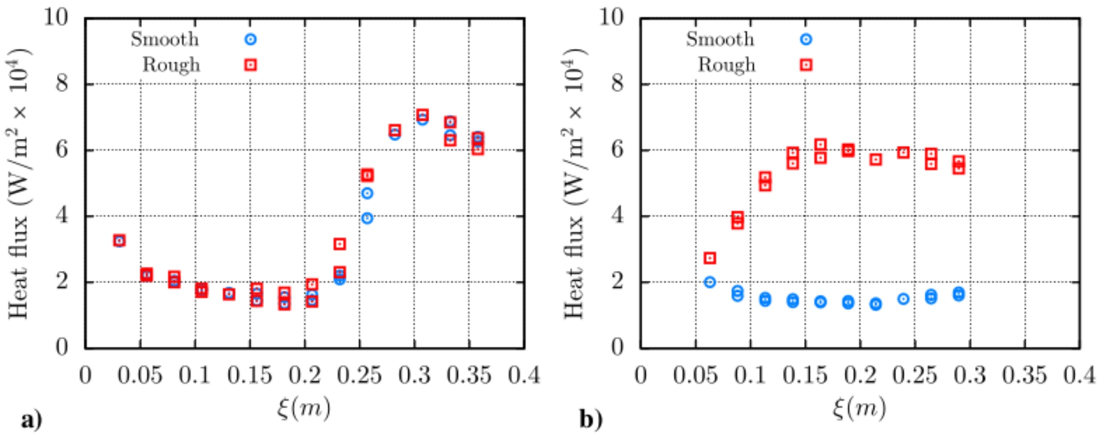

Figure 2.13: Heat flux measurements for cones with and without roughness at $M_\infty = 5.9$ for nose radii of a) 5.08mm and b) 15.23mm. From Paredes et al. [80].

2.1.4 Medium Bluntness

The medium bluntness regime is the one of interest in this work, and as such deserves its own section. At the time of writing, there is no clear consensus among the academic community regarding the transition mechanism in this region. One fact that is clear is that the entropy layer can support growing disturbances, but the the precise nature of these disturbances, or indeed whether there is a single type of disturbance supported by the entropy layer flow or many is still unclear.

Experimental Observations

The clear first evidence of growing disturbances in the entropy layer came from Stetson et al. [85] in their Mach 8 experiments. The disturbances were associated with a maximum in the angular momentum, the density times the vorticity, known as a generalised inflection point. Inflection points are a well known source of inviscid flow instability (see Lin [90] for a mathematical explanation or Brown [91] for a physical explanation of the inflection point instability). This inflection point exists in all compressible boundary layers, but this second inflection point outside the boundary layer does not exist in sharp body flow. The wall-normal angular momentum profile generated using a compressible flow simulation of the geometry of interest is shown in Figure 2.14 for a location deep within the entropy layer.

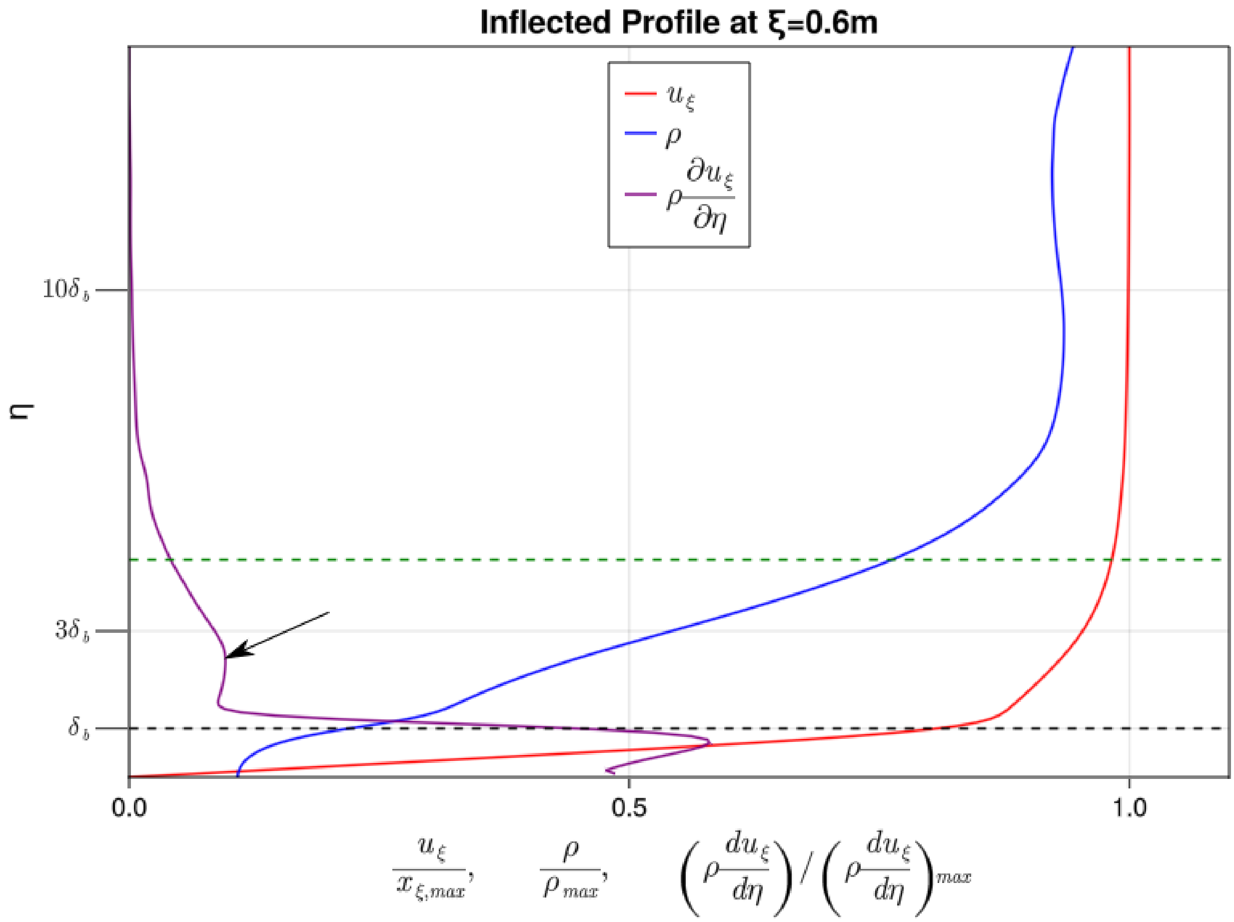

Figure 2.14: Wall-normal angular momentum profile over a 17.78mm nose radius cone in Mach 7.99 flow from simulations presented in this work, with the second inflection point in the entropy layer noted by the arrow. The black and green lines denote the local boundary layer and entropy layer edges.

This disturbance grew as it progressed downstream, with the wall-normal location of maximum disturbance amplitude tracking the inflection point. The inflection point moves towards the wall as it travels downstream, eventually entering the boundary layer and merging with the inflection point within the boundary layer. The associated disturbance grows slowly in the entropy layer, is attenuated as the entropy layer and boundary layer inflection points merge, then grows rapidly inside the boundary layer. Figure 2.15 from Stetson et al. [85] shows the wall-normal profiles and hot-wire output (directly correlated to mass fluctuation amplitude) for 3 streamwise stations, as well as the amplitude of said disturbance as it progressed downstream.

A similar phenomenon was observed by Greenwood and Schneider [92] in their hotwire and surface pressure measurements over a blunted cone-ogive cylinder in a Mach 6 'quiet' tunnel. A disturbance of constant frequency grows slowly, attenuates, then grows rapidly as

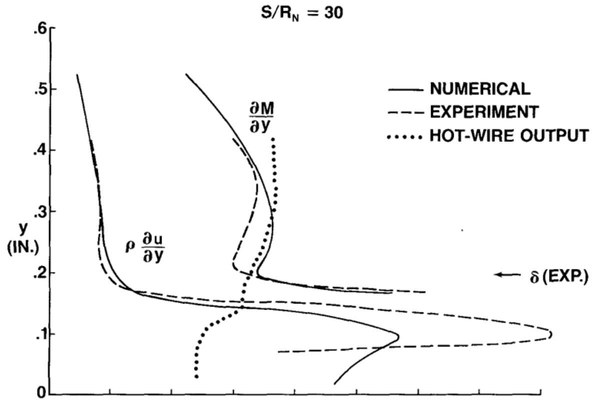

(a) Wall-normal profiles at $S/R_N = 30$.

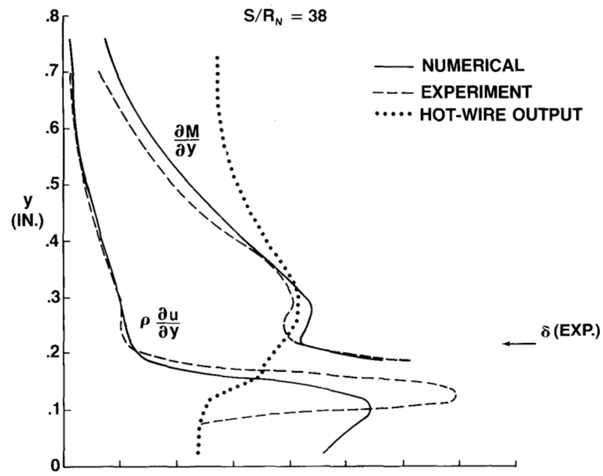

(b) Wall-normal profiles at $S/R_N = 38$.

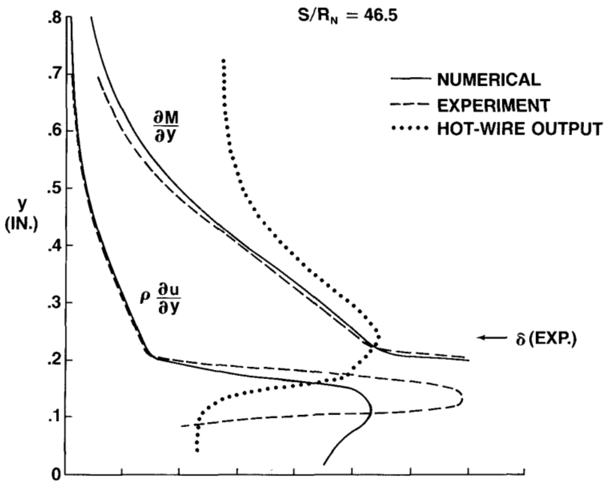

(c) Wall-normal profiles at $S/R_N = 46.5$.

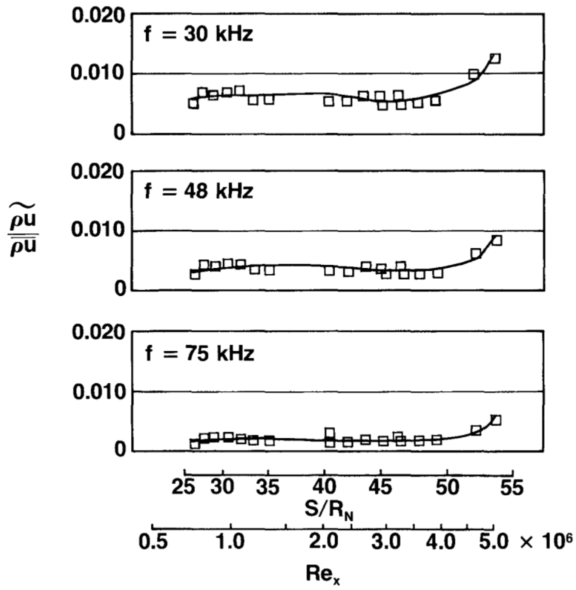

(d) Mass-flow fluctuation amplitudes.

Figure 2.15: Development of the wall-normal profiles and mass-flow perturbations as they progress downstream over a 0.7 in (17.78 mm) nose cone. From Stetson et al. [85].

illustrated in Figure 2.17. The disturbance is distingished from a boundary layer instability by the constant frequency. A boundary layer instability should decrease in frequency with increasing boundary layer thickness, as the second mode behaves is a trapped acoustic wave [49]. Their measurements also showed the instability was insensitive to obstacles in the boundary layer, further evidence that surface effects are not important in this medium bluntness regime. Note that the dominant frequency range for the entropy layer disturbances in both these experiments was low, of the order 50kHz for both cases.

Recent experiments by Kennedy et al. [93] and Grossir et al. [94] observed very similar structures extending outside the boundary layer using schlieren imaging. The structures tilt further in the direction of the flow as they convect downstream with velocity very close to the computed boundary layer edge velocity. A selection of such images is shown in Figure 2.16, demonstrating this phenomenon. Short bursts of medium frequency content, in the 150kHz to 250kHz range, were observed in surface pressure measurements for a single condition, but transition is not observed on the model.

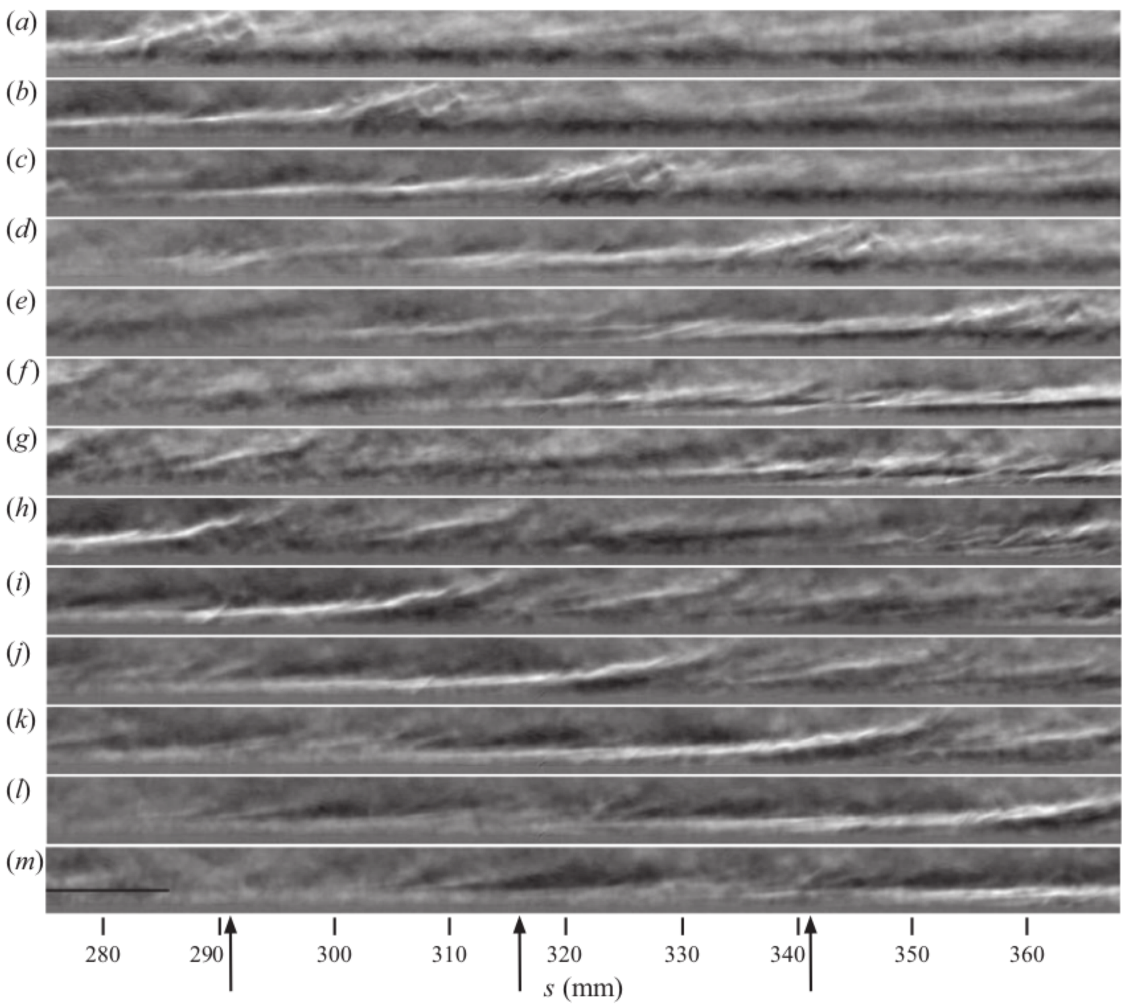

Figure 2.16: Set of schlieren images from Kennedy et al. [93] in Mach 6.14 flow over a 5.08 mm nose radius cone, showing density structures extending outside the boundary layer. The images are separated by 21.3 μs. The arrows denote pressure sensor locations, and the black line in the final figure denotes the boundary layer edge.

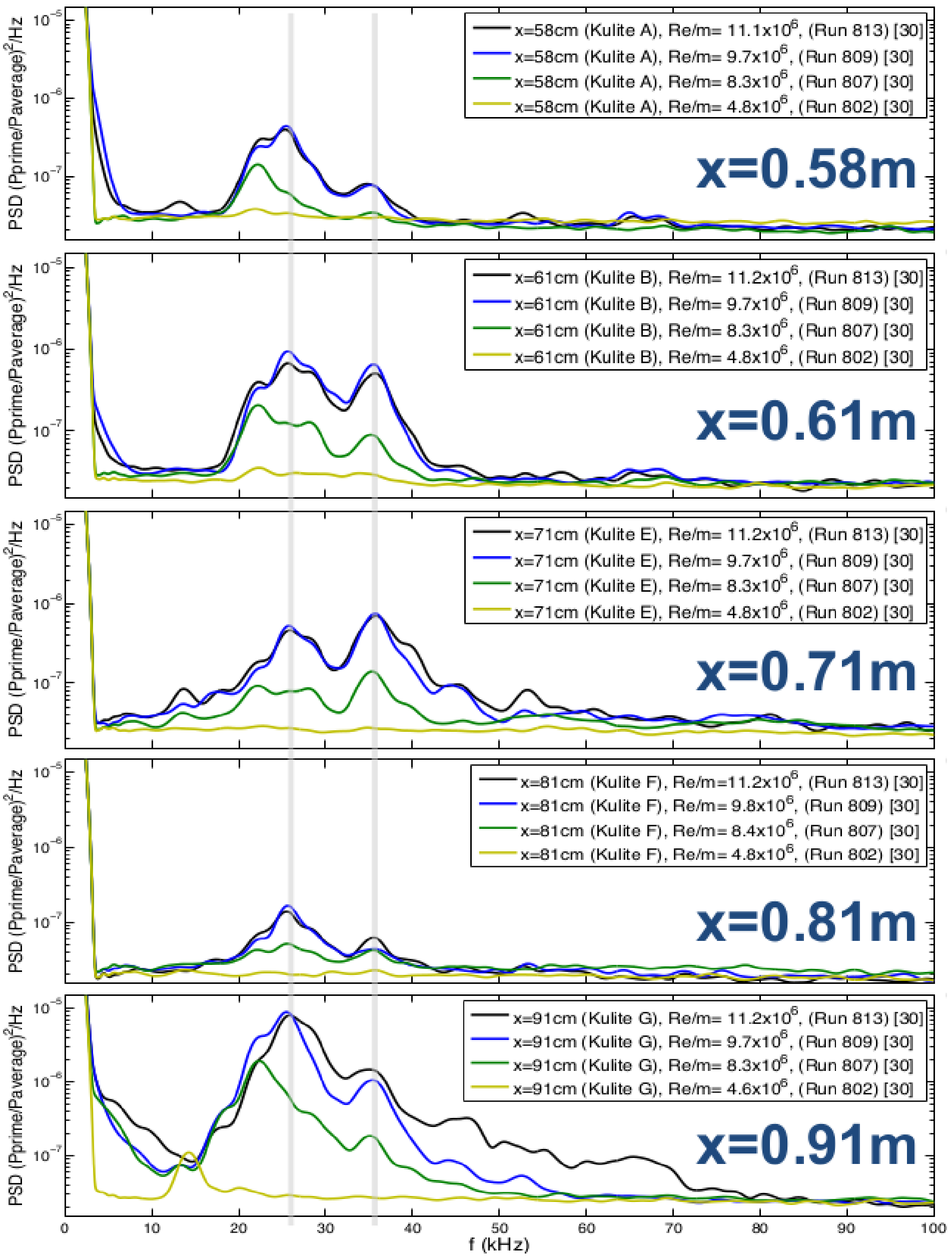

Figure 2.17: Fluctuation spectra measured by surface pressure probes in Mach 6 quiet flow over an ogive-cone cylinder. Unchanging peak frequencies indicate the disturbance originates outside the boundary layer, as boundary layer disturbances should change in frequency as boundary thickness increases. From Greenwood and Schneider [92].

These experimental measurements provide conclusive evidence that entropy layer disturbances exist, but questions of their precise nature and their link with boundary layer transition were not answered. Performing high fidelity and comprehensive measurements of these entropy layer disturbances is practically difficult as performing off-surface measurements in a hypersonic environment is challenging, so numerical techniques are employed.

Numerical Results

Before discussing the numerical results, it is important to introduce the numerical techniques introduced such that their limitations can be understood. The classic stability tool of LST predicts the existence of unstable inviscid disturbance modes [95–97]. These disturbance modes are associated with the inflection point in the entropy layer, as was observed by Stetson et al. [85]. However, the prediction is that they are weakly unstable, with modal amplification rates too low to be the driving factor for transition.

With modal theory failing to yield an explanation for transition, attention turned to non-modal theory, referred to as transient growth. Non-modal growth is considerably more difficult to analyse analytically, as it dispenses with the orthogonal mode assumption of LST. If the modes are allowed to be non-orthogonal (i.e. not normal to each other), then the total fluctuation amplitudes may increase in time or space, even when the individual modes are stable. To demonstrate this concept, the example from Reshotko [10] is introduced, using the Orr-Summerfield/Squire system of equations. The Orr-Summerfield/Squire equations can be written as

$$\frac{\partial}{dt}\begin{pmatrix}\zeta\\ \eta\end{pmatrix} = \begin{pmatrix}L_{OS} & 0\\ \gamma & L_s\end{pmatrix}\begin{pmatrix}\zeta\\ \eta\end{pmatrix} \tag{2.4}$$

where ζ, η are the disturbance vorticities in the x-z and y planes respectively, L_{OS} and L_S are the time-indepdent Orr-Summerfield and Squire operators and γ is the coupling coefficient. The non-orthogonality of the system is represented by the coupling coefficient. To illustrate the concept of transient growth, the operators L_{OS} and L_S are replaced with stable eigenvalues $-\lambda, -\mu$, though this is not a true solution to the system, only representative. The solution to the system is given by

$$\begin{aligned}\zeta &= \zeta_0 \exp^{-\lambda t}\\ \eta &= -\gamma\zeta_0\left(\frac{\exp^{-\lambda t} - \exp^{-\mu t}}{\lambda - \mu}\right) + \eta_0 \exp^{-\mu t}\end{aligned} \tag{2.5}$$

which clearly shows the homogeneous solutions are stable. The character of the coupling term is not immediately obvious: it becomes clear by observing the behaviour as $\lambda \to \mu$. Invoking L'Hopital's rule, the coupling term takes the form $t\exp^{-\mu t}$, a term that is initially linearly increasing in time followed by exponential decay. This trend is characteristic of transient growth. It has been shown that arbitrary shear layers, regardless of the presence of an inflection point, are "unstable" to such finite two and three dimensional disturbances [98–100].

It is worth noting at this point that the terms "stable" and "unstable" (and consequently "flow instability") do not have a consistent meaning in transition theory. The most common usage of the terms is in regards to the modal stability of the flow, where it simply refers to the character of the eigenvalues, where unstable means an eigenvalues with $\Im(\lambda) < 0$ exists. In the context of non-modal growth, unstable simply means that fluctuations are growing at an instant in time, usually linearly. From here on, unqualified mentions of stability will refer to the general form as in the non-modal growth literature, and references to the eigenmodal stability will be qualified as such.

It is clear from Equation 2.5 that the problem is an initial value problem, and consequently can be addressed with optimisation techniques. Early work analysed the problem in the transient growth framework using optimisation techniques and found the maximum transient growth scales with Re^2 and can reach amplification factors of order 10^3 [101, 102]. While this can be of interest in some flows, experimental observations suggest that spatial growth phenomena are dominant in boundary layer transition scenarios. The formulation of the problem is significantly different in the spatial growth framework compared to the temporal framework, although the general trend of linear growth followed by exponential decay remains. Early analyses using the linearized boundary layer equations found that the flow is particularly unstable to counter-rotating streamwise vortices with 0 streamwise wavenumber [59, 103, 104] i.e. stationary longitudinal vortices which drive mixing of high and low momentum fluids in the upper and lower regions of the boundary layer. An example of such an optimal disturbance distribution from Andersson et al. [59] is shown in Figure 2.18.

Tumin and Reshotko applied the spatial growth framework to compressible boundary layers [105] [106], particularly in the context of transition on capsule geometries. Even with the significant simplifications made in their analysis, it led to a significant improvement to the transition correlation developed through the Passive Nosetip Technology (PANT) program. They found that in general disturbances in the continuous spectrum i.e. entropy and vortical disturbances experience the greatest growth, as opposed to waves from the discrete spectrum such as T-S waves or the Mack mode. Paredes et al. [62] further the analysis of Tumin and Reshotko by including non-parallel effects and arrive at a similar correlation, demonstrating the effectiveness of transient growth theory in the predicting the transition location for such geometries.

The issue with these transient growth analysis, in particular those which are used in conjunction with an optimisation procedure to determine the initial conditions which yield the largest disturbance growth, is that these optimal initial conditions are not necessarily physically realistic. Taking the work of Luchini [103, 104] referenced prior as an example, he

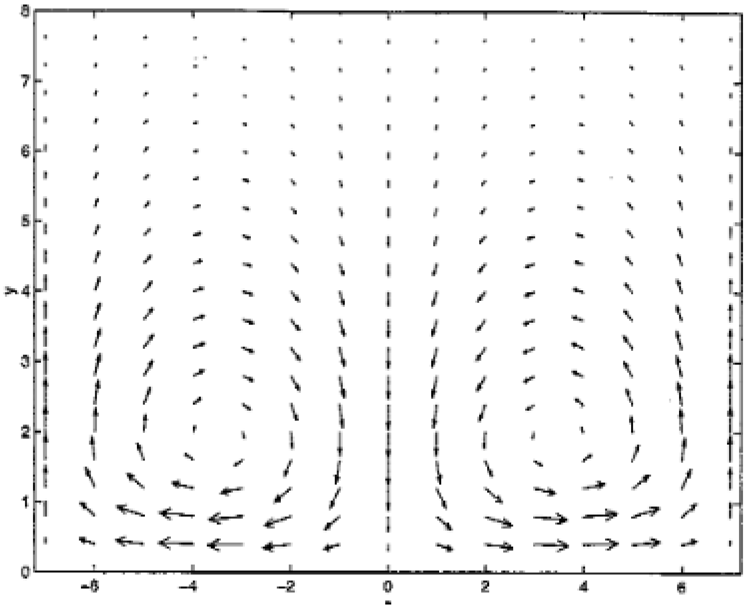

Figure 2.18: Disturbance velocity field corresponding to optimal downstream energy gain in an incompressible boundary layer, due to the calculations of Andersson et al. [59]. A pair of counter-rotating vortices redistribute the high and low momentum fluid, resulting in a large deviation from a steady base flow.

predicted longitudinal streamwise vortices are the optimal initial conditions for transient growth, but how likely is such a disturbance to be realised in a real flow? And if the initial condition is slightly different from the prescribed optimum condition, how different is the result? This is a question that permeates all transition study as a whole, but is particularly relevant to the transient growth and optimal growth framework. Now that the tool has been briefly critiqued, discussion of the results will continue.

Recent computational analyses show that the nose region over blunted slender cones is similarly susceptible to transient growth of stationary or low frequency streamwise vortices [82,89,107,108]. However, transition on these geometries (prior to transition reversal) does not occur until much further downstream, so these being the direct cause of transition is unlikely. Further, the most feasible way to generate such types of disturbances is through surface roughnesses, but experimental evidence showed that surface roughness had minimal effect on transition for these conditions. They may still play a role through the excitation of other disturbances. Such phenomena has been observed in other scenarios, most relevant of which is the excitation of Kelvin-Helmholtz instabilities over separation bubbles [109–111] by upstream disturbances.

A more reasonable candidate for a realisable optimal disturbance in the entropy layer was revealed by Paredes et al. [80,82,89], who applied the spatial growth framework to the problem of interest in this work, the blunt slender cone in the maximum transition delay regime. The map of the energy growth in the frequency-azimuthal wavenumber space in Figure 2.19 over a 5.08 mm nose radius cone revealed a secondary maximum in the optimal energy growth corresponding to a high frequency planar disturbance, in addition to the stationary three dimensional disturbance found in boundary layer flows. This non-stationary planar disturbance is dominated by the internal energy contribution i.e. temperature/density fluctuations in the continuous spectrum.

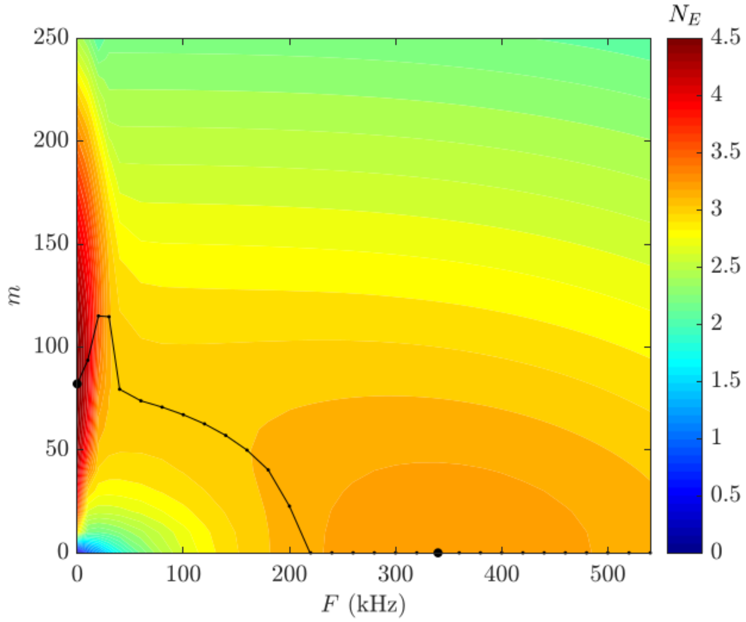

Figure 2.19: Calculated optimal growth N factors for Mach 5.9 flow over a 5.08mm nose radius cone, a measure of the exponential disturbance energy growth. The peak along the $f = 0Hz$ axis, denoted by the left black dot, corresponds to the typical stationary streamwise vortices, with the secondary peak along the $m = 0$ axis denoted by the second black dot are axisymmetric entropy fluctuations. From Paredes et al. [89].

The growth of this planar disturbance was not associated with the generalised inflection point, and the frequency range was around 300kHz, significantly different to experimental observations. Even if a particular set of disturbances or fluctuations experiences significant growth, there is still no guarantee that it will lead to turbulence in the boundary layer. Hartman et al. [107] demonstrated a feasible route to transition through disturbances originating in the entropy layer. Using the same geometry as Paredes et al. in the previously mentioned studies, the entropy layer was seeded by a pair of oblique entropy disturbances. The deformation of the entropy structures and the subsequent breakdown to turbulence in Figure 2.20 show the way they penetrate into the boundary layer.

These entropy fluctuations appear are similar in nature to the optimal disturbances computed by Paredes et al. [80] in that these disturbances are entropy disturbances. However, the pseudo linear stability analysis of Hartman et al. predicted strictly oblique travelling disturbances to be amplified, whereas the optimal disturbances predicted travelling axisymmetric disturbances to be most amplified for the same geometry and Reynolds number. It is possible that the axisymmetric disturbances are more sensitive to the *shape* of the incident disturbances, hence the reason they are observed by Paredes et al. and not the pseudo linear stability analysis of Hartman et al.

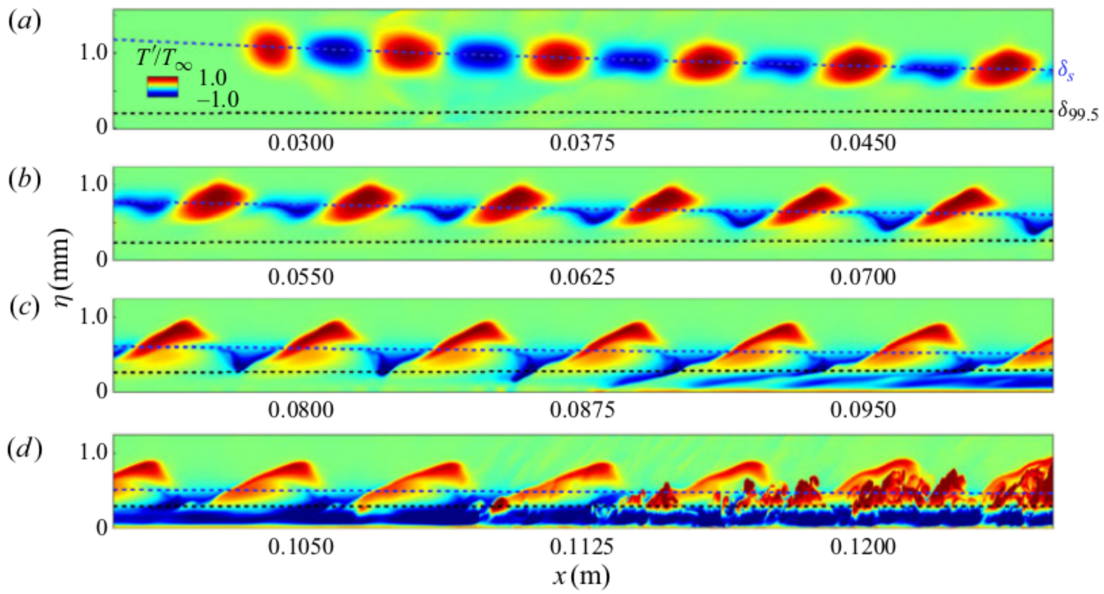

Figure 2.20: Simulations of Hartman et al. [107] demonstrating a feasible path to boundary layer turbulence through disturbances originating in the entropy layer. Blue and black dotted lines denote the entropy and boundary layer edges. Contours of temperature show the lower temperature fluid sinks and the structure rapidly breaks down after entering the boundary layer.

Liu et al. [112] performed full three dimensional DNS of hypersonic flow over a 5.2mm cone to investigate the effect of freestream noise on these entropy layer instabilities. To generate the freestream conditions for this simulations, the environment in the Sandia HWT-8 tunnel was modelled with a precursor DNS [113] and then decomposed into ≈375000 acoustic waves, which were then imposed on the pre-shock inflow condition for the cone DNS. Isosurfaces of the density gradient in Figure 2.21 show a dominant spanwise structure with streamwise-periodic structures extending outside the boundary layer.

There is also evidence that the nose affects the behaviour of the second mode at the intersection between the small and medium bluntness regimes. Numerical studies have shown that disturbances in the entropy layer modify the behaviour of the second mode, acting as an additional forcing effect and modifying the growth rates [114, 115].

The state of the art provides strong evidence that the entropy layer phenomena play a leading role in hypersonic boundary layer transition over blunt cones in the maximum delay regime. The questions "Is the entropy layer unstable?" and "Can phenomena in the entropy layer cause boundary layer transition?" have been answered in broad strokes, although the links between the expected dominant instabilities and the structures that drive breakdown is still not clear. There is still significant disconnect between experimental observations and numerical results. Numerical simulations using both direct simulations and the transient growth framework suggest the inflection point is not significant, and there is disagreement between these methods on whether axisymmetric or three dimensional disturbances are dominant. Given many experimental techniques are based on line of sight integration,

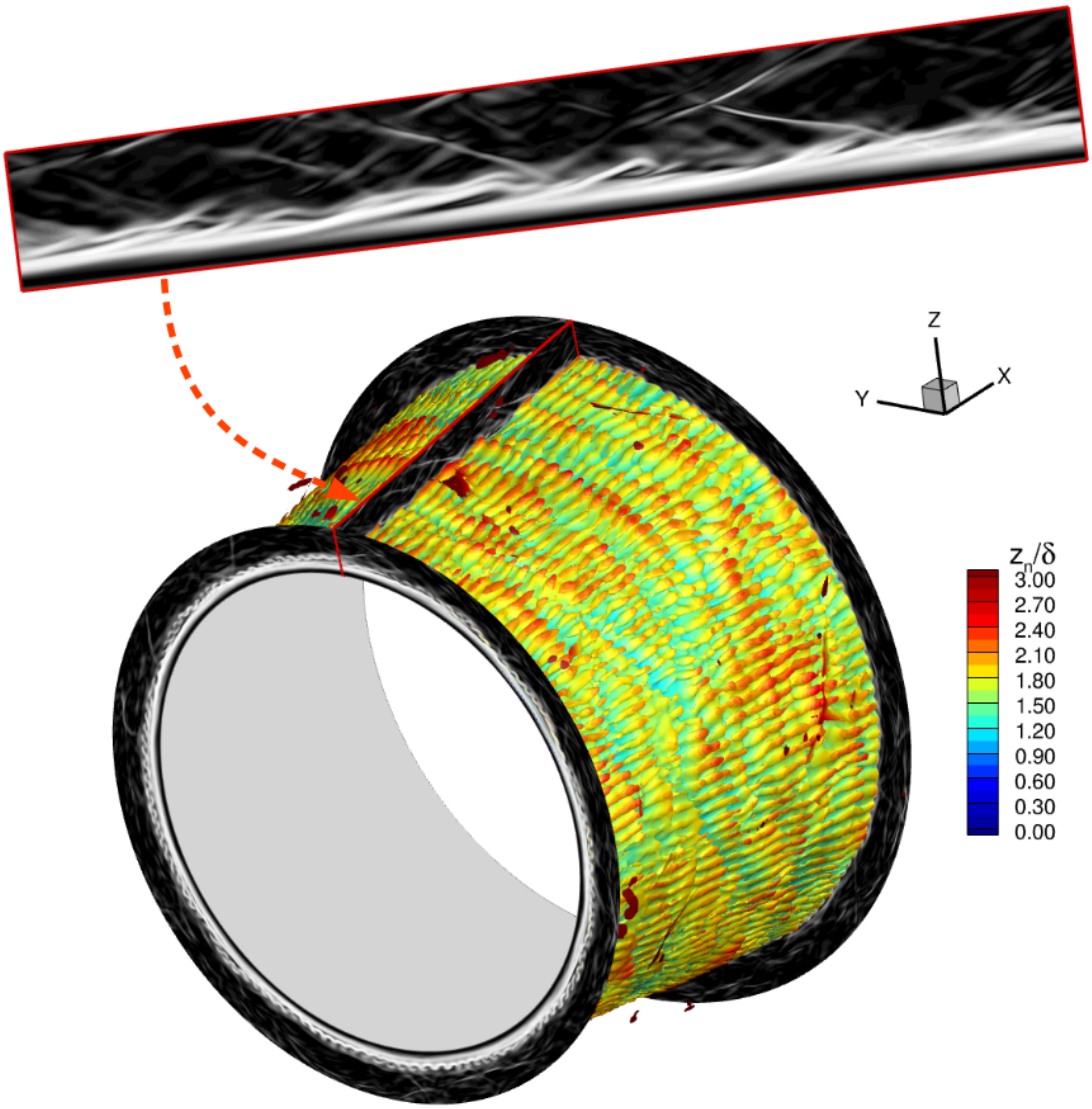

Figure 2.21: Instantaneous isosurfaces of the wall-normal density gradient coloured by the local wall-normal distance, with slices of the numerical schlieren imposed. The strctures show a clear dominant spanwise structure, with the streamwise-periodic structures extending outside the boundary layer.

knowing whether these disturbances are three dimensional or not is important. The role of the inflection point is still not clear, so the observations of Stetson et al. [85] are yet to be explained and as such is the primary focus of this thesis.

2.2 Numerical Schemes for Direct Numerical Simulations

Direct Numerical Simulations (DNS) is the process of directly solving the Navier-Stokes (NS) partial differential equations (in this context, the compressible Navier-Stokes equations) in a discrete manner, as opposed to solving the equations either with models for particular phenomena or simplifications such as linearization. The NS equations are a representation of the conservation equations of mass, energy and momentum in the (x, y, z) directions. The NS partial differential equations (PDEs) can be expressed in many forms, with the form from Anderson [7] given in Equation 2.6.

$$
\begin{aligned}
&\frac{\partial \rho}{\partial t} + \nabla \cdot (\rho U) = 0 \\
&\rho \frac{Du}{Dt} + \frac{\partial p}{\partial x} = \frac{\partial \tau_{xx}}{\partial x} + \frac{\partial \tau_{yx}}{\partial x} + \frac{\partial \tau_{zx}}{\partial z} \\
&\rho \frac{Dv}{Dt} + \frac{\partial p}{\partial y} = \frac{\partial \tau_{xy}}{\partial x} + \frac{\partial \tau_{yy}}{\partial x} + \frac{\partial \tau_{zy}}{\partial z} \\
&\rho \frac{Dw}{Dt} + \frac{\partial p}{\partial z} = \frac{\partial \tau_{xz}}{\partial x} + \frac{\partial \tau_{yz}}{\partial x} + \frac{\partial \tau_{zz}}{\partial z} \\
&\rho \frac{D\left(e + \mathbf{V}^2/2\right)}{Dt} = \frac{\partial}{\partial x}\left(k \frac{\partial T}{\partial x}\right) + \frac{\partial}{\partial y}\left(k \frac{\partial T}{\partial y}\right) + \frac{\partial}{\partial z}\left(k \frac{\partial T}{\partial z}\right) - \\
&\qquad \nabla \cdot p\mathbf{U} + \frac{\partial u \tau_{xx}}{\partial x} + \frac{\partial u \tau_{yx}}{\partial y} + \frac{\partial u \tau_{zx}}{\partial z} + \frac{\partial v \tau_{xy}}{\partial x} + \\
&\qquad \frac{\partial v \tau_{yy}}{\partial y} + \frac{\partial v \tau_{zy}}{\partial z} + \frac{\partial w \tau_{xz}}{\partial x} + \frac{\partial w \tau_{yz}}{\partial y} + \frac{\partial u \tau_{zz}}{\partial z}
\end{aligned}
\tag{2.6}
$$

Here the term $\frac{D}{Dt}$ denotes the material derivative, $\frac{\partial q}{\partial t} + \mathbf{U} \cdot \nabla q$, with q being a conserved quantity. The heat generation term $\rho \dot{q}$ from Anderson has been dropped from the energy equations as radiation is assumed to be negligible. The viscous shear stress terms are

$$
\begin{aligned}
\tau_{xy} &= \tau_{yx} = \mu \left(\frac{\partial v}{\partial x} + \frac{\partial u}{\partial y} \right) \\
\tau_{yz} &= \tau_{zy} = \mu \left(\frac{\partial w}{\partial y} + \frac{\partial v}{\partial z} \right) \\
\tau_{zx} &= \tau_{xz} = \mu \left(\frac{\partial u}{\partial z} + \frac{\partial w}{\partial x} \right) \\
\tau_{xx} &= \lambda (\nabla \cdot \mathbf{U}) + 2\mu \frac{\partial u}{\partial x} \\
\tau_{yy} &= \lambda (\nabla \cdot \mathbf{U}) + 2\mu \frac{\partial v}{\partial y} \\
\tau_{zz} &= \lambda (\nabla \cdot \mathbf{U}) + 2\mu \frac{\partial w}{\partial z}
\end{aligned}
\tag{2.7}
$$

with the symbols meaning the same as in Equation 2.2. The visocosity and thermal conductivity are computed using Sutherland's law, and Stoke's hypothesis is used for the second viscosity coefficient. The equations are generally closed with an equation of state; for the flows investigated in this work, this is the ideal gas equation of state

$$
p = \rho R_{gas} T \tag{2.8}
$$

where R_{gas} is the specific gas constant. The NS equations do not in general have an exact solution, so discrete methods are utilized to solve the an approximation of the system. Given that the Reynolds number in the flows of interest are of the order 10^6, the inviscid terms are dominant and of the most interest.

The inviscid system constitutes a set of hyperbolic PDEs. As such, they are governed by the propagation of a continuous spectrum of waves each with an amplitude and phase. In this context, the waves are acoustic waves which travel with a group velocity equal to the local flow velocity plus/minus the local sound speed, and entropy/vorticity waves travelling with the local flow (the same as those referenced in relation to the transient growth analysis by Reshotko and Tumin [106]).

2.2.1 Methods for Computational Fluid Dynamics

There are four common frameworks for solving a discretized set of partial differential equations (PDEs): finite difference, finite volume, finite element and spectral methods. While the earliest work was performed in the finite difference or spectral framework, they have for the most part phased out in favour of finite volume methods, due to the fact the finite volume formulation enforces the conservation of the set of conserved quantities in the discrete formulation and is simpler to apply to complex geometries. The finite volume approach discretizes the domain of interest into a set of small volumes, which fill the domain, as opposed to the infinitesmally sized solution points used in finite differences. The rate of change of each of the conserved quantities in each volume is computed using Gauss' theorem,

$$\iiint_V (\nabla \cdot \mathbf{F}) dV = \oiint_S (\mathbf{F} \cdot \hat{n}) dS, \tag{2.9}$$

i.e. the change of a quantity in a volume is the summation of the flux of the quantity through the volume's faces. Each of the volumes has a set of faces, through which mass, momentum and energy can pass from one volume to another. As any amount of conserved quantity lost by one cell is gained by another (discounting boundary conditions), the conservation laws are obeyed even in the discrete domain.

This property makes finite volume methods generally more numerically stable, which is desirable for the computation of engineering flows. On the other hand, DNSs are usually employed for fundamental physics investigations, for which accuracy is of utmost importance. To this end, high order numerical schemes (the consensus on "high order" being third order or higher [116]) are frequently utilised for DNS, as they are generally more accurate as they retain higher order terms. Multiple factors come in to play when considering the true order of accuracy for a numerical scheme, and the order does not itself tell the whole story regarding the way errors can manifest in a simulation.

Numerical errors come in two forms: dissipation and dispersion. Dissipation error is non-physical damping of the continuous waves that govern the PDEs, and dispersion error arises from incorrect phase speeds. The magnitude of these errors is proportional to the wavenumber: higher wavenumbers (smaller structures) are affected more than lower wavenumbers (larger structures). The manifestations of these types of error is illustrated by the numerical solution to an advection problem by Takacs [117] in Figure 2.22. Dissipation is characterized by the smoothing out of gradients as the energy is diffused, and dispersion by non-physical oscillations in the solution as the higher wavenumbers desynchronize from the wave group.

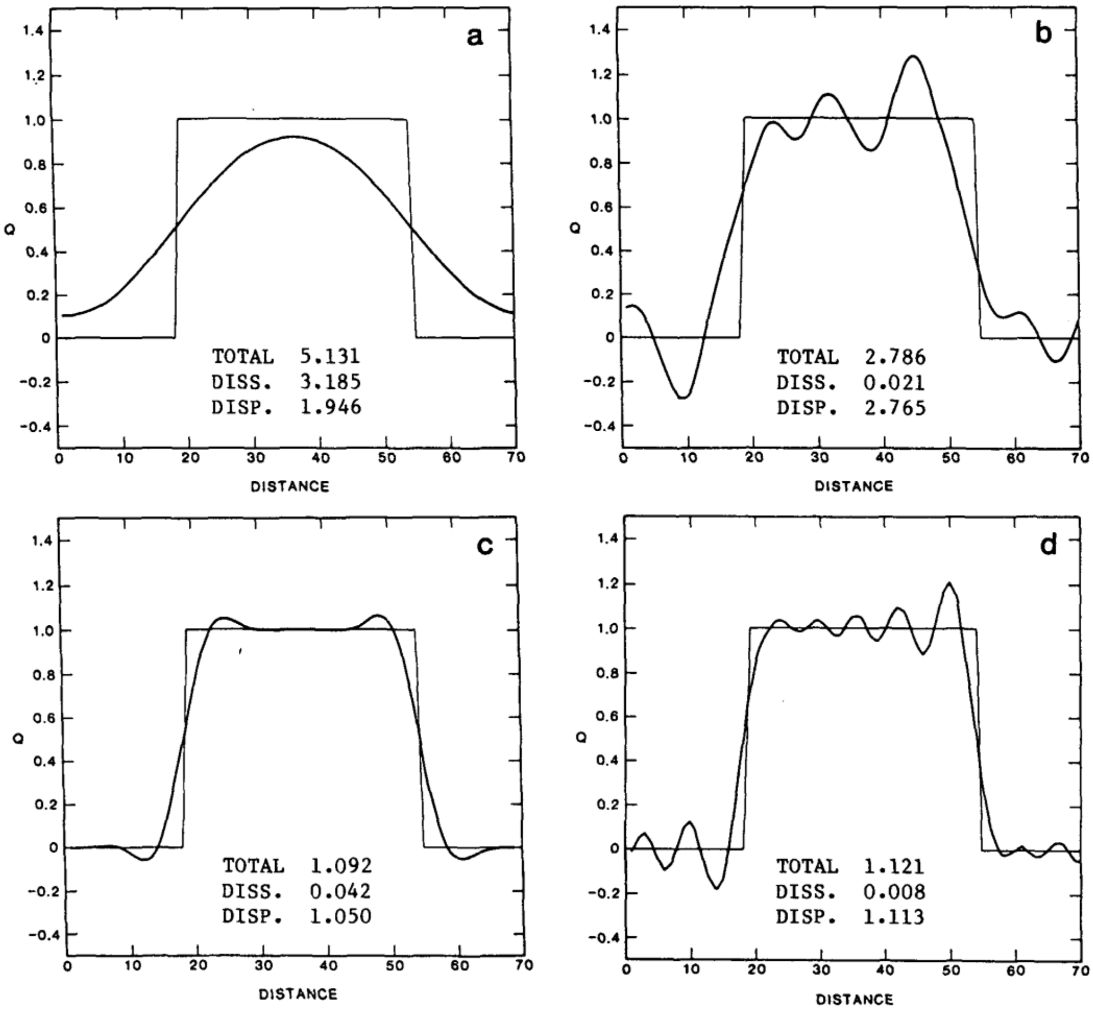

Figure 2.22: Results of the advection of a stepped pulse in a hyperbolic system. Figures (a)-(d) use schemes of increasing order of accuracy from 1 to 4. The noted quantities on each figure are the errors; total, dissipation and dispersion.

While the net error generally decreases with increasing order of the numerical scheme, the accuracy from an *engineering* point of view does not necessarily improve. High-order schemes are famously poor at accurately capturing sharp discontinuities, generating Gibbs phenomena [118] (the oscillations around sharp discontinuities, particularly obvious in (b) and (d) in Figure 2.22), which is cause for concern in supersonic and hypersonic flows due to the presence of shock waves. In simulated scenarios, such spurious oscillations generally grow in time due to the inability of the schemes to dissipate them and eventually destroy the simulation, if one naively applies a simple high-order scheme to the problem. Given current wisdom states that minimizing numerical dissipation is of utmost importance in DNS, this is clearly problematic.

Many methods have been proposed to address this issue, but they all have the same effect: to add numerical dissipation to the scheme at the discontinuity. The three most common methods are:

- Artificial dissipation: terms are added to the NS equations that act as additional dissipation, usually based on higher order derivatives [119].
- (Weighted) Essentially Non-Oscillatory schemes ((W)ENO): adjust the sources of the data used to construct the derivatives based on the local smoothness of the data [120,121].
- Blended Schemes: Take a linear combination of high order and low order fluxes, based on the local smoothness of the flow usually based off some shock detector [122, 123].

Each method has advantages and disadvantages, and there is no consensus in the community as to which method is "best" for DNSs. To illustrate this lack of consensus, a brief survey of some of the numerical techniques used to simulate hypersonic transitional DNSs is included here. There codes which a finite volume framework, such as the US3D code from the University of Minnesota [124] (fourth order central-difference based convective fluxes [125] blended with second order Steger-Warming, second order viscous fluxes with fourth order Runge-Kutta explicit or second order Crank-Nicholson implicit temporal scheme) or the NSMB code (fourth order central-difference based convective fluxes and viscous fluxes [126] with fourth order artificial dissipation, fourth order Runge-Kutta explicit temporal scheme).

On the other hand, there are finite difference codes. These codes are generally built to perform high fidelity simulations for a particular type of geometry. Prominent examples are the code from the University of Arizona [127] (cylindrical coordinate ninth order convective fluxes with winded with van Leer's splitting [128], 6th and 4th order viscous fluxes in the streamwise and wall-normal direction and a spectral scheme in the azimuthal direction with fourth order Runge-Kutta temporal scheme) or Ohio State University [112] (cylindrical coorindate seventh order WENO-JS [129] for convective fluxes, fourth order viscous fluxes and a third order low-storage Runge-Kutta temporal scheme).

While there appears to be little rhyme or reason to the spatial schemes chosen for these simulations, there is a trend that is not immediately obvious; the finite volume schemes are additions to pre-existing multi-physics codes, while the finite difference schemes are standalone codes strictly for the purpose of direct numerical simulations of a specific type of problem. Given that the intention in this work is to use the finite volume multi-physics solver Eilmer [17] developed in-house at the University of Queensland, focus is on methods that fit well within the pre-existing architecture of the code. The desire is to choose a numerical scheme that is high accuracy, has been validated in some sense for high speed compressible flows, and can be applied in a finite volume framework.

The quality of the numerical solution is not only dependent on the spatial and temporal schemes. There is also a strong dependence on the manner in which the domain is discretized, especially in the vicinity of shock waves. Alignment of the mesh with the shocks is essential for high quality solutions, which can be achieved either through tight manual control of the mesh generation or through shock fitting techniques. Poor alignment can lead to generation of unwanted numerical disturbances [130] and poor or stalled steady state convergence [131], an example of which is shown in Figure2.23.

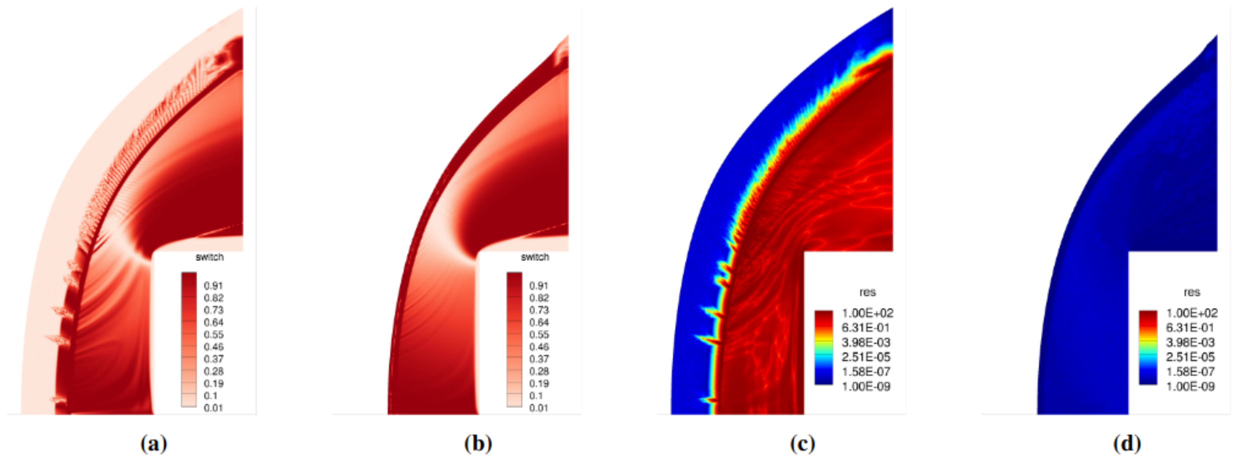

Figure 2.23: Effect of grid alignment on shock detection using the Ducros shock sensor and numerical convergence for supersonic flow over a forward facing step from Hendrickson et al. [131].

Given the constraints outlined above, the candidate numerical scheme should be applicable in a finite volume framework, low dissipation and high order accurate. For pragmatic reasons, the scheme should also be simple to implement, both for the implementer's and any future user's sake. Given the goal is to use the finite volume code Eilmer and its range of dissipative schemes for modelling of shock waves, blended central schemes are the ideal candidates for this work.

Chapter 3

Implementation and Verification of Numerical Schemes For Hypersonic DNS

Before introducing the numerical scheme chosen for this work, a brief introduction to the Eilmer flow code is described, in particular the convective flux methods, to provide context for the following numerical tests. Eilmer is a finite volume multi-physics code developed in-house at the University of Queensland. The code simulates the compressible Navier-Stokes equations with chemistry models up to the complexity of thermochemical non-equilibrium, though the ideal gas assumption is used in this work.

3.0.1 Approximate Riemann Schemes in Eilmer

The focus of this chapter is the calculation of the inviscid fluxes. The existing inviscid flux methods within Eilmer are approximate Riemann methods. Approximate methods are described in some detail by Roe [132], but for completeness are explained briefly here so that the comparisons made are meaningful. The Riemann problem is an initial problem involving the interaction of two discontinuous states,

$$\mathbf{Q}(x < x_0, 0) = Q_L, \qquad \mathbf{Q}(x > x_0, 0) = Q_R \tag{3.1}$$

where Q is some state vector and x_0 is a generally arbitrary point in space. In the finite volume framework, the interfaces between finite volume cells form a series of such problems. The Riemann problem at each interface is solved in an approximate manner using a specified method using input states Q_L and Q_R. These left and right initial states are computed either by copying of the cell centre data related to the relevant interface, or by the construction of local polynomials using a *stencil* of cells. The process is illustrated in Figure 3.1. The polynomial orders available in Eilmer are zeroth (cell centre data copied to the interface), second order and fourth order.

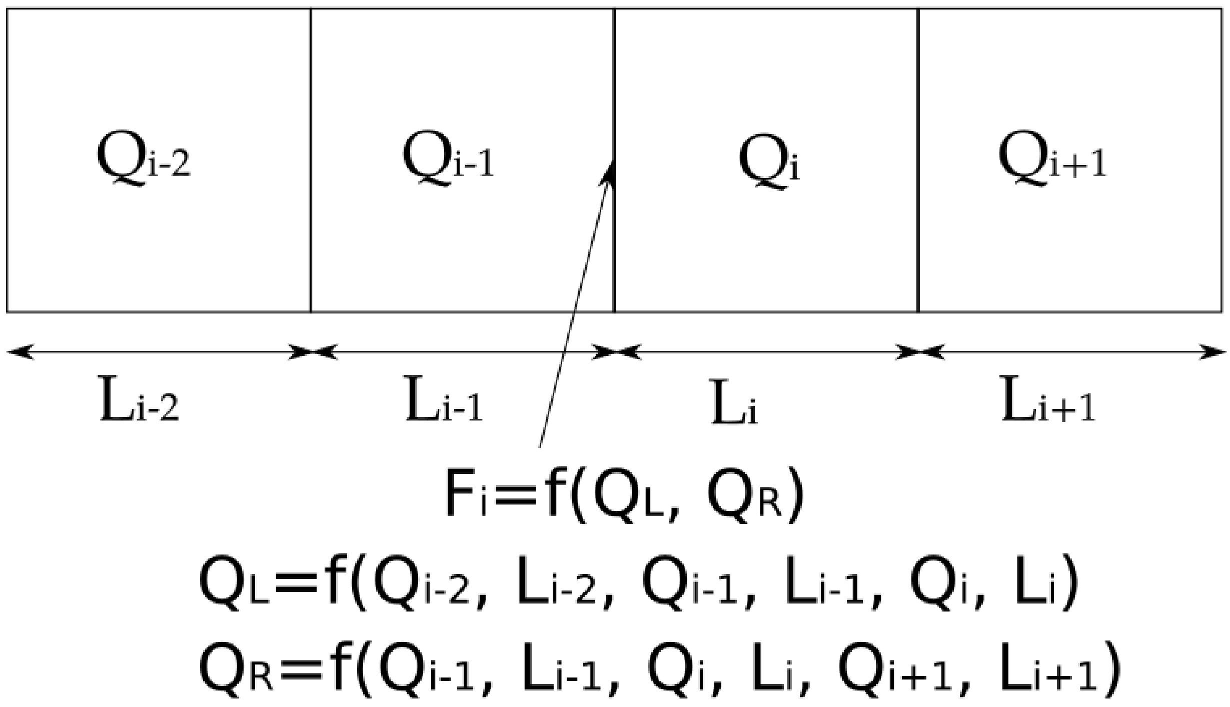

Figure 3.1: Illustration of the construction of the left and right Riemann states in Eilmer. This particular example uses quadratic polynomials for state construction; fourth order polynomials which use 6 cell stencils are also available. The cell states Q are the state variable vectors, and L is the width of the cell in the interface normal direction.

The choice of numerical scheme implemented for this work was limited to schemes applicable to finite-volume codes and that have published evidence of their performance for hypersonic applications. Additionally, the scheme should fit well within the framework existing within the Eilmer flow code from a programmatic point of view.

3.1 The Summation-by-Parts Alpha-Split-Flux Convective Flux Scheme

The high-order, low dissipation convective scheme chosen for this work was the Summation-by-Parts Alpha-Split-Flux (SBP-ASF) scheme of Fisher et al. [133]. This scheme linearly combines the convective fluxes from the divergence and product rule forms of a set of advection equations. For an arbitrary advection equation in continuous form $\frac{\partial Q}{\partial t} + \frac{\partial uq}{\partial x} = 0$, the convective term is split as

$$\frac{\partial uq}{\partial x} = \alpha \frac{\partial uq}{\partial x} + (1-\alpha)\left(u\frac{\partial q}{\partial x} + q\frac{\partial u}{\partial x}\right) \tag{3.2}$$

with Q being the conserved quantity and q, u being a separated form of the product of the conserved quantity and the convection velocity. It is common to set q as the conserved quantity and u as the velocity, but this is not necessary. To disambiguate the term u from the convective velocity and to follow the nomenclature of the reference work, the quantity uq will be written as vw. In a discrete context, the flux of the conserved quantity at a given flux point is given by

$$\overline{f} = \alpha\overline{f}_d + (1-\alpha)\overline{f}_z \tag{3.3}$$

where $\overline{f}$ is the numerical flux and $\overline{f}_d$, $\overline{f}_z$ are the divergence and product rule fluxes respectively. In the 4th order form, these fluxes are given by

$$\begin{aligned}\overline{f}_d &= \frac{1}{12}\left(-w_{i-1}v_{i-1} + 7w_iv_i + 7w_{i+1}v_{i+1} - w_{i+2}v_{i+2}\right)\\ \overline{f}_z &= \frac{1}{12}\left(-w_{i-1}v_{i+1} - w_{i+1}v_{i-1} + 8w_iv_{i+1} + 8w_{i+1}v_i - w_iv_{i+2} - w_{i+2}v_i\right)\end{aligned} \tag{3.4}$$

with the subscripts denoting the values of v and w at solution points either side of the flux point located at $i+1/2$. While this method was derived in a finite difference context, it can be mapped to a finite volume context by treating the values v and w as cell centre values and the flux point as the cell interface between cells i and $i+1$. Though the reference work includes boundary closure stencils, as is necessary in finite difference schemes, the use of ghost cells common in CFD negates their necessity. Applying the alpha splitting to the compressible Euler equations gives

$$\begin{aligned}\frac{\partial\rho}{\partial t} + \frac{\partial\rho u_r}{\partial x_r} &= 0\\ \frac{\rho u_s}{\partial t} + \alpha_m\frac{\rho u_r u_s}{\partial x_i} + (1-\alpha_m)\left(\rho u_r\frac{\partial u_s}{\partial x_r} + u_s\frac{\rho u_i}{\partial x_r}\right) + \frac{\partial p}{\partial x_s} &= 0\\ \frac{\rho E}{\partial t} + \alpha_e\frac{\partial\rho u_r e}{\partial x_r} - (1-\alpha_e)\left(\rho u_r\frac{\partial e}{\partial x_r} + e\frac{\partial\rho u_r}{\partial x_r}\right)&\\ +\alpha_k\frac{1}{2}\frac{\partial\rho u_r u_s^2}{\partial x_r} + (1-\alpha_k)\frac{1}{2}\left(\rho u_r u_s\frac{\partial u_s}{\partial x_r} + u_s\frac{\partial\rho u_r u_s}{\partial x_r}\right)&\\ +\alpha_p\frac{\partial p u_r}{\partial x_r} + (1-\alpha_p)\left(p\frac{\partial u_r}{\partial x_r} + u_r\frac{\partial p}{\partial x_r}\right) &= 0\end{aligned} \tag{3.5}$$

with the variables u, ρ, p and e denoting the velocity, density, pressure and internal energy in this context. The subscripts r and s denote the Cartesian directions, with r representing the direction of convection and s representing the direction of the conserved momentum/kinetic energy. The pressure term in the momentum equation does not fit the separable form, so is given the decomposition $vw \equiv 1\cdot p$ and taken purely from the divergence form. Different choices of the splitting terms $\alpha = [\alpha_m, \alpha_e, \alpha_k, \alpha_p]$ result in the conservation of different invarients. For example, setting $\alpha = [0.5, 1, 1, 1]$ yields the Kinetic-Energy Consistent (KEC) scheme of Subbareddy and Candler [125], while $\alpha = [0.5, 0.5, 0, 0]$ yields the entropy conserving scheme of Honein and Moin [134].

The scheme was comprehensively verified and validated for the purpose of engineering hypersonic flows using LES by White et al. [135]. A selection of verification and validation cases are presented here to confirm the implementation of the scheme within the Eilmer flow code is correct and appropriate for transitional DNS. Its performance is compared to the more traditional finite volume schemes already present within the code. The order of the Riemann state construction polynomial used in the traditional finite volume methods is denoted by the postfix (p) (e.g. AUSMDV(2) denotes the AUSMDV method with parabolic Riemann state reconstruction) in figure captions. The classic third-order Runge-Kutta explicit scheme is used for time stepping.

3.1.1 Approximate Riemann Solvers in Eilmer

The primary target for the Eilmer flow code is engineering-style calculations, where numerical stability and robustness are prioritised higher than high-order accuracy. Approximate Riemann solvers are ideal for this purpose. The left and right Riemann states are calculated using reconstruction polynomials of a specified order. The reconstruction takes into account non-uniform cell spacing in the Lagrangian formulation of the polynomial, as opposed to most high-order central schemes. Higher order polynomials require larger stencils and are more expensive to calculate, but generally improve the accuracy of the Riemann states and therefore the net accuracy. The polynomial orders currently available in Eilmer are 0 (cell centre state copied to the interface), quadratic and quartic.

3.2 Verification

Two verification cases are presented here. The first is the classical Advection of an Isentropic Vortex, which is used to verify the nominal order of accuracy of the SBP-ASF scheme and investigate the dissipation and dispersion characteristics of both the SBP-ASF scheme and the approximate Riemann solvers present within Eilmer. The second is the Steepening Wave Problem, used to investigate the effect of the scheme on higher wavenumbers and determine the number of cells required to adequately resolve a given wavelength. An abridged version of this section was presented at the 22nd Australasian Fluid Mechanics Conference and included in the proceedings of said conference [1].

3.2.1 Advection of an Isentropic Vortex

The Advection of an Isentropic Vortex test case is commonly used in the verification of numerical schemes for the purpose of LES and DNS. The resolution of convected vortical structures is essential for real flow problems. Given the initial vortex state is isentropic and an exact solution to the Euler equations, it should remain constant forever (neglecting the advection from the bulk velocity). The solution also allows for a purely periodic domain, avoiding the complications that come with boundary conditions. The definition of the two-dimensional compressible vortex is given by [136]

$$
\begin{aligned}
\delta u &= -\frac{y}{R}\Omega \qquad \delta v = \frac{x}{R}\Omega \\
\delta T &= -\frac{\gamma - 1}{2}\Omega^2
\end{aligned}
\tag{3.6}
$$

with u, v here being the x, y velocities, T the temperature, γ the ratio of specific heats and R, Ω being the vortex radius and the vortex strength respectively. The strength of the vortex is given by

$$
\begin{aligned}
\Omega &= \beta e^{f} \\
f &= -\frac{1}{2\sigma^2}\left(\left(\frac{x}{R}\right)^2 + \left(\frac{y}{R}\right)^2\right)
\end{aligned}
\tag{3.7}
$$

with f being a constant controlling the strength of the vortex and σ representing its spread. The perturbation quantities $\delta(u, v, T)$ are imposed onto a uniform base flow. The choice of constants matches that of Wang et al. [116], with vortex constants $[\beta, \sigma, R] = [1/5, 1, 0.005]$ and base flow quantities $[M_\infty, p_\infty, T_\infty] = [0.5, 100\text{kPa}, 300\text{K}]$. The bulk velocity is purely in the x direction. The initial density field is shown in Figure 3.2. The domain is two dimensional, with bounds $-L \leq x \leq L$ in both directions.

Given the domain is periodic, care must be taken in choosing the domain length L to prevent the vortex from interacting with itself across the periodic boundaries. The magnitude of the perturbations should be effectively 0 to prevent this self-interaction. This means that the magnitude should be less than the smallest number representatable by the floating point precision used on the given architecture. 64-bit precision is typical of most modern systems, so the smallest number representable ϵ is 2^{-52}. The relation governing the lower limit of the domain size is given by Eq. 3.8. For this choice of constants, the minimum domain width L is 0.043m, so L was set to 0.05m for convenience.

$$
\epsilon \leq \frac{L}{R} e^{\frac{-L^2}{2R^2\sigma^2}}
\tag{3.8}
$$

The flow is simulated for one advection period, with a CFL number of 0.25 to minimise temporal error and isolate the spatial accuracy of the schemes. The size of the time step is fixed. The density field at 0.4τ, 0.8τ and τ, where $\tau = 2L/a_\infty M_\infty$ is the advection period, using the SBP-ASF method and AUSMDV [137] method with parabolic state reconstruction on a 64x64 cell grid are shown in Figure 3.3. The effect of the numerical dissipation present in the approximate Riemann schemes on the gradients is visually obvious and demonstrates the importance of high-order schemes in LES and DNS. The density profiles along the centreline shown in Figure 3.4 illustrate the effect of the higher order reconstruction stencils on the numerical dissipation.

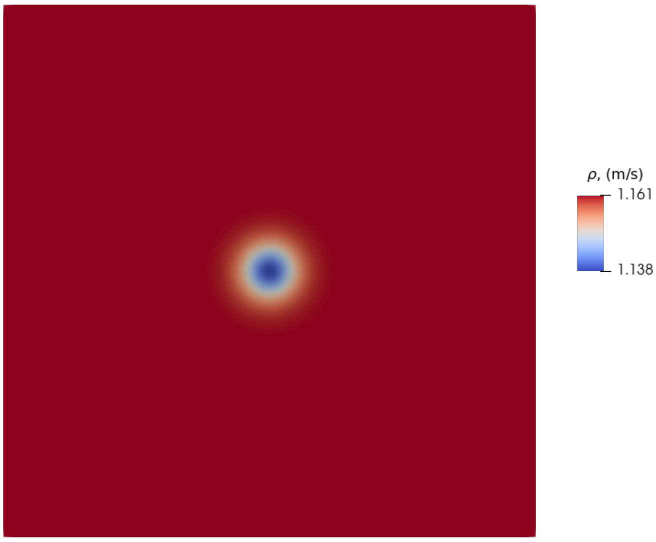

Figure 3.2: Density field of the Isentropc Vortex at t=0.

To verify the implementation of the SBP-ASF scheme within Eilmer is correct, the spatial convergence of the scheme was calculated using the root-mean-square (L2) density error as the reference quantity. Given the final time is equal to one advection period, the initial solution is identical to the analytic solution at the final time. The L2 error is calculated in the usual manner described by Eq. 3.9 and plotted for increasing cell count in Figure 3.5, where N is the total number of cells in the domain.

$$L_2 = \sqrt{\frac{\sum_{m=1}^{N} (\rho_{m,t=t_f} - \rho_{m,t=t_0})^2}{N}} \tag{3.9}$$

Included for reference are the results using a range of pre-existing Riemann schemes: the AUSMDV, Roe [138] and LDFSS(0) [139] schemes. The SBP-ASF scheme demonstrates the expected fourth-order convergence, giving confidence that the scheme is implemented correctly. The convergence rates with using the approximate Riemann schemes indicate that increasing the accuracy of the state reconstruction past second order has limited benefit- the schemes do not surpass second order spatial accuracy, even with quartic state reconstruction.

Before drawing conclusions regarding the cause of this limitation in the approximate Riemann schemes, the error can be further split into dissipation and dispersion components using the methods of Takacs [117]. Beginning with the mean square error (the L_2 error squared), one can arrive at an equivalent definition for the error given by

$$E_{MS} = (\sigma(\rho_{t=t_0}) - \sigma(\rho_{t=t_f}))^2 + (\overline{\rho_{t=t_0}} - \overline{\rho_{t=t_f}})^2 + 2(1-c)\sigma(\rho_{t=t_0})\sigma(\rho_{t=t_f}). \tag{3.10}$$

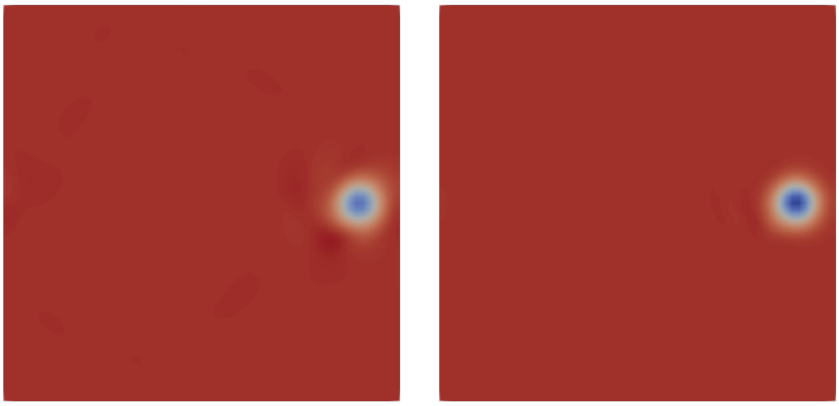

(a) Density at $t = 0.4\tau$.

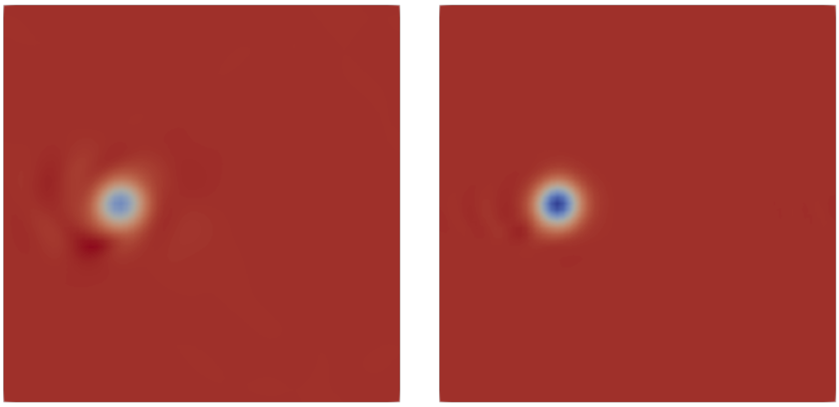

(b) Density at $t = 0.8\tau$.

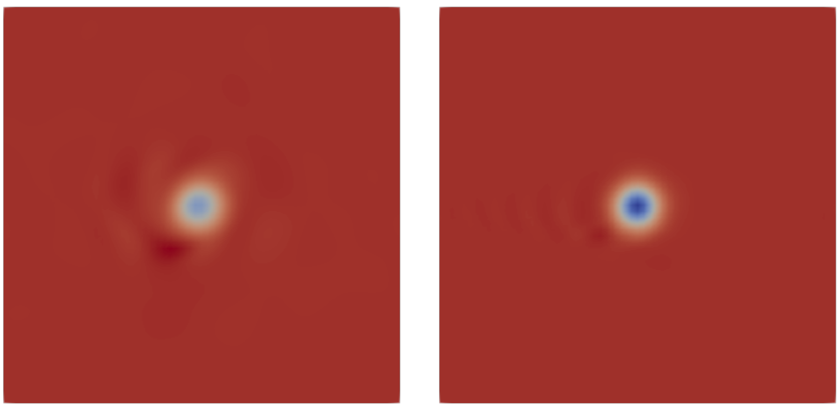

(c) Density at $t = \tau$.

Figure 3.3: Visualisation of the advection of the vortex across a uniform grid using the Euler equations. Left uses the AUSMDV approximate Riemann method with parabolic state reconstruction for the convective fluxes, right uses the SBP-ASF scheme.

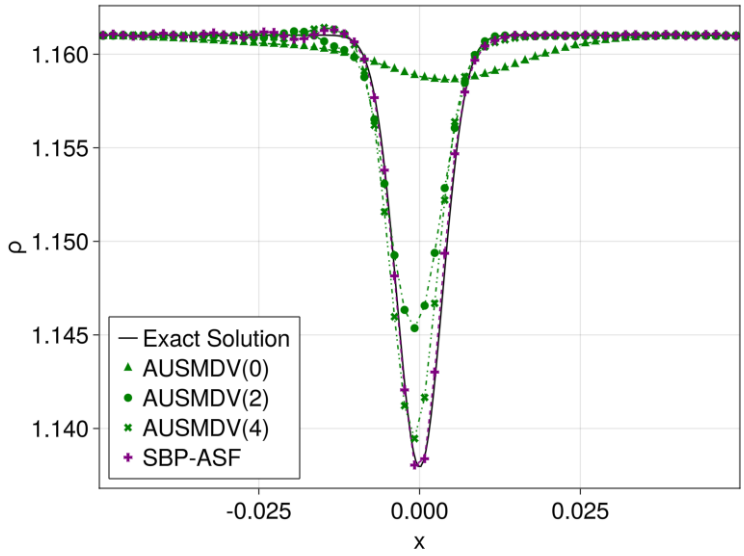

Figure 3.4: Density of isentropic vortex after one advection period along the line $y = 0$ on a 64x64 cell mesh. Increased numerical dissipation in the approximate Riemann schemes acts to smooth the gradients and dissipate the vortex.

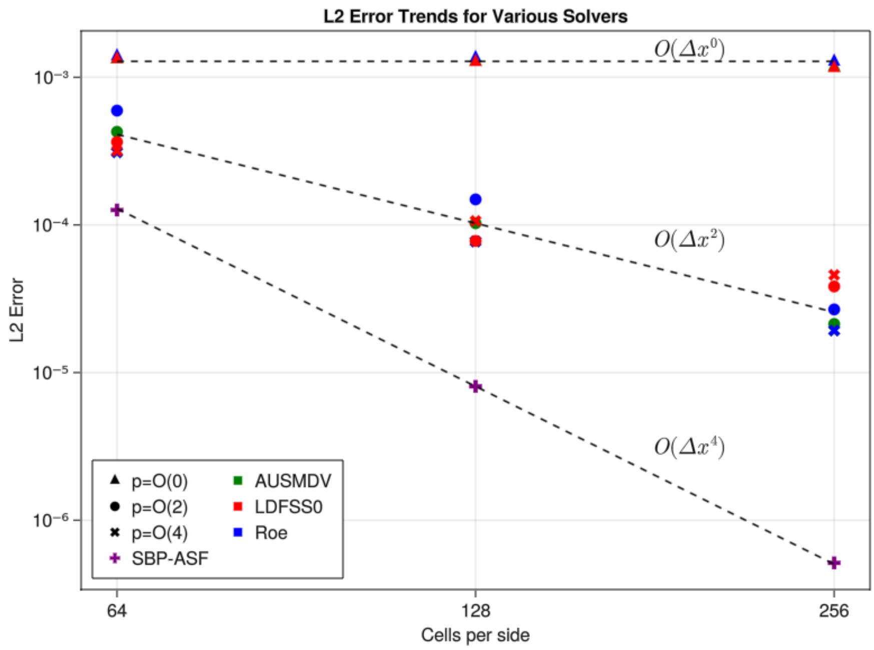

Figure 3.5: L2 density norm for a range of flux schemes. The SBP-ASF method achieves the nominal fourth-order convergence, while the approximate Riemann schemes are capped at second-order. For the Riemann schemes, Colour denotes the scheme and marker denotes the order of the reconstruction polynomial.

Here σ denotes the standard deviation, the bar denotes a mean quantity and c is the correlation coefficient between $\rho_{t=t_f}$ and $\rho_{t=t_0}$. The argument is made that if the solutions are perfectly correlated ($c = 1$), the error can only be from numerical dissipation. It follows that the mean square error definition in Eq. 3.10 can be split into dissipation and dispersion terms by Eq. 3.11. Given that the definition originates from the mean square error, rather than the root mean square error, the error contributions are square rooted so that they can be compared easily to the L2 error trends.

$$
\begin{aligned}
E_{diss} &= (\sigma(\rho_{t=t_0}) - \sigma(\rho_{t=t_f}))^2 + (\overline{\rho_{t=t_0}} - \overline{\rho_{t=t_f}})^2 \\
E_{disp} &= 2(1-c)\sigma(\rho_{t=t_0})\sigma(\rho_{t=t_f})
\end{aligned}
\tag{3.11}
$$

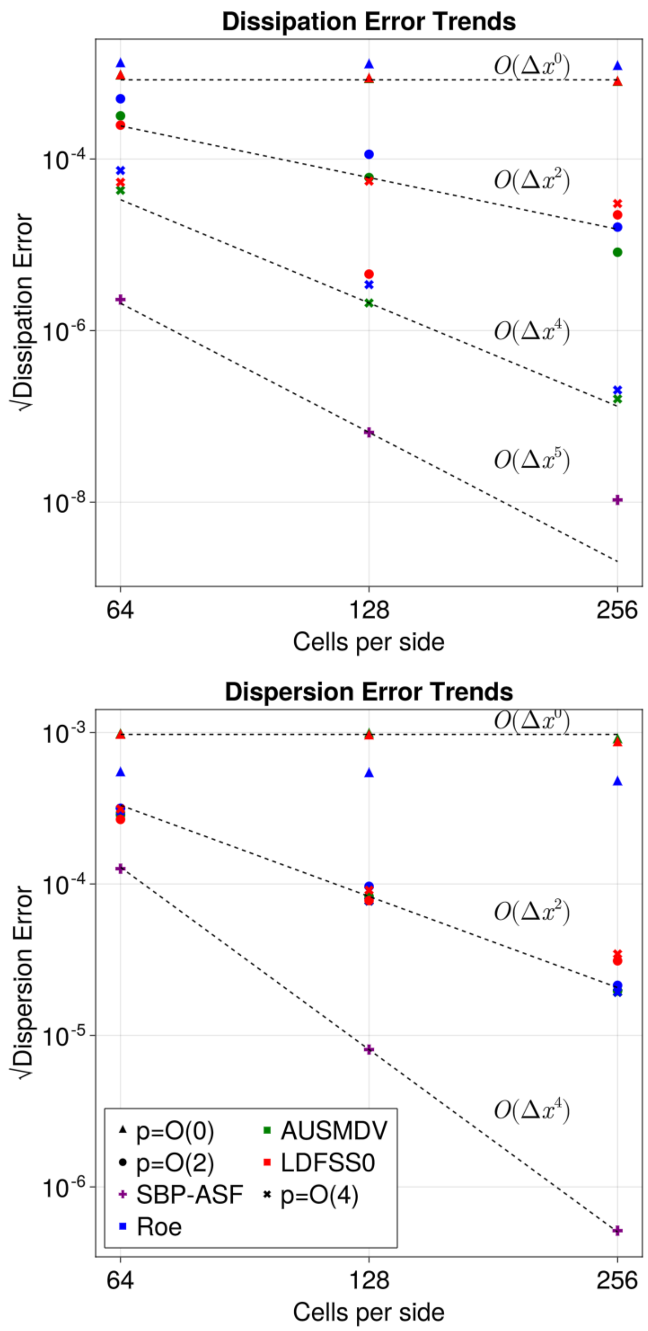

Figure 3.6: Breakdown of the error into dissipation and dispersion error contributions. The approximate Riemann schemes achieve high order dissipation accuracy, but are limited to second order by the dispersion error.

The dissipation behaviour of the Riemann schemes is improved by the higher order reconstruction polynomials, but the dispersion error does not get past second order convergence, limiting the overall accuracy. This matches the trends observed in the density profiles in Figure 3.4. The higher order reconstruction maintains the strength of the vortex more accurately, but the error is dominated by the slight mismatch in the vortex position. The accuracy of the Riemann schemes may be limited by the order of the quadrature, with single point quadrature across the interface being used within Eilmer. The SBP-ASF method gets past this limitation as it is essentially a finite difference scheme, so is not limited by the quadrature.

The high-order methods are limited by their numerical stability. The same numerical dissipation which degrades the accuracy of the Riemann methods stabilises the calculation, making it more resistant to numerical instability. Central schemes, of which the SBP-ASF scheme is one, are nominally zero dissipation, putting severe constraints on the flows that can be simulated and the size of the time step that can be taken. The effect is not obvious after a single advection period, but in longer runtimes the instability of the scheme becomes obvious. The density profile after 10 periods using the SBP-ASF scheme shown in Figure 3.7 illustrates the effect this has on the solution.

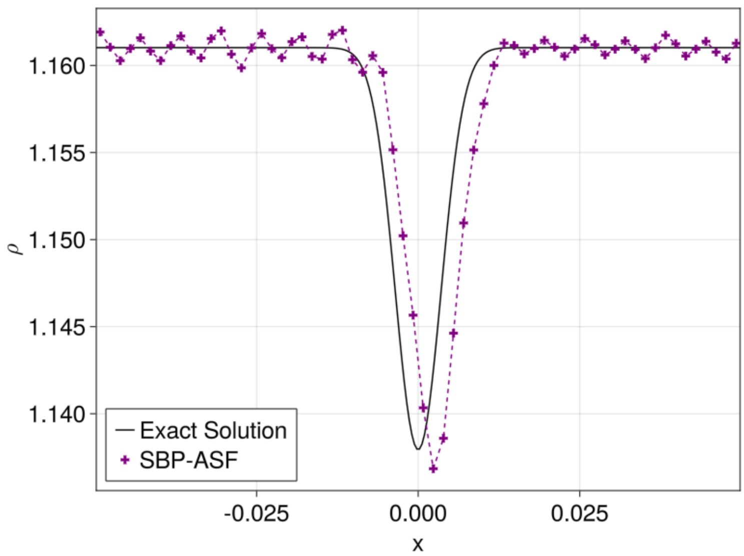

Figure 3.7: Density profiles after 10 advection periods using the SBP-ASF scheme, illustrating the instability of low dissipation schemes.

The temporal stability of the schemes are problem dependent, but in general a central scheme will have tighter stability limits than the approximate Riemann schemes for a given temporal scheme. For this test case, the CFL of 0.25 was close to the stability limit of the SBP-ASF scheme, while the Riemann schemes were stable up to approximately 1.5. Whether the high-order scheme actually achieves a net improved performance in terms of the compute resources used is dependent on how many more cells the robust schemes need to achieve equivalent accuracy and the relative cost per flux evaluation. This particular aspect is investigated further in Section 3.2.2, where the number of cells required to resolve a given wavelength is tested.

These tests were all performed on strictly Cartesian meshes. In most real-world calculations, the mesh will be neither Cartesian nor uniform, so the accuracy of the schemes on such meshes should be quantified. The effect of non-uniform grid spacing is addressed by applying a Gaussian clustering to the mesh, such that the grid spacing is considerably non-uniform at the centre of the grid and effectively uniform at the boundaries, to prevent discontinuities in the spacing over the periodic boundaries. The specific mapping function used is described in Equation 3.12, with an image of the resulting mesh in Figure 3.8. The parameters m,s,r are the location of peak clustering, the spread of the Gaussian and the ratio of the smallest to largest cell sizes and are set to 0.5,0.5,0.33 for this example. Additionally, erf denotes the error function which is approximated via approximation 7.1.26 in [140].

$$\begin{aligned}
x(\xi) &= a\xi + as(1-r)\sqrt{0.5\pi}\,\mathrm{erf}\left(\frac{(m-\xi)}{s\sqrt{2}}\right) + c \\
a &= \frac{1}{\left(s(1-r)1 + \sqrt{0.5\pi}\left(\mathrm{erf}\left(\frac{(m-1)}{s\sqrt{2}}\right) - \mathrm{erf}(\frac{m}{s\sqrt{2}}\right)\right)} \\
c &= -as(1-r)\sqrt{0.5\pi}\,\mathrm{erf}\left(\frac{m}{s\sqrt{2}}\right)
\end{aligned} \tag{3.12}$$

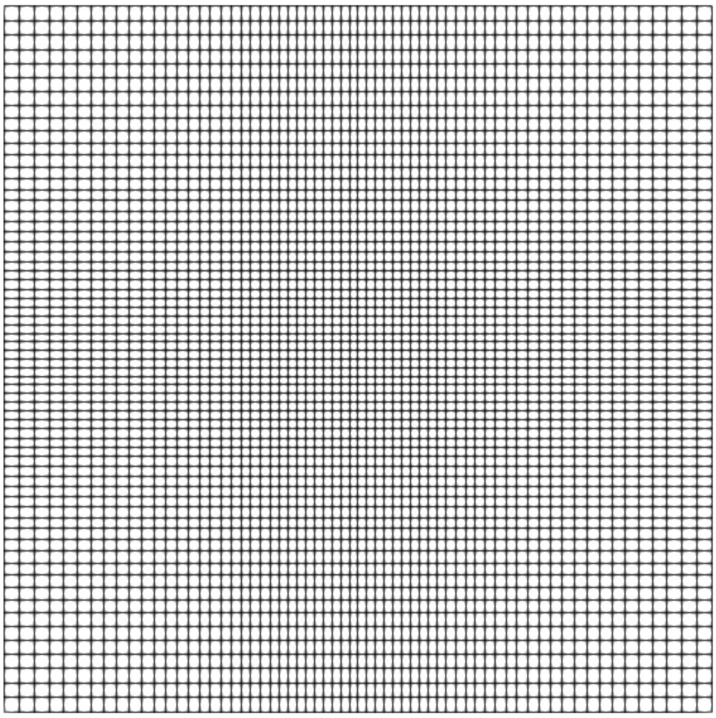

Figure 3.8: 64x64 cell mesh clustered using a Gaussian function used to test the accuracy of the convective schemes on nonuniform meshes.

Here only the AUSMDV Riemann method is included for comparison to improve clarity. The convergence on the non-uniform grid is shown in Figure 3.9, with the separation into dissipation and dispersion contributions in Figure 3.10.

The SBP-ASF method still performs well with non-uniform grid spacing, as long as the grid spacing is smoothly changing. The density profiles in Figure 3.11a show that the

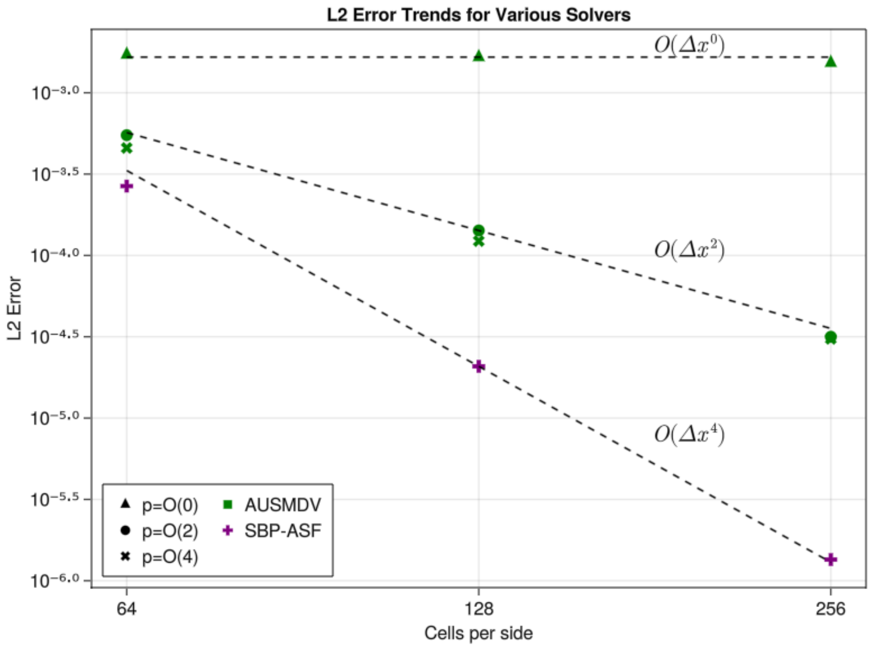

Figure 3.9: L2 density norms on a non-uniform grid. The SBP-ASF scheme maintains the desired high-order accuracy.

instability of the method is slightly exacerbated by the non-uniformity, but the performance is still clearly superior to the Riemann methods. Results with halving the cell spacing in Figure 3.11b results in similar resolution of the vortex with the SBP-ASF scheme and the AUSMDV with quartic reconstruction.

The isentropic vortex demonstrates both the net error behaviour of the numerical schemes as well as some insights into the dissipation and dispersion behaviours. It does not tell us quantitatively the effect of numerical dissipation on structures approaching the grid spacing. The question ultimately is "How many cells does one need to resolve a given wavelength?", and the following Steepening Wave test case attempts to answer this question.

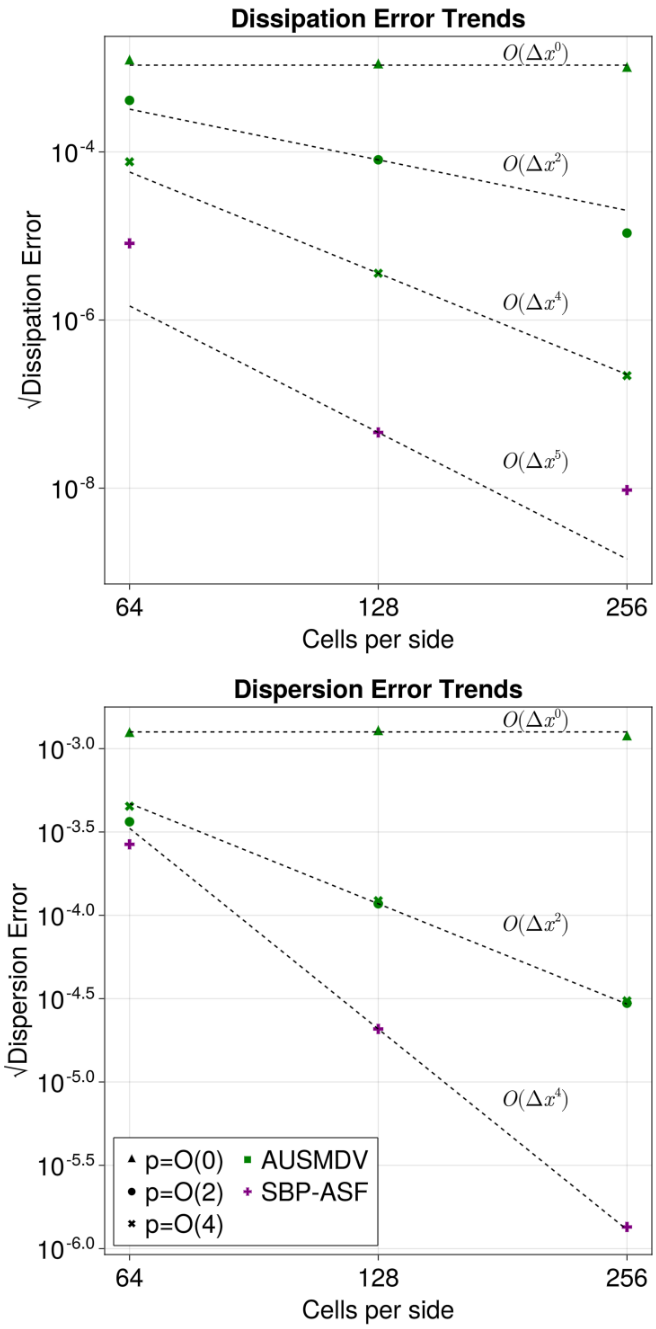

Figure 3.10: Dissipation and dispersion error on a non-uniform grid. Minor degradation in the SBP-ASF performance, but still maintains high order dissipation and dispersion accuracy.

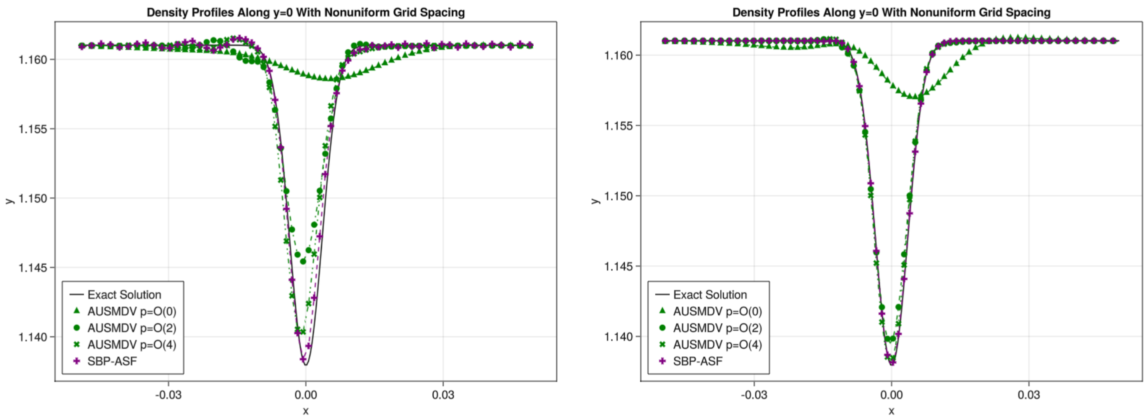

(a) Non-uniform 64x64 cell grid. (b) Non-uniform 128x128 cell grid.

Figure 3.11: Density profiles along y=0 on grids with increasing resolution. On the 128x128 cell grid, the SBP-ASF and AUSMDV schemes are effectively identical when using the quartic state reconstruction.

3.2.2 Steepening Wave

The Steepening Wave from Landau and Lifshitz [141] is a one-dimensional test problem which can be used to test the effect of numerical dissipation on wavelengths approaching the grid spacing. Beginning from an initially sinusoidal starting condition, the wave steepens to form a shock due to different characteristic speeds along the profile, demonstrated by Figure 3.12. The initial velocity profile is described by Eq. 3.13 and the remaining flow properties can be calculated at any time based on the velocity by Eq. 3.14. Each point in the profile travels at the local characteristic speed, so the analytic solution is known at any time up to the shock formation time defined by Eq. 3.15.

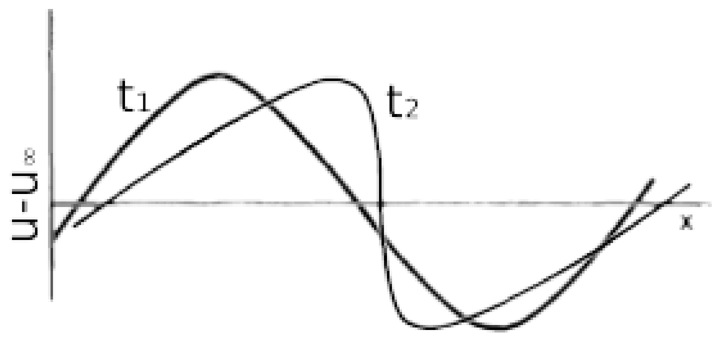

Figure 3.12: The steepening of the wave profile due to differing local characteristic speeds. Modified from Landau and Lifshitz [141].

$$u(x,0) = u_\infty \sin(2\pi x) \tag{3.13}$$

$$\begin{aligned} \rho(x,t) &= \rho_\infty \left(1 + \frac{(\gamma-1)u(x,t)}{2a_0}\right)^{\frac{2}{\gamma-1}} \\ p(x,t) &= p_\infty \left(1 + \frac{(\gamma-1)u(x,t)}{2a_0}\right)^{\frac{2\gamma}{\gamma-1}} \end{aligned} \tag{3.14}$$

$$t_s = \left|\frac{2}{u_\infty \pi(\gamma+1}\right| \tag{3.15}$$

Here a_0 is the sound speed based on the initial conditions $a_0 = \sqrt{\gamma p_\infty / \rho_\infty}$. The steepening of the wave is represented by the growth of higher wavenumbers in the Fourier space. Analysis of the problem in the Fourier space yields quantitative information about the action of the convective flux schemes on a given wavelength, in terms of the number of cells used to resolve that wavelength. The analytical solution for the velocity profile at any time is given by the non-linear equation

$$0 = \frac{u(x,t)}{u_\infty} - \sin(\pi(x - t(a_0 + 1/2(\gamma+1)u(x,t)))). \tag{3.16}$$

The base velocity is set to be a_0 for the purposes of visualisation, so that the profile remains centred in the local domain. The base pressure and density are 1×10^5Pa and 1kg/m^3. Periodic boundary conditions are used in the flow direction. While the problem is nominally one dimensional, the Eilmer code requires at minimum 2 dimensions, so 3 cells are used in the y direction to allow room for the quartic reconstruction stencils.

The steepening of the profile is represented in the Fourier space by the growth of higher wavenumbers. Comparing the analytic and numerical solutions in the Fourier space prior to shock formation allows quantitative statements regarding the effect of numerical dissipation as the wavelength approaches the grid scale. The flow is simulated up to 99% of the shock formation time, and the results processed by the spatial Fast Fourier Transform (FFT). The results in the Fourier space are shown for the SBP-ASF scheme and a range of approximate Riemann methods in Figure 3.13a and the effect of the reconstruction polynomial in Figure 3.13b. The SBP-ASF scheme only requires four cells to accurately capture a given wavelength, while the dissipation in the Riemann schemes becomes noticeable when the wavelength is shorter than 10 cells.

3.3 Validation

The validation cases demonstrate that the equations behave as desired in situations similar to the target situation. The first is the breakdown of the inviscid Taylor-Green vortex [142], analogous to a turbulent breakdown in the Navier-Stokes equations. The second is the Kelvin-Helmholtz instability [143], the growth of a an eigenmode in an unstable shear layer.

3.3.1 Inviscid Taylor-Green Vortex

The inviscid Taylor-Green vortex begins with initially well-defined vortices that are deformed to break down to ever-smaller structures. The lack of viscosity means that the structures can in theory break down in perpetuity, with the smallest length scale only limited by the action of numerical dissipation. The SBP-ASF scheme should nominally maintain constant net kinetic energy and entropy until the size of the structures approaches the grid scale. At this point the behaviour is not well defined as the kinetic energy attempts to cascade down to smaller scales, but there are no smaller scales to contain it and the scheme has no mechanism for dissipating energy.

The specific form of the problem is that described by Johnson et al. [144]. The initial conditions are given by Eq. 3.17, with freestream conditions $[M_\infty, p_\infty, \rho_\infty] = [0.1, 1e5\,\mathrm{Pa}, 1\,\mathrm{kg\,m^{-3}}]$. The domain is a periodic box with side lengths of 2π, with 128 cells in each direction. The vortex kinetic energy and entropy per volume, described in Eq. 3.18, are the measured quantities of interest and are isolated by subtracting away the mean quantities. The initial state with isosurfaces of kinetic energy coloured by the entropy in Figure 3.14 show the initial shape and distribution of the vortices.

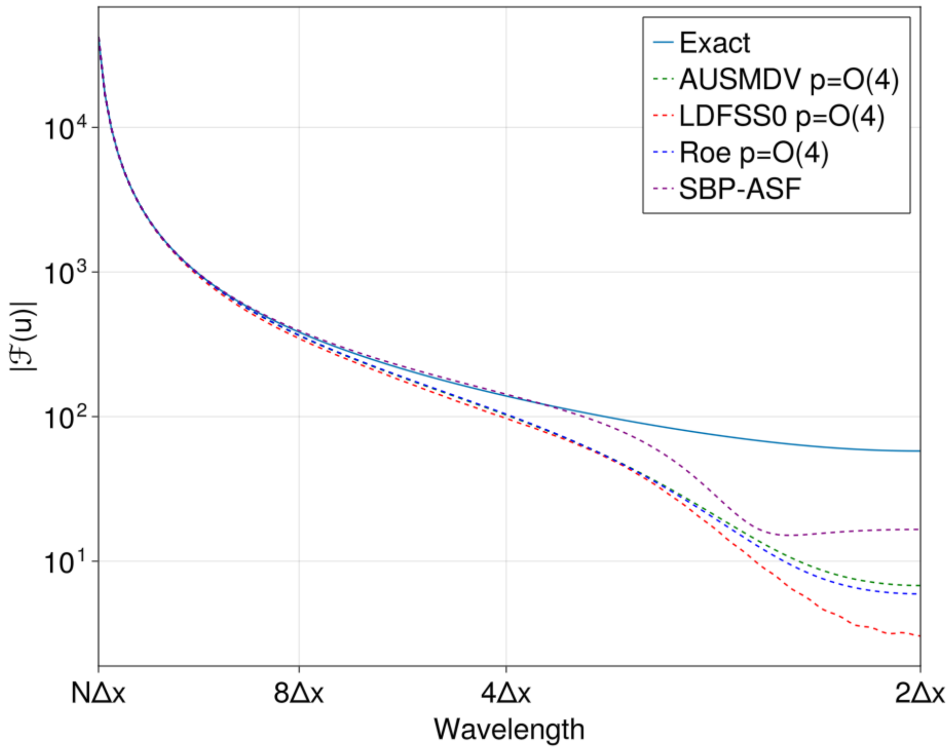

(a) Different numerical schemes.

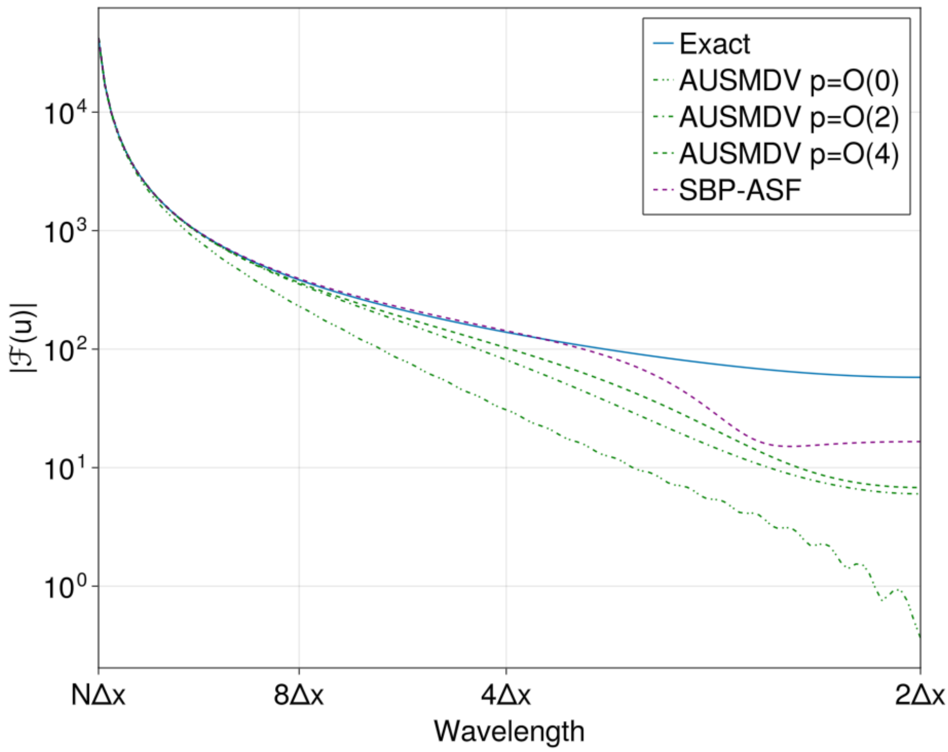

(b) Increasing state construction accuracy.

Figure 3.13: Representation of the numerical solution to the steepening wave problem in the Fourier space at 99% of the shock formation time, demonstrating the effect of the numerical scheme on spatial resolution. The SBP-ASF method only requires four cells to accurately resolve a wavelength, while the Riemann schemes required 10 cells even with higher order polynomials for the Riemann state construction.

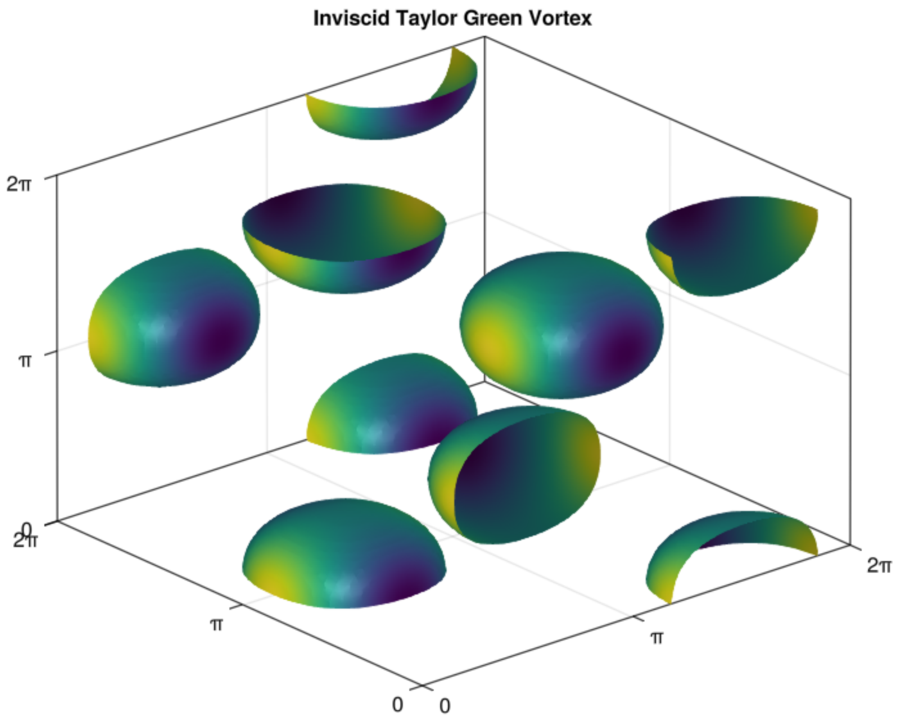

Figure 3.14: Initial condition of the Inviscid Taylor-Green vortex. Isosurface of the vortex kinetic energy coloured by the entropy.

$$
\begin{aligned}
u(x,y,z,0) &= \sin(x)\cos(y)\cos(z) + M_\infty a_\infty \\
v(x,y,z,0) &= -\cos(x)\sin(y)\cos(z) \\
w(x,y,z,0) &= 0 \\
p(x,y,z,0) &= p_\infty + \frac{(\cos(2z)+2)(\cos(2x)+\cos(2y))-2}{16} \\
\rho(x,y,z,0) &= \rho_\infty
\end{aligned}
\tag{3.17}
$$

$$
\begin{aligned}
KE_{vortex} &= \frac{\sum_{i=1}^{N} 0.5(\rho_i |u_i|^2 - \rho_\infty (a_\infty M_\infty)^2) \times \Omega_i}{\sum_{i=1}^{N} \Omega_i} \\
\rho S_{vortex} &= \frac{\left(\sum_{i=1}^{N} \rho \frac{\log(T^{\frac{\gamma}{\gamma-1}})}{\log(p)} - \rho_\infty \frac{\log(T_\infty^{\frac{\gamma}{\gamma-1}})}{\log(p_\infty)} \right) \times \Omega_i}{\sum_{i=1}^{N} \Omega_i}
\end{aligned}
\tag{3.18}
$$

Here Ω is the cell volume. The net kinetic energy and entropy should remain constant in time due to the lack of viscosity. The only mechanism to dissipate the energy is numerical dissipation. The simulation is run for a true time of 5s. The evolution of the kinetic energy and entropy is shown in Figure 3.15. The SBP-ASF method maintains the kinetic energy and entropy effectively perfectly, while the AUSMDV method dissipates the kinetic energy into entropy even with the high-order state reconstruction, although at a much slower rate. In real flows, a limiter is often applied to the state reconstruction for the approximate Riemann methods to suppress oscillations at discontinuities, at the cost of adding numerical dissipation. The Van-Albada limiter [145] is included with the parabolic state reconstruction to illustrate the effect of limiting on the solution. The breakdown of the vortex structures after 4s with schemes of increasing dissipation is demonstrated in Figure 3.16.

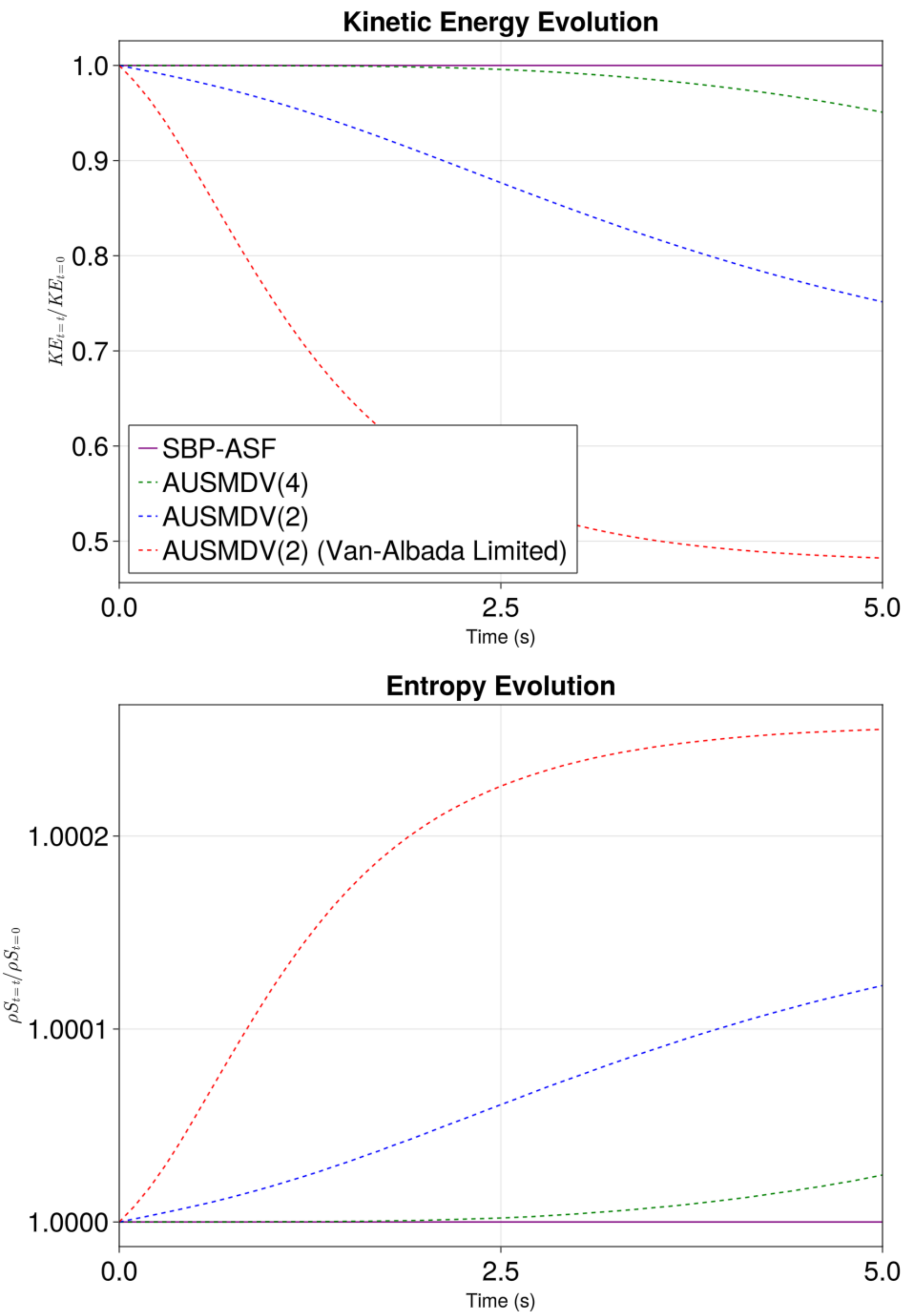

Figure 3.15: Evolution of the vortex kinetic energy and entropy. The SBP-ASF scheme maintains the kinetic energy and entropy perfectly, while the AUSMDV methods dissipate the energy into entropy.

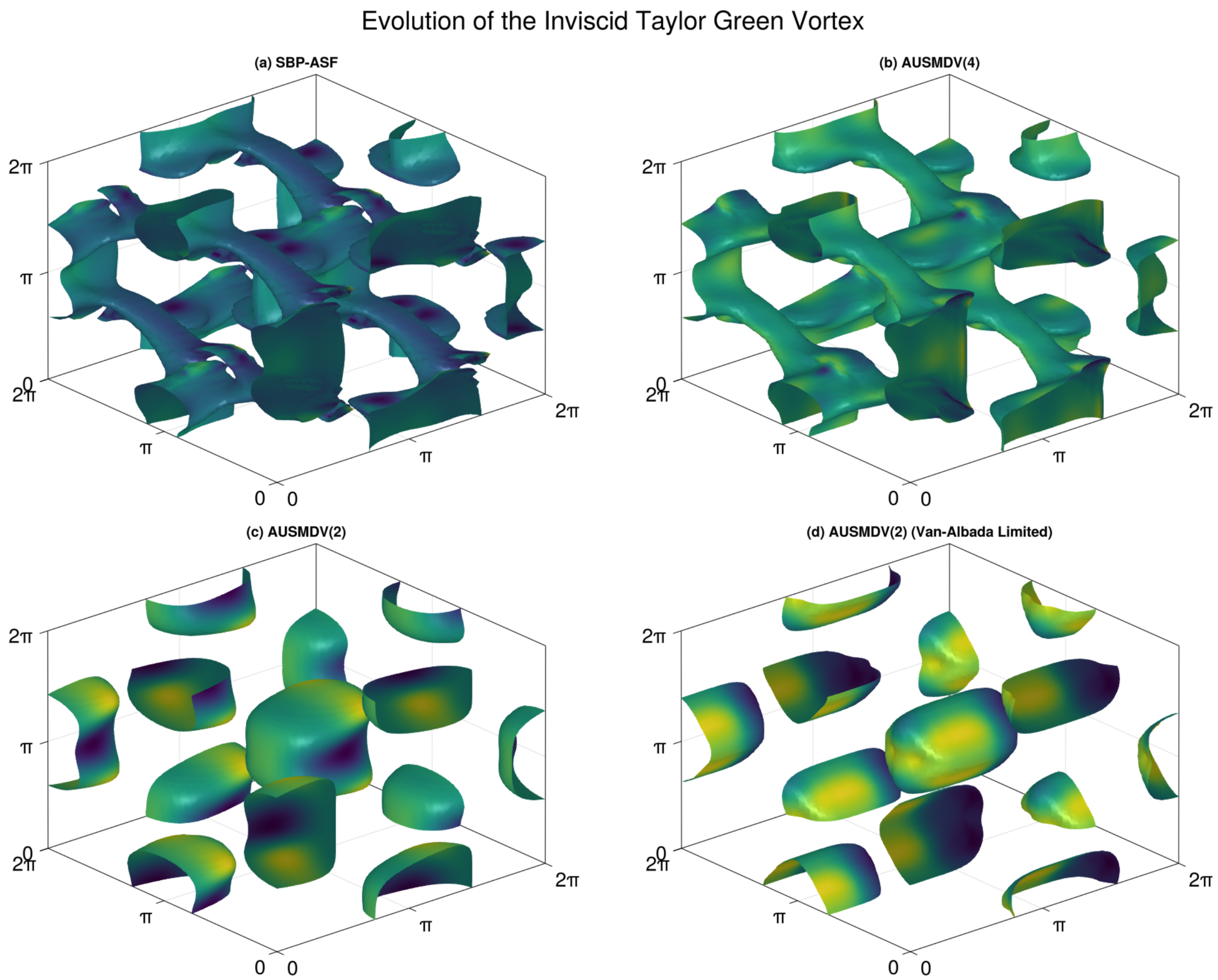

Figure 3.16: Isosurface of the kinetic energy coloured by the entropy demonstrating the stretching and breakdown of the vortex structures. Ordered from lowest dissipation to highest, the convective schemes are the SBP-ASF scheme, followed by AUSMDV with quartic state reconstruction, parabolic reconstruction and parabolic reconstruction with the Van-Albada limiter.

3.3.2 Continuous Kelvin-Helmholtz Instability

The Kelvin-Helmholtz Instability (KHI) is a naturally occuring unstable flow phenomenon which occurs when two parallel flow streams are moving relative to eachother. This is particularly relevant to the study of the stability of hypersonic blunt body flow, as the KHI is a specialised version of the generalised inflection point instability. The model KHI, which assumes incompressibility and a discontinuous interface between the flow streams, has an analytic solution due to Chandrasehkar [146] for the linear stability of the interface to perturbations. For the pure Euler equations, the discontinuous interface is unstable for all non-zero wavenumbers, and the growth of the instability is proportional to the wavenumber. That is, the shorter the wavelength of the perturbation, the more unstable it is. The trend is similar with a continuous interface, except that there is an upper bound on the growth.

The form of the KHI used here is from McNally et al. [143] and is one designed to be numerically well-posed. The interface is continuous in the density and velocity, and the flow is set up such that periodic boundary conditions can be applied in every direction. The spatially varying initial conditions are described by Eq. 3.19 with constant pressure. The constants $[\rho_1, \rho_2, U_1, U_2, L_0] = [1.0, 2.0, 50, 50, 0.025]$ in SI units, with $q_m = 1/2(q_1 + q_2)$. The simulation domain is $[0,1]$ discretized into 1024 cells in the x and y directions. A perturbation in the y velocity is imposed as per Eq. 3.20. The initial x and y velocity fields are shown in Figure 3.17.

$$
\begin{aligned}
\rho &= \begin{cases} \rho_1 - \rho_m e^{\frac{y-0.25}{L_0}}, & 0 \le y < 0.25 \\ \rho_2 + \rho_m e^{\frac{-y+0.25}{L_0}}, & 0.25 \le y < 0.5 \\ \rho_2 + \rho_m e^{\frac{-(0.75-y)}{L_0}}, & 0.5 \le y < 0.75 \\ \rho_t - \rho_m e^{\frac{-(y-0.75)}{L_0}}, & 0.75 \le y < 1 \end{cases} \\
u &= \begin{cases} U_1 - U_m e^{\frac{y-0.25}{L_0}}, & 0 \le y < 0.25 \\ U_2 + U_m e^{\frac{-y+0.25}{L_0}}, & 0.25 \le y < 0.5 \\ U_2 + U_m e^{\frac{-(0.75-y)}{L_0}}, & 0.5 \le y < 0.75 \\ U_t - U_m e^{\frac{-(y-0.75)}{L_0}}, & 0.75 \le y < 1 \end{cases}
\end{aligned}
\tag{3.19}
$$

$$
v = \sin(4\pi x) \tag{3.20}
$$

The instability is simulated up to 25τ, where τ is the reference time $1/|U_1 - U_2|$. The quantitative metrics taken are the peak y kinetic energy and the magnitude of the y velocity perturbation mode. The peak kinetic energy is effectively the same for each scheme until just prior to the final time, when the LDFSS0 scheme diverges. Visualising the final solutions for each scheme suggests the cause for this is the rapid breakdown of the shear interface. The density field

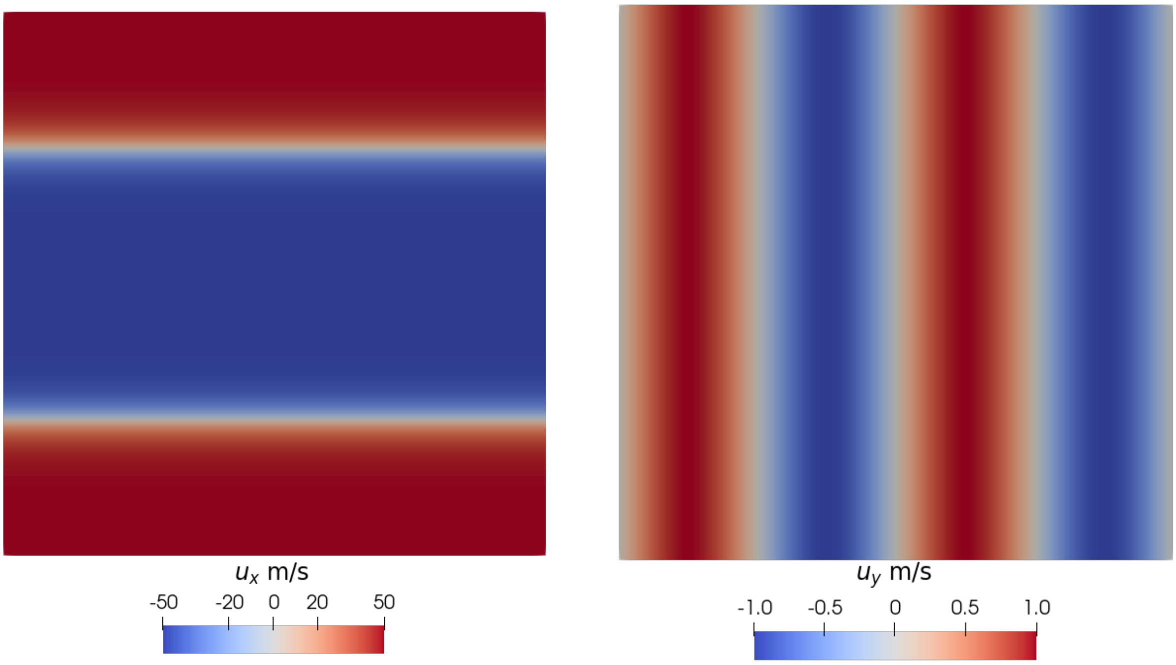

(a) Initial x velocity field.

(b) Initial y velocity field.

Figure 3.17: Initial velocity conditions for the continuous Kelvin-Helmholtz instability due to McNally et al. [143]. The initial y velocity disturbance is intentionally seeded at a relatively large value to trigger the roll up of the shear layer.

at this time for the SBP-ASF, AUSMDV and LDFSS0 schemes with quartic reconstruction is shown in Figure 3.18.

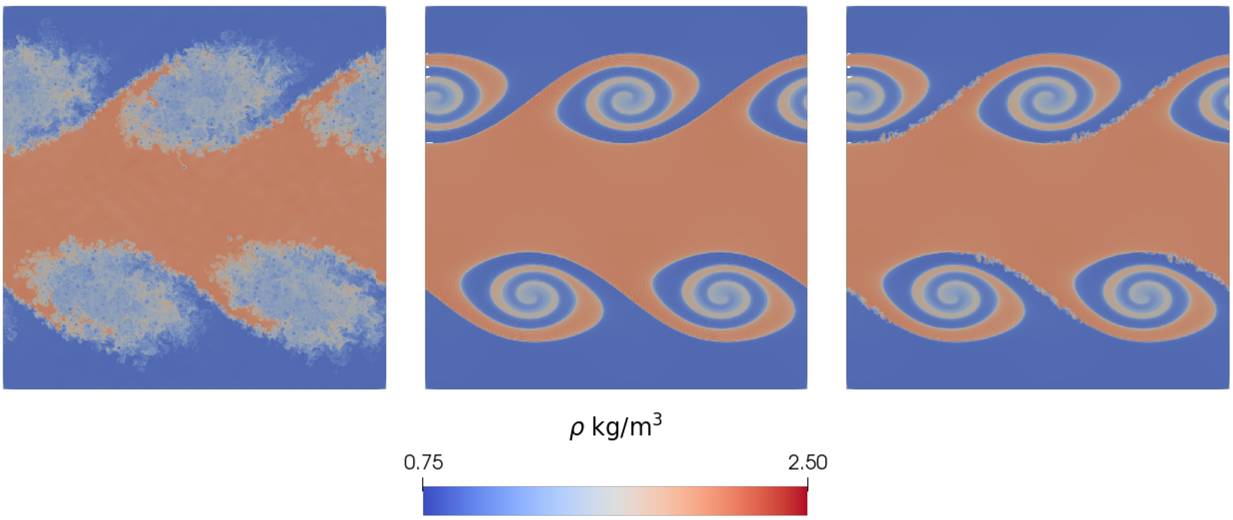

Figure 3.18: Density of the Kelvin-Helmholtz instability after 25τ using the LDFSS0 scheme (left), SBP-ASF scheme (middle) and AUSMDV scheme (right).

The behaviour of the interfaces is contrary to one would expect, given the characteristics of the schemes. Given that the interface is most unstable to small wavelengths, any numerical disturbance should cause the interface to break down rapidly, only limited by the numerical dissipation of the scheme. Following this train of thought, one would assume that the interface would be most sensitive to these numerical disturbances using the SBP-ASF scheme, which is clearly not the case. The numerical dissipation in the Riemann schemes also acts to smear out the gradients at the interface, effectively thickening the shear layer. The effect of the shear layer thickness in the linear regime is illustrated in Figure 3.19 using the expression derived by Wang et al. [147] in the incompressible limit. A thicker shear layer leads to reduced growth, so the effect of numerical dissipation should be compounding.

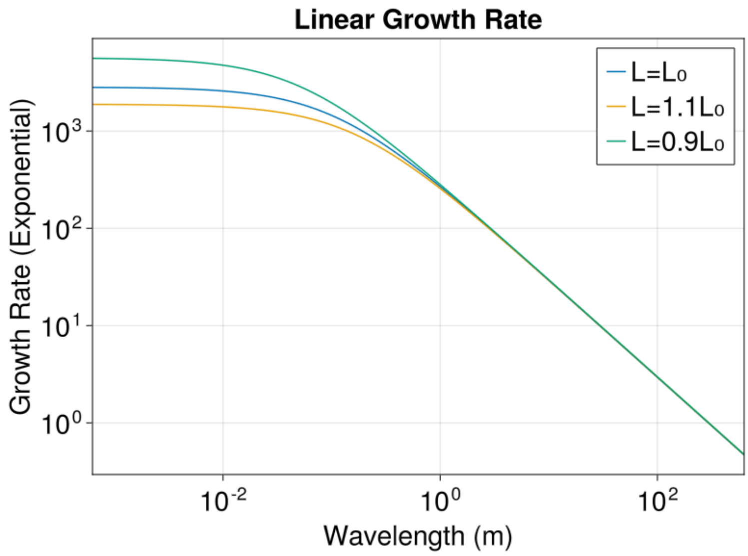

Figure 3.19: Growth rate of the continuous Kelvin-Helmholtz instability in the linear incompressible regime using the expression of Wang et al. [147].

While the snapshot in time shown in Figure 3.18 is clearly far past the linear regime, it should still be indicative of the overall behaviour. The instability appears to be seeded close to discontinuity that appears in the solution near the shear layer, which is similar to the phenomena identified by Chen and Hou in the 3D Euler equations [148]. Local streamlines around this discontinuity shown in Figure 3.20 show the location of this phenomena. Due to the different fashion in which the Riemann and central difference schemes handle the derivatives, the Riemann schemes seed stronger disturbances in the shear layer relative to the SBP-ASF scheme, causing them to break down.

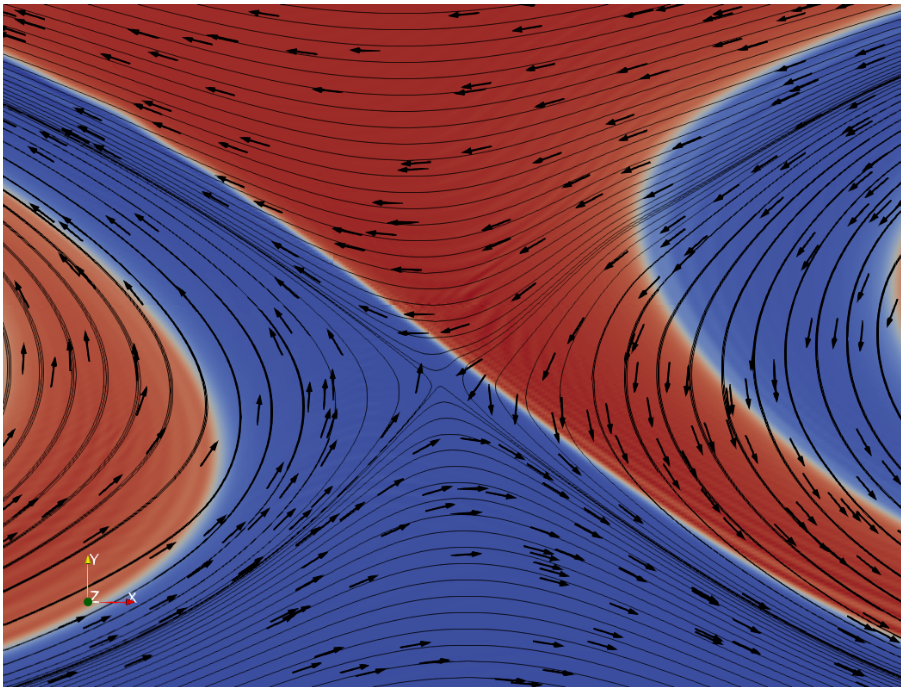

Figure 3.20: Streamlines overlaid on the final density field using the SBP-ASF convective flux. There is a discontinuity in the velocity field where the generated vortex flows meet, which is not well handled by the approximate Riemann methods.

3.4 Concluding Remarks

The SBP-ASF convective flux scheme is correctly implemented with the Eilmer flow code. The scheme behaves well for smooth flows on uniform and non-uniform meshes, assuming the change in cell spacing in smooth in the non-uniform case. One caveat that must be noted is the behaviour of the SBP-ASF scheme, and central schemes in general, with implicit temporal schemes. The flux Jacobian required for implicit schemes central schemes is not guaranteed to be diagonally dominant when using central schemes, thus can be temporally unstable. Implicit schemes are crucial for computing the steady state solutions required for transitional DNS, as the expense required to reach steady state with explicit schemes is prohibitive. Subbareddy and Candler [125] suggest using a dissipative scheme for the Jacobian computation to stabilise the scheme, at the cost of adding numerical dissipation. The approach taken in Eilmer is to compute a steady state using a Newton-Krylov scheme [149] with the approximate Riemann schemes, then switch to the SBP-ASF method.

Given the results presented here, it is reasonable to conject that to achieve ”adequate resolution”, two to three times as many cells are required in each direction when using an approximate Riemann scheme compared to the SBP-ASF scheme. Taking into account the considerable larger CFL number enabled (for arguments sake, a factor 5 is assumed though this is problem dependent) with the Riemann schemes, the computational expense required to simulate a given flow is comparable in one and two dimensions. The difference between the approximate Riemann methods and the SBP-ASF scheme, and indeed high order/low dissipation schemes in general, comes to the fore in three dimensions. Even taking the most generous estimates for the estimated resolution and time-stepping requirements for the Riemann schemes relative to the low dissipation schemes (assuming twice the number of cells in each direction and six times larger CFL), the computational cost is thrice larger; for more realistic estimates (3 times cells, 4 times CFL), the cost ratio is $\tilde{2}0$.

Chapter 4

Preliminary Simulations of the 17.78mm Nose Radius Hypersonic Blunt Cone

The geometry and conditions simulated in this work are the conditions from Stetson et al. [85] as illustrated in Figure 4.1 in which the mass flux fluctuations associated with the generalised inflection point were observed. The primary purpose of this chapter is to demonstrate the preparation process for a high fidelity DNS and highlight the finer details that must be accounted for. First, the steps required to generate a high quality initial state are described, which is used as a starting point for the forced direct simulations. This preparation stage includes the preliminary shock fitting stage, the mesh generation and the convergence to a steady state. Second, under-resolved time accurate axisymmetric simulations, forced by white noise in the freestream, are used to inform an appropriate region of interest for the high fidelity simulations in Chapter 5.

The two dimensional computations were performed in cylindrical coordinates (with x being the axial direction and y being the radial) and three dimensionalal simulations in Cartsian coordinates, but the results are presented in body-fitted coordinates i.e. (ξ, η, ζ) where ξ denotes the streamwise distance measured along the cone surface (so u_ξ is the velocity parallel to the wall in the downstream direction), η denotes the wallnormal direction and ζ denotes the azimuthal angle to make the results more easily interpretable.

4.1 Generation of the Base Flow

The preparation process for the time-accurate DNSs are outlined here. Some numerical considerations, particularly the choice and implementation of boundary conditions and the precise handling of the convective fluxes are covered first. Description of the shock fitting process and the grid generation follow. The adjustments to the steady-state acceleration algorithm required for a high-order base solution are also explained.

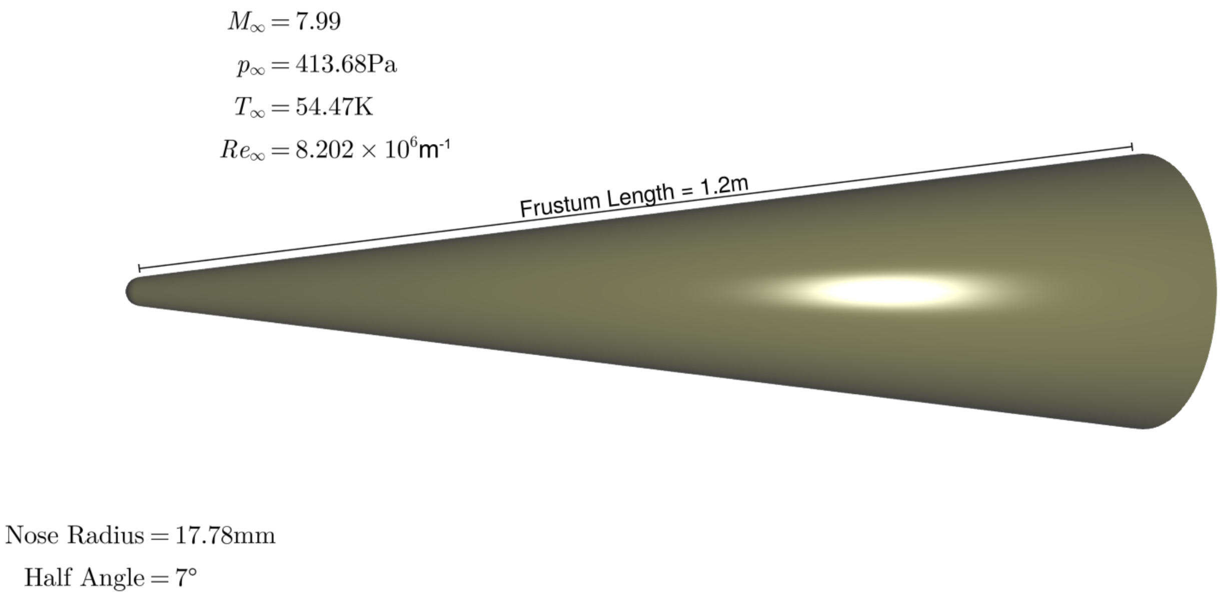

Figure 4.1: Geometry and conditions used in this work.

4.1.1 Numerical Considerations

Unless otherwise stated, the boundary conditions in the full domain simulations are a constant freestream condition for the inflow, a reflecting condition along the axis of symmetry, a first-order extrapolation for the outflow and an adiabatic no-slip condition for the cone surface. Ghost-cell implementations of each of these conditions are used for each of these boundary conditions, bar the shock fitting simulation which uses a prescribed flux condition for the inflow boundary. The convective fluxes were computed with the SBP-ASF scheme (reverting to the AUSMDV scheme at shocks) or the AUSMDV approximate Riemann scheme with second order state reconstruction, augmented with the Van Albada limiter [145], while the viscous fluxes are computed using second order least squares based at the cell centre.

It is well known that high-order schemes are generally incompatible with discontinuities due to Gibbs phenomenon. To mitigate this issue, a linear combination of the high order, low dissipation convective flux computed via the SBP-ASF method and the dissipative flux of the AUSMDV method is taken at shocks as per Equation 4.1.

$$F(\mathbf{U}) = (1 - \Theta)F(\mathbf{U})_{SBP-ASF} + \Theta F(\mathbf{U})_{AUSMDV}. \tag{4.1}$$

Here Θ is the shock detector value. The shocks are detected using a compression threshold based on the local velocities, described in Equation 4.2. An interface is considered shocked and given a shock detector value $\Theta = 1$ if the condition

$$\frac{u_R - u_L}{\min a_R, a_L} < Tol \tag{4.2}$$

is true, where the subscripts R, L denote the values in the cell to the "right" and "left" of the interface, in the interface's local coordinate system and u, a are the interface-normal velocity and sound speed. The shock detector value Θ is propagated to the cell attached to the interface, then each interface's shock detector value is set to the maximum of its attached cells. This process is illustrated in Figure 4.2. This means if any of the interfaces of a cell are detected as "shocked" by Equation 4.2, then the convective fluxes through all the interfaces of the cell will use the AUSMDV flux. The compression tolerance used in this work -0.15.

The binary detector was chosen over the more commonly utilised vorticity-based Ducros sensor as the Ducros sensor tends to give non-zero estimates for Θ even in smooth regions of the flow, effectively adding unnecessary numerical dissipation. This issue is demonstrated in the example of supersonic flow over a cylinder in Figure 18 from White et al. [135]. Switching immediately from the dissipative fluxes close to shocks to the low dissipation scheme can generate numerical disturbances, so to smooth the transition between the dissipative fluxes at the shock to the high order fluxes elsewhere, a blending step is employed to "diffuse" the shock detector. The diffusion process begins after the shock detection step, so all cells and interfaces initially contain a Θ value of 0 or 1. Then the process is as follows:

1. Each cell is assigned a shock detector value Θ equal to the average of the shock detector values of its interfaces.

2. The shock detector value at each interface is set to the maximum of the Θ values in its attached cells.

3. Repeat N times.

For the simulations in this work, N is set to 5. An illustration of the shock detector propagation process in 1 dimension is shown in Figure 4.2.

4.1.2 First Stage: Shock Fitting

The shock fitting process as implemented within Eilmer requires time-accuracy, therefore is generally quite expensive if one naively begins with the resolution required to have an accurate enough shock position for the subsequent simulations. The shock fitting algorithm within Eilmer was extended to work in parallel computing contexts using the OpenMPI library, as the global communication required for the movement of the mesh vertices was not yet implemented. To accelerate the process, 3 shock fitting stages are employed, in this case beginning with a 30×500 cell mesh and doubling the cell count for each iteration, so the final stage uses 120×2000 cells. The meshes in all stages are clustered toward the nose region to capture the sharper gradients, while only the second and third stages are clustered to the

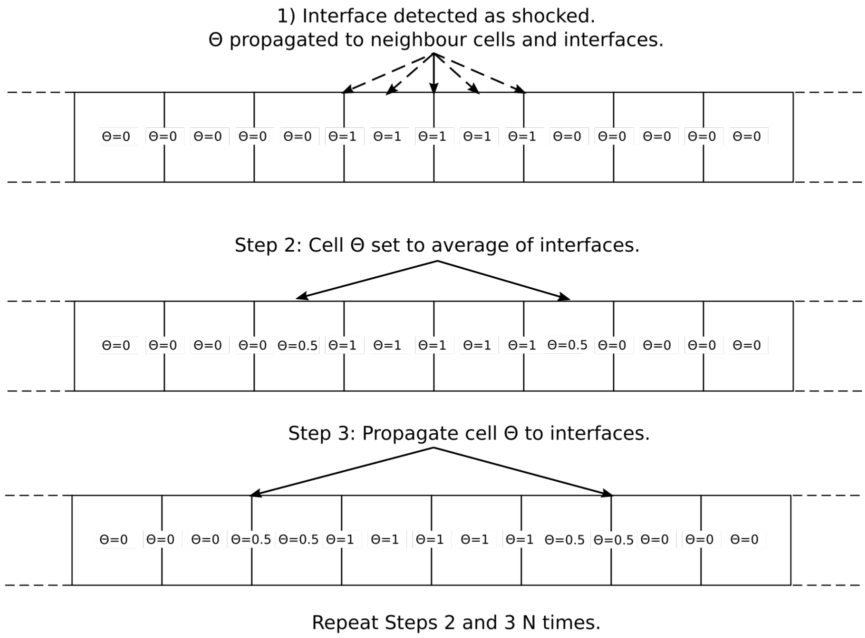

Figure 4.2: Illustration of the shock detector diffusion process in the Eilmer code.

wall to resolve the boundary layer to a reasonable degree of accuracy. The initial mesh and the final mesh after 3 stages, with only every 8th mesh point shown on the final mesh, are shown in Figure 4.3.

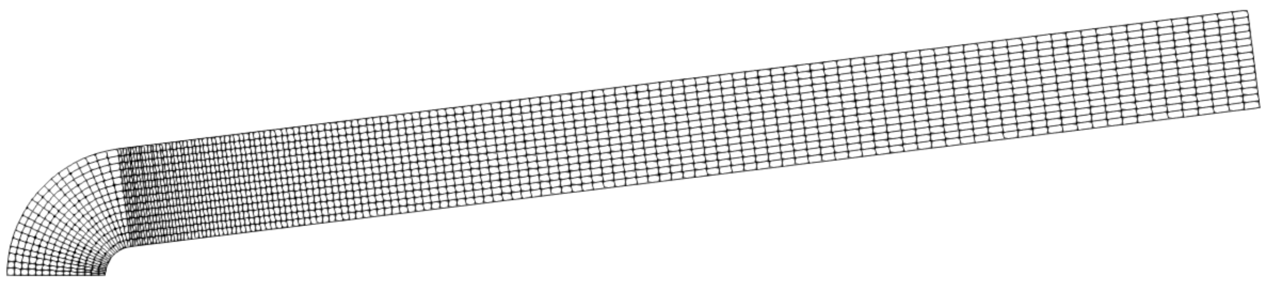

(a) Starting mesh used for the shock fitting simulations.

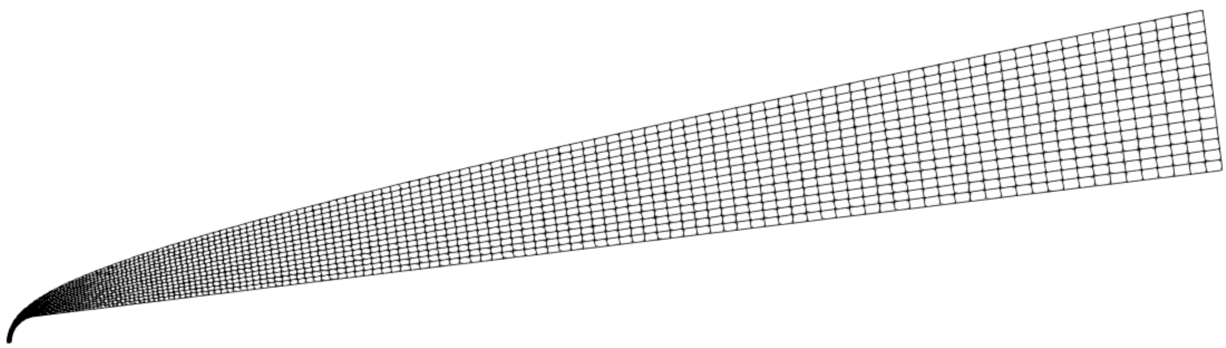

(b) Mesh after 3 stages of shock fitting. Every 8th grid point shown.

Figure 4.3: Progress from the starting mesh to the final mesh using the shock fitting method of Johnston [150] with three stages of refinement.

The convective flux scheme used in this stage is the AUSMDV scheme, as it is more robust than the SBP-ASF scheme which is relevant when dealing with grid motion, which can generate numerically troublesome cell configurations during the initial shock alignment. The Riemann state reconstruction process accounts for arbitrary cell spacing and does not require the mesh to be high-order smooth, which is a huge benefit during the shock fitting stage.

Given this scheme does not utilise steady-state acceleration tools, the run-time is insufficient to generate a steady state solution of high enough quality as a base flow for time-accurate DNSs because the transients in the boundary layer take a prohibitively long time to wash out of the solution (hence the popularity of steady state acceleration schemes). This is justified in this case, as the purpose of these simulations is to accurately determine the position of the shock, which is dominated by inviscid effects. The transients that still exist in the boundary layer are of the order of 10^{-4} times the base quantity in the steady flow. The effect of such transients on the shock position is negligibly small.

4.1.3 Mesh Generation

Using the shock position generated by the shock fitting simulations as the domain boundary, the mesh used for the high fidelity DNSs can be generated. Because of the immense computational cost of these simulations, every effort is made to improve their efficiency. Taking tight control of the construction of the mesh and deviating from one of the standard conventions of CFD can gain an order of magnitude speed-up of these simulations. The convention broken is that guiding the way in which the boundary layer is resolved.

Given that the gradients in the boundary layer are orders of magnitude of larger than the gradients elsewhere in the flow (at least for the geometry of interest here), it is logical to locally refine the mesh in the boundary layer to accurately capture these gradients while not over-resolving the flow elsewhere. This has been standard practice in CFD for decades. The standard practice method to achieve this is to use a "clustering" function to the edges perpendicular to the wall, which adjusts the distribution of points along these edges, so that the mesh spacing increases in some usually non-linear fashion away from the wall. This results in exceptionally small cells at the wall, which is perfectly reasonable, and in fact required, for turbulent simulations as the smallest eddies are at the wall. These small cells restrict the size of the time steps to extremely small values. However, for laminar boundary layers, the gradients are close to uniform across most of the boundary layer, so this growing of the cells is unnecessary. If the cells can be uniform across the boundary layer, then one must only prescribe the number of cells in the boundary layer.

To allow this uniform spacing in the boundary layer and coarser spacing outside the boundary layer while maintaining the smoothness of the mesh required for high quality solutions, the GridPro software [151] was used. An internal surface was placed at the boundary layer edge, so that the number of cells within the boundary layer and the number of cells between the boundary layer edge and the shock could be prescribed and the automatic topology generator will smoothly blend between these two regions. The GridPro software also attempts to optimise the "quality" of the mesh, which is dominated by the mesh smoothness and orthogonality, which is not a trivial exercise to do by hand given the shock curvature. Additional internal control points in the streamwise direction were used to control the refinement in the streamwise direction and capture the gradients in the nose region. The GridPro topology used to generate the mesh for the full domain simulations is included in Figure 4.4. These mesh for these full domain axisymmetric simulations has 8600 cells in the streamwise direction and 180 cells in the wallnormal direction, with 60 cells in the boundary layer.

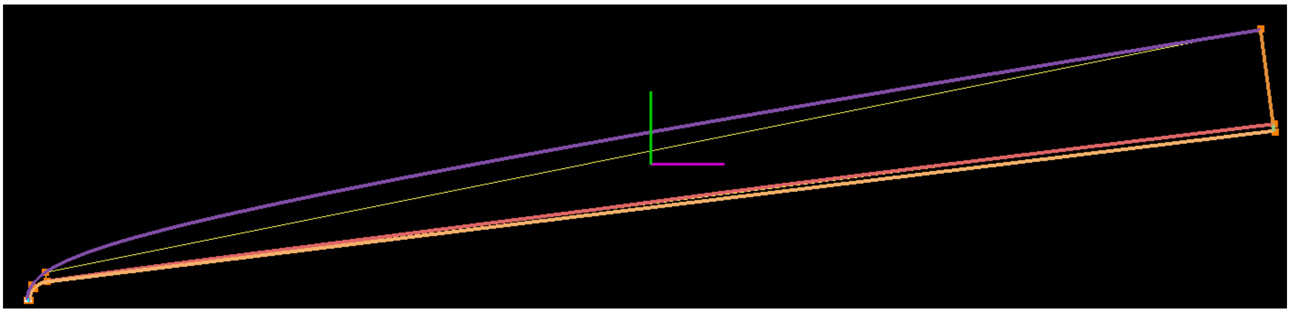

(a) GridPro topology for the full domain.

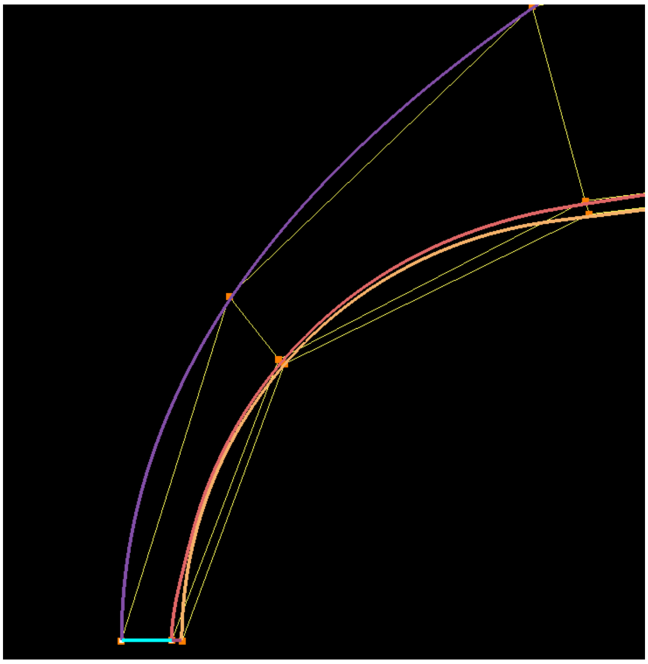

(b) Zoom in of the nose region.

Figure 4.4: GridPro topology used to generate the mesh used for the full domain simulations. The connectors between the control points form the "starting" mesh, after which the mesh boundaries snap to the corresponding surfaces. The program then iterates towards a mesh that is optimised for smoothness and orthogonality.

In the remainder of this work, many visualisations will show wallnormal profiles of specified quantities. This is trivial for straight geometries as the mesh will usually be rectilinear, so a wallnormal profile is simply a series of cell centre values along a column of cells. Unfortunately, a high quality mesh over blunt geometries does not have this rectilinear quality due to the curvature and obliqueness of the shock. To generate these wall-normal profiles, the solution is interpolated from the solution points to points which form wallnormal profiles that are equispaced in the streamwise direction. The interpolation scheme used is the Clough-Tocher interpolator. This particular interpolator was chosen as it generates smooth interpolating surfaces and its locality, which makes it computationally efficient [152].

Computing the boundary layer edge in blunt body flows is more complicated than the sharp body counterparts, due to the gradients in the entropy layer. The typical boundary layer edge definition of $u_\xi(\eta = \delta_b) = 0.99u_\infty$ is not applicable here, as there is no clear choice for u_∞, or indeed for the other base quantities, as demonstrated by the wallnormal profiles measured in 4 locations ($\xi = 0.01\text{m}, 0.05\text{m}, 0.5\text{m}, 1.0\text{m}$) shown in Figure 4.5. These profiles are taken from the proceeding steady state simulation to illustrate the issue of determining a boundary layer edge location. Even when considering the derivatives, there is no obvious *programmatic* way to determine the boundary layer edge for the entire domain, even if there is a visually obvious edge for any given profile.

This problem is discussed in Bertin [153]. An enthalpy criterion is suggested to define the boundary layer edge, as the flow outside the entropy layer is adiabatic so the enthalpy is constant. This is utilised in other works on blunt cones [89, 107] with the boundary layer being defined as $h_{tot}(\eta = \delta_b) = 0.995h_{tot,\infty}$, where h_∞ is the freestream total enthalpy $h + 0.5(u^2 + v^2 + w^2)$. For certain flows, the enthalpy actually exceeds the freestream enthalpy close to the boundary layer edge, so this cutoff criterion is inappropriate. Instead, the location of this enthalpy maximum was used, which is a simply calculated metric that was used by Jewell and Kimmel [154] in a stability analysis of hypersonic blunt cones.

The entropy layer edge is also defined for visualisation purposes. While the definition of the entropy layer edge in absolute terms is clear— the streamline emanating from the point where the shock becomes straight— but a practical definition is not so obvious, as it is an asymptotic process. A simple choice is to use an entropy cutoff, and this is the approach taken by other authors [80, 107, 108]. Specifically, a cutoff relative to the entropy at the wall is used, when the entropy change becomes 10% of the wall entropy, i.e. $\Delta S(\eta = \delta_e) = 0.1\Delta S(\eta = 0.0)$ where $\Delta S = c_p \ln(T/T_\infty) - R_{gas} \ln(p/p_\infty)$. The cutoff used in the referenced works was 25%, but the flow gradients are still significant at this location using this criterion for the specific conditions used here, so the 10% cutoff was used. The entropy and boundary layer edges on the full flow field and imposed onto wallnormal profiles at the same locations used prior in Figure 4.5 is shown in Figure 4.6.

The next step in the process is the generation of a high quality base flow. The full domain mesh used for the base flow uses 8600 cells in the streamwise direction and 180 cells in the wallnormal direction, with 60 cells located within the boundary layer. The base mesh, with every 64th point in the streamwise direction and every 6th point in the wallnormal direction included, is shown in Figure 4.7.

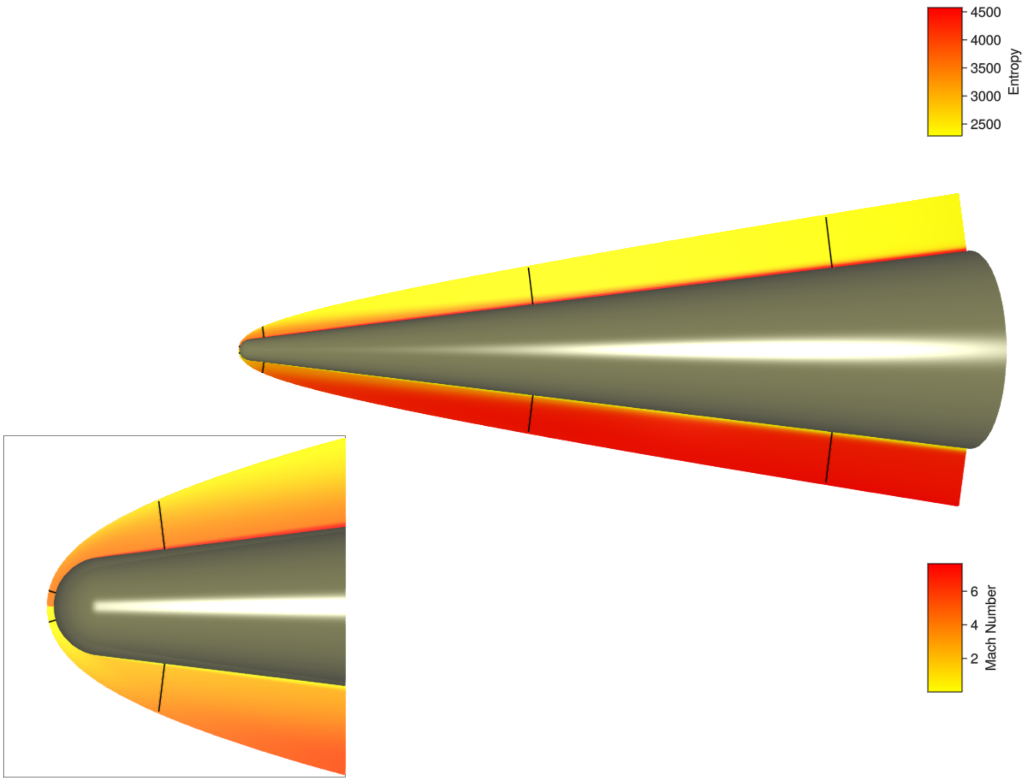

(a) Domain and flowfield after the shock fitting stage. Lines denote the locations of the wallnormal profiles in the following figures.

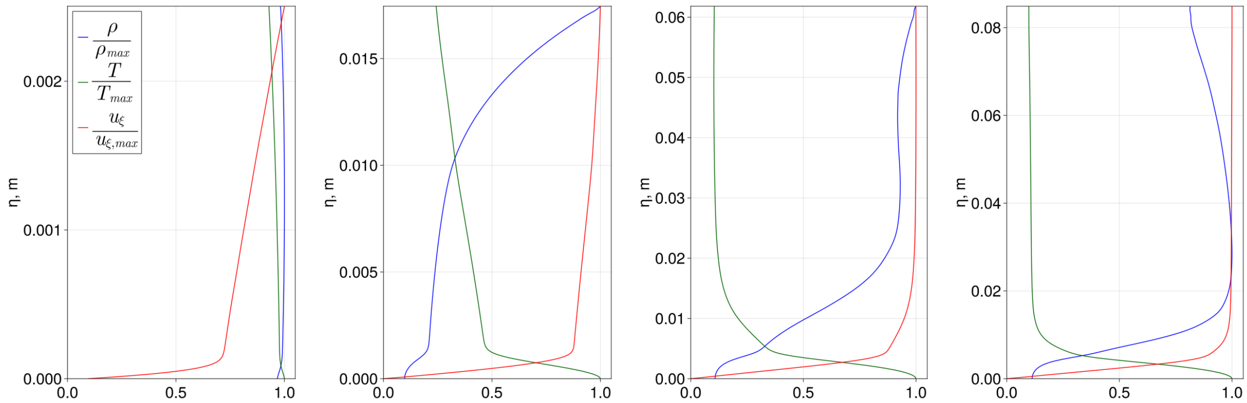

(b) $\xi = 0.005m$. (c) $\xi = 0.05m$. (d) $\xi = 0.5m$. (e) $\xi = 1.0m$.

Figure 4.5: Entropy and Mach number fields after the shock fitting stage. Wallnormal profiles of the base quantities of density, temperature and streamwise velocity show the significant gradients outside the boundary layer, making the typical boundary layer edge definition of $u_\xi(\eta = \delta_b) = 0.99u_\infty$ unusable as there is no clear choice for u_∞.

4.1.4 The Newton-Krylov Steady-State Accelerator

Achieving a steady base flow solution on a mesh with adequate resolution to accurately resolve the gradients in the flow is an impractical task using time-accurate temporal schemes, primarily due to slow convection of transients within the boundary layer. Thus it is typical to turn to pseudo-time methods, typical based on implicit temporal schemes, to accelerate the convergence of the flow to a steady state. Implicit temporal schemes are typically unstable

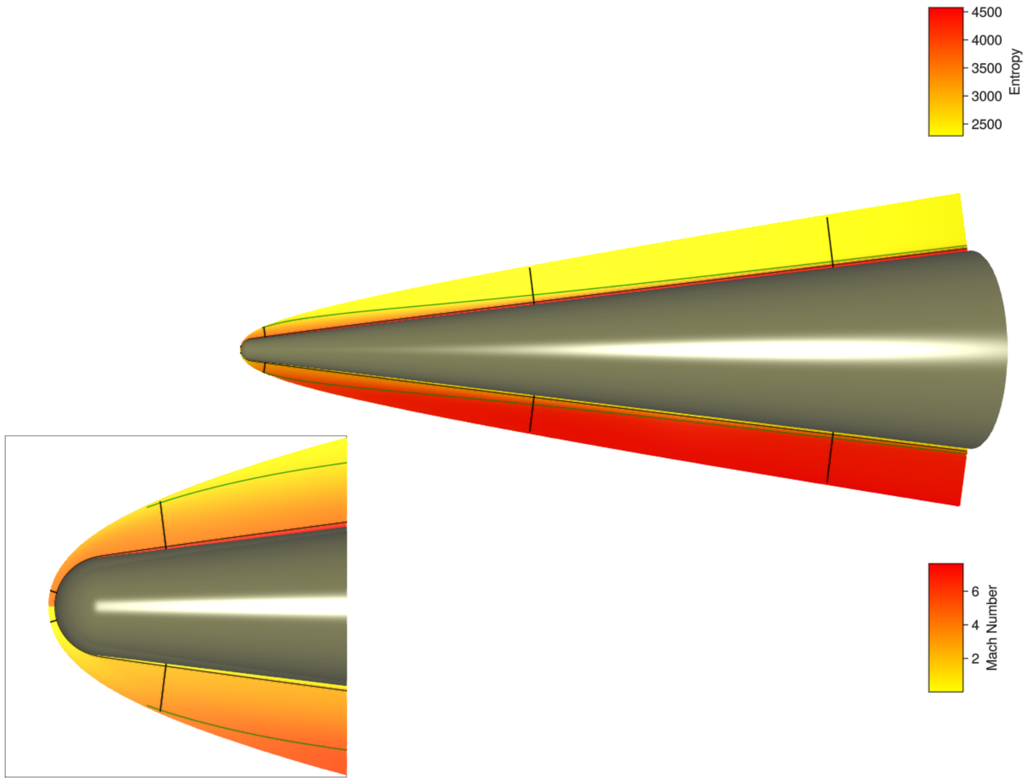

(a) Domain and flowfield after the shock fitting stage, with the computed boundary and entropy layer edges overlaid in black and green respectively.

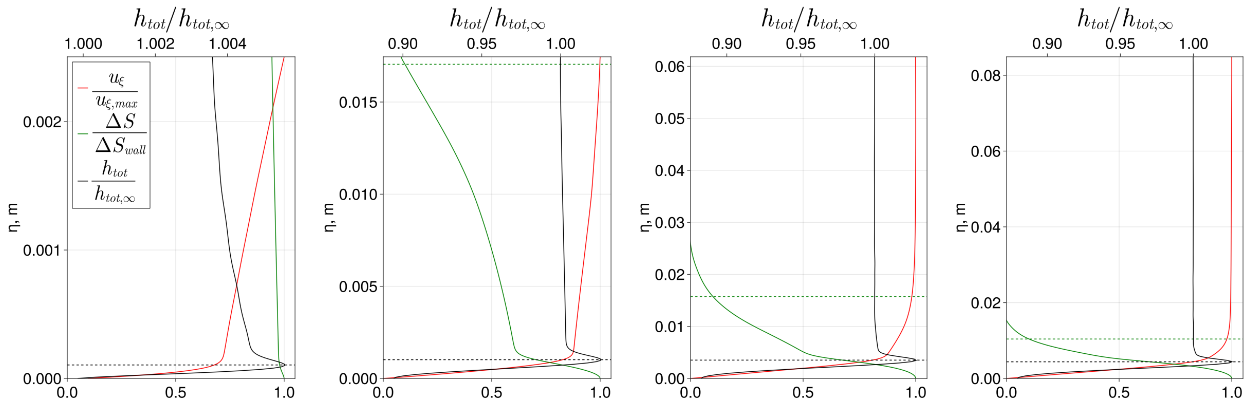

(b) $\xi = 0.005m$. (c) $\xi = 0.05m$. (d) $\xi = 0.5m$. (e) $\xi = 1.0m$.

Figure 4.6: Entropy and Mach number fields after the shock fitting stage, with black and green lines denoting the computed boundary and entropy layer edge locations. The wallnormal profiles of streamwise velocity, enthalpy and entropy increment demonstrate the criteria used for locating the edge of these layers.

when coupled with high order spatial schemes [155], as the diagonal dominance of the Jacobian is not guaranteed. However, the acceleration scheme utilised in the Eilmer flow code is a Jacobian-Free Newton-Krylov method [156], so the effect of high-order spatial schemes on the convergence and stability of this scheme was not well known. The use of the desired SBP-ASF scheme proved troublesome- the solution diverges even in smooth regions of the flow, an example of which is shown in Figure 4.8. The simulations were continued

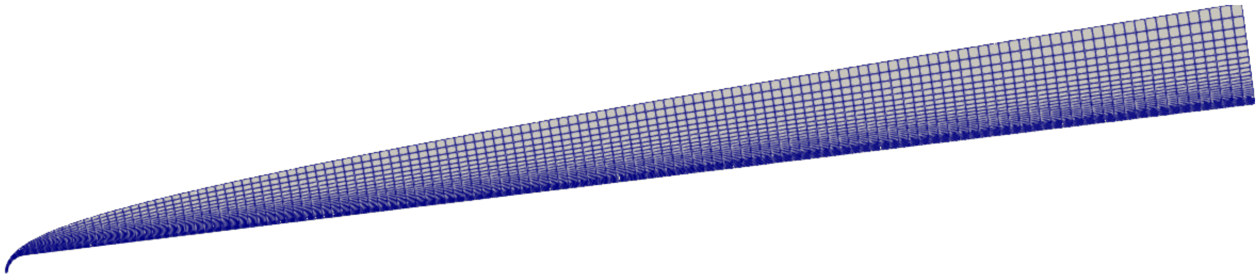

Figure 4.7: Quadrilateral mesh used for the generation of a high quality axisymmetric base flow. Every 64th cell in the streamwise direction and every 6th cell in the wallnormal direction are shown.

using the AUSMDV convective flux scheme, while a solution to the numerical instability of the SBP-ASF scheme was sought. It was expected that this choice of continuing with the dissipative AUSMDV scheme would have demonstrable quantitative effects on the results, manifesting in errors in the amplitude of the disturbances in the flow, but the fundamental physics would remain the same in the linear regime which was of primary interest in this work.

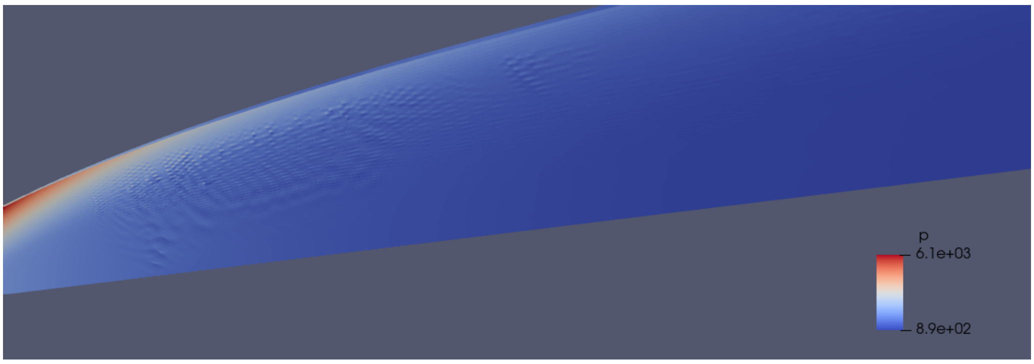

Figure 4.8: Pressure field demonstrating the numerical instabilities in the smooth region which occur when iterating to steady state using the SBP-ASF scheme for the convective fluxes. These instabilities grow with successive iterations, effectively ending the simulation as values become non-physical.

Given that the SBP-ASF method is fundamentally a finite difference method, this places an additional constraint on the mesh in that it should be high-order smooth, meaning that both the mapping from the physical space (which is generally non-uniform and curvilinear) to the uniform computational space and its derivatives should be smooth. The grid generation algorithm in GridPro is based on a control point formulation, which means this constraint is met in a continuous sense. In a discrete sense, this is harder to quantify: How does one measure the smoothness of a discrete quantity? The smoothness is one of the metrics optimised by the meshing algorithm and the generated meshes do not feature sharp changes in the smoothness, so it is unlikely to be the driver of the stability issues.

Attention is given to the configuration of the Newton-Krylov method. Naive direct application of iterative techniques are known to have robustness issues, and will often diverge. The iteration procedure is usually assisted by preconditioning the original linear system. An appropriate choice of preconditioner is essential for the success of these steady state acceleration techniques. Improved accuracy of the preconditioner is actually often detrimental to the robustness of the technique [157], so low order approximations of the operator A are often used.

This adjustment was made in the Newton-Krylov method implemented within Eilmer by dropping back to one of the approximate Riemann schemes, in this instance the AUSMDV scheme, to construct the preconditioner matrix. No reconstruction of the Riemann states was used here, which means cell centre values were used as the left and right Riemann states. The convergence of the method was vastly improved with this adjustment. The resulting base flow generated using the SBP-ASF scheme (with the AUSMDV preconditioner) is shown in Figure 4.9. The base flow generated using this adaptation was sufficient for engineering-style calculations.

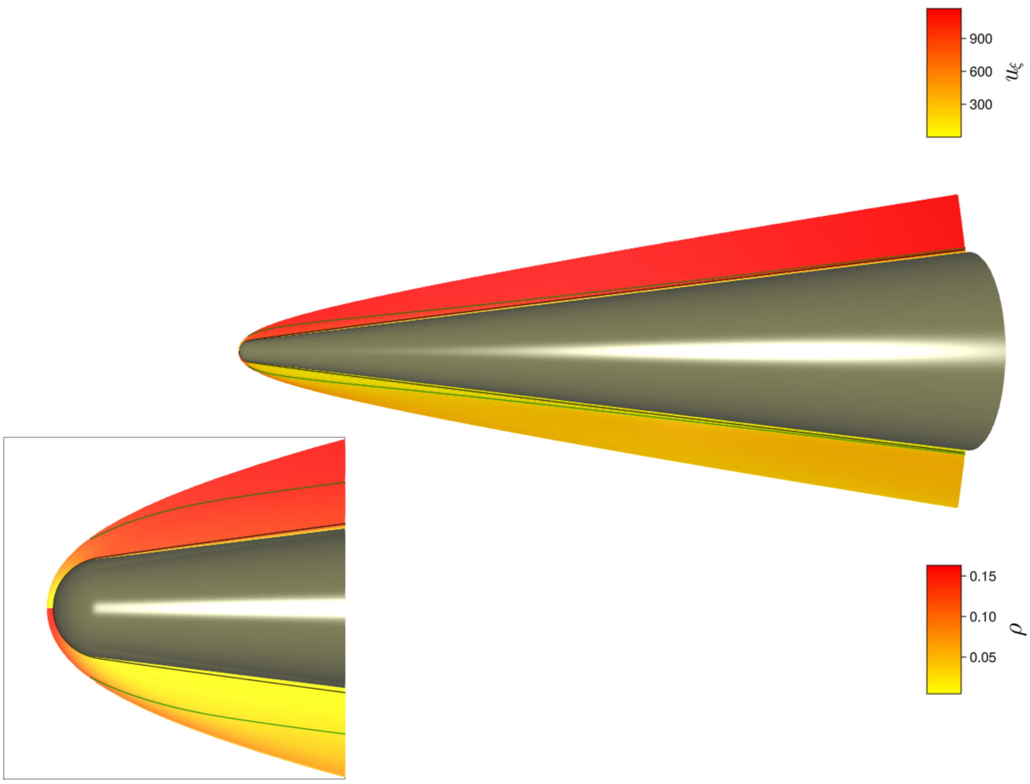

Figure 4.9: Streamwise velocity and density fields after adjusting the preconditioner matrix to use the low order AUSMDV convective scheme in its construction.

Unfortunately, the solution was not of high enough quality for time-accurate simulations with the intention to capture the evolution of very small disturbances. When switching from the AUSMDV scheme to the SBP-ASF scheme (in smooth regions), it is effectively adding a small perturbation to the solution. This perturbation will have some content in all wavenumbers that are resolved by the mesh. This is problematic for the the SBP-ASF scheme, as it is based on a central difference scheme and has no mechanism for dissipating these introduced waves.

The solution then is to mitigate this sharp change in the solution. This was achieved by smoothly transitioning from the robust AUSMDV scheme to the SBP-ASF scheme. Once the solution was converged to a desired residual threshold, the contribution to the convective fluxes from the SBP-ASF scheme is linearly increased and the contribution from the AUSMDV fluxes was linearly decreased over a chosen number of pseudo time steps, as described by Equation 4.3.

$$Flux_{conv} = min(1, N/N_t)Flux_{SBP-ASF} + max(0, 1 - N/N_t)Flux_{AUSMDV} \tag{4.3}$$

Here N is the current step count and N_t is the number of steps to perform the ramping over. For this case, 500 steps were used for the number of ramping steps. As the flow approaches the high-order solution, the contribution from the AUSMDV scheme adds sufficient numerical dissipation to prevent the formation of the grid scale oscillations that polluted the solution when an instant switch was used.

A global relative residual of 10^{-11} was used as the threshold for a converged solution, though measuring this relative residual is strongly dependent on the method of calculating the initial residuals so this value is only included for completeness. The residual convergence behaviour is shown in Figure 4.10. Likewise, an appropriate range of pseudo time steps for the gradual switching from the AUSMDV to the SBPASF scheme is strongly dependent on the flow and the acceleration algorithm, but for reference the switching was spread over 2500 steps.

Properties of the Base Flow

To understand the dynamics of the unsteady behaviour of the flow, the characteristics of the steady flow must first be described. The steady base flow determines the flow's response to environmental disturbances. The boundary and entropy thicknesses along the length of the cone, using the definitions described above, are shown in Figure 4.11 outline the regions of significant shear. Any arbitrary shear layer can be susceptible to transient disturbances per the simple analysis of Ellingson and Palm [98], so these regions are most likely to be of interest. The boundary layer edge Mach number and local unit Reynolds number are included in Figure 4.12.

Linear analysis of the boundary layer of blunt cones in this regime have been utilised in the past [76, 154] and yield negligible or no presence of unstable boundary layer modes (first or second modes). The most likely source of modal instabilities in the flow, if they exist at all, is the inflection point in the entropy layer. Prior analysis using linear techniques [96, 97] applied to the blunt plate, which contains similar entropy layer behaviour, indicate the existence of weak modal instabilities, so it is likely this inflection point is of interest. Recall that the inflection point is a point of maximum compressible vorticity. For parallel flows, this is simplified to the condition $\frac{d}{d\eta}\left(\rho\frac{du_\xi}{d\eta}\right) = 0$ as the flow is uniform in the η direction. For

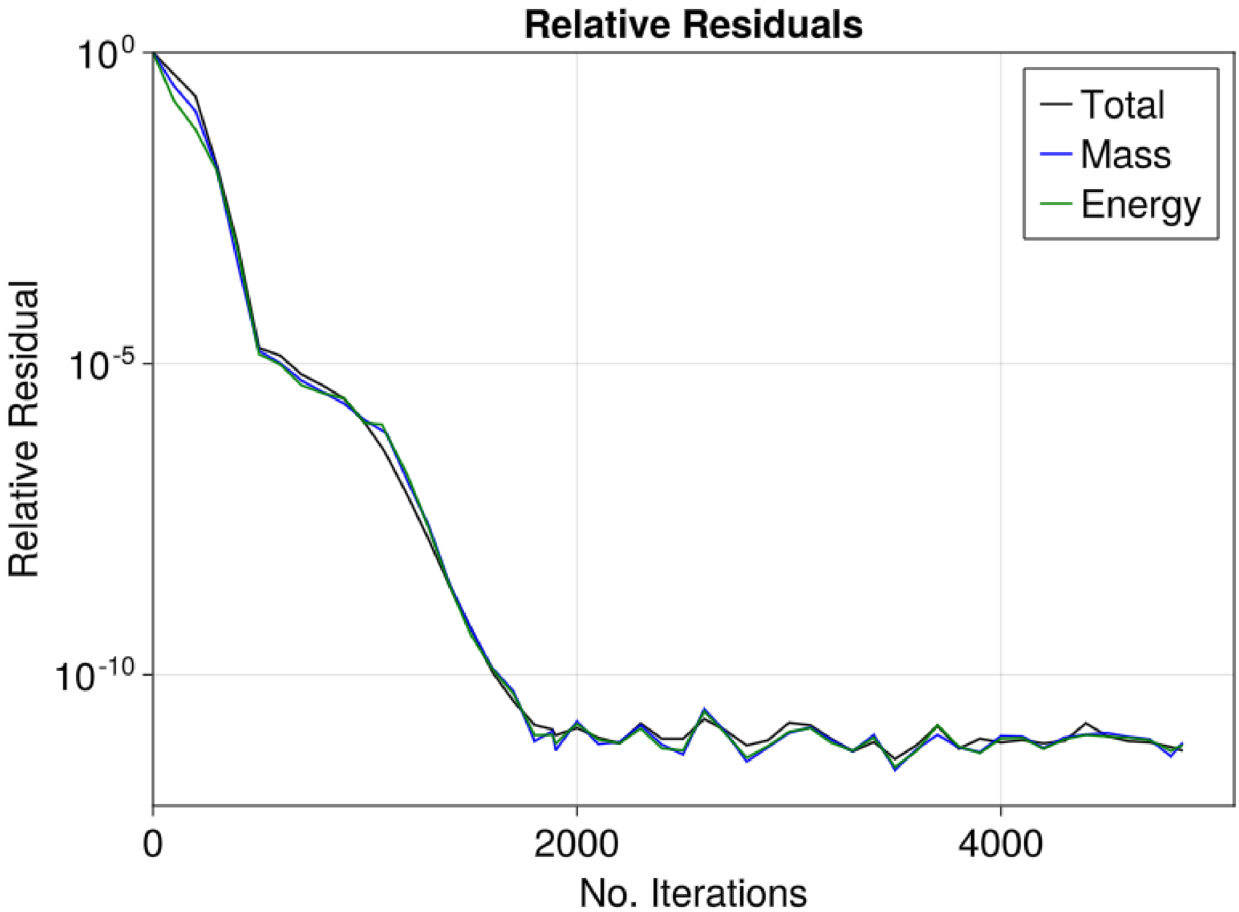

Figure 4.10: Total, mass, and energy residuals (relative to initial residuals) with the Jacobian-Free Newton-Krylov scheme.

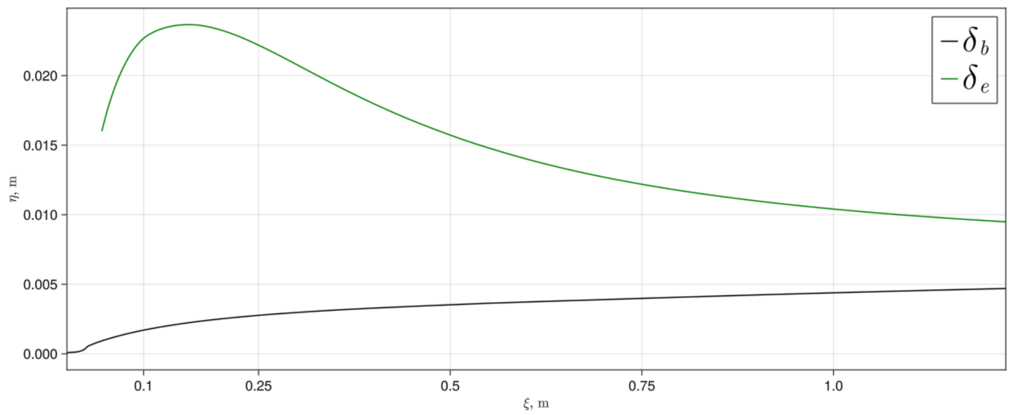

Figure 4.11: Boundary and entropy layer thicknesses for Mach 8 flow over a 17.78mm nose radius cone, assuming adiabatic wall conditions.

non-parallel flows, the $\frac{du_\eta}{d\xi}$ term is non-zero. For this particular flow, the contribution of the streamwise derivative is small enough that the location of the computed inflection point is unchanged whether it is included or not. The profiles of the compressible shear $\rho\frac{du_\xi}{d\eta}$ at the same locations as in Figure 4.5 and 4.6 are shown in Figure 4.13.

The combined effect of the shear and density gradients create a maximum in the vorticity, beginning a short distance downstream of the nose-frustum join. The inflection point shifts

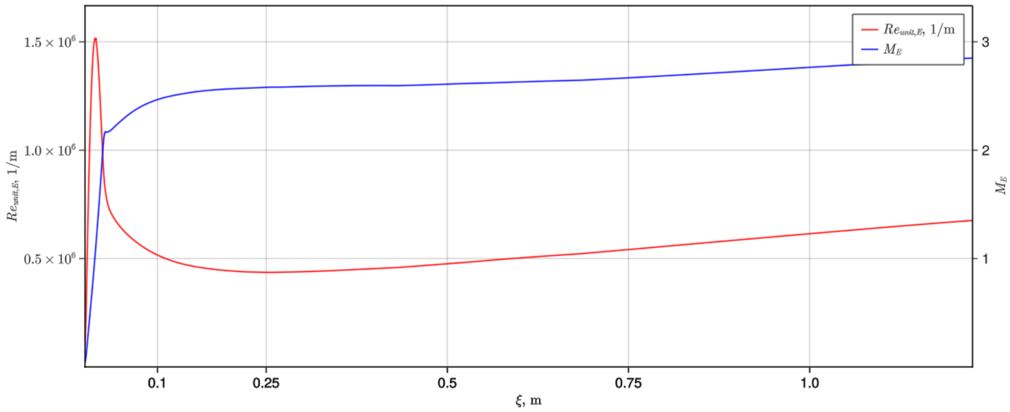

Figure 4.12: Unit Reynolds number and Mach number along the edge of the boundary layer.

towards the boundary layer edge downstream, eventually dissipating as it merges with the maxima in the boundary layer. Figure 4.11 is repeated here with the inclusion of the entropy layer inflection point to show the location of this vorticity maximum. The measurement of the inflection is noisy in the upstream region as the gradients here are close to 0, so the error induced by the interpolation process causes some difficulty in the accurate location of the maximum, but downstream the maximum becomes more pronounced and easier to identify.

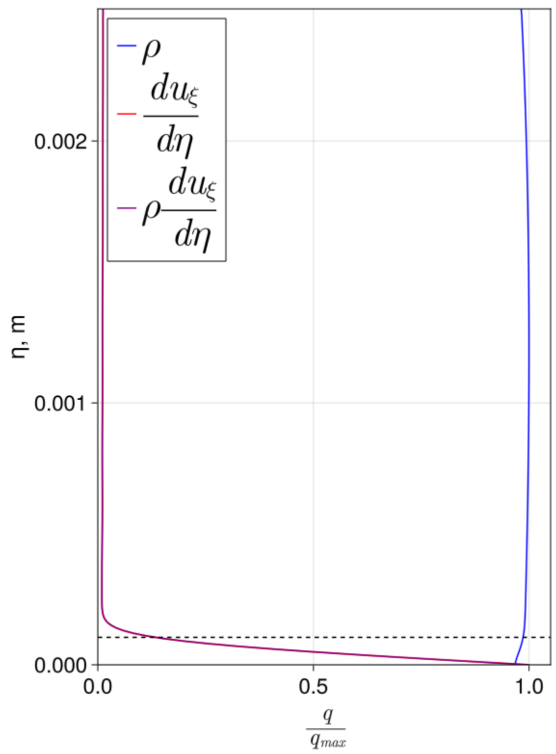

(a) $\xi = 0.005m$.

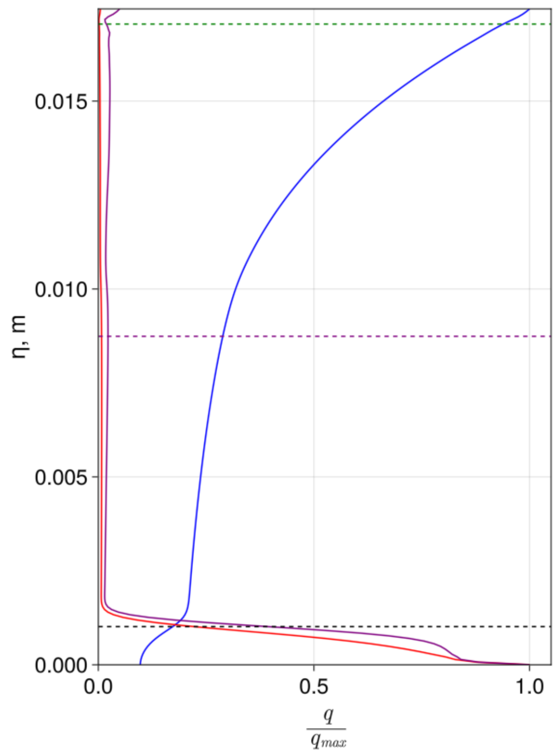

(b) $\xi = 0.05m$.

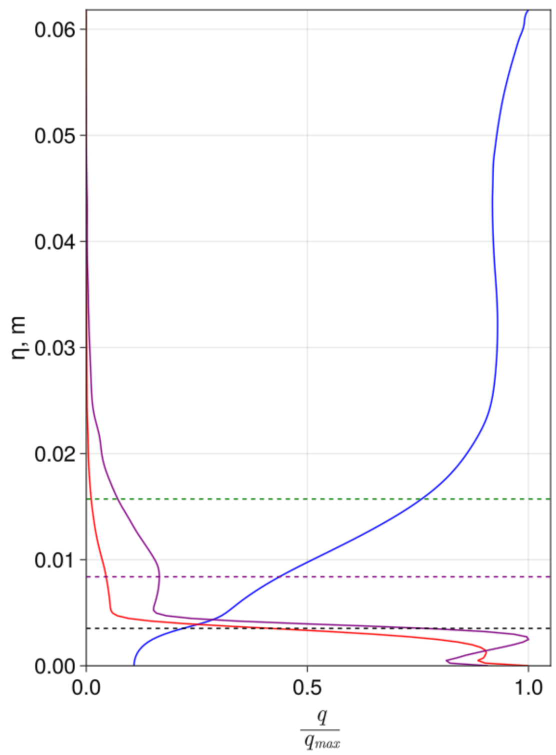

(c) $\xi = 0.5m$.

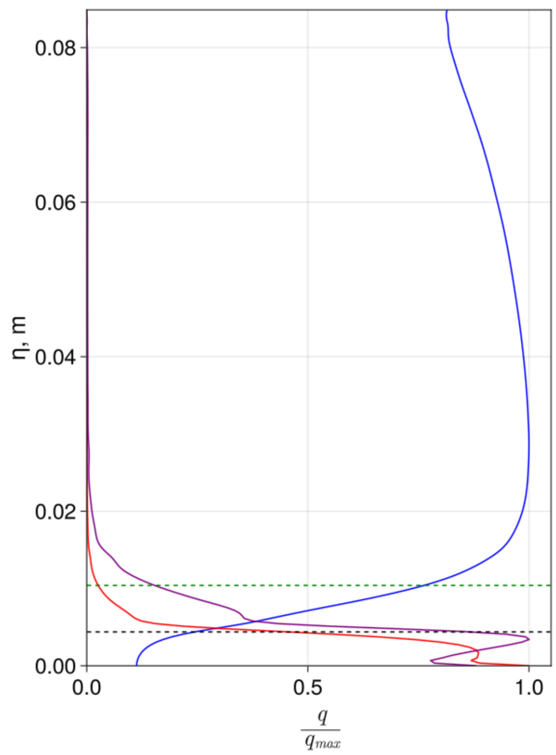

(d) $\xi = 1.0m$.

Figure 4.13: Profiles of density, velocity shear $\frac{du_\xi}{d\eta}$ and compressible shear $\rho\frac{du_\xi}{d\eta}$ (which serves as the vorticity) showing formation of an inflection point, a maximum in the vorticity denoted by the purple dashed line, within the entropy layer in the profile at $\xi = 0.5m$. The inflection point is a known source of inviscid instability. Black and green lines denote the boundary and entropy layer edges.

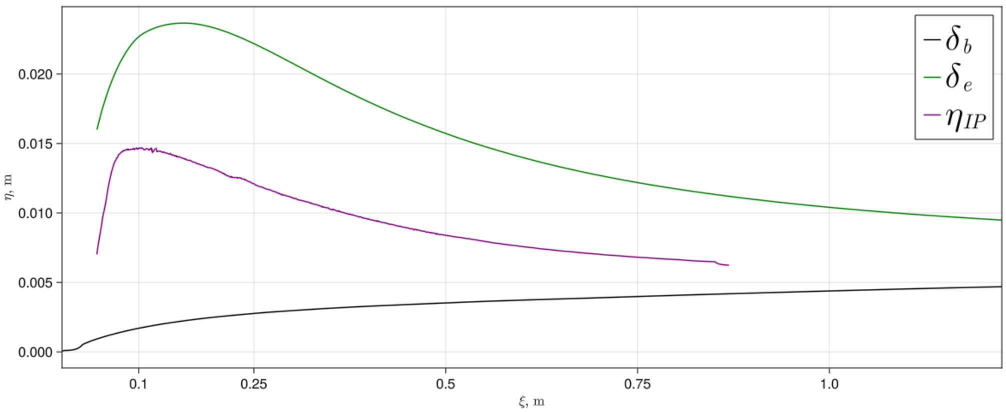

Figure 4.14: Location of the inflection point (vorticity maximum) relative the boundary and entropy layer edge locations. The inflection point shifts towards the boundary layer edge downstream, eventually merging with the inflection point in the boundary layer.

4.2 Time-Accurate Simulations

A time-accurate simulation on the full domain was performed first using the robust AUSMDV scheme while addressing the stability issues of the SBP-ASF scheme. The intention of these initial time-accurate simulations is to perform a pseudo linear stability analysis and provide insight to what features and frequencies are likely to be interesting for high fidelity simulations. Results from these simulations were presented at the 2nd International Conference on Flight Vehicles, Aerothermodynamics and Re-entry Missions [2]. The disturbance amplitudes are likely to be underestimated, but the qualitative behaviour should remain similar enough to inform subsequent simulations with the low dissipation scheme. The robustness of the scheme means it remains stable at significantly larger time steps than the low dissipation scheme, which is useful in this exploratory stage. The time-step used for these simulations was 2×10^{-9}s, which resulted in a maximum CFL value slightly above 2 using the third order Runge-Kutta scheme.

It is common practice when dealing with these blunt cone geometries to perform time-accurate simulations only in the region downstream of the nose-frustum join [89, 107]. This is for two reasons: the maximum stable time-step scales with $1/M$, so the time-step becomes prohibitively small in the stagnation region; and there is significant experimental evidence that phenomena originating in the nose region do not affect the transition process in the regime of interest [79]. The starting point of the simulation should be chosen so that the physics of interest is still captured, which for this work is the linear or transient stability of the entropy layer flow. To this end, full field axisymmetric simulations i.e. including the nose region, were performed to determine an appropriate starting location for subsequent higher fidelity axisymmetric and three dimensional simulations. The same mesh is used for these simulations as the steady state simulation, with 8600 cells in the streamwise direction and 180 cells in the wallnormal direction.

Three dimensional simulations are not performed on the full domain due to computational expense. This excludes the possibility of capturing three dimensional disturbances in the current simulation, which was justified due to the numerical results of Paredes et al. [80] which predicted axisymmetric disturbances to be most amplified. Three dimensional simulations on a truncated domain are performed in the Chapter 5.

A second aspect that must be considered prior to the high fidelity simulations is the frequency band of interest for these conditions. To determine the relevant frequency band, a forcing function that does not favour any particular frequency or disturbance type was used. The choice of forcing used in this simulation was a white noise disturbance imposed onto the freestream conditions that follows the form of Johnston et al. [130], described in Equation 4.4. This particular choice of relation between the pressure noise and the other base flow quantities was chosen so that the mass flux fluctuations are of the same order of magnitude as the estimate based on density perturbations [158] (Equation 4.5).

$$
\begin{aligned}
p' &= A(2R-1) \\
\rho' &= p' \frac{1}{\bar{a}_\infty^2} \\
u_i' &= p' \\
T' &= p' \frac{(\gamma-1)\bar{T}}{\bar{\rho}\bar{a}_\infty^2}
\end{aligned}
\tag{4.4}
$$

$$
\frac{(\rho u)'}{\bar{\rho}\bar{u}} = \frac{\rho'}{\bar{\rho}}\left(1 + \frac{1}{(\gamma-1)M^2}\right) \tag{4.5}
$$

Here R is a random floating point number between 0 and 1 and the amplitude A is set to the very low amplitude of 1×10^{-6} to ensure the magnitudes disturbance remain in the linear regime. This random forcing is applied in every ghost cell along the inflow boundary. For the axisymmetric simulations, the u_i is both the axial and radial (x and y) velocity. The time-accurate simulation was run until the solution becomes *statistically* steady. This took approximately 1ms, and was determined by comparison of computed Fourier modes for consecutive intervals. A snapshot of the fluctuations fields (mean minus instantaneous) in density, pressure, streamwise velocity and mass flux in the nose and downstream frustum region are shown in Figures 4.15 and 4.16. The reasoning for this set of variables are as follows: the density and streamwise velocity fields were chosen to capture convective waves from the continuous spectrum i.e. entropy and vorticity waves, pressure to capture both continuous acoustic waves and possible second mode waves, and mass flux as this was the quantity measured by hot wire anenometry by Stetson et al. [85].

4.2.1 Frequency Domain

Most of the conclusions drawn from these simulations comes from probing the results in the Fourier space, so the Discrete Fourier Transform of a select subset of variables was performed *in situ* as the amount of data required to perform the Fast Fourier Transform in post-processing quickly becomes difficult to manage as the number of captured frequencies increases, especially given not all variables recorded and written by the Eilmer code are useful. The incremental building of the Fourier coefficients is described by

$$
A_k^i = \sum_{n=0}^{N-1} e^{-i\frac{2\pi}{N}kn} q_n^i \tag{4.6}
$$

where A_k^i is the Fourier coefficient of the kth frequency in the ith cell in the domain, N is the number of frequencies captured and q_n^i is the value of the variable in cell i at snapshot k. The frequency of the snapshots is determined by the highest frequency captured, and the size of the time step is fixed such that the recorded snapshots always fall at equally spaced intervals. The result is a set of Fourier coefficients for each captured frequency for each cell in

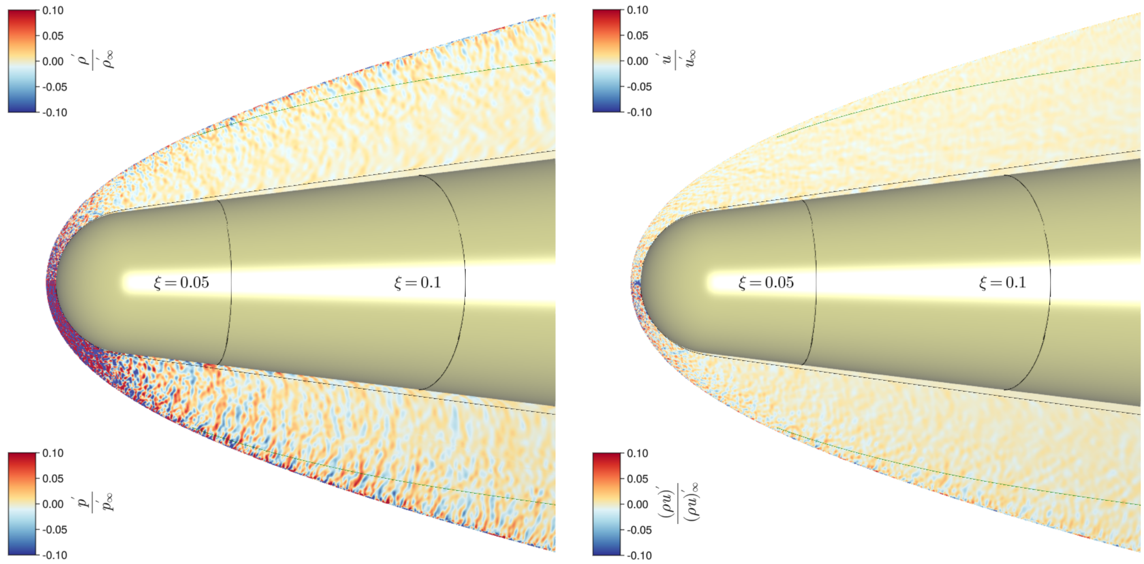

(a) Instantaneous snapshot of the density (top) and pressure (bottom) fluctuations in the nose region.

(b) Instantaneous snapshot of the streamwise velocity (top) and mass flux (bottom) fluctuations in the nose region.

Figure 4.15: Instantaneous snapshot of the fluctuations in density, pressure, streamwise velocity and mass flux, relative to the freestream fluctuations. Snapshot taken 1.5ms after the introduction of white noise disturbances in the freestream. Pressure fluctuations in the nose are considerably larger due to the repeated reflections of the acoustic waves off the wall and the shock.

the domain. Each positive frequency, bar the 0 frequency and the Nyquist frequency, will have a corresponding negative frequency that is its complex conjugate that can be discarded given the flow variables are purely real. The results in the Fourier space are interpolated onto a set of wallnormal profiles in the same manner as the base flow quantities.

The relevance of a given disturbance mode was determined by its amplitude and growth rate. The calculation of these quantities in a direct simulation is ambiguous, so the process is outlined here. The amplitude of a Fourier mode $A(\xi_i)$ is defined as the peak in the absolute magnitude of a given mode along a wallnormal profile at ξ_i. A local second order polynomial is created around the discrete maximum to estimate the true maximum, as demonstrated in Figure 4.17. The magnitudes of the Fourier modes are normalised using the factor $2/N_f$, where N_f is the number of Fourier modes computed (included the negative frequency conjugates) so that results can be compared directly while recording different numbers of modes. For the purely real source data used here, this means that the resulting magnitude is equivalent to the true magnitude of the fluctuations associated with that frequency.

There is some argument to include some consideration for the local mean flow quantities in the normalisation process. For example, should pressure fluctuations of amplitude 10Pa at a location where the mean pressure is 1×10^5Pa be considered equivalent to the same fluctuations when the mean pressure is 1×10^3Pa? When considering the non-linear

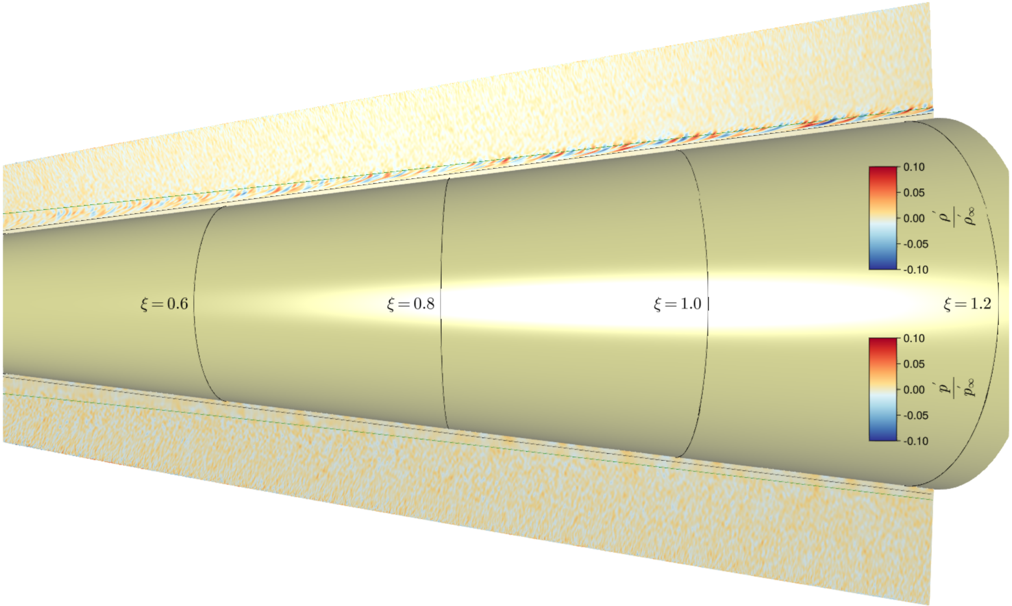

(a) Instantaneous snapshot of the density (top) and pressure (bottom) fluctuations in the frustum region.

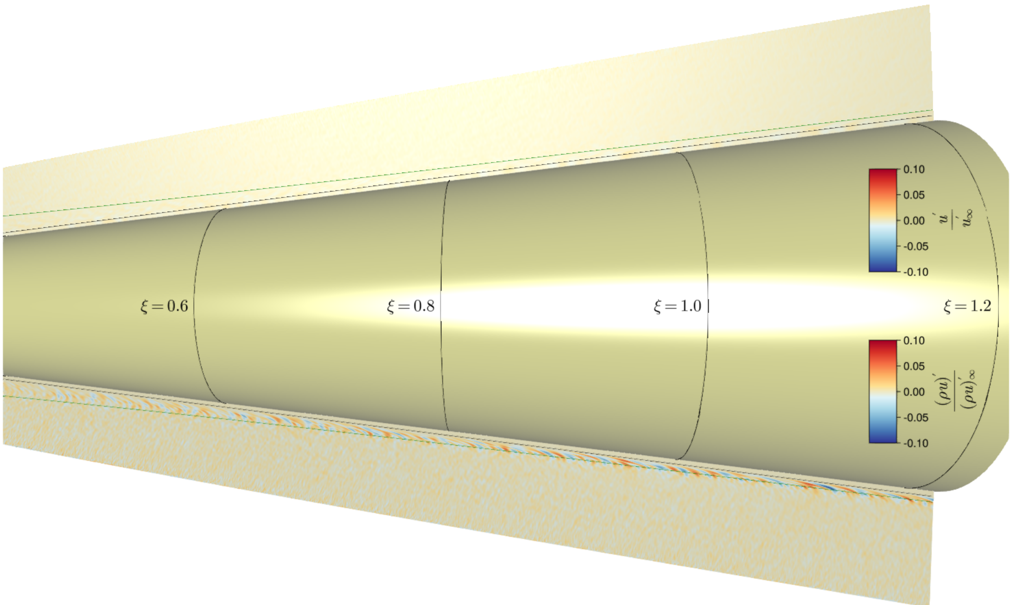

(b) Instantaneous snapshot of the streamwise velocity (top) and mass flux (bottom) fluctuations in the frustum region.

Figure 4.16: Instantaneous snapshots of the fluctuations in density, pressure, streamwise velocity and mass flux, relative to the maximum freestream fluctuations. Snapshot taken 1.5ms after the introduction of white noise disturbances in the freestream. Coherent structures in the density and mass flux fields form within the entropy layer. The lack of similar signature in the velocity field means the density contribution dominates the content in the mass flux fluctuations.

and breakdown stages of boundary layer transition, the answer is probably no due as the amplitude of the non-linear effects is 4 orders of magnitude larger in the latter case, relative

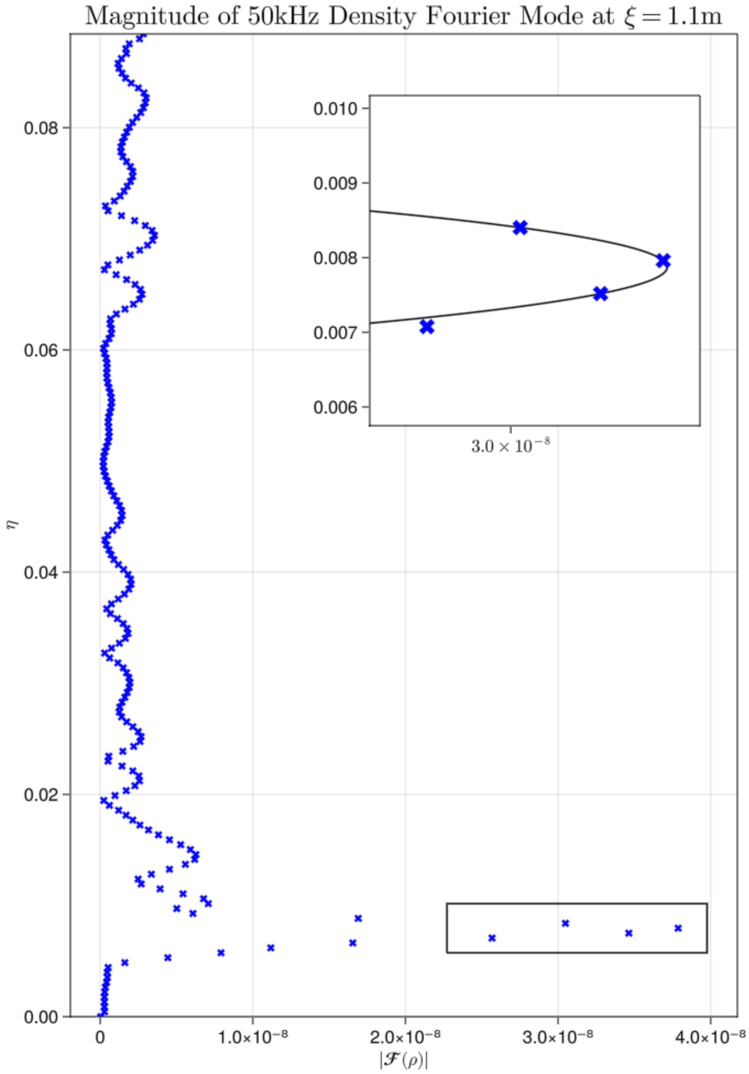

Figure 4.17: Wallnormal profile of the magnitude of the 50kHz density Fourier mode at $\xi = 1.1$m, with the inset demonstrating the process of extracting the amplitude of a mode using a local quadratic.

to the mean flow effects. Given that the focus in this work is primarily on the linear stage, this is less relevant so the problematic question of what to use as the normalisation is avoided. In any case, the instabilities are usually restricted to a specific common region of the flow, so the normalisation factor would be close to constant.

The growth rate of a disturbance mode is calculated by comparing the amplitudes calculated at preceding streamwise stations. It is customary to report the growth rate in logarithmic terms for historical reasons tied to LST. This is logical for eigenmodal disturbances, whose spatial evolution is described by $A(\xi) \propto e^{-\alpha\xi}$, but not so logical for non-modal disturbances which amplify linearly in space as $A(\xi) \propto \alpha\xi$. Consequently, the appropriate growth metric depends on the situation. The definitions for the local growth rate are either

$$\alpha_{non-modal} = \frac{A(\xi_i)/A(\xi_{i-1})}{\xi_i/\xi_{i-1}} \tag{4.7}$$

for non-modal disturbances, or

$$\alpha_{modal} = \frac{\ln(A(\xi_i)/A(\xi_{i-1}))}{\xi_i - \xi_{i-1}} \tag{4.8}$$

for modal disturbances. Here the subscript i denotes values at a particular wallnormal profile at location ξ_i. The net growth is calculated using the amplitude at the first streamwise station as the reference amplitude and removing the streamwise increment scaling i.e. $A(\xi_i)/A(\xi_1)$ for non-modal and $\ln(A(\xi_i)/A(\xi_1))$ for modal. The modal net growth rate is the N-factor commonly employed in the study of boundary layer transition, so N will only refer to the net modal growth to prevent confusion.

For the full domain simulations, a frequency range from 0 to 250kHz with 5kHz intervals was captured. The spatial evolution of the mode amplitudes in Figure 4.18 shows that the density (and mass flux) fluctuations are the only quantities that show any significant growth. The reference amplitude is taken at the nose-frustum junction. The growth is predominantly in the 20-100kHz range and begins at $\xi \approx 0.6$m, both of which match well with the hot-wire measurements of Stetson et al. [85]. There is suggestion of a weak instability at ~80kHz in the streamwise velocity and pressure fields at $\xi \approx 0.8$m, but it is not clear at this stage whether this is simply an artifact of the random forcing or a physical phenomena.

To gain some insight to the character of these disturbances, the full flow fields in the Fourier space are visualised. Given that each solution point in space has a series of Fourier modes associated with it, the flow response at a certain frequency can be visualised in the same way as a fundamental variable flow field to determine the locations of interest. Taking the magnitude of the Fourier mode is most effective in determining the big picture regarding the response of the flow to external disturbances, while taking the real part shows the local shape of the response which would correspond to structures seen is physical visualisation techniques such as schlieren imaging.

There is little value in showing the representation of every recorded frequency, so a subset of frequencies and fields which highlight the phenomena of the interest in this flowfield were chosen to show here. The color mapping in each figure is chosen to highlight particular features of each field, so the scale of the color map changes between figures.

First, the weak signature in the pressure and streamwise velocity fluctuations was identified to ensure it is a not a second mode response. The boundary layer is expected to be stable to first and second mode disturbances. Typical first and second mode responses would generate content in lower frequencies as the boundary layer thickens downstream, which is clearly not the case. The pressure Fourier field at 80kHz in Figure 4.19 shows the amplitude is a maximum at the wall, as opposed to the second mode which has a minimum at the wall and a maximum near the critical point (where the flow is sonic with respect to the boundary layer edge). The first mode does fit the profile, with a maximum amplitude at the wall, but the boundary layer edge Mach number should be too high for a first mode response. The

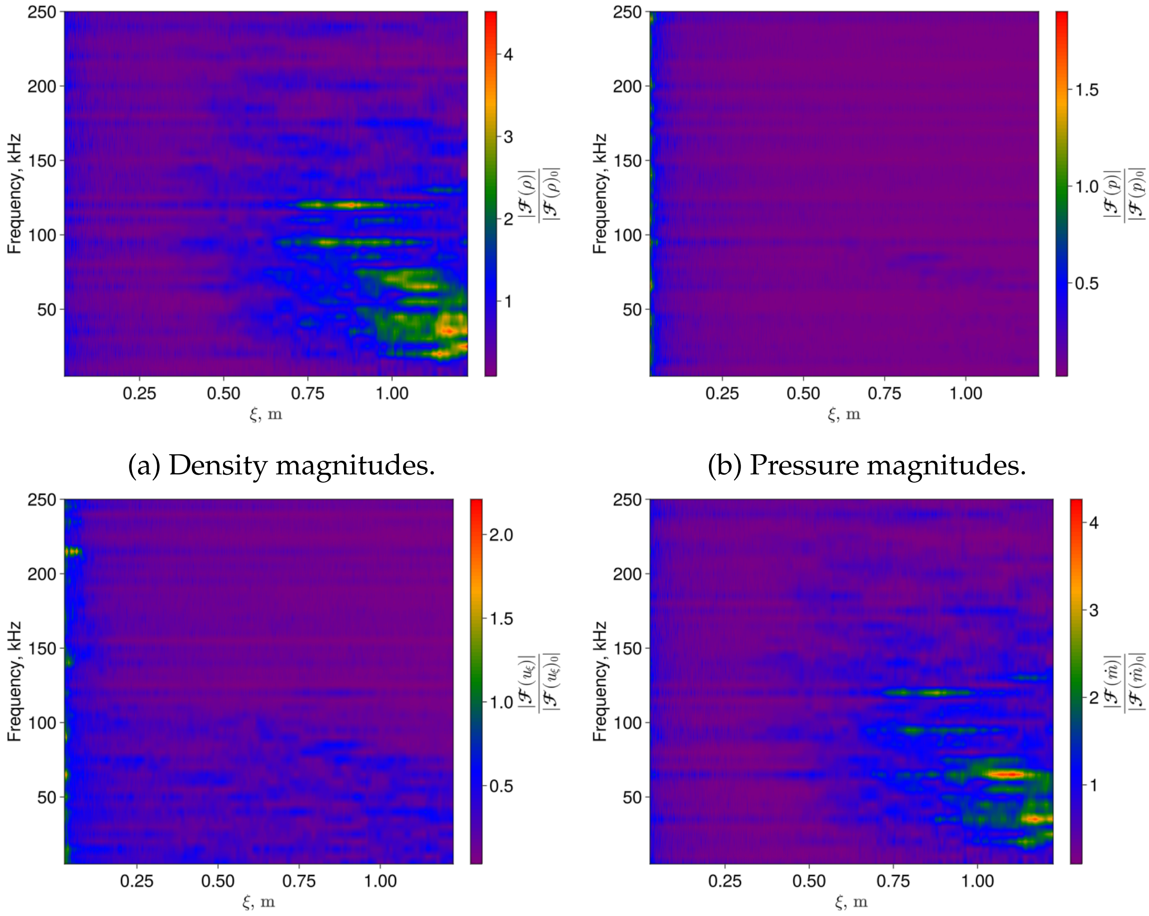

(a) Density magnitudes.

(b) Pressure magnitudes.

(c) Streamwise velocity magnitudes.

(d) Mass flux magnitudes.

Figure 4.18: Amplitude of Fourier modes for the density (top left), pressure (top right), streamwise velocity (bottom left) and mass flux (bottom right), relative to the amplitude at the nose-frumstum junction, show that the density is the only quantity that sees significant growth in the 20-100kHz range. Streamwise velocity and pressure fields suggest that there may be a weak instability around 80kHz.

most likely explanation for the response seen in Figures 4.18b and 4.18c is an artifact of the random forcing.

The Fourier field of the density at 55kHz in Figure 4.20, with the magnitude shown on top and the real part on bottom, shows that the strongest response is localised within the entropy layer near the end of the model. This matches the location of the dominant density fluctuations in Figure 4.15, and this particular disturbance is the source of most of the content in Figure 4.18a and Figure 4.18d. The shape of the fluctuations are tilted in the direction of the flow due to the streamwise velocity gradient.

This particular disturbance region, characterised by the shape of the density structures seen in the real part of the Fourier field, shifts downstream as the frequency decreases. This is a similar trend to that scene in second mode instabilities, but this similarity is misleading- the second mode unstable frequency changes due to the thickening of the boundary layer affecting the resonance, but the entropy layer thins downstream so the driver of this trend cannot be the same. The frequency response of this particular disturbance is broad, and

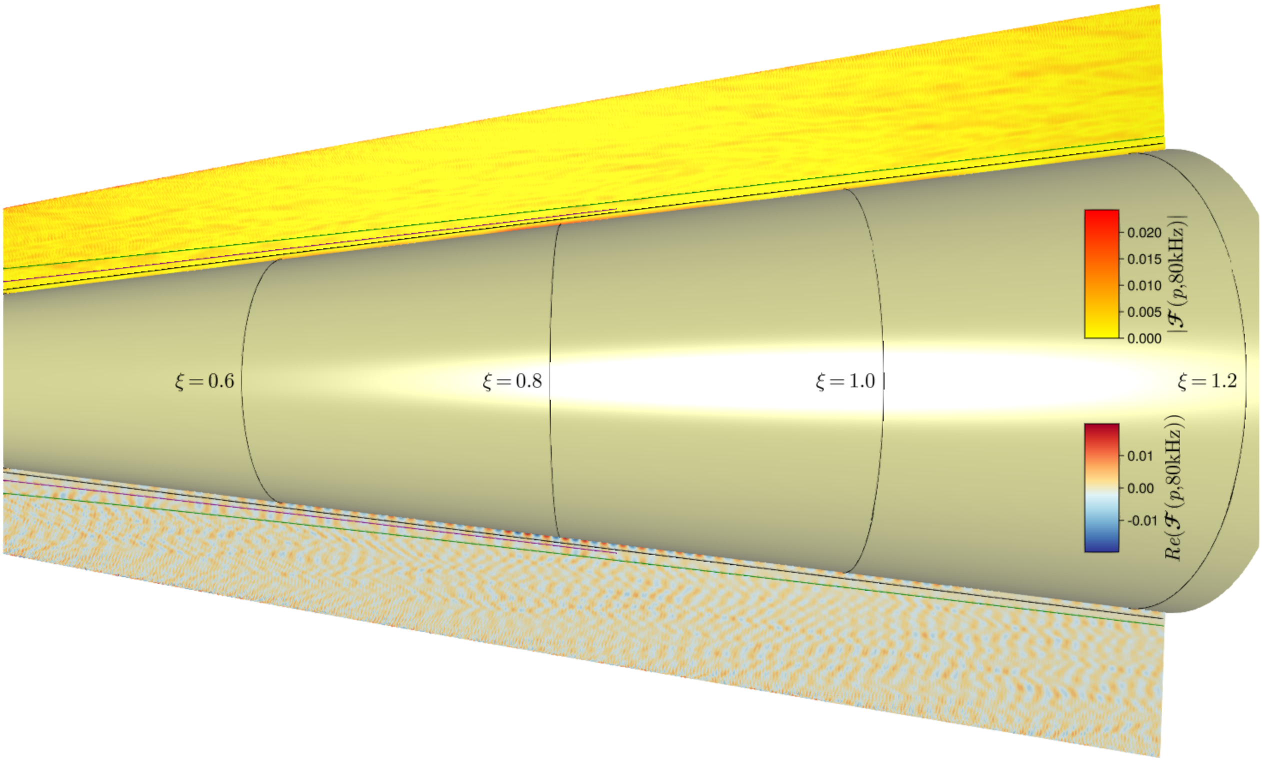

Figure 4.19: Magnitude and real part of the pressure Fourier field at 80kHz, targeting the weak signature seen in Figures 4.18b and 4.18c. The localised response and profile are not indicative of first or second modes, indicating that it is an artefact of the random external forcing.

accounts for the the bulk of the content visible in Figure 4.18a.

It also shows a second peak in content associated with the inflection point in the entropy layer, denoted by the purple dashed line. This particular disturbance is most obvious in the 90kHz density field, in the region shortly downstream of the nose-frustum join shown in Figure 4.21. The magnitude of this disturbance is significantly lower than the disturbance highlighted in the 55kHz field, but given the dissipative nature of the numerical scheme and the resolution of this simulation, the amplitudes may be noticeably different in a fully resolved simulation. The structures associated with this disturbance are initially close to perpendicular to the plane of the inflection point, tilting in the direction of the flow as they progress downstream.

There is a a third peak in content at the edge of the entropy layer which is visually obvious in the 90kHz density field in the downstream region shown in Figure 4.22. This disturbance appears considerably weaker than the disturbance within the entropy layer or the inflection point mode, but extends outside the entropy layer.

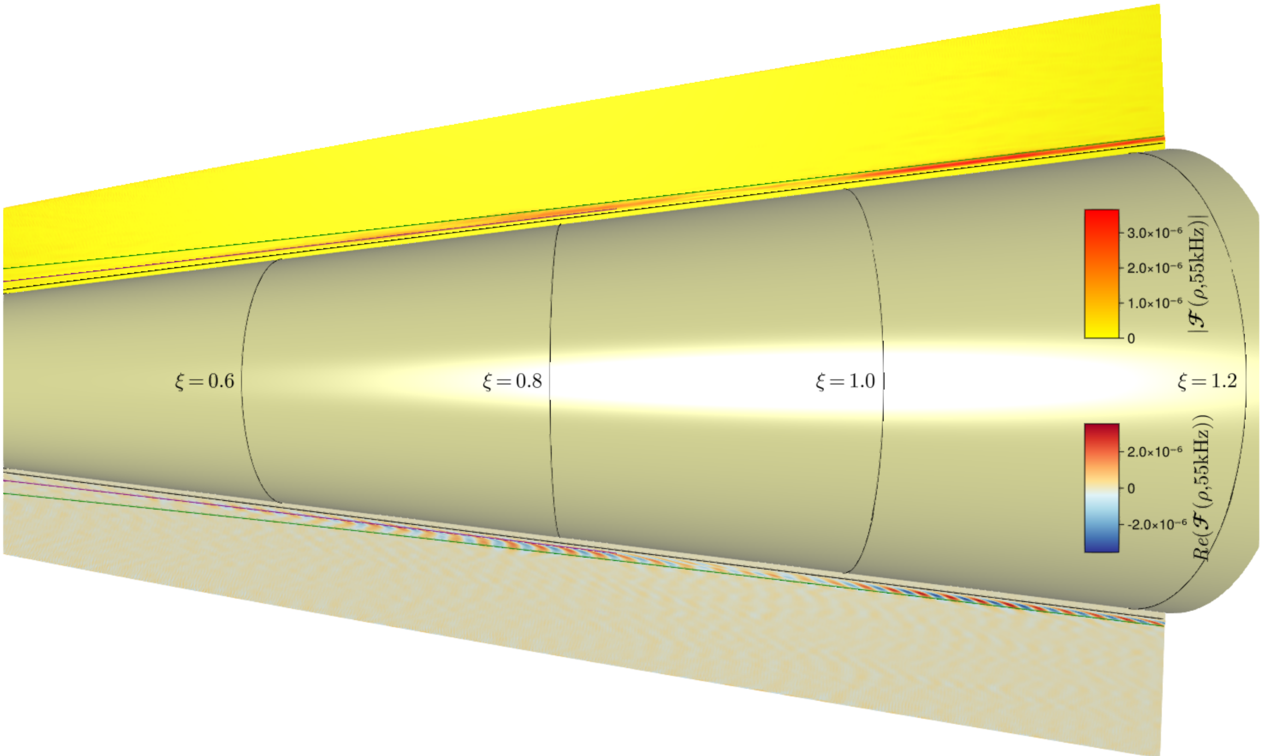

Figure 4.20: Magnitude and real part of the density Fourier field at 55kHz, which shows the dominant response is in the entropy layer close in the far downstream region. The structures in the entropy layer are tilted in the direction of the flow due to the local velocity gradient. There is a second peak in content associated with the inflection point in the entropy layer.

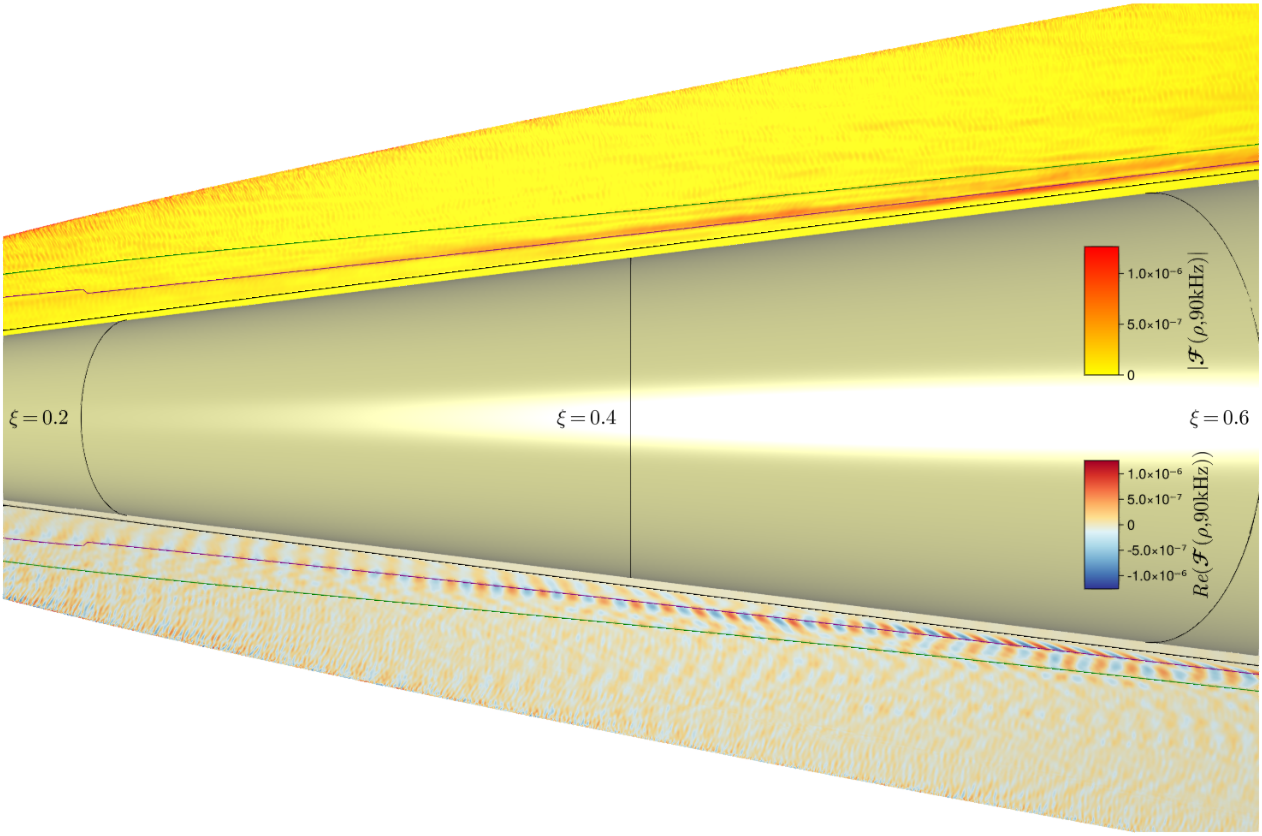

Figure 4.21: Magnitude and real part of the density Fourier field at 90kHz in the upstream region highlighting the disturbances associated with the inflection point. The structures begin normal to the plane of the inflection point, then begin to tilt as they progress downstream.

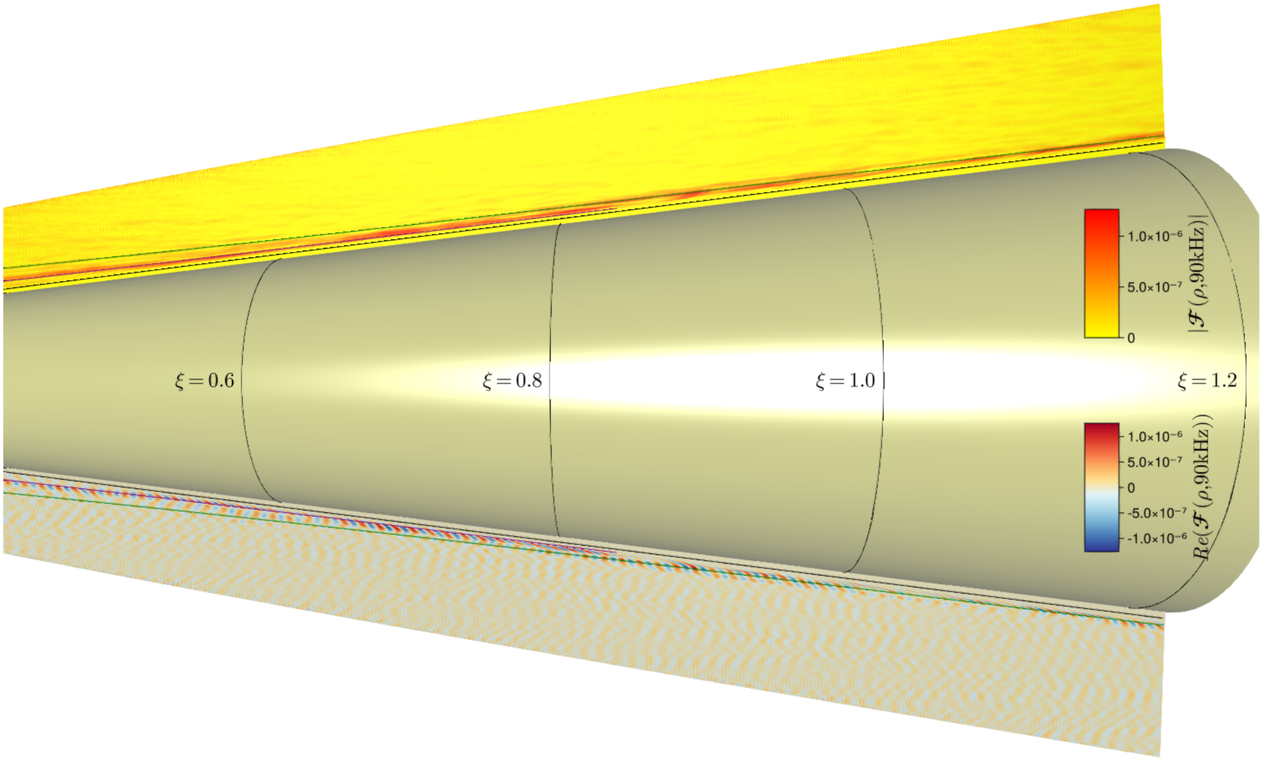

Figure 4.22: Magnitude and real part of the density Fourier field at 90kHz in the downstream region highlighting the disturbances associated with the inflection point. The structures begin localised at the edge of the entropy layer, then stretch and tilt in the flow direction.

4.2.2 Concluding Remarks

The entropy layer is susceptible to fluctuations of density, with minimal response in the velocity and pressure fields. This indicates the fluctuations are entropic in nature. The dominant frequency band for these disturbances was 20-100kHz. Based on the results of this full domain simulation, the starting point for the high-fidelity truncated domain simulations in Chapter 5 is set to $\xi \approx 0.1$m. The new domain for the simulations in the following section is illustrated in Figure 4.23. These high-fidelity simulations will be focused in the low frequency regime. While there is a weak flow response to the inflection point, the dominant response is in the entropy layer downstream of the location where the inflection point in the boundary layer merges with that in the boundary layer. The simulations in Chapter 5 were designed to excite these instabilities in particular.

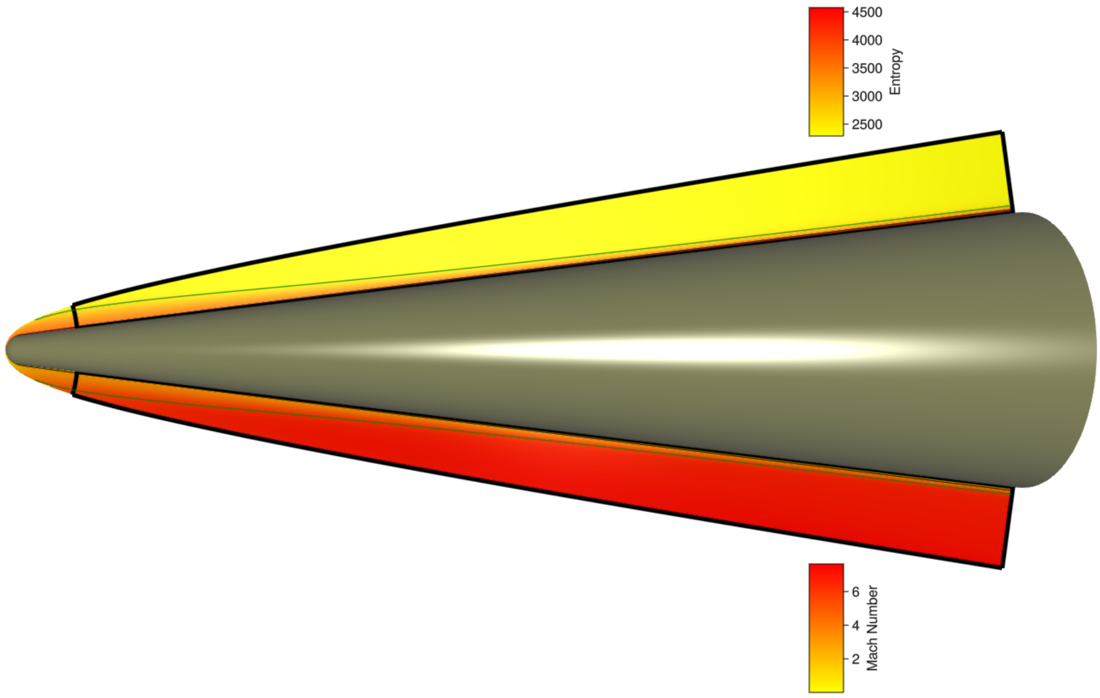

Figure 4.23: Representation of the truncated domain used in the following simulations.

Chapter 5

High-Fidelity Simulations of the 17.78mm Nose Radius Hypersonic Blunt Cone

The simulations in this section are performed on the truncated domain described at the end of 4.2, in Figure 4.23. The simulations in this section are more finely resolved and include three dimensional simulations. This was not possible with the resources available to this project primarily due to computational expense considerations, as the nose region requires extremely small time steps due to the viscous signal speed scaling with $^1/_M$. Truncation of the domain in this fashion permits an order of magnitude speed-up of simulations solely due to the increased stable time step, and makes three dimensional simulations palatable with the compute resources available to the project. Thus this section contains an axisymmetric and a 3D simulation performed on the same streamwise extent.

The ghost cells which form the boundary condition at this truncated boundary are filled using using data from the precursor full field steady state simulation. Given the mesh resolution of these truncated simulations is finer than the full field domain, the ghost cells are not located at the same location as the cells used in precursor simulation, so the data is interpolated from the precursor cell centre locations to the ghost cell centre locations using the same Clough-Tocher interpolator [152] as used for the data reduction to wall coordinates.

The solution on the truncated domain is reconverged to a steady state using the same process as in Section 4.1.4 due to the small perturbation introduced in transferring the solution from the precursor domain to the more refined truncated domain. Once the new refined solution is converged, the simulations are advanced time accurately with a forcing function added to the flow condition at the truncated boundary.

The Forcing Fucntion

The white noise forcing used in Section 4.2 also makes quantitative analysis more difficult, specifically due to its random nature. For this reason, a ”clean” disturbance, with a fixed magnitude at each tracked frequency, is used to simplify analysis and make it easier to draw conclusions regarding the underlying physics of the disturbances. The specific shape of the forcing function was chosen to target the inflection point instability and the downstream entropy disturbances. The forcing function is Gaussian shaped, with the maximum located close to the inflection point and centred in the entropy layer. The pressure is directly forced via

$$p' = Ap_0 \sum_{i=1}^{N_f} cos(2\pi f_i + R_i) \tag{5.1}$$

with A being the relative amplitude of the forcing, f_i being the chosen input frequencies in hertz and R being a random number between 0 and 2π to desynchronise the disturbance waves. The amplitude function A is given by

$$A(\eta,\zeta) = A_0 \exp^{-(\eta-0.0125)^2/\sigma_\eta - \zeta^2/\sigma_\zeta} \tag{5.2}$$

where A_0 is a chosen maximum amplitude and $\sigma_\eta, \sigma_\zeta$ control the spread of the forcing in the wallnormal and azimuthal directions. They are chosen such that the amplitude is reduced by an order of magnitude after 0.005m or 1° in the wallnormal or azimuthal direction respectively. A visualisation of the coefficient A_0 is shown in Figure 5.1. For the axisymmetric simulations, $\zeta = 0$ so the amplitude is taken along the centreline.

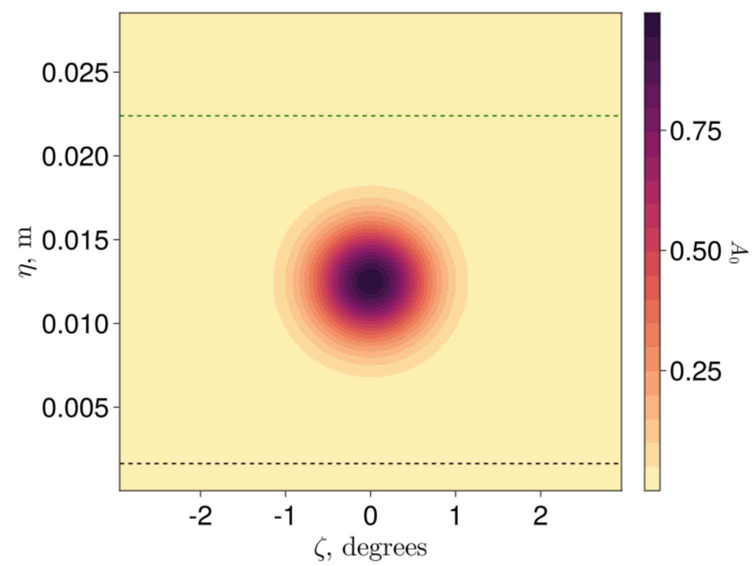

Figure 5.1: Shape of the forcing used at the truncated boundary for the high-fidelity simulations. Black and green dashed lines denote the local boundary and entropy layer edges.

The remaining flow quantities (u_x, u_y, u_z, T) are forced relative to the pressure in the same manner as in Equation4.4. The difference is that the reference values are the values that are being used to fill in the respective ghost cells, rather than the freestream values.

The mesh used for the truncated simulations is shown in Figure 5.2. The total number of cells is 8000 in the streamwise direction and 240 in the wallnormal direction. For the three dimensional simulations, 60 cells are used over an azimuthal range of 6 degrees. In this configuration, there are just over 100 points per wavelength in the streamwise direction under the assumption the entropy waves are dominant, which is overly sufficient for the linear regime.

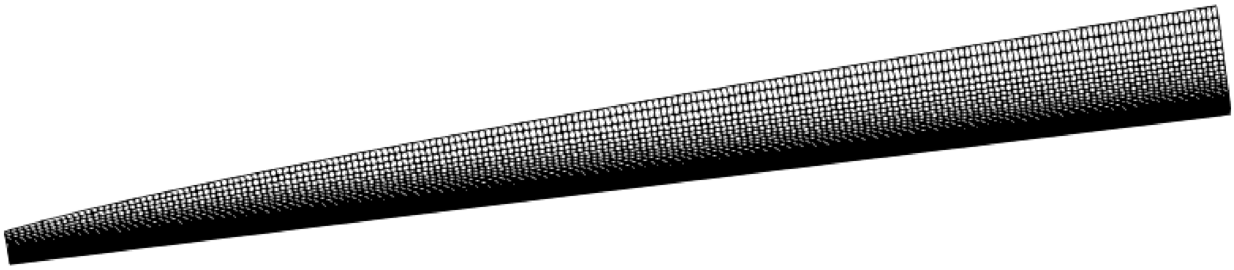

Figure 5.2: Mesh used for the simulations in the truncated domain. Every 40th grid point is shown in the streamwise direction, and every 6th in the wallnormal direction.

5.1 Axisymmetric Simulations

Attention is first given to the axisymmetric domain. The intent of this simulation is to explore the linear response of the flow to forcing, so a maximum disturbance amplitude A_0 is set to 1×10^{-4}. This amplitude is chosen so that non-linear effects were negligible. The frequency range chosen for this simulation is 10-150kHz, with 10kHz intervals. Preliminary results from these simulations were presented at the 23rd Australasian Fluid Mechanics Conference [3], with more detailed analysis presented at the AIAA SciTech Forum 2023 [4].

The variables tracked in the Fourier space here are the density and the vorticity ($du_y/dx - du_x/dy$). In the results presented in Section 4.2, the mass flux fluctuations are dominated by the density fluctuations, so there is little benefit to tracking the both the density and the mass flux. The vorticity is tracked for two reason: the inflection point instability is fundamentally a vortical Kelvin-Helmholtz type instability and vorticity waves form part of the continuous spectrum of the Navier-Stokes equations so are potential mechanisms for transient growth.

The linear response of the flow is most simply characterised by considering the amplitude of the disturbances, relative to a reference disturbance amplitude. Here, the reference amplitude is the amplitude computed at the first streamwise station at the truncated inflow boundary. This choice of reference station is not a perfect solution, because the addition of the disturbance along the truncated inflow plane is essentially prescribing a state that is not quite the solution to the Navier-Stokes equations and the correction introduces some noise to the spectrum, but it effective at demonstrating qualitative behaviour. The relative amplitudes of the density and vorticity disturbances in Figure 5.3 demonstrate similar qualitative behaviour to the full domain simulations, validating the forcing approach used in these simulations.

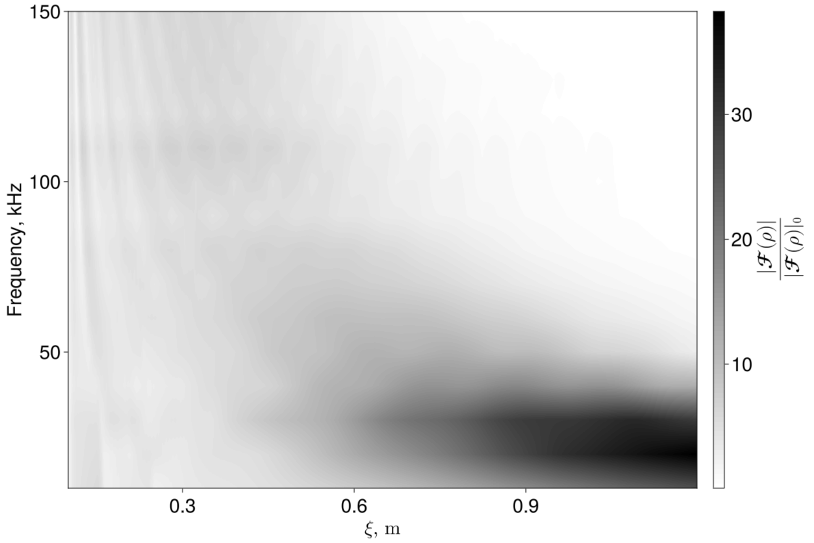

(a) Density fluctuations.

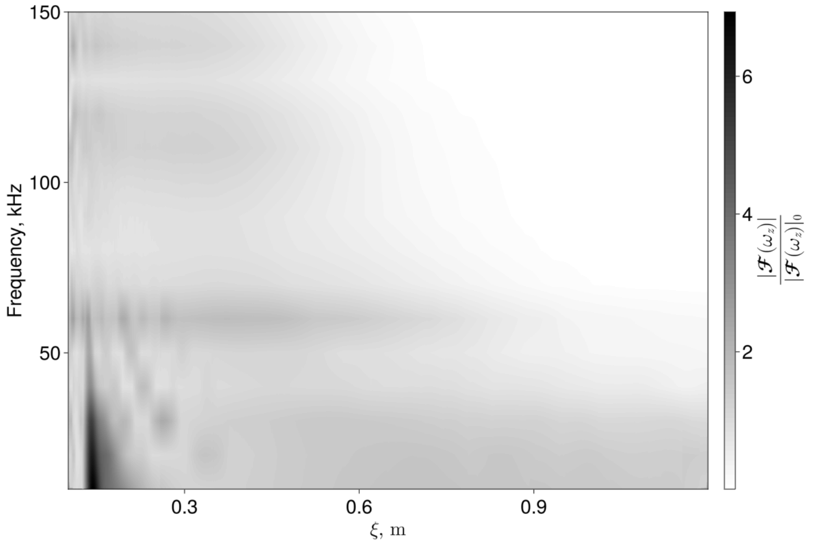

(b) Vorticity fluctuations.

Figure 5.3: Contours of the relative density and vorticity disturbance amplitudes, relative to the magnitudes at the truncated inflow plane, in the (ξ, f) space show the same qualitative behaviour as the full-field simulations, with the dominant response being in the density far downstream with a weak vortical response upstream.

The density disturbances are amplified downstream, with an unstable frequency range of 10-50kHz. There is no evidence of higher harmonics in the spectrum. To determine the character of these disturbances, it is more informative to visualise the frequencies individually. Recalling the theory presented in Sections 2.1.2 and 2.1.4, modal disturbances amplify and decay exponentially in space, while transient disturbances amplify linearly then decay exponentially. The growth trends in Figure 5.4 approximately follow the linear growth/exponential decay behaviour of transient growth, highlighted by the local linear fit on the 20kHz disturbance.

The amplitudes are modulated with a constant periodicity, indicative of multiple modes at the same frequency with different wavelengths constructively and destructively interfering.

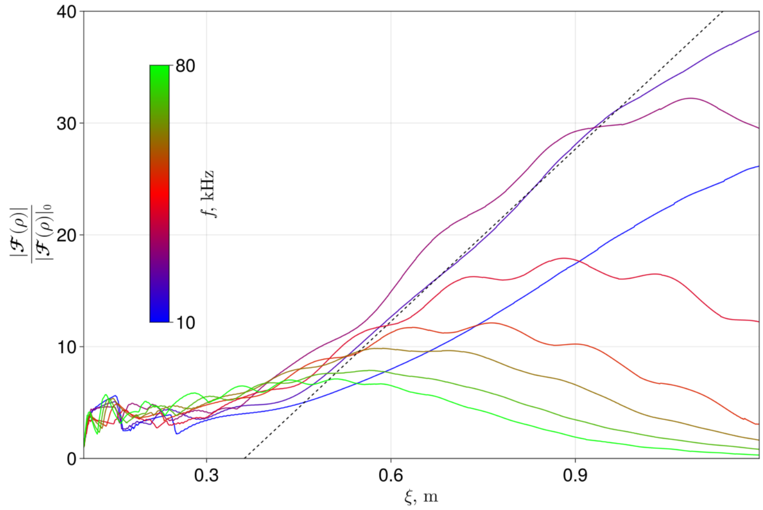

Figure 5.4: Relative amplitude of individual frequencies from 10-80kHz follow the linear growth/exponential decay behaviour associated with transient growth. The dashed line illustrates the linear growth trend on the 20kHz disturbance.

The source of this interference becomes clear when the spatial distribution of these modes is visualised as in Figure 5.5, which shows the magnitude and real part of the Fourier field at 40kHz. There are clear peaks in the frequency content above and below the inflection point which are out of phase with eachother, as evidenced by the real part of the Fourier field, causing the interference.

The magnitude of the fluctuations is actually a *minimum*, rather than a maximum as observed in the experiments of Stetson et al. [85]. The physical origins of the inflection point instability may provide an explanation for this behaviour.

5.1.1 Relationship to the theory of Lees and Lin [5]

To explain this origin, consider the equation for the force on a displaced parcel of fluid in a fluid with a vorticity gradient from Lin [90]:

$$F = \frac{1}{m\Delta\omega}\int v^2 \frac{d\omega}{dy} dA \tag{5.3}$$

where $\Delta\omega$ is the vorticity difference between the fluid parcel and the mean local vorticity (specifically $\omega_{\text{displaced}} - \omega_{\text{local mean}}$), m is the mass of the parcel, v is the velocity induced by the vorticity change and $\frac{d\omega}{dy}$ is the vorticity gradient. If the vorticity gradient is monotonically positive and a fluid parcel is displaced in the positive y direction, then the vorticity difference is negative and the resulting force is in the negative y direction and the fluid parcel is pushed back to its original location. However, if the vorticity gradient contains a maxima, then a parcel of fluid that is displaced across this maxima is forced further away from its original streamline until reaching the location of equivalent vorticity on the other side of the maxima. The vorticity may be equivalent at the parcel's original and final locations, but the entropy will not be the same.

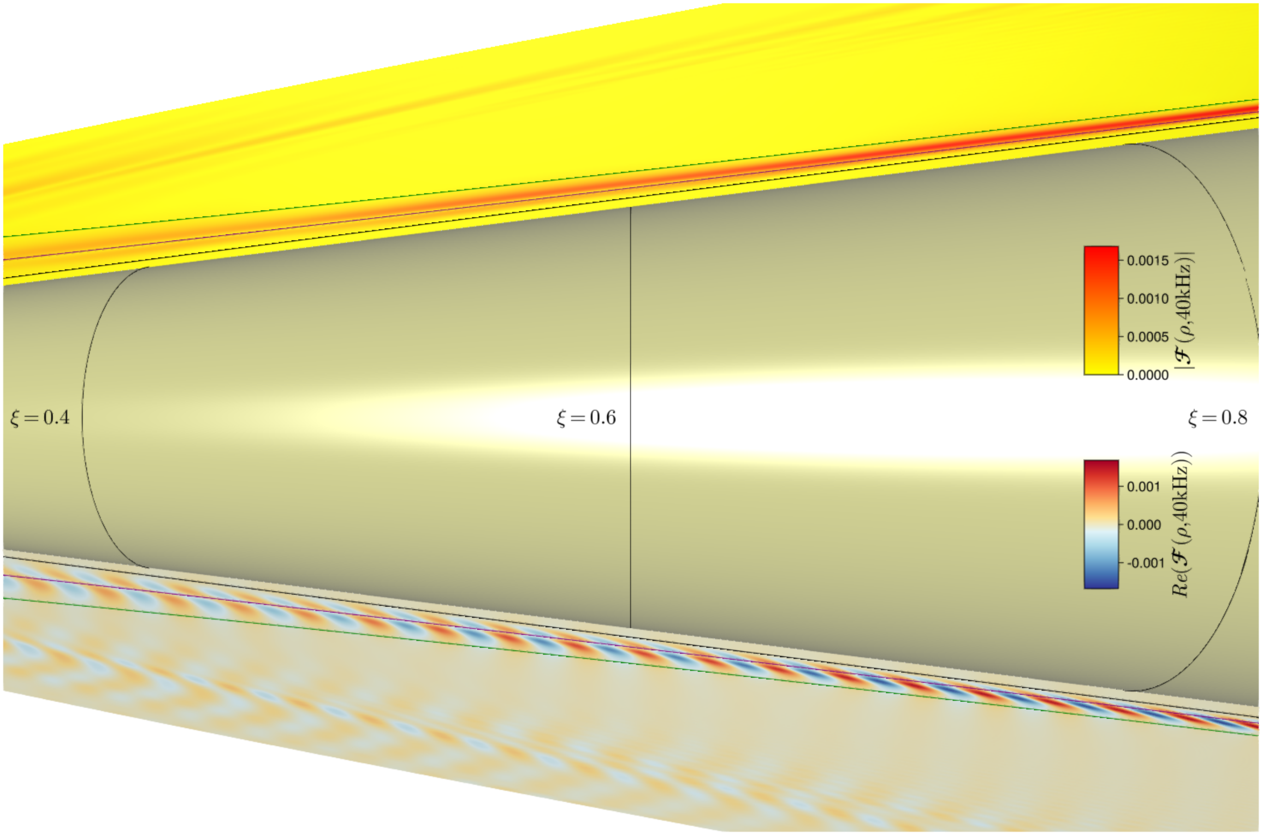

Figure 5.5: Magnitude (top) and real part (bottom) of the 40kHz density Fourier mode which on a portion of the full domain illustrates the cause of the periodic amplitute modulation. The fluctuations above and below the inflection point are out of phase and interacting, affecting the computed magnitude.

A further result from Lees and Lin [5], which at first seems contrary to this result but actually explains this behaviour well, is that the transport of the the angular momentum $(\rho \frac{du_\xi}{d\eta})$ must be zero at the location where the phase velocity is equal to the mean velocity, specifically in the temporal theory. This distinction of the temporal theory, rather than the spatial theory, is important as in the temporal theory the phase speed is in general complex, with the imaginary part containing information about the growth rate of the wave. This means that in the temporal theory, the only time the phase speed can be equal to the mean velocity is when the imaginary part is zero i.e. the wave is neutral. This is compatible with the theory in the previous paragraph, as a general disturbance does not necessarily meet the condition of the phase and mean flow velocities being equal. So if the disturbances have a phase velocity equal to the mean flow velocity at the inflection point, then this would explain the minima in fluctuation content at the inflection point and imply that the disturbance is neutral.

Further, the theory predicts a discontinuity in the phase of the disturbance across this critical layer where the phase speed and flow velocity are equal, which is clearly evident in in Figure 5.5. The real parts of the disturbances above and below the generalised inflection point are clearly out of phase. Naturally, the next step is to compare the phase velocity of the disturbance to the velocity at the inflection point. Additionally, this gives insight into the nature of the disturbances, for if this correlation $u_{phase} = \overline{u}$, then the disturbances should be entropy waves of the continuous spectrum as the response is restricted to the density (temperature) field, and entropy waves are density fluctuations at constant pressure [159]. The dispersion relation relates the wavenumber k and frequency f to the phase velocity u_{phase}, which for entropy waves is

$$f - \mathbf{u_{phase}} \cdot \mathbf{k} = 0 \tag{5.4}$$

where f is the frequency and k is the wavenumber. Given the wavenumber is related to the wavelength by $k = \lambda^{-1}$, the relation can be simplified to (assuming the frequency is in Hertz and k was in units of m^{-1})

$$u = f\lambda. \tag{5.5}$$

If the wavelength is constant, or at least varying slowly enough that it can be treated as constant, then this can be calculated trivially using a spatial Fourier transform of the real part of the temporal Fourier coefficients or programmatic location of the peaks. For this case, the peaks were located programmtically as the wavelengths were of similar order in size as the domain used for analysis. Here the wavelength is calculated along the path of the peak of the Fourier mode i.e. the location where the magnitude of the Fourier mode at each frequency is a maximum along each wall normal profile. The streamwise region is chosen to match the region where the disturbances of the given frequency are being amplified. The process is illustrated using the 40kHz mode.

Based on Figure 5.4, the 40kHz mode is amplified in the region $0.4m < \xi < 0.7m$, so the analysis is restricted to this spatial region. The real part of the Fourier modes along a series of streamlines is taken and the locations of the maxima are used to calculate a wavelength. The dominant wavelength computed using this method, for the 40kHz mode, is 27.6mm which gives a computed phase velocity of 1104m/s. This process was applied to frequencies from 10-80kHz and compared to the local mean velocities. The computed velocities fell within a few percent of the local mean flow velocities for all frequencies, further supporting the hypothesis that the fluctuations are indeed neutral entropy waves from the continuous spectrum. The gradient in the phase speed due to the velocity gradient causes the tilting of these density structures as the outer edges of the structure propagate faster than the inner edges.

This conclusion is consistent with experimental observations of density structures in the entropy layer by Kennedy et al. [93, 160], an example of which was shown in Figure 2.16 which is repeated here. As noted in Section 2.1.4, these structures propagated with the mean velocity at the edge of the entropy layer. The direct simulations of Hartmann et al. [107] demonstrated a feasible path to turbulence via the breaking down of coherent entropy layer structures as they penetrate the boundary layer, due to the strong velocity gradient. Then the structures observed in experiment are likely to be of the same nature as density structures observed here, at the point where they begin to enter the boundary layer.

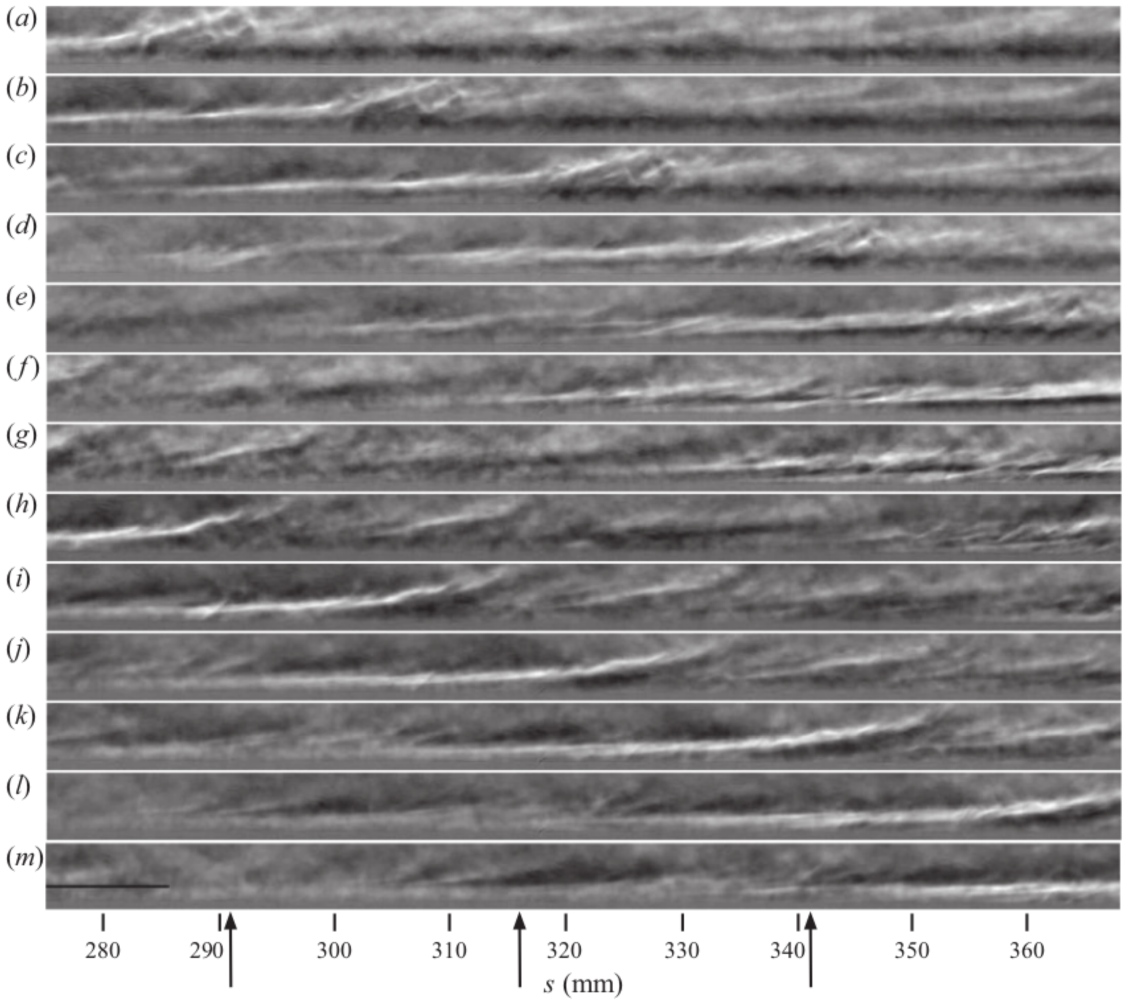

Figure 5.6: Set of schlieren iamges from Kennedy et al. [93] in Mach 6.14 flow over a 5.08mm nose radius cone, showing density structures extending outside the boundary layer. The images are separated by 21.3μs. The arrows denote pressure sensor locations, and the black line in the final figure denotes the boundary layer edge.

5.1.2 Transfer of Energy from the Base Flow to Disturbances

It is clear at this point that the entropy layer flow is susceptible to entropy disturbances, so now our attention can turn to *why*. The other works which have identified this planar non-modal growth phenomena [80, 161] did not deliver any insight into the origin of these entropy layer disturbances. It is important to not draw false connections between the entropy layer and entropy waves simply due to naming convention. The entropy layer is simply a region of entropy gradients generated by the non-isentropic process of flow passing through a shock, and has nothing to do with entropy fluctuations *directly* (bar the processing of disturbances by the shock as described by McKenzie [159], which is clearly not the driving factor here as the disturbances are imposed post-shock). The gradients in the entropy layer of this particular flow are such that entropy fluctuations can amplify transiently, but this is not necessarily a property of all entropy layers.

For some insight into the source of this entropy generation, inspiration is taken from the analyses of Liang et al. [162] and Kuehl [163] on the origins of the first and second mode instabilities. They begin with the fluctuation energy equation of Nicoud and Poinsot [164] given by

$$\begin{aligned}\frac{\partial e'}{\partial t} + &\nabla\cdot(p'\mathbf{u}') = \\ &\frac{\gamma-1}{\gamma\overline{p}}\left(\nabla\cdot(\lambda\nabla T')\right)p' + \mathbf{u}'\cdot(\nabla\cdot\tau')\end{aligned} \tag{5.6}$$

where λ is the thermal diffusivity and e is a measure of the total energy (a summation of the kinetic energy $\overline{\rho}\mathbf{u}'^2/2$ and the acoustic energy $\frac{1}{2\overline{\rho a}^2}p'^2$). Analysis of the character of the terms in this energy equation yielded valuable insight into the origins of the second mode instabilities, and drew clear relations between the acoustic impedance and the Reynolds stress contribution to the fluctuation energy. However, these analyses did not account for contribution from entropy fluctuations. The entropy contribution to the total energy (defined in the total energy definition as $\frac{\overline{p}}{2R_{gas}C_p}s'^2$).

$$-\frac{\overline{p}}{R_{gas}C_p}s'u'\cdot\nabla\overline{s} - \frac{1}{C_p}\left(\nabla\cdot(\lambda\nabla T) + \tau' : u'\right) \tag{5.7}$$

where R_{gas} is the difference between the specific heats $C_p - C_v$, λ is the thermal diffusivity and τ are the shear stresses. For the boundary layer flows studied in Liang et al. and Kuehl, the flow is isentropic so the mean entropy gradient is zero so dropping the entropy contribution was justified. For flows over a blunt cone, the entropy gradient is non-zero due to the curved bow shock so this term should be included. It is important to note the flow was assumed to be static in the derivation of Equation 5.7, so terms dependent on the mean velocity were dropped. The most significant term neglected under this assumption is the entropy convection, $\overline{\mathbf{u}}\cdot\nabla\overline{s}$. Based on this, and the dependence of Equation 5.7 on the entropy gradient, the entropy gradient term should be of importance (specifically the negative of the gradient).

Given the flow is close to parallel, the divergence of the entropy is simplified to simply the wallnormal entropy gradient, with the entropy defined as $C_v\ln(\overline{T}) - R_{gas}\ln(\overline{p})$. The wall-normal entropy gradient is plotted against the root-mean-square (RMS) of the density fluctuations at $\xi = 0.25$m, the location where the density (entropy) fluctuations begin to be amplified, and a location downstream at $\xi = 0.6$m. The maximum in the gradient aligns with the peak of the RMS fluctuations at the location where the fluctuations begin to be amplified, but the same does not apply downstream.

This behaviour could be explained by considering the terms in Equation 5.7. In the early upstream region, the amplitude of the disturbances are close to uniform across the entropy

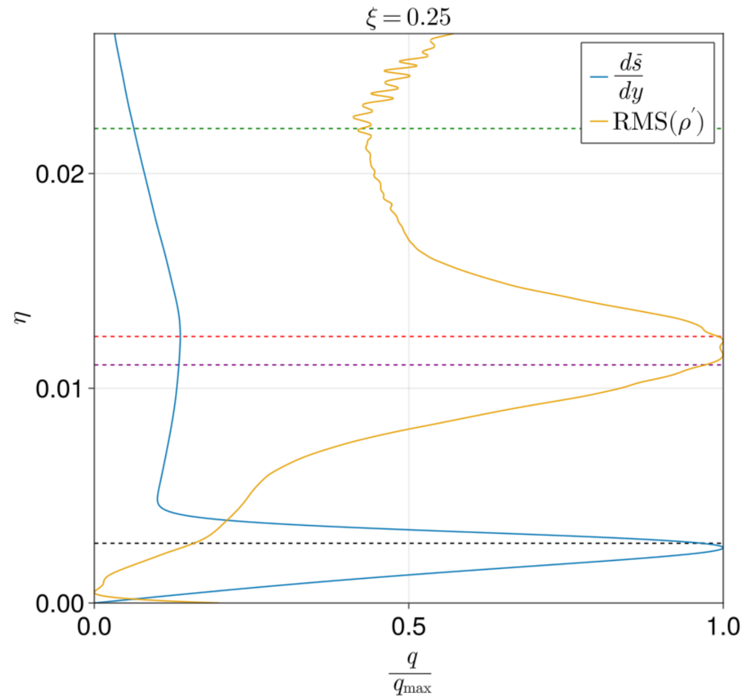

(a) $\xi = 0.25m$.

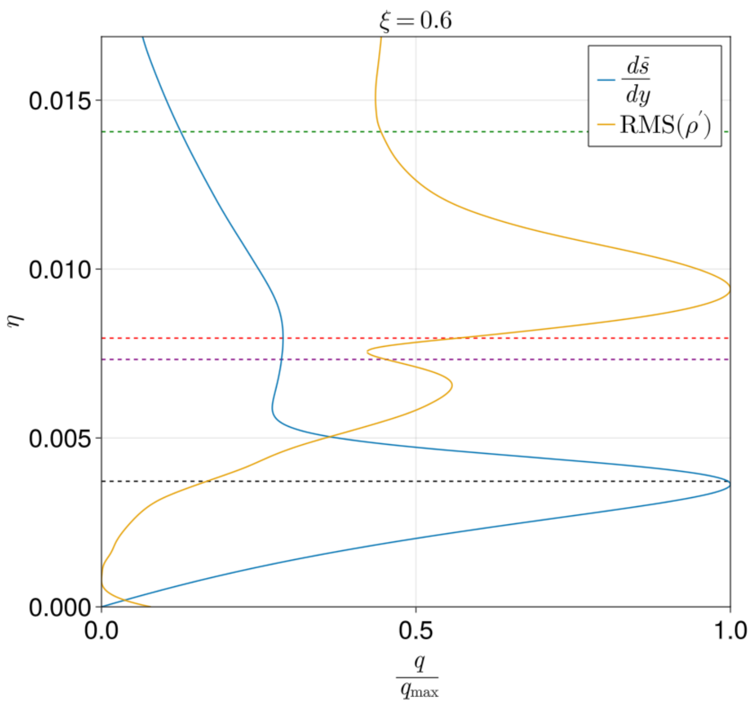

(b) $\xi = 0.6m$.

Figure 5.7: Profiles of the entropy gradient and RMS density fluctuations (which correspond to entropy fluctuations) at $\xi = 0.25$m, where the fluctuations begin to amplify, and at $\xi = 0.6$m. The peak in the entropy gradient (dashed red) matches the location of the peak fluctuations at the upstream profile, but not at the downstream profile. The black and green lines denote the boundary and entropy layer edges, while the purple and red lines denote the local vorticity maxima (inflection point) and entropy gradient maxima.

layer, so the contribution to the fluctuation energy is dominated by the mean entropy gradient term. As the entropy fluctuations grow, the contribution from the s' term becomes more significant and the fluctuations become self-sufficient in a sense.

It is important to remember that this discussion is regarding the energy in a disturbance, not the energy of an arbitrary flow. The entropy is usually considered a ”disorder” energy, or energy unavailable for ”useful” work when discussed in terms of a mean flow. However, the entropy fluctuations are characterised by density fluctuations, so the energy contained in the density fluctuations can be converted to kinetic energy fluctuations through changes in density, which generate velocity fluctuations through the continuity equation. This is a possible mechanism for the breakdown of laminar flow to turbulence through the path of entropy disturbances. This is the argument used by Chu [165] for including an entropy fluctuation term in the total energy equation when considering the transfer of energy from a mean flow to small disturbances. Under the restriction of a strictly parallel shear flow without pressure gradient, he arrived at an expression for the rate of transfer from the mean flow to small disturbances which, neglecting the viscous dissipation terms to emphasise the production terms, is given by

$$\frac{\partial E}{\partial t} = -\int \bar{\rho} u' v' - \int \bar{\rho} v' s' \frac{d\overline{T}}{dy} d\tau + \text{visc. diss. terms} \tag{5.8}$$

where $d\tau$ is the a volume element. The first term is the work due to the classic Reynolds stresses, and the second term is due to the entropy gradient (it is written as the temperature gradient in the initial work as the pressure gradient is assumed to be 0, in which case the temperature gradient is the entropy gradient). The second term is due to the transport of entropy fluctuations across a temperature gradient. The initial generation of fluctuation energy is driven by the local entropy gradient, then becoming self-sufficient downstream through the contribution of the entropy fluctuation term. Unfortunately, the second part of this explanation is not satisfying: if the growth rate of the entropy fluctuations becomes dependent on their local magnitude, the instability should be experience exponential growth.

Returning to the idea that these waves are neutral waves as described by Lees and Lin [5], this can also provide an explanation for the growth behaviour of these disturbances. In the case of neutral sonic or supersonic waves ($u_{phase} \geq u_\infty - a_\infty$, where ∞ is with respect to some freestream) propagating both inwards and outwards, there can be a net exchange of energy if the balance between the energy carried by the incoming and outgoing waves is not equal, then the rate of energy exchange should be linear. Unfortunately, this does not seem to be the case in this instance: the location where the flow is sonic with respect to the freestream, if we take the conditions at the edge of the entropy layer as the freestream, is close to the boundary layer edge, so the disturbance seen in these simulations appears subsonic.

A sufficient condition for a neutral subsonic wave is that the quantity $\frac{d}{d\eta}\left(\frac{1}{\overline{T}}\frac{du_\xi}{d\eta}\right)$ vanishes between the edge of the entropy layer and the sonic location. The profile of $\frac{1}{T}\frac{du_\xi}{d\eta}$ is shown in Figure 5.8 at 3 streamwise locations demonstrates that this is true, and naturally the location where $\frac{1}{T}\frac{du_\xi}{d\eta}$ vanishes is almost identical to the generalised inflection point as the pressure gradient is weak. If the temperature gradient is zero at the point where $u_{phase} = \overline{u_\xi}$, as it is in this case, then there should be zero net exchange in energy between the mean flow and the disturbance. Additionally, the solution to the wave equation for subsonic waves is unique, so there is not a continuous spectrum of waves as appears to be the case here.

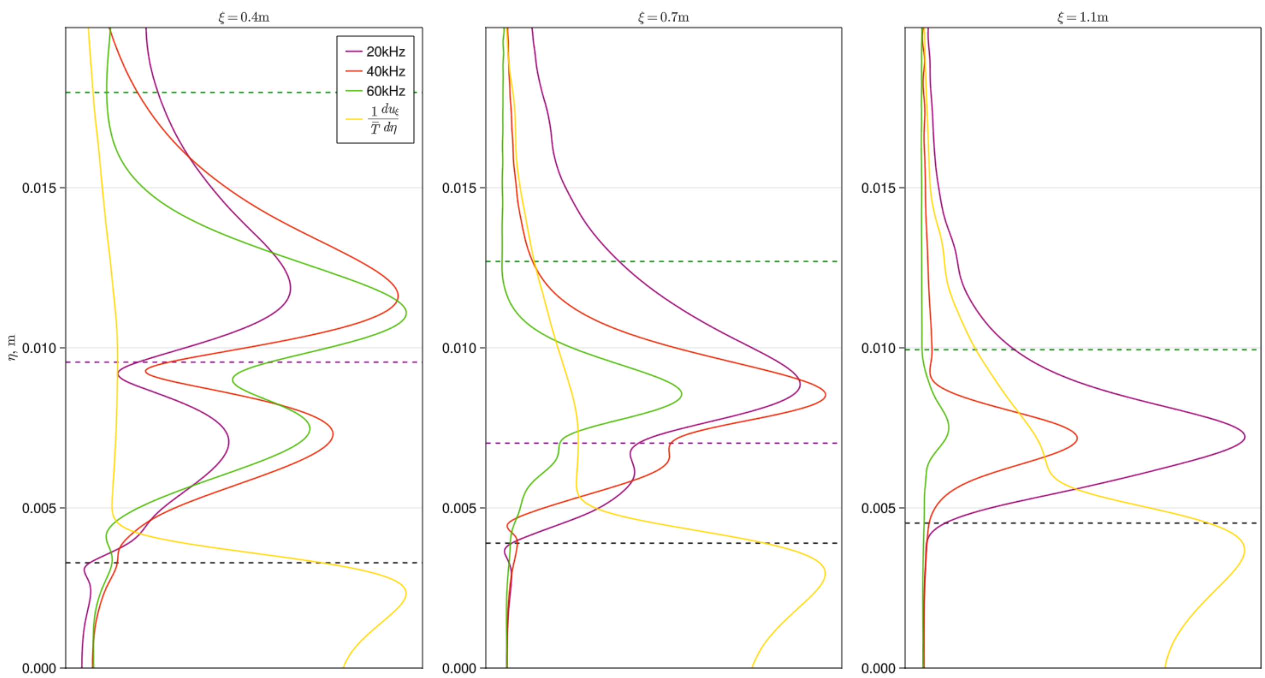

Figure 5.8: Profiles of the quantity $\frac{1}{T}\frac{du_\xi}{d\eta}$ and the magnitude of density fluctuations at select frequencies at three locations along the cone. The black, green and purple dashed lines denote the boundary layer edge, entropy layer edge and location of the inflection point.

The theory of Lees and Lin does not seem to provide a concrete explanation for the growth of these entropy disturbances. While the is typically applied to boundary layers, there is no obvious reason should not be applicable to flows with entropy layers. Consider the assumptions made in the work. First, the disturbances are small enough that terms quadratic or higher in the disturbance can be neglected. Second, that the flow is locally parallel, so the magnitude of the gradients in the wallnormal direction are much larger than in the streamwise direction so they can be ignored without significant detriment to the solution. Third, which is applied for the majority of the work, is that the pressure gradient is zero. The non-parallel effects are certainly stronger in flows with entropy layers compared to sharp cone/flat plate boundary layers, but the gradients are still significantly larger in the wall normal direction and this assumption was applied in the PSE work of Paredes et al. [89, 161] which saw similar results. The disturbances are chosen to be small enough that the linear approximation is reasonable. The pressure gradient is weak, but non-zero, so this would affect the energy transport equation and therefore the conclusions based on energy balances.

These axisymmetric simulations indicate the entropy layer is receptive to transiently growing planar entropy waves, which manifest as temperature and density fluctuations at effectively constant pressure. Contrary to experiment where the maximum in the fluctuations was associated with the generalised inflection point, the maximum in the density fluctuations was situated between the inflection point and the edge of the entropy layer. The fluctuations are in fact a local minimum at the inflection point. The growth of the entropy waves is initially associated with a maximum in the entropy gradient, in qualitative agreement with the fluctuation energy equation, but the association does not hold downstream. The theory of Lees and Lin does not provide a concrete explanation for the fluctuation energy growth in the entropy layer. The transient growth, phase behaviour and amplitude profile suggest neutral supersonic waves, but the phase speed is subsonic with respect to the conditions at the edge of the entropy layer.

Now attention is given to the vorticity fluctuations. Based on Figure 5.3b, there is a small region at 0.11m $< \xi <$ 0.25m where the vorticity fluctuations appear to be amplified, close to the truncated boundary which forms the start of the simulation domain. The relative amplitudes of the fluctuations in the 10-80kHz range are plotted individually for the vorticity fluctuations in Figure 5.9, with the inset axes detailing the short region of interest at 0.11m $< \xi <$ 0.25m. The growth of the vorticity fluctuations is exponential, more typical of modal instabilities.

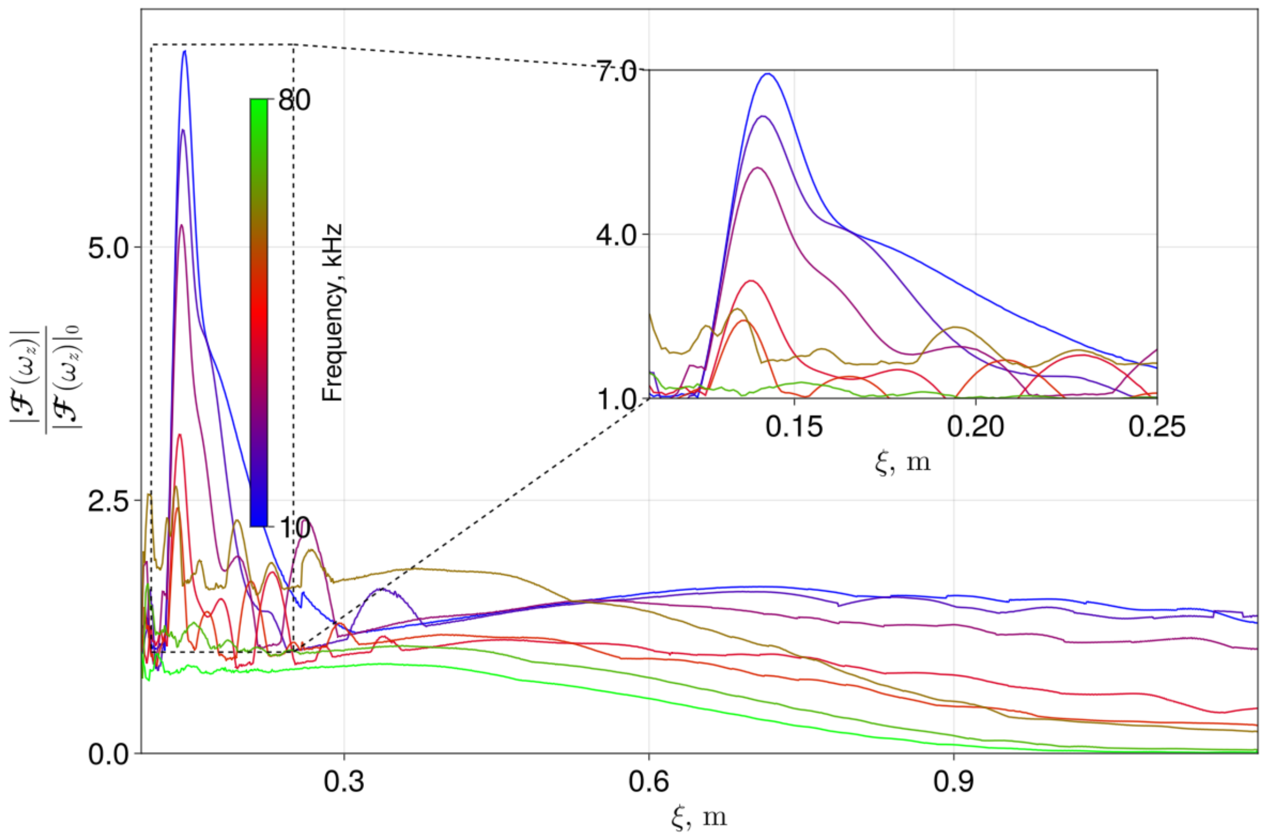

Figure 5.9: Relative amplitude of the vorticity fluctuations, relative to their initial amplitudes. Inset highlights the region from 0.11m $< \xi <$ 0.25m.

The spatial distribution of the vorticity fluctuations in Figure 5.10 actually suggests the "instability" is a direct result of the forcing function, in the sense that the "growth" of the mode is actually an artifact of the disturbance profile applied at the truncated boundary. Traveling along the boundary layer edge, the amplitude of the fluctuations carried by the acoustic waves grows exponentially simply due to the gaussian spread of the forcing amplitude. The path of a characteristic originating around the maximum in the forcing function is shown as the solid black line in Figure 5.10.

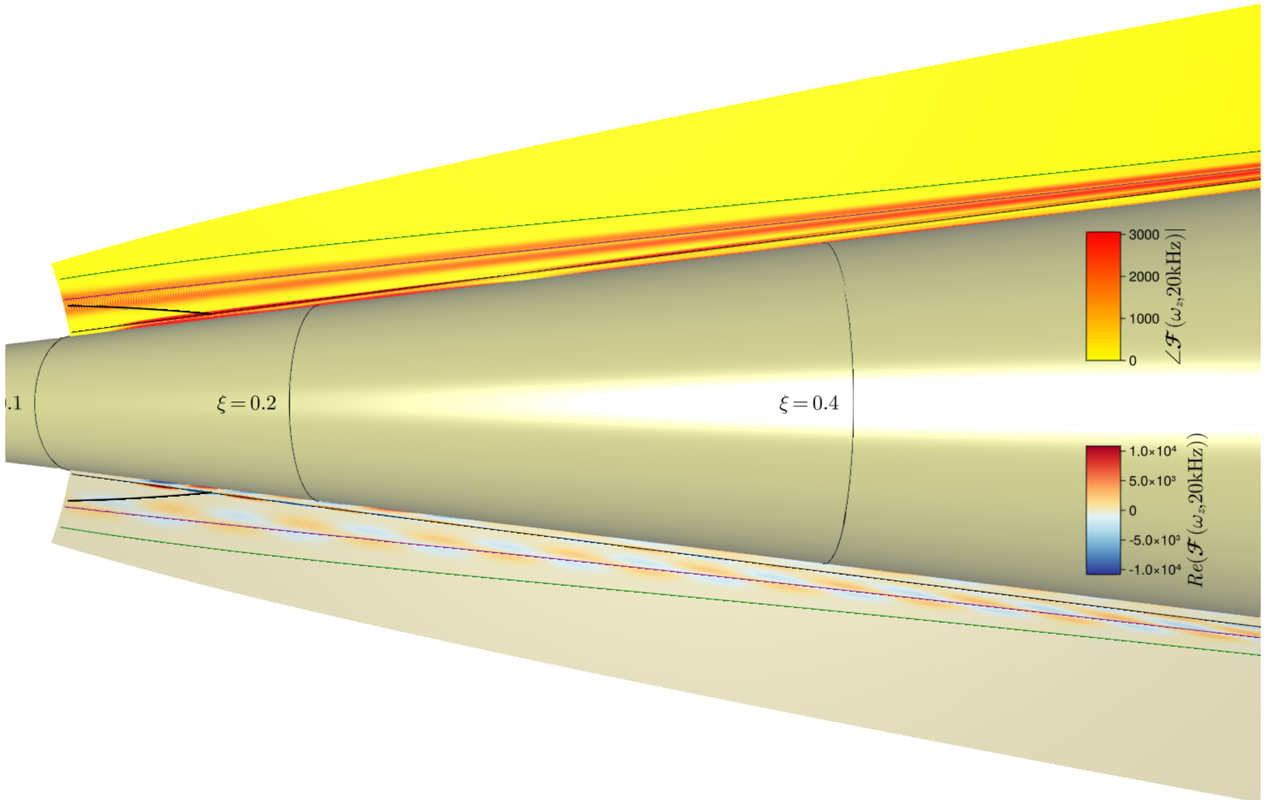

Figure 5.10: Amplitude (top) and real part (bottom) of the 20kHz Fourier field of the vorticity in the axisymmetric plane. There is a significant response to the forcing in the boundary layer, which is amplified for a short distance downstream as opposed to the content generated directly by the forcing which is damped. The solid black line shows the path of a characteristic from the epicentre of the forcing function to the edge of the boundary layer.

The Fourier coefficient along the boundary layer edge compared to the location at which the characteristic originating from the epicentre of the forcing function in Figure 5.11 supports this conclusion that the "instability" is not actually so. The amplitude of the fluctuations increases by orders of magnitude over the space of two wavelengths and reaches the peak amplitude at the location where the characteristic enters the boundary layer. The exponential growth seen here is the acoustic waves originating from points ever close to the epicentre of the forcing function hitting the edge of the boundary layer and inducing vorticity proportional to their initial amplitude. It seems that any vortical disturbances associated with the inflection point are at the very most weakly unstable, and likely stable, in agreement with linear theory.

These results do not directly provide an explanation for the experimental results of Stetson et al. [85] where the maximum in the fluctuations was associated with the inflection point. However, if the conclusions reached regarding the nature of the density fluctuations under the theory of Lees and Lin, particularly that the fluctuations are associated with neutral waves associated with the inflection point, then the three dimensional disturbances should have

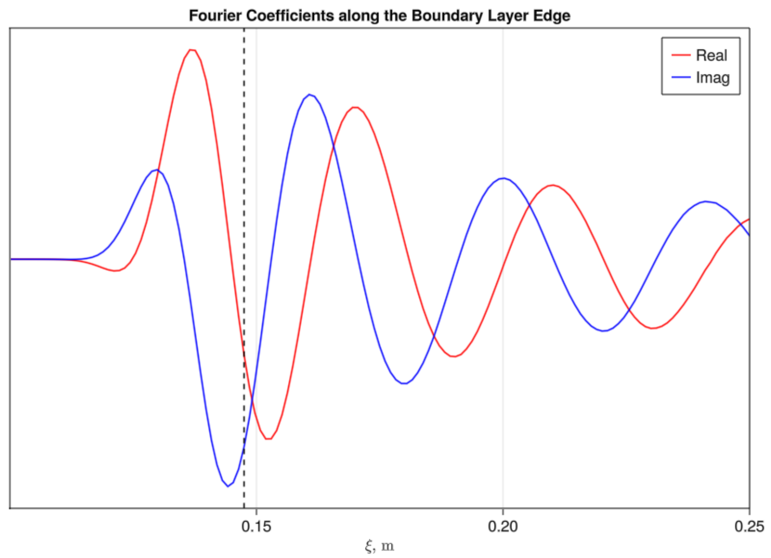

Figure 5.11: Fourier coefficient of the 20kHz vorticity mode along the edge of the boundary layer. The dashed line denotes the location where the characteristic from the epicentre of the disturbance enters the boundary layer.

the maximum in amplitude at the inflection point. This is because the phase speed of the three dimensional waves will have a non-zero spanwise wavenumbers, and so the phase speed cannot equal the mean velocity. In this instance, the transport of angular momentum across the inflection point can be non-zero and there cannot be a discontinuity in phase. The following three dimensional simulation were performed to test this hypothesis.

5.2 Three-Dimensional Domain

The three dimensional simulation was performed on the same streamwise domain, with an spanwise extent of six degrees discretized by 60 cells. The justification for this specific choice of spanwise extent is that it is unlikely that the size of the spanwise structures would be larger than 6 degrees based on experimental evidence. AUSMDV convective fluxes were used for this simulation due to the stability issues mentioned in Section 4.1.4. The inflow forcing is that described in Equation 5.2, with the magnitude reduced by a factor of 10 relative to the axisymmetric simulations to remain in the linear regime. Using the original forcing magnitude, non-linear effects became noticeable and caused numerical stability issues. The forcing function is gaussian in the spanwise direction, so will contain content in all resolved spanwise wavenumbers. The flow profile imposed at the beginning of the domain is rotationally extruded, and the spanwise boundary conditions are rotationally periodic. For the three dimensional domain, the in situ discrete Fourier transform is only performed for the density due to data management considerations.

The instantaneous density fluctuations along the $\zeta = 0$ centreline were compared to the same quantity from the axisymmetric simulations, shown in Figure 5.12. The amplitude of the fluctuations in the three dimensional domain is scaled up by a factor of 10 to account for the reduced amplitude of the forcing function. The magnitude of the density fluctuations in the three dimensional domain were noticeably larger than those in the axisymmetric domain, despite the action of the increased numerical dissipation in the three dimensional simulations. The structures are significantly larger, indicating the fluctuations are dominated by lower frequency content.

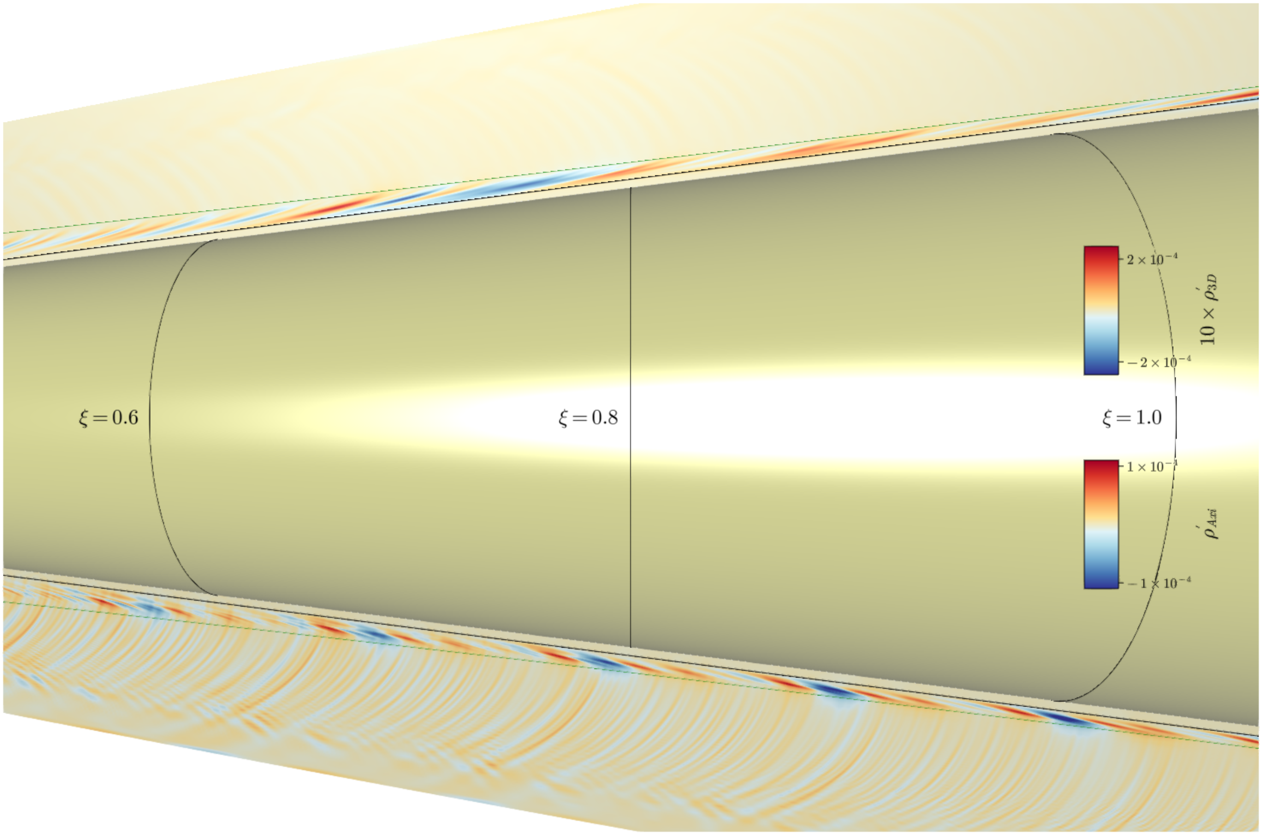

Figure 5.12: Instantaneous density fluctuations in the three dimensional simulation (top) and axisymmetric simulation (bottom). The magnitude of the fluctuations in the three dimensional simulation are increased by a factor of 10 to account for the lower forcing amplitude.

The Fourier transform is applied in the spanwise direction to break down the fluctuations into their three dimensional components. The spanwise wavenumbers are left in terms of their wavenumbers relative to the mesh, so a wavenumber of 0 denotes the axisymmetric mode, the $k_\zeta = 1$ has wavelength equal to the domain span, $k_\zeta = 2$ half the domain span and so on. Given the dissipative numerical scheme used, only the spanwise wavenumbers resolved by 8 cells or more (i.e. the first 7 spanwise wavenumbers) are included as the higher wavenumbers are likely to be artificially damped too much to be at all reliable. This is not to say that the retained wavenumbers are unaffected by numerical dissipation, simply that the resolution is enough such that some useful qualitative statements may be made regarding the physics. The peak relative magnitude of the density fluctuations for the frequencies and included spanwise wavenumbers in Figure 5.13 indicate that low frequency content dominates the solution, in qualitative agreement with the shape of the density fluctuations.

To characterize the behaviour of these low frequency disturbances, the 10kHz and 40kHz

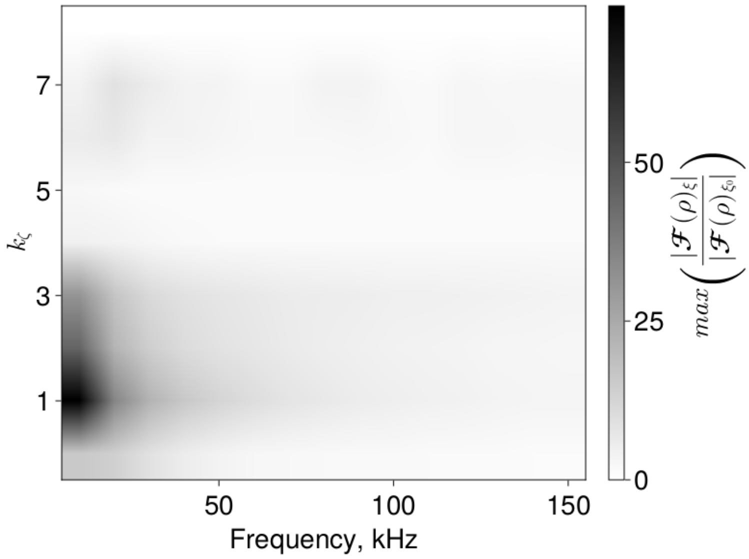

Figure 5.13: Peak relative amplitudes of the density fluctuations for the axisymmetric and first 8 spanwise modes. The low frequency three dimensional disturbances dominate the solution.

modes were chosen to investigate further. The streamwise variation of the relative amplitudes in Figure 5.14, calculated in the same manner as in the axisymmetric simulation, shows that the growth rate of the disturbances in the three dimensional domain is transient. The three dimensional disturbances do not undergo the same periodic modulation of the amplitude observed in axisymmetric disturbance.

The three dimensional modes grow significantly more than the axisymmetric mode. The amplitude also peaks significantly earlier for all frequencies. The location where the response is strongest is at the location of the generalized inflection point for the three dimensional modes, as opposed to the axisymmetric modes which were located between the inflection point and the edge of the entropy layer. The magnitude of the Fourier field of the axisymmetric mode and the first 2 spanwise modes at 10kHz is shown in Figure 5.15.

The linear stability of the generalised inflection point has been investigated in the context of blunted flat plates [96, 97] and blunt cones and wedges [81], and each came to the conclusion that the inflection point instability was only weakly unstable to two dimensional (i.e. planar/axisymmetric) disturbances, in accordance with the broader theory of Kelvin-Helmholtz type instabilities. But these disturbances are transient in nature, so cannot correspond directly to the instabilities predicted in these analyses, even if the three dimensionality were neglected.

The phase speed of the three dimensional disturbances in the streamwise direction is the same in the axisymmetric disturbances. The reason that the three dimensional disturbances have the peak amplitude at the inflection point, as opposed to a minimum for the axisymmetric disturbances, is that the phase speed now has a spanwise component so it is not equal to the mean velocity. Additionally, the three dimensional modes do not show the same discontinuity in the phase as the axisymmetric mode as demonstrated by the real part of the 40kHz Fourier

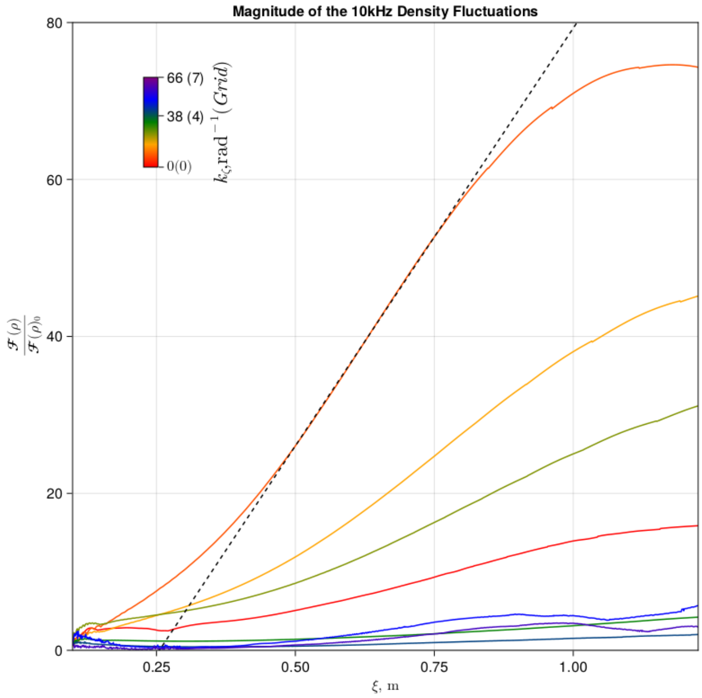

(a) 10kHz disturbances.

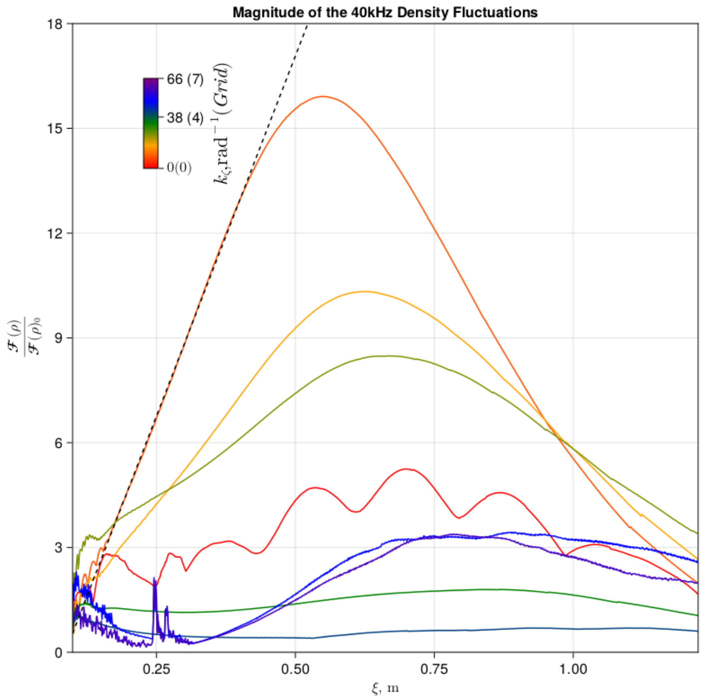

(b) 40kHz disturbances.

Figure 5.14: Relative amplitudes of the density fluctuations for the axisymmetric and first 7 spanwise modes. The legend shows the absolute spanwise wavenumber in units rad^{-1} and the grid wavenumber in brackets. The linear trends shows the growth is transient in nature, and the first spanwise modes grow significantly more than the axisymmetric mode.

field in Figure 5.16. The three dimensional simulations support the conclusions reached by the axisymmetric simulations, that the disturbances are formed of sonic or supersonic neutral waves.

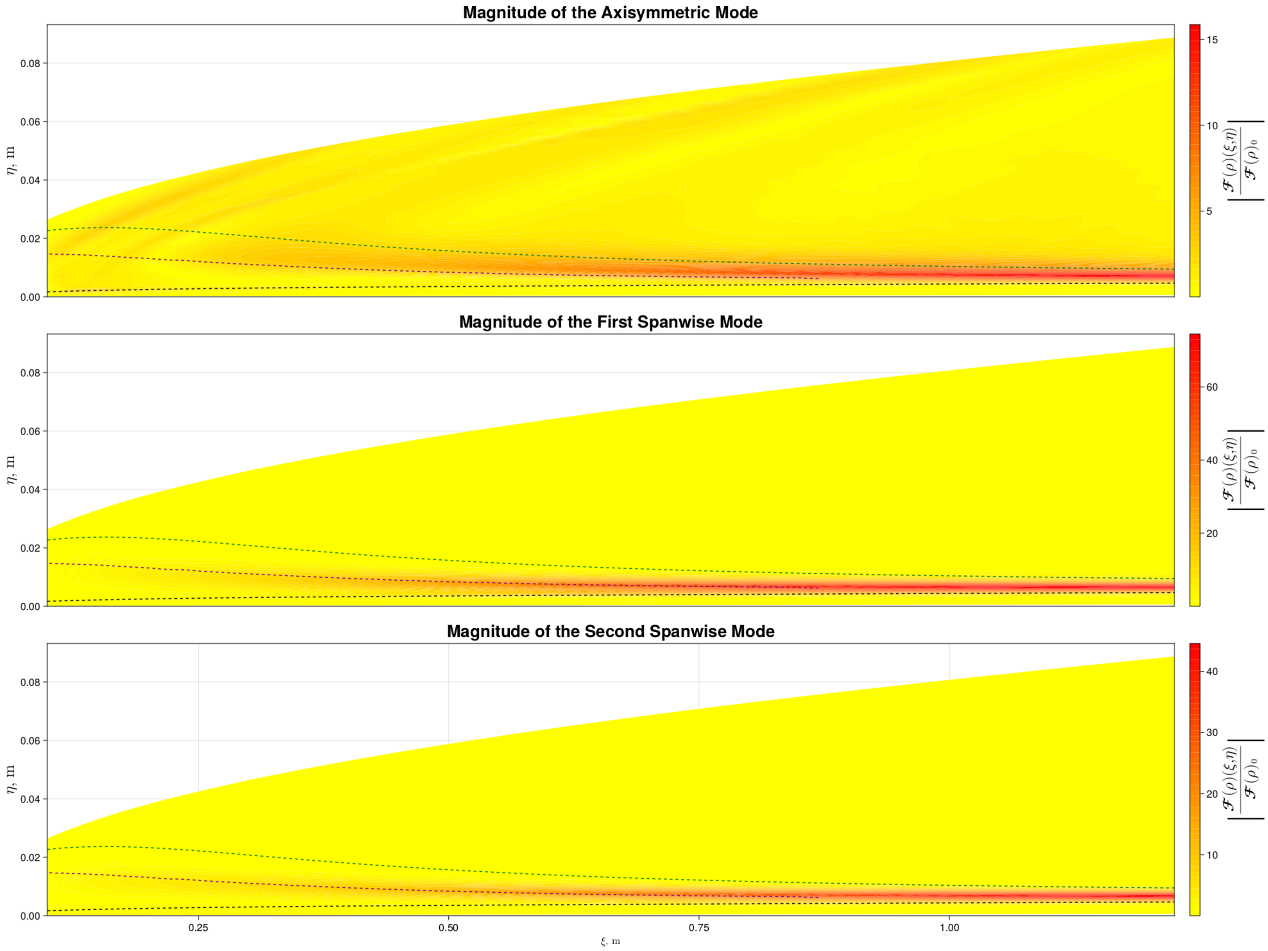

Figure 5.15: Magnitude of the axisymmetric (top), first (middle) and second (bottom) spanwise density Fourier modes at 10kHz. The axisymmetric mode peaks between the entropy layer and the inflection point, while the three dimensional modes are maxima at the inflection point. Black and green dashed lines denote the boundary and entropy layer edges, with purple denoting the location of the inflection point.

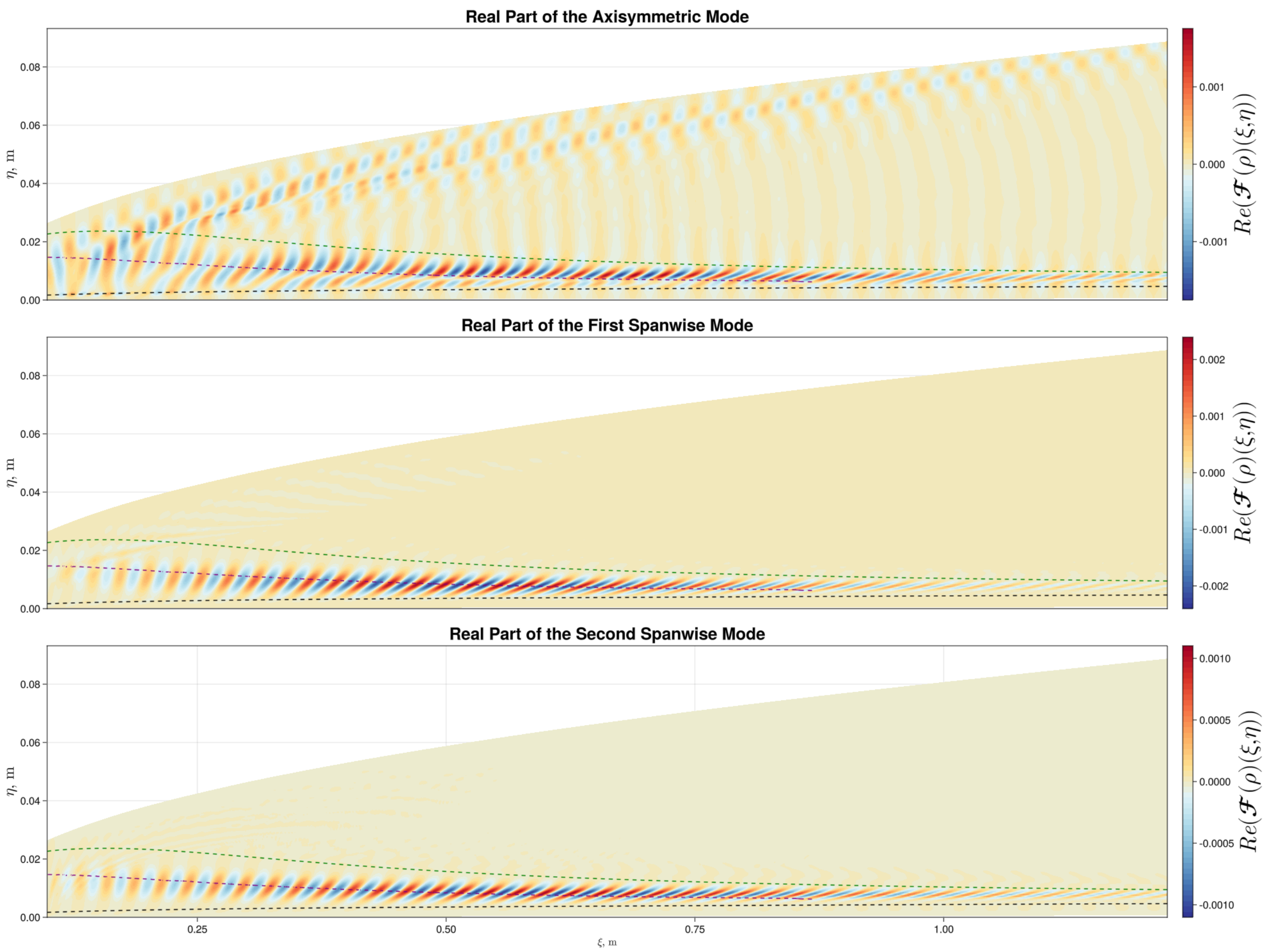

Figure 5.16: Real part of the axisymmetric (top), first (middle) and second (bottom) spanwise density Fourier modes at 40kHz. The axisymmetric mode demonstrates the same discontinuity in the phase as in the axisymmetric simulations, while the three dimensional modes have continuous phase.

To make qualitative comparison to the measurements of Stetson et al. [85], the RMS of the density fluctuations for the 3 dimensional and axisymmetric domains were computed and compared to the angular momentum distribution in Figure 5.17. The measurements are taken at the same location as those in the original work (Figures 10c-e), at streamwise locations of $\xi/R = 30, 38, 46.5$. The wallnormal angular momentum profiles are different, likely due to incorrect modelling of the wall temperature, but the quantitative comparison desired is that of the peak fluctuations relative to the inflection point. The peak in the RMS fluctuations is at the inflection point in the 3 dimensional domain, but not for the axisymmetric domain. Thus the phenomena observed by Stetson et al. were three dimensional in nature.

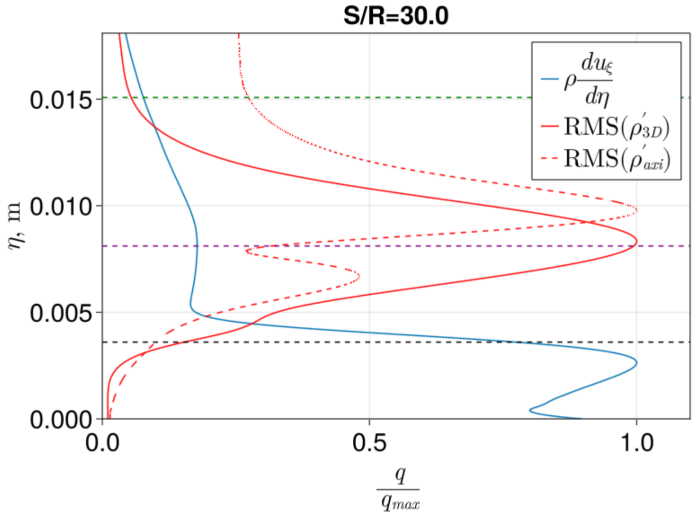

(a) RMS density fluctuations at $\xi/R = 30$.

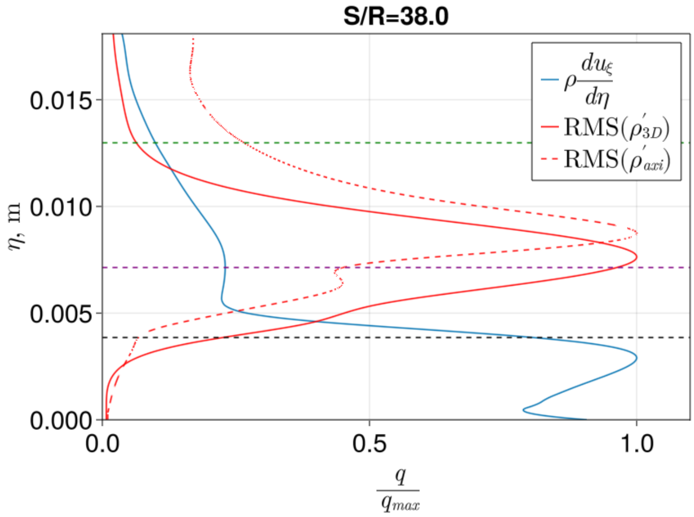

(b) RMS density fluctuations at $\xi/R = 38$.

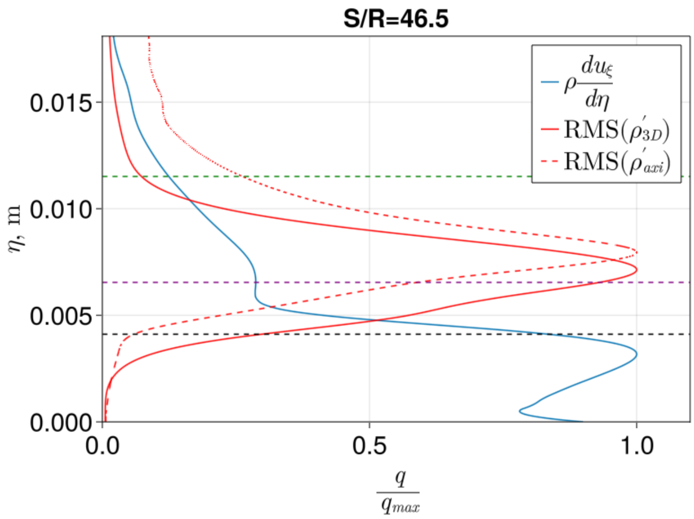

(c) RMS density fluctuations at $\xi/R = 46.5$.

Figure 5.17: RMS density fluctuations in the axisymmetric and three dimensional domains, taken at the same location as the measurements of Stetson et al. [85] in Figures 10c-e. The peak in fluctuations is at the inflection point in three dimensional simulation, but not the axisymmetric simulation, suggesting the phenomena observed by Stetson et al. were three dimensional in nature.

5.3 Relationship with other Numerical and Experimental Results

There is little value in only recounting numerical results without discussing how said results fit into the larger picture of boundary layer transition, specifically on blunt cones. The first topic addressed is that on the mechanism by which these disturbances may lead to transition. The transition process requires the breakdown of the coherent structures into the cascading series of ever smaller eddies and the randomness associated with true turbulence. This requires an increasing rate of energy exchange between the mean flow and the fluctuations, a means to convert the entropy fluctuations to kinetic energy fluctuations, and a means for the fluctuations to enter the boundary. The rate of change of the fluctuation energy in Equation 5.8 clearly provides such a mechanism for the ever increasing cascade of energy, with the dependence of the fluctuation energy on the magnitude of the entropy fluctuations.

The easiest way to illustrate that the entropy fluctuations can give rise to changes in the kinetic energy is by simply considering the perfect gas equation for density from Chu [165] given by

$$\frac{\rho}{\rho_0} = \left(\frac{p}{p_0}\right)^{\frac{1}{\gamma}} e^{\frac{S'}{C_p}} \tag{5.9}$$

with the 0 subscript denoting the total. It is clear that changes in density can be driven by either the compression work done by the pressure change or by heat exchange through the change in entropy. If the density is changing, then this leads to a change in the fluid motion due to the coupling of the density and velocity through the continuity equation. By this mechanism, energy can pass from the fluctuation potential energy to the fluctuation kinetic energy and lead to a breakdown of the laminar mean flow. However, the rate of heat conduction in gases is generally quite small, so this exchange between entropy fluctuations and kinetic energy fluctuations is typically small unless the fluctuations are high frequency, or the fluctuations are very large amplitude.

The fluctuations are clearly not of high frequency, at least with respect to the typical timescales of interest in hypersonic flows. The growth rate of the entropy fluctuations observed in the simulations results in relative amplitudes much lower than typically associated with turbulent breakdown for first and second mode phenomena. Typically N factors between 5 and 10 are associated with turbulent breakdown due to these boundary layer modes in tunnel scenarios, depending on the noise level, which corresponds to relative amplitudes of 10^2 to 10^4. The upper limit for the relative disturbance amplitudes in these simulations of order 10^2 for the three dimensional disturbances, and the frequency is much lower, so the amplitude of the lower frequency entropy layer phenomena would have to be larger amplitude to initiate non-linear behaviour and breakdown compared to the boundary layer modes.

This is likely true, but when the spectrum of the noise in these hypersonic wind tunnels is considered, transition via this mechanism appears more feasible. There are many sources of noise in tunnels, including tunnel wall roughess effects, acoustic radiation from the wall boundary layer and unsteadiness in the driving gas. Numerous works have attempted to characterise the noise in hypersonic tunnels, and the dominant source appears to be related to turbulent effects, likely from the wall boundary layer, illustrated by Figure 5.18 from Duan et al. [113]. The magnitude of the acoustic disturbances in the tunnel freestream, measured by pitot probe, follow the classic turbulent energy cascade so low frequency disturbances apparently relevant to these entropy layer fluctuations (10^4Hz) are an order of magnitude or more larger than those associated with modal instabilities (10^5Hz). The disturbance amplitudes relative to the starting amplitude is lower for these low frequency disturbances, but their initial amplitudes are significantly higher. These are only acoustic fluctuations, but the processing of any type of fluctuations, acoustic, vortical or entropy, will generate all three types when passing through a shock.

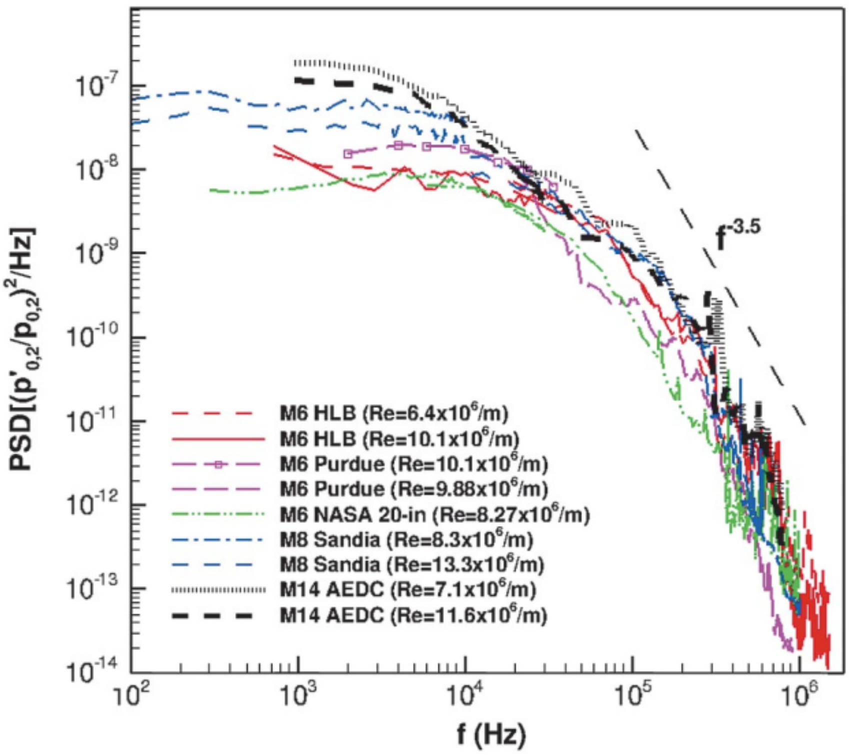

Figure 5.18: Measurements of freestream pressure fluctuations measured in a series of tunnels at varying Mach and Reynolds numbers from Duan et al. [113]. Shape is similar to the classic turbulent energy cascade, so lower frequency fluctuations have larger amplitude.

Experimental observations of entropy layer structures are distinctly different to observations of the boundary layer modal phenomena, particularly the rope-like structures associated with the second mode, in that they not periodic. The structures associated with the second mode are spatially periodic, at least locally, an example of which is shown in Figure 5.19. The structures in the entropy layer are sporadic and generally do not display the same spatial coherence as the boundary layer modes, with an exceptional example of this in Figure 5.20.

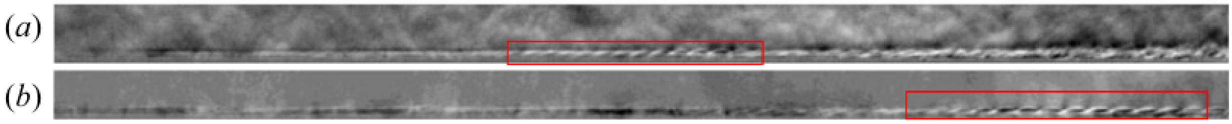

Figure 5.19: Schlieren images highlighting the rope-like structures associated with the 2nd mode on (*a*) 0.508mm and (*b*) 1.524mm nose radius cones in Mach 6.14 flow with a freestream Reynolds number of $13.7\times10^6\mathrm{m}^{-1}$ and $18.3\times10^6\mathrm{m}^{-1}$ respectively from Kennedy et al. [93]. Boxes show the locations of the second mode structures.

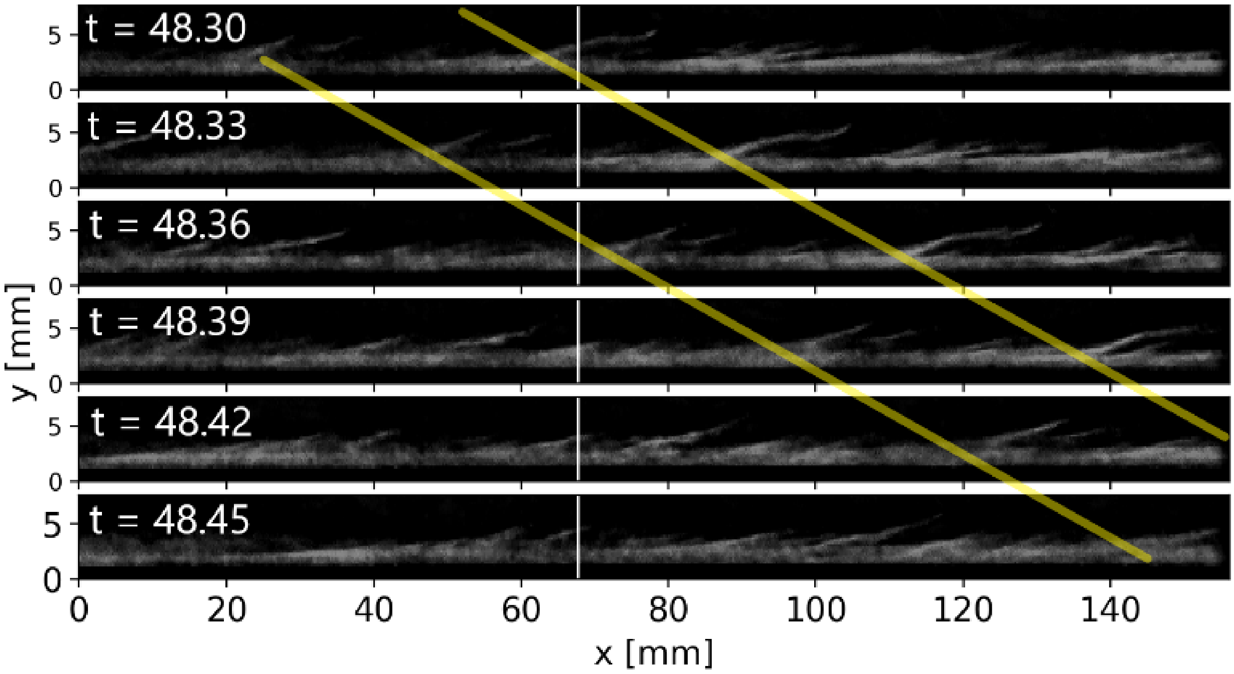

Figure 5.20: Schlieren image of entropy layer structures extending outside the boundary layer on a 5.08mm nose radius cone in Mach 6.14 flow with a freestream Reynolds number of $25\times10^6\mathrm{m}^{-1}$ from Berger and Borg [166].

The sporadic nature of these entropy layer structures could be due to entropy spots in the freestream, caused by non-uniformity in the test gas and exacerbated by the nozzle expansion. These entropy spots are sproradic, so their passing would generate a temporary distortion of the mean flow field and a large response from low frequency phenomena as predicted by these simulations. So there is a clear mechanism for high amplitude disturbances to enter the entropy layer with temporal behaviour that matches experimental measurements.

Finally, there must be a mechanism for the disturbances to enter the boundary layer. Clearly the disturbances move towards the wall as the entropy layer thins downstream, as well as the boundary layer thickening due to viscous action. When the density disturbances enter the boundary layer, they will be rapidly distorted due to the strong velocity gradient. The density structures will tilt further in the streamwise direction, and the resulting effect on the flow velocity from the continuity equation would generate further shear stresses and progress the breakdown to turbulence. This hypothesis is supported by the direct simulations of non-linear breakdown of Hartman et al. [107], where similar density structures entering the boundary layer support secondary instability mechanisms and rapidly progress towards turbulence. Based on these results, these entropy layer disturbances meet all the criteria necessary for a given disturbance to be a possible cause of transition.

5.3.1 Concluding Remarks

These simulations demonstrate that the entropy layer is susceptible to transiently growing entropy disturbances. The axisymmetric disturbances saw a minimum in amplitude and a discontunity of the phase of the disturbances at the inflection point. This indicates the disturbances consist of neutral supersonic waves with phase speed equal to the mean velocity at the inflection point indicating the disturbances consist of neutral waves associated with the inflection point according to the theory of Lees and Lin [5]. The three dimensional simulations further support this theory, as the three dimensional disturbances reach maximum amplitude at the inflection point and have no phase discontinuity here. The phase speed of these disturbances have a spanwise component, so can not have the same velocity as the mean flow.

The disturbance energy equation from Chu [165] provides a mechanism for these entropy fluctuations to fuel further transfer of energy from the mean flow to the disturbances. But for a given disturbance to cause transition, it requires transfer of energy to the disturbance kinetic energy. The entropy fluctuations can be converted to kinetic energy fluctuations through the continuity equation. Further, the density gradients created by the entropy disturbances can support secondary shear instabilities as evidenced by the simulations of Hartman et al. [107].

The unstable frequency range for these disturbances is under 100kHz, about an order of magnitude lower than typical second mode frequencies, and as such is expected to need higher amplitudes to cause transition. The noise in typical tunnel environments is orders of magnitude larger in this lower frequency range compared to the second mode unstable range, providing a potential origin for larger amplitude disturbances. These simulations, put in context with other works on the topic, provide solid evidence that the entropy layer disturbances exist and could lead to transition in the boundary layer.

Chapter 6

Conclusions

6.1 Method Development and Verification

The finite volume computational fluid dynamics software Eilmer, which was used for this project, was improved via the addition of a high order method for the convective fluxes.T he Summation-by-Parts Alpha-Split Flux (SBP-ASF) convective flux scheme, originally derived in a dual grid finite difference context, was successfully implemented within the software. The scheme was verified as fourth order accurate when applied in a finite volume context. The method of Takacs [117] for splitting numerical errors into dissipation and dispersion errors was applied to the canonical isentropic vortex advection test case to characterise the accuracy of convective flux schemes in more detail. The SBP-ASF method showed fifth order convergence for the dissipation error and fourth order dispersion error. The performance of approximate Riemann schemes, overwhelmingly popular in finite volume codes, was limited to second order accuracy even when reconstructing the left and right Riemann states with higher order polynomials. The dissipation error was found to be in general equal to the order of the reconstructing polynomial, but the dispersion error was limited to second order preventing approximate Riemann schemes from achieving high order accuracy and highlighting the need for true high order schemes for Direct Numerical Simulations (DNS).

A test problem was extended to function as a pseudo Modified Wavenumber Analysis. The Steepening Wave problem, first introduced by Landau and Lifshitz [141], is a one dimensional problem where an initially sinusoidal flow profile steepens to form a shock due to the varying characteristic speed across the profile. The steepening of the wave is represented in the spatial Fourier domain by the appearence of successively higher wavenumbers. Given the exact solution is known at any point, numerical and exact solutions can be compared in the spatial Fourier domain to determine the effect of numerical dissipation on respective wavenumbers in a similar fashion to a Modified Wavenumber Analysis, but much simpler to apply to schemes which are algebraically complex. This test case determined that the SBP-ASF scheme required 4 cells to accurately resolve a wavelength, compared to ~10 for the approximate Riemann schemes, even without the action of limiters.

6.2 Findings from Direct Numerical Simulations

The study of instabilities in the entropy layer was carried out on the geometry and flow conditions used in Stetson et al. [85] in which an instability was measured using hot wire anenometry at the generalised inflection point, the point of maximum angular momentum, in the entropy layer. The geometry is a 7° half-angle circular cone with a 17.78mm (0.7in) nose radius, hosted in the AEDC tunnel B with freestream Mach number and unit Reynolds number of 7.99 and $8.202 \times 10^6 \mathrm{m}^{-1}$. The frustum length of the cone was extended in the simulations relative to the experimental setup to 1.2m, as the measured instability has begun to amplify toward the end of the model so this region was likely to be of interest. Surface pressure measurements found no evidence of unstable first and second boundary layer modes, typical in hypersonic flow, making this an ideal case for isolating the entropy layer phenomena.

6.2.1 Workflow for Base Flow Generation in Eilmer

The steady base flow was built using multiple stages. First, shock fitting simulations with multiple stages of mesh refinement were used to define the location of the shock and approximate the boundary layer thickness to assist the generation of high quality meshes for the proceeding high fidelity simulations. The GridPro mesh generation software [151] was used to generate a high quality mesh for the full domain simulations. A Newton-Krylov convergence acceleration method [156] was used to generate the steady base flow field. To this point, the AUSMDV [137] approximate Riemann solver was used for the convective fluxes due to stability considerations.

Before high fidelity, time accurate simulations using the SBP-ASF convective flux scheme could begin, a steady base flow using the SBP-ASF scheme was generated. The SBP-ASF scheme was augmented with the AUSMDV scheme at shocks, with the shock points detected using a velocity-based sensor. There were numerous stability issues encountered when utilising the Newton-Krylov acceleration scheme with the SBP-ASF scheme. It was known that high-order central schemes, of which the SBP-ASF scheme is one, have issues with implicit temporal schemes as the construction of the flow Jacobian is not guaranteed to have diagonal dominance [125]. The specific implementation of the Newton-Krylov within the Eilmer flow code is specifically a Jacobian-free method, so it was unclear how the central scheme would interact with such a scheme. The problem was addressed by constructing the preconditioner, which serves to augment the iteration procedure used to solve the linear system, with one of the approximate Riemann schemes without state reconstruction i.e. a high dissipation, robust flux method.

The second numerical issue encountered was the with switching from the AUSMDV convective fluxes to the SBP-ASF fluxes. Beginning immediately from the SBP-ASF scheme is generally not appropriate, as the scheme lacks the numerical dissipation required to be robust to start-up phenomena. This issue was addressed by converging the solution using a robust scheme (AUSMDV in this case), then ramping up the SBP-ASF contribution to the net convective flux linearly, and the AUSMDV contribution down at the same rate, as described in Equation 4.3.

Using the augmented Newton-Krylov scheme, a steady base flow was generated on the truncated domain that began downstream of the nose-frustum join, at a distance of 0.1m measured along the cone surface. The inflow boundary for the truncated domain was generated using the prior full domain steady solution. The forcing used for the simulations on this reduced domain were applied at the truncated boundary rather than the freestream, as the freestream streamlines would not enter the entropy layer. A series of discrete frequency disturbances that are gaussian-shaped in the wall normal (and spanwise in three dimensions) direction are applied in the entropy layer to excite the entropy layer disturbances, with particular focus on the generalised inflection point. The magnitude of the disturbances is kept small to investigate the linear behaviour of the disturbances. The discrete Fourier transform was performed in situ during the simulation to facilitate investigation of the fluctuation spectra.

6.2.2 Findings from Time-Accurate Simulations

Preliminary time accurate full field simulations were performed to scope a follow on set of refined simulations. The maximum stable time step restrictions due to the subsonic region around the the nose of the cone makes fully resolved full-field simulations infeasible with the computational resources available to the project. These simulations were forced with small white noise disturbances added to the freestream quantities, similar to the method utilised by Johnston [130] in simulations of the Boundary Layer Turbulence II flight experiment. These simulations used the AUSMDV method for the convective fluxes and was expected to be under-resolved, but the intention of the simulations was only to determine appropriate starting locations for reduced domain simulations and verify that phenomena in the entropy layer dominate the solution. In this context, the full-field simulations were successful and verified that the entropy layer is susceptible to growing density fluctuations as demonstrated by Figure 6.1. Additionally, the phenomena in the nose region had minimal effect on the qualitative behaviour downstream, so the subsequent approach of truncating the domain downstream of the nose-frustum join was justified.

For the axisymmetric simulations, the dominant response was in the density fluctuations in 20-80kHz frequency range with negligible response in the pressure and vorticity fluctuations, in agreement with experimental observations Stetson [85]. The growth of the the fluctuations

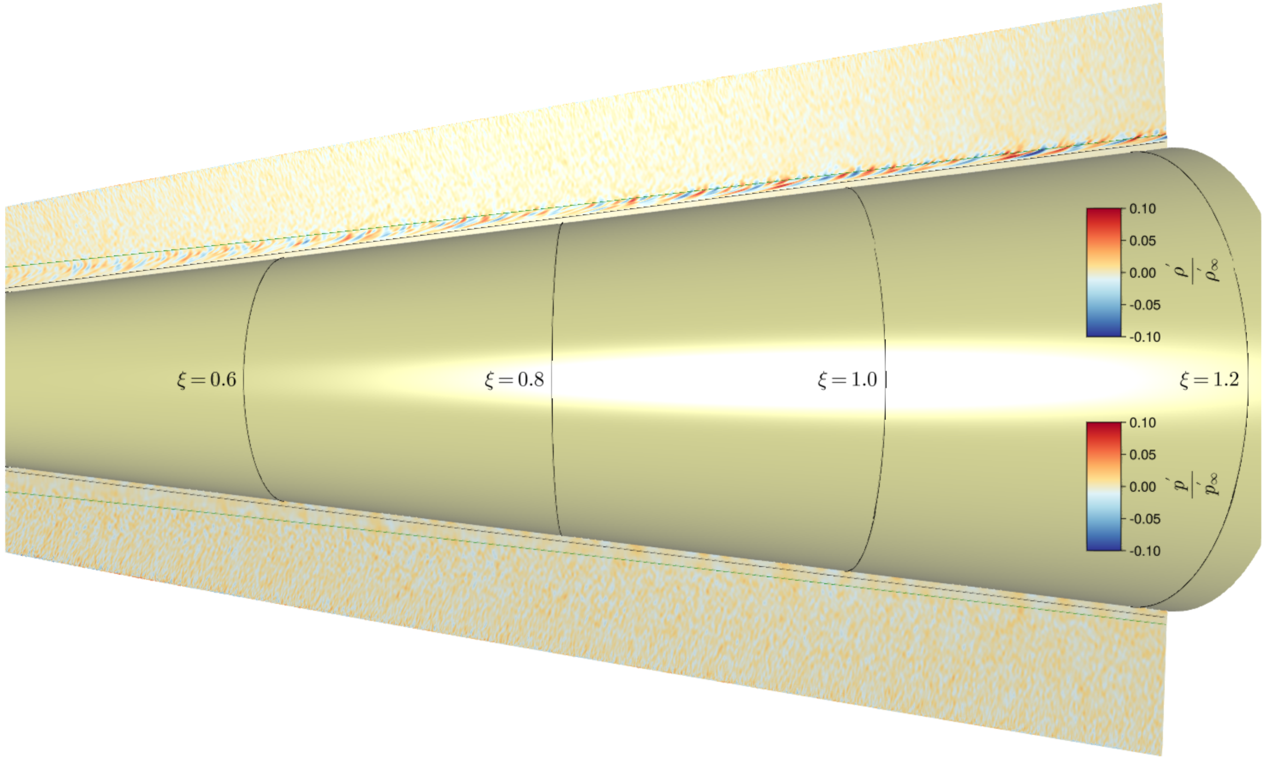

Figure 6.1: Instantaneous density (top) and pressure (bottom) fluctuations in the frustum with white noise forcing in the freestream.

matched the transient growth trend of linear amplification followed by exponential decay, and the amplitude of the wall normal fluctuation profile peaked either side of the inflection point, with a local minimum at the inflection point. The phase speed of the fluctuations was equal to the mean flow velocity, causing the tilting of the density structures illustrated in Figure 6.2. The observations are explained by the theory of Lees and Lin [5] if the waves are sonic or supersonic (in their nomenclature, this with respect to some freestream velocity) neutral waves. The theory also predicts a discontinuity in the phase at the critical point where the phase speed equals the mean velocity, which is clearly evident at the generalised inflection point in the upstream region in Figure 6.2. These waves have a continuous spectrum of eigenvalues, which is required for transient growth phenomena [10]. Given that the disturbances have a strong signature in the density response and effectively no response in the pressure or vorticity, the fluctuations must then be entropy waves [159].

The maximum of the density (entropy) disturbances is associated with the minimum in the entropy gradient. This is in agreement with the result of Nicoud and Poinsot [164] which states that the rate of total entropy fluctuation energy should be proportional to the negative of the entropy gradient. This term is often neglected in energy considerations as in boundary layers over flat plates and sharp cones because the entropy gradient is zero and so this term is zero. This is not the case for flows over blunt cones, as the entropy generated by the flow passing through the shock is dependent on the local shock angle, thus any flow

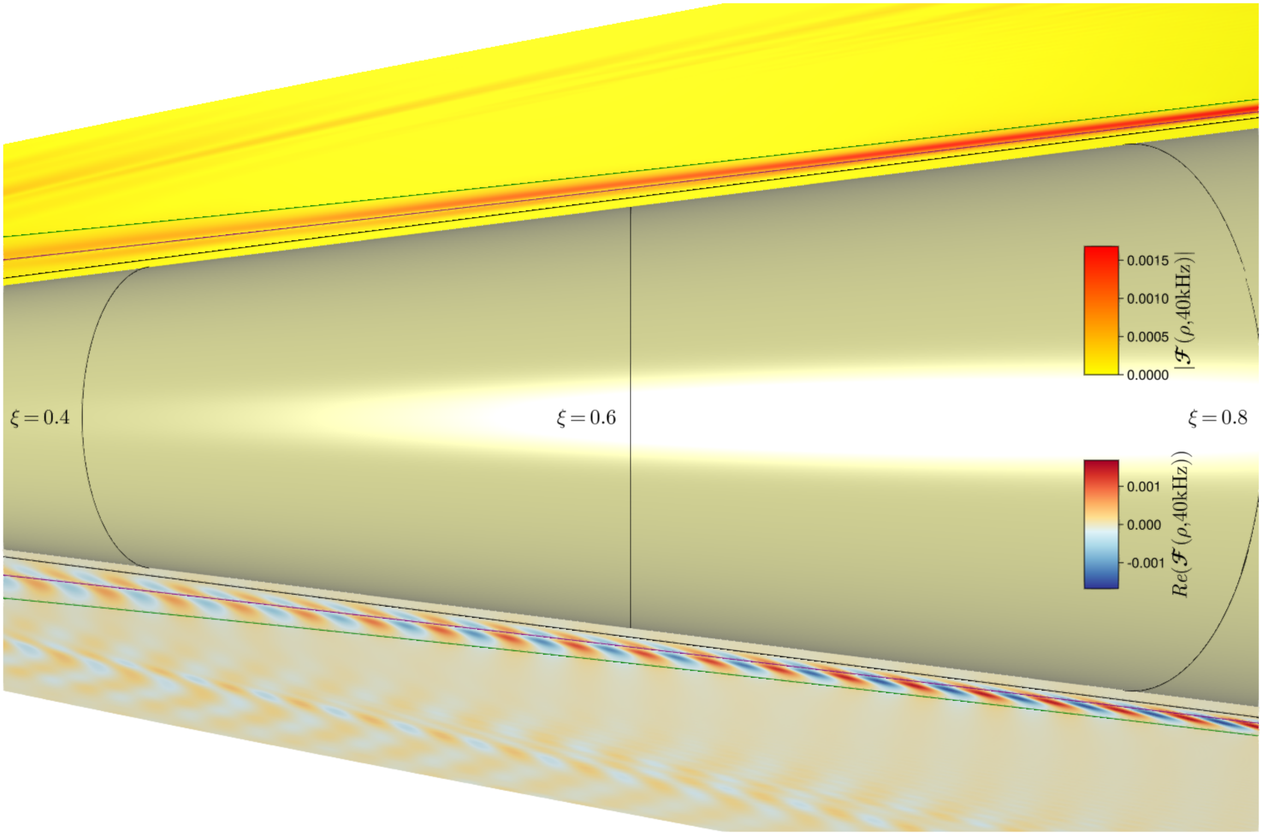

Figure 6.2: Magnitude (top) and real part (bottom) of the density field associated with the 40kHz temporal Fourier mode. The disturbances travel with the mean flow so tilt in the streamwise direction due to the velocity gradient. The magnitude is a local minimum at the inflection point in the upstream region, and there is a continuity in the phase at the same location indicating the waves are sonic or supersonic neutral waves.

passing through a curved shock will generate an entropy gradient.

The hypothesis that the observed waves are neutral waves as described by Lees and Lin is supported by the three dimensional simulations. In three dimensions, the waves with non-zero spanwise wavenumber (so non-zero spanwise phase speed) do not have phase speed equal to the mean velocity. This means the inflection point is no longer a critical point, so there should be no discontinuity in phase or local minima in the fluctuation amplitudes which was shown to be true. Finally, feasible mechanisms for the conversion of the fluctuations in entropy to fluctuations in the kinetic energy required for the breakdown of laminar boundary layer are presented, which qualitatively agree with the simulations of non-linear breakdown due to entropy layer disturbances from Hartman et al. [107].

6.3 Contributions of this Work

This work demonstrates the feasability of using high-order dual-grid finite difference schemes in a structured finite volume code. The Steepening Wave problem is extended to act as a pseudo Modified Wavenumber analysis, particularly useful for analysing schemes that are algebraically complex and difficult to apply the classic Modified Wavenumber analysis to.

The workflow for direct numerical simulations of the linear stages of the transition process in the Eilmer flow code is described in detail. The process can be extended to the simulations in the non-linear regime, with sufficient adjustment of resolution to accurately capture non-linear effects. The Newton-Krylov method is adjusted to improve stability with high order schemes.

Full field simulations confirm that the entropy layer over a hypersonically traveling blunt cone is receptive to density disturbances. The disturbances consist of transiently growing entropy waves, which fall under the classification of supersonic neutral waves in the theory of Lees and Lin [5]. The waves are associated with the generalised inflection point in the entropy layer. These insights improve our physical understanding of transition in the maximum transition delay regime.

6.4 Further Work

The clearest path to further this work is to extend the simulations into the non-linear regime. Unfortunately, the Eilmer software is not the ideal candidate for this work. Some of Eilmer's strengths are its generality and useability, which come at the cost of computational efficiency. Three dimensional non-linear direct simulations are likely to be out of reach for the compute resources available to the research group for the near future.

The alternative is to apply linear techniques, such as the Parabolized Stability Equations (PSE) or One-Way Navier Stokes (OWNS) equations. The Newton-Krylov steady-state accelerator permits the generation of high-quality base flows, required for the application of such linear techniques. Given the possibility of multiple disturbances being present in the entropy layer, OWNS is an ideal candidate for this work. The growth mechanisms are transient, so the problem becomes an initial value problem, lending itself to optimisation as in optimal growth work.

The sensitivity of the problem to the initial disturbance shape poses a problem when comparing computational and experimental results. There has been some work in characterising the disturbances in the freestream in wind tunnels, which has yielded insight into the amplitude and spectrum of acoustic disturbances. The shape of disturbances is significantly more difficult to characterise due to point nature of most measurement techniques. Before quantitative comparisons can be made between experimental and computational results, more detail on the freestream is required. Without such comparisons, development of transition models is exceptionally difficult which is the ultimate goal of studies such as this.

Bibliography

[1] L. Whyborn, R. Gollan, P. Jacobs, Quantitative comparison of numerical errors for high-speed flux schemes, in: Proceedings of the 22nd Australasian Fluid Mechanics Conference, The University of Queensland, 2020.

[2] L. Whyborn, R. Gollan, P. Jacobs, Multiple instabilities in the entropy layer of a hypersonic blunt cone, in: Proceedings of the 2nd International Conference on Flight Vehicles, Aerothermodynamics and Re-entry Missions, ESA, 2022.

[3] L. Whyborn, R. Gollan, P. Jacobs, Hypersonic entropy layer instabilities forced by coherent freestream disturbances, in: Proceedings of the 23rd Australasian Fluid Mechanics Conference, AFMS, 2022.

[4] L. Whyborn, R. Gollan, P. Jacobs, Simulation of multiple instabilities in the entropy layer of a hypersonic blunt cone, in: AIAA SciTech Forum 2023, American Institute of Aeronautics and Astronautics, 2023.

[5] L. Lees, C. Lin, Investigation of the stability of the laminar boundary layer, Technical Report 1115, NACA (1946).

[6] D. S. Board, Repeart of the defense science board task force on national aero-space plane (NASP) program, Tech. Rep. ADA274530 (November 1992).

[7] J. D. J. Anderson, Hypersonic and High Temperature Gas Dynamics, McGraw-Hill, 1989.

[8] D. Masutti, Ground testing investigation of hypersonic transition phenomena for a re-entry vehicle, Ph.D. thesis, Technische Universtiteot Delft (2013).

[9] M. Van Dyke, An Album of Fluid Motion, The Parabolic Press, 1982.

[10] E. Reshotko, Transient growth: A factor in bypass transition, Physics of Fluids 13 (April 2001).

[11] M. V. Morkovin, E. Reshotko, T. Herbert, Transition in open flow systems— a reassessment, Bull. Am. Phys. Soc 39 (1994).

[12] K. Stetson, G. Rushton, Shock tunnel investigation of boundary layer transition at m=5.5, American Institute of Aeronautics and Astronautics Journal 5 (5) (May 1967).

[13] E. Softley, Boundary layer transition on hypersonic blunt, slender cones, in: 2nd Fluid and Plasma Dynamics Conference, American Institute of Aeronautics and Astronautics, 1969.

[14] N. J. Parziale, J. E. Shepherd, H. G. Hornung, Differential interferometric measurement of instability in a hypervelocity boundary layer, American Institute of Aeronautics and Astronautics Journal 51 (3) (February 2013).

[15] A. Ceruzzi, B. Callis, D. Weber, C. P. Cadou, Application of focused laser differential interferometry (FLDI) in a supersonic boundary layer, in: AIAA SciTech 2020 Forum, American Institute of Aeronautics and Astronautics, 2020.

[16] K. J. Hopkins, H. Porat, T. J. McIntyre, V. Wheatley, A. Veeraragavan, Measurements and analysis of hypersonic tripped boundary layer turbulence, Experiments in Fluids 62 (July 2021).

[17] N. N. Gibbons, K. A. Damm, P. A. Jacobs, R. J. Gollan, Eilmer: an open-source multi-physics hypersonic flow solver, Computer Physics Communications 282 (2023).

[18] W. Tollmein, On the origin of turbulence, Proceeds from the Society of Sciences in GöttingenReference translated from German (1929).

[19] W. Tollmien, A general criterion of the instability of laminar velocity distributions, Proceeds from the Society of Sciences in GöttingenReference translated from German (1935).

[20] H. Schlichting, The origin of turbulence in flow over a flat plate, Proceeds from the Society of Sciences in GöttingenReference translated from German (1933).

[21] H. Schlichting, Calculation of the incidence of small disturbances in flow over a flat plate, Journal of Applied Mathematics 13, reference translated from German (1933).

[22] H. Schlichting, Amplitude and energy distribution of small disturbances in flow over a flat plate, Proceeds from the Society of Sciences in GöttingenReference translated from German (1935).

[23] H. Schlichting, On the theoretical calculation of the critical reynold's number of a boundary layer in accelerated and decelerated flow, Journal of German AviationReference translated from German (1940).

[24] G. Schubauer, H. Skramstad, Laminar boundary-layer oscillations and transition on a flat plate, Journal of Research of the National Bureau of Standards 38 (February 1947).

[25] J. Pretsch, The stability of two-dimensional laminar flow with pressure drop and pressure rise, Tech. rep., Joint Intelligence Objectives Agency (1946).

[26] C. Gazley, Boundary-layer stability and transition in subsonic and supersonic flow, Journal of Aeronautical Sciences 20 (January 1953).

[27] A. Wazzan, T. Okamura, A. Smith, Spatial and temporal stability charts for the falkner-skan boundary layer profiles, Tech. Rep. 67086, Douglas Aircraft Company (September 1968).

[28] A. Wazzan, T. Okamura, A. Smith, The stability of water flow over heated and cooled flat plates, Journal of Heat Transfer 90 (1968).

[29] H. Emmons, The laminar-turbulent transition in a boundary layer, Journal of Aeronautical Sciences 18 (July 1951).

[30] P. Klebanoff, K. Tidstrom, Evolution of amplified waves leading to transition in a boundary layer with zero pressure gradient, Technical Note D-195, NASA (1959).

[31] C. Knapp, P. Roache, A combined visual and hot-wire anemometer investigation of boundary-layer transition, American Institute of Aeronautics and Astronautics Journal 6 (January 1968).

[32] D. Dunn, C. Lin, On the stability of the laminar boundary layer in a compressible fluid, Journal of Aeronautical Sciences 22 (7) (July 1955).

[33] L. Mack, Numerical calclation of the stability of the compressible laminar boundary layer, Tech. Rep. 20-122, Jet Propulsion Laboratory (1960).

[34] J. Buglia, Heat transfer and boundary-layer transition on a highly polished hemisphere-cone in free flight at Mach numbers up to 3.14 and Reynolds numbers up to 24e6, NASA Technical Report 955, NASA (September 1961).

[35] J. Murphy, A re-evaluation of heat-transfer data obtained in flight tests of heat-sink shield re-entry vehicles, Journal of Spacecraft and Rockets 3 (January 1966).

[36] A. von Doenhoff, E. Horton, A low speed experimental investigation of the effect of sandpaper type roughness on boundary-layer transition, Technical Report 4253, NACA (1958).

[37] A. Braslow, Review of the effect of distributed surface roughness on boundary-layer transition, Tech. Rep. 254, AGARD (April 1960).

[38] E. Van Driest, C. Blumer, Boundary layer transition at supersonic speeds- three dimensional roughness effects (spheres), Tech. Rep. 1493, Space Sciences Laboratory (August 1961).

[39] W. Gray, The effect of wing sweep on laminar flow, Technical memorandum, Royal Aircraft Establishment (1952).

[40] N. Gregory, J. Stuart, W. Walker, On the stability of three-dimensional boundary layers with application to the flow due to a rotating disk, Philosophical Transactions of the Royal Society A 248 (943) (July 1955).

[41] I. Tani, Boundary-layer transition, Annual Review of Fluid Mechanics 1 (January 1969).

[42] E. Reshotko, Boundary layer stability and transition, Annual Review of Fluid Mechanics 8 (January 1976).

[43] E. Reshotko, Boundary layer instability, transition and control, in: 32nd Aerospace Sciences Meeting and Exhibit, 1994.

[44] Y. Kachanov, Physical mechanisms of laminar-boundary-layer transition, Annual Review of Fluid Mechanics 26 (January 1994).

[45] M. Morkovin, Critical evaluation of transition from laminar to turbulent shear layers with emphasis on hypersonically travelling bodies, Tech. rep., Air Force Flight Dynamics Laboratory (March 1969).

[46] M. Morkovin, Transition at hypersonic speeds, ICASE Interim Report 1, NASA (May 1987).

[47] M. Morkovin, Recent insights into instability and transition to turbulence in open-flow systems, ICASE 88-44, NASA (August 1988).

[48] K. Stetson, Hypersonic boundary layer transition, in: Advances in Hypersonics, Springer Science, 1992, pp. 324–417.

[49] A. Fedorov, Transition and stability of high-speed boundary layers, Annual Review of Fluid Mechanics 43 (January 2011).

[50] S. Schneider, Hypersonic laminar-turbulent transition on circular cones and scramjet forebodies, Progress in Aerospace Sciences 40 (1-2) (February 2004).

[51] S. Schneider, Summary of hypersonic boundary-layer transition experiments on blunt bodies with roughness, Journal of Spacecraft and Rockets 45 (6) (December 2008).

[52] L. Mack, Boundary-layer linear stability theory, Special Report on the Stability and Transition of Laminar Flow 709, AGARD (1984).

[53] M. R. Malik, Numerical methods for hypersonic boundary layer stability, Journal of Computational Physics 86 (1990) 376–413.

[54] L. M. Mack, The inviscid stability of the compressible laminar boundary layer, Space Programs Summary 37-23, Jet Propulsion Laboratory (1963).

[55] L. M. Mack, The inviscid stability of the compressible laminar boundary layer: Part ii, Space Programs Summary 37-26, Jet Propulsion Laboratory (1964).

[56] A. E. Gill, Instabilities of "top-hat" jets and wakes in compressible fluids", Physics of Fluids 8 (1965) 1428–1430.

[57] C. Alba, K. Casper, S. Beresh, S. Schneider, Comparison of experimentally measured and computed second-mode disturbances in hypersonic boundary-layers, in: 48th AIAA Aerospace Sciences Meeting, American Institute of Aeronautics and Astronautics, 2010.

[58] T. Herbert, Parabolized stability equations, Annual Reviews of Fluid Mechanics 29:245-283 (1997).

[59] P. Andersson, M. Berggren, D. S. Henningson, Optimal disturbances and bypass transition in boundary layers, Physics of Fluids 11 (1) (1999).

[60] P. Paredes, M. Choudhari, F. Li, Blunt-body paradox and transient growth on a hypersonic spherical forebody, Physical Review Fluids 2 (5) (2017).

[61] J. O. Pralits, A. C., A. Hanifi, D. S. Henningson, Sensitivity analysis using adjoint parabolized stability equations for compressible flows, Flow, Turbulence and Combustion 65 (2000) 321–346.

[62] P. Paredes, M. M. Choudhari, F. Li, Transition delay via vortex generators in a hypersonic boundary layer at flight conditions, 2018 Fluid Dynamics Conference (June 2018).

[63] X.-C. Zhang, L.-K. Ran, D.-J. Sun, Z.-H. Wan, Optimal 'quiet' inlet perturbation using adjoint-based pse in supersonic jets, Fluid Dynamics Research 50 (4) (June 2018).

[64] A. Sinha, D. Rodriguez, G. A. Bres, T. Colonius, Wavepacket models for supersonic jet noise, Journal of Fluid Mechanics 742 (2014) 71–95.

[65] A. Towne, G. Rigas, T. Colonius, A critical assessment of the parabolized stability equations, Theoretical and Computational Fluid Dynamics 33 (2019) 359–382.

[66] A. Towne, T. Colonius, One-way spatial integration of hyperbolic equations, Journal of Computational Physics 300 (2015) 844–861.

[67] O. Kamal, G. Rigas, M. Lakebrink, T. Colonius, Application of the one-way navier-stokes (owns) equations to hypersonic boundary layers, in: AIAA Aviation 2020 Forum, American Institute of Aeronautics and Astronautics, 2020.

[68] P. Stainback, Some effects of roughness and variable entropy on transition at a Mach number of 8, in: 5th Aerospace Sciences Meeting, American Institute of Aeronautics and Astronautics, 1967.

[69] P. Brinich, Effect of leading-edge geometry on boundary layer transition at Mach 3.1, Technical Note 3659, NACA (1956).

[70] W. Moeckel, Some effects of bluntness on boundary layer transition and heat transfer at supersonic speeds, Report 1312, NACA (1957).

[71] D. Jillie, J. Hopkins, Effects of Mach number, leading edge bluntness, and sweep on boundary-layer transition on a flat plate, Technical report, NASA (1961).

[72] P. Brinich, N. Sands, Effect of bluntness on transition for a cone and a hollow cylinder at Mach 3.1, Technical report, NASA (1957).

[73] V. Lysenko, Influence of the entropy layer on the stability of a supersonic shock layer and transition of the laminar layer to turbulence, Journal of Applied Mechanics and Technical Physics 31 (6) (1990).

[74] M. Malik, R. Spall, C. Chang, Effect of nose bluntness on boundary layer stability and transition, in: 28th Aerospace Sciences Meeting, American Institute of Aeronautics and Astronautics, 1990.

[75] X. Zhong, Y. Ma, Boundary-layer receptivity of Mach 7.99 flow over a blunt cone to free-stream acoustic waves, Journal of Fluid Mechanics 556 (June 2006).

[76] J. Lei, X. Zhong, Linear stability analysis of nose bluntness effects on hypersonic boundary layer transition, Journal of Spacecraft and Rockets 49 (1) (January 2012).

[77] E. Reshotko, Transition issues for atmospheric entry, Journal of Spacecraft and Rockets 45 (2) (March 2008).

[78] G. Moretti, M. Pandolfi, Entropy layers, PIBAL 71-33, Polytechnic Institute of Brooklyn (November 1971).

[79] K. Stetson, Nosetip bluntness effects on cone frustum boundary layer transition in hypersonic flow, in: AIAA 16th Fluid and Plasma Dynamics Conference, American Institute of Aeronautics and Astronautics, 1983.

[80] P. Paredes, M. Choudhari, F. Li, J. Jewell, R. Kimmel, Nonmodal growth of traveling waves on blunt cones at hypersonic speeds, in: AIAA 2019 SciTech Forum, American Institute of Aeronautics and Astronautics, 2019.

[81] B. Wan, G. Tu, Effects of nose bluntness on entropy-layer stabilities over cones and wedges, Acta Mechanica Sinica 39 (1) (September 2022).

[82] P. Paredes, M. Choudhari, F. Li, Laminar-turbulent transition upstream of the entropy layer swallowing location in hypersonic boundary layers, in: AIAA Aviation 2019 Forum, American Institute of Aeronautics and Astronautics, 2019.

[83] E. Marineau, C. Moraru, D. Lewis, J. Norris, J. Lafferty, R. Wagnild, J. Smith, Mach 10 boundary-layer transition experiments on sharp and blunted cones, Astrophysical Journal Supplement Series 301 (2012).

[84] N. Rotta, Effects of nose bluntness on the boundary layer characteristics of conical bodies at hypersonic speeds, in: New York University Report, no. 66-66 in NYU-AA, 1966.

[85] K. Stetson, E. Thompson, J. Donaldson, Laminar boundary layer stability experiments on a cone at Mach 8, part 2: Blunt cone, in: AIAA 22nd Aerospace Sciences Meeting, American Institute of Aeronautics and Astronautics, 1984.

[86] K. Kara, P. Balakumar, O. Kandil, Effects of nose bluntness on hypersonic boundary-layer receptivity and stability over cones, American Institute of Aeronautics and Astronautics Journal 49 (12) (December 2011).

[87] K. Stetson, E. Thompson, J. Donaldson, Laminar boundary layer stability experiments on a cone at Mach 8, part 1: Sharp cone, in: AIAA 16th Fluid and Plasma Dynamics Conference, American Institute of Aeronautics and Astronautics, 1983.

[88] P. Balakumer, R. K. King, A. Chou, L. R. Owens, M. A. Kegerise, Receptivity and forced response to acoustic disturbances in high-speed boundary layers, American Institute of Aeronautics and Astronautics Journal 56 (2) (February 2018).

[89] P. Paredes, M. Choudhari, F. Li, J. Jewell, R. Kimmel, E. Marineau, G. Grossir, Nose-tip bluntness effects on transition at hypersonic speeds, Journal of Spacecraft and Rockets 56 (2) (March 2019).

[90] C. C. Lin, On the stability of two-dimensional parallel flows, Proceedings of the National Academy of Sciences 30 (10) (October 1944).

[91] R. Brown, On the physical mechanism of the inflection point instability, Journal of the Atmospheric Sciences 29 (July 1972).

[92] R. Greenwood, S. Schneider, Measurements of entropy-layer instabilities over a cone-ogive cylinder in a Mach-6 quiet tunnel, in: AIAA 2019 SciTech Forum, American Institute of Aeronautics and Astronautics, 2019.

[93] R. E. Kennedy, J. S. Jewell, P. Paredes, S. J. Laurence, Characterization of instability mechanisms on sharp and blunt slender cones at Mach 6, Journal of Fluid Mechanics 936 (January 2022).

[94] G. Grossir, F. Pinna, C. Olivier, Influence of nose-tip bluntness on conical boundary-layer instabilities at Mach 10, AIAA Journal 57 (9) (September 2019).

[95] A. Fedorov, Instability of the entropy layer on a blunt plate in supersonic gas flow, Journal of Applied Mechanics and Technical Physics 31 (1990).

[96] A. Fedorov, A. Tumin, Evolution of disturbances in entropy layer on blunted plate in supersonic flow, American Institute of Aeronautics and Astronautics Journal 42 (1) (January 2004).

[97] G. Dietz, S. Hein, Entropy layer instabilities over a blunted flat plate in supersonic flow, Physics of Fluids 11 (1) (January 1999).

[98] T. Ellingsen, E. Palm, Stability of linear flow, The Physics of Fluids 18 (4) (April 1975).

[99] L. H. Gustavsson, Initial-value problem for boundary layer flows, The Physics of Fluids 22 (9) (September 1979).

[100] M. T. Landahl, A note on an algebraic instability of inviscid parallel shear layers, Journal of Fluid Mechanics 98 (1980) 243–251.

[101] K. M. Butler, B. F. Farrell, Three-dimensional optimal perturbations in viscous shear flow, Physics of Fluids 4 (8) (1992).

[102] S. C. Reddy, D. S. Henningson, Energy growth in viscous channel flows, Journal of Fluid Mechanics 252 (1993) 209–238.

[103] P. Luchini, Reynolds-number-independent instability of the boundary layer over a flat surface, Journal of Fluid Mechanics 327 (1996) 101–115.

[104] P. Luchini, Reynolds-number-independent instability of the boundary layer over a flat surface: Optimal perturbations, Journal of Fluid Mechanics 404 (2000) 289–309.

[105] A. Tumin, E. Reshotko, Spatial theory of optimal disturbances in boundary layers, Physics of Fluids 13 (7) (2001).

[106] E. Reshotko, A. Tumin, Role of transient growth in roughness-induced transition, American Institute of Aeronautics and Astronautics Journal 42 (4) (2004).

[107] A. B. Hartman, C. Hader, H. F. Fasel, Nonlinear transition mechanism on a blunt cone at Mach 6: Oblique breakdown, Journal of Fluid Mechanics 915 (February 2021).

[108] L. Melander, A. Dwivendi, G. V. Candler, Nose bluntness effects on the amplification of external disturbances in hypersonic flows, in: AIAA SciTech, American Institute of Aeronautics and Astronautics, 2022.

[109] J. D. Crouch, A. Garbaruk, D. Magidov, Predicting the onset of flow unsteadiness based on global instability, Journal of Computational Physics 224 (2) (2007) 924–940.

[110] J.-P. Boin, J. Robinet, C. Corre, H. Deniau, 3d steady and unsteady bifurcations in a shockwave/laminar boundary layer interaction: A numerical study, Theoretical and Computational Fluid Dynamics 20 (2006) 163–180.

[111] J.-C. Robinet, Bifurcations in shockwave/laminar-boundary-layer interaction: Global instability approach, Journal of Fluid Mechanics 579 (2007).

[112] Y. Liu, M. Schuabb, L. Duan, P. Paredes, M. M. Choudhari, Interaction of a tunnel-like acoustic disturbance field with a blunt cone boundary layer at Mach 8, in: AIAA Aviation 2022 Forum, American Institute of Aeronautics and Astronautics, 2022.

[113] L. Duan, M. Choudhari, A. Chou, F. Munoz, R. Radspiel, T. Schilden, W. Schröder, E. Marineau, K. Casper, R. Chaudry, G. Candler, K. Gray, S. Schneider, Characterization of freestream disturbances in conventional hypersonic wind tunnels, Journal of Spacecraft and Rockets 56 (2) (March 2019).

[114] B. Wan, C. Su, J. Chen, Receptivity of a hypersonic blunt cone: Role of disturbances in the entropy layer, American Institute of Aeronautics and Astronautics Journal 58 (9) (September 2020).

[115] H. Goparaju, S. Unnikrishnan, D. V. Gaitonde, Effects of nose bluntness on hypersonic boundary-layer receptivity and stability, Journal of Spacecraft and Rockets 58 (3) (May 2021).

[116] Z. Wang, K. Fidkowski, R. Abgrall, F. Bassi, D. Caraeni, A. Cary, H. Deconinck, R. Hartmann, K. Hillewaert, H. Huynh, N. Kroll, G. May, P. Persson, B. Leer, M. Visbal, High-order CFD methods: Current status and perspective, International Journal for Numerical Methods in Fluids 72 (January 2013).

[117] L. Takacs, A two-step scheme for the advection equation with minimized dissipation and dispersion errors, Monthly Weather Review 113 (1988).

[118] J. W. Gibbs, Fourier's series, Nature 59 (1522) (1898).

[119] S. Yoon, D. Kwak, Artificial dissipation models for hypersonic external flow, in: 24th Joint Propulsion Conference, American Institute of Aeronautics and Astronautics, 1988.

[120] A. Harten, B. Engquist, S. Osher, S. R. Chakravarthy, Uniformly high order accurate essentially non-oscillatory schemes iii, Journal of Computational Physics 71 (2) (1987) 231–303.

[121] X.-D. Liu, S. Osher, T. Chan, Weighted essentially non-oscillatory schemes, Journal of Computational Physics 115 (1) (1994) 200–212.

[122] D. Ducros, V. Ferrand, F. Nicoud, C. Weber, D. Darracq, C. Gacherieu, T. Poinsot, Large-eddy simulation of the shock/turbulence interaction, Journal of Computational Physics 152 (1999) 517–549.

[123] J. Larsson, S. Lele, P. Moin, Effect of numerical dissipation on the predicted spectra for compressible turbulence, Annual Research Briefs (2007).

[124] G. Candler, M. Barnhardt, T. Drayna, I. Nompelis, D. Peterson, P. Subbareddy, Unstructed grid approaches for accurate aeroheating simulations, in: 18th AIAA Computational Fluid Dynamics Conference, Vol. 3959, 2007.

[125] P. K. Subbareddy, G. V. Candler, A fully discrete, kinetic energy consistent finite-volume scheme for compressible flows, Journal of Computational Physics 228 (5) (2009) 1347–1364.

[126] Y. Hourau, D. Pena, J. B. Vos, D. Charbonnier, A. Gehri, M. Braza, T. Deloze, E. Laurendeau, Recent developments in the navier-stokes multi-block (NSMB) CFD solver, in: 54th AIAA Aerospace Sciences Meeting, American Institute of Aeronautics and Astronautics, 2016.

[127] A. C. Laible, H. F. Fasel, Numerical investigation of hypersonic transition for a flared and a straight cone at Mach 6, in: 41st AIAA Fluid Dynamics Conference and Exhibit, American Institute of Aeronautics and Astronautics, 2011.

[128] B. van Leer, Flux-vector splitting for the euler equations, in: Eighth International Conference on Numerical Methods in Fluid Dynamics, Springer, 1982.

[129] G.-S. Jiang, C.-H. Shu, Efficient implementation of weighted eno schemes, Journal of Computational Physics 126 (1996).

[130] Z. M. Johnston, M. S. Hemati, V. Candler, G, Modal analysis of instabilities in the bolt-2 flowfield, in: AIAA SciTech Forum, American Institute of Aeronautics and Astronautics, 2022.

[131] T. Hendrickson, A. Kartha, G. V. Candler, An improved ducros sensor for the simulation of compressible flow with shocks, in: AIAA Aviation Forum, American Institute of Aeronautics and Astronautics, 2018.

[132] P. L. Roe, Approximate riemann solvers, parameter vectors and difference schemes, Journal of Computational Physics 43 (1981) 357–372.

[133] T. C. Fisher, M. H. Carpenter, J. Nordström, N. K. Yamaleev, C. Swanson, Discrete conservative finite-difference formulations for nonlinear conservation laws in split form: Theory and boundary conditions, Journal of Computational Physics 234 (September 2012).

[134] A. Honein, P. Moin, Higher entropy conservation and numerical stability of compressible turbulence simulations, Journal of Computational Physics 201 (2) (December 2004).

[135] J. A. White, R. A. Baurle, T. C. Fisher, J. R. Quinlan, W. S. Black, Low-dissipation advection schemes designed for large eddy simulations of hypersonic propulsion systems, 48th AIAA/ASME/SAE/ASEE Joint Propulsion Conference and Exhibit (September 2012).

[136] S. Spiegel, H. Huynh, J. DeBonis, A survey of the isentropic euler vortex problem using higher-order methods, in: 22nd AIAA Computational Fluid Dynamics Conference, American Institute of Aeronautics and Astronautics, 2015.

[137] Y. Wada, M.-S. Liou, An accurate and robust flux splitting scheme for shock and contact discontinuities, Journal of Scientific Computing (May 1997).

[138] P. L. Roe, J. Pike, Efficient reconstruction and utilisation of approximate riemann solutions, in: Proceedings of the 6th Int'l Symposium on Computing Methods in Applied Sciences and Engineering, VI, 1985, pp. 499–518.

[139] J. Edwards, A low-diffusion flux splitting scheme for navier-stokes calculations, Computers and Fluids 26 (6) (July 1997).

[140] M. Abramawitz, I. A. Stegun, Handbook of Mathemetical Functions with Formulas, Graphs, and Mathematical Tables, Vol. 55, United States Department of Commerce, 1972.

[141] L. D. Landau, E. M. Lifshitz, Fluid Mechanics, Pergamon Press, Headington Hill Hall, Oxford, England, 1987.

[142] G. I. Taylor, A. E. Green, Mechanism for the production of small eddies from large ones, Proceedings of the Royal Society of London 158 (1937).

[143] C. McNally, W. Lyra, J. Passy, A well-posed kelvin-helmholtz instability test and comparison, The Astrophysical Journal Supplement Series 201 (18) (AUGUST 2012).

[144] E. Johnsen, J. Larsson, A. Bhagatwala, W. Cabot, P. Moin, B. Olsen, P. Rawat, S. Shankar, B. Sjögreen, H. Yee, X. Zhong, S. Lele, Assessment of high-resolution methods for numerical simulations of compressible turbulence with shock waves, Journal of Computational Physics 229 (October 2010).

[145] G. D. van Albada, B. van Leer, W. W. J. Roberts, A comparative study of computational methods for cosmic gas dynamics, Astronomy and Astrophysics 108 (1) (April 1982).

[146] S. Chandrasekhar, Hydrodynamic and Hydromagnetic Instabilities, Clarendon Press, Oxford, 1961.

[147] L. Wang, C. Xue, W. Ye, Y. Li, Destabilizing effect of density gradient on the kelvin-helmholtz instability, Physics of Plasmas 16 (2009).

[148] J. Chen, T. Y. Hou, Stable nearly self-similar blowup of the 2d boussinesq and 3d euler equations with smooth data (2022). doi:10.48550/ARXIV.2210.07191.
URL https://arxiv.org/abs/2210.07191

[149] K. A. Damm, R. J. Gollan, P. A. Jacobs, M. K. Smart, S. Lee, E. Kim, C. Kim, Discrete adjoint optimization of a hypersonic inlet, AIAA Journal 58 (6) (June 2020).

[150] I. Johnston, Simulation of flow around hypersonic blunt-nosed vehicles for calibration of air data systems, Ph.D. thesis, School of Mechanical and Mining Engineering, University of Queensland (1999).

[151] P. Eiseman, K. Rajagopalan, Automatic topology generation, in: New Developments in Computational Fluid Dynamics. Notes on Numerical Fluid Mechanincs and Multidisciplinary Design (NNFM), Vol. 90, Springer.

[152] R. W. Clough, J. L. Tocher, Finite element stiffness matrices for analysis of plates in bending, in: Proceedings of the Conference on Matrix Methods in Structural Mechanics, 1965, pp. 515–545.

[153] J. J. Bertin, Hypersonic Aerothermodynamics, American Institute of Aeronautics and Astronautics, 1993.

[154] J. Jewell, R. Kimmel, Boundary-layer analysis for stetson's Mach 6 blunt-cone experiments, Journal of Spacecraft and Rockets 54 (1) (January 2017).

[155] J. S. Kim, O. J. Kwon, An efficient and robust implicit operator for upwind point gauss-seidel scheme, Journal of Computational Physics 224 (2007) 1124–1144.

[156] K. A. Damm, N. N. Gibbons, P. A. Jacobs, R. Gollan, Application of a jacobian-free newton-kryloc method to the simulation of hypersonic flows, in: AIAA Scitech 2023 Forum, American Institute of Aeronautics and Astronautics, 2023. doi:https://doi.org/10.2514/6.2023-2295.

[157] A. Chapman, Y. Saad, L. Wigton, High-order ILU preconditioners for CFD problems, International Journal for Numerical Methods in Fluids 33 (33) (2000).

[158] A. J. Smits, J.-P. Dussauge, Turbulent Shear Layers in Supersonic Flow: Second Edition, Springer, 2006.

[159] J. F. McKenzie, K. O. Westphal, Interaction of linear waves with oblique shock waves, Physics of Fluids 11 (11) (November 1968).

[160] R. E. Kennedy, E. K. Jadge, S. J. Laurence, J. S. Jewell, R. L. Kimmel, Visualizations of hypersonic boundary-layer transition on a variable bluntness cone, in: AIAA Aviation Forum, American Institute of Aeronautics and Astronautics, 2019.

[161] P. Paredes, M. M. Choudhari, F. Li, Mechanism for frustum transition over blunt cones at hypersonic speeds, Journal of Fluid Mechanics 894 (May 2020).

[162] T. Liang, S. Kafle, A. A. Khan, P. Paredes, J. Kuehl, On the inviscid energetics of mack's first mode instability, Theoretical and Computational Fluid Dynamics 37 (2023) 1–15.

[163] J. J. Kuehl, Thermoacoustic interpretation of second mode instability, American Institute of Aeronautics and Astronautics Journal 56 (9) (September 2018).

[164] F. Nicoud, T. Poinsot, Thermoacoustic instabilities: Should the rayleigh criterion be extended to include entropy changes?, Combustion and Flame 142 (2005) 153–159.

[165] B.-T. Chu, On the energy transfer to small disturbances in fluid flow, Acta Mechanica 1 (1965) 215–234.

[166] A. R. Berger, M. P. Borg, Study of bluntness-induced elongated structures in hypersonic flow over a 7° circular cone, in: AIAA SciTech 2023 Forum, American Institute of Aeronautics and Astronautics, 2023.